



**UNIVERSIDAD NACIONAL AUTÓNOMA DE MÉXICO**  
PROGRAMA DE MAESTRÍA Y DOCTORADO EN INGENIERÍA  
INGENIERÍA CIVIL – HIDRÁULICA

ANÁLISIS TEÓRICO Y NUMÉRICO DE LA INFLUENCIA DE LOS PARÁMETROS  
GEOMÉTRICOS DE UN DISPOSITIVO OWC EN SU DESEMPEÑO  
HIDRODINÁMICO

TESIS  
QUE PARA OPTAR POR EL GRADO DE:  
DOCTOR EN INGENIERÍA

PRESENTA:  
AYRTON ALFONSO MEDINA RODRÍGUEZ

TUTORES PRINCIPALES  
RODOLFO SILVA CASARÍN, INSTITUTO DE INGENIERÍA UNAM  
JESÚS MARÍA BLANCO ILZARBE, UNIVERSIDAD DEL PAÍS VASCO

COMITÉ TUTOR  
EDGAR GERARDO MENDOZA BALDWIN, INSTITUTO DE INGENIERÍA UNAM  
GREGORIO POSADA VANEGAS, UNIVERSIDAD AUTÓNOMA DE CAMPECHE  
LILIA REYES CHÁVEZ, INSTITUTO DE INGENIERÍA UNAM

CIUDAD DE MÉXICO, OCTUBRE 2021



Universidad Nacional  
Autónoma de México



**UNAM – Dirección General de Bibliotecas**  
**Tesis Digitales**  
**Restricciones de uso**

**DERECHOS RESERVADOS ©**  
**PROHIBIDA SU REPRODUCCIÓN TOTAL O PARCIAL**

Todo el material contenido en esta tesis esta protegido por la Ley Federal del Derecho de Autor (LFDA) de los Estados Unidos Mexicanos (México).

El uso de imágenes, fragmentos de videos, y demás material que sea objeto de protección de los derechos de autor, será exclusivamente para fines educativos e informativos y deberá citar la fuente donde la obtuvo mencionando el autor o autores. Cualquier uso distinto como el lucro, reproducción, edición o modificación, será perseguido y sancionado por el respectivo titular de los Derechos de Autor.

**JURADO ASIGNADO:**

Presidente: DRA. LILIA REYES CHAVEZ  
Secretario: DR. EDGAR GERARDO MENDOZA BALDWIN  
1 er. Vocal: DR. RODOLFO SILVA CASARIN  
2 do. Vocal: DR. GREGORIO POSADA VANEGAS  
3 er. Vocal: DR. JESÚS MARÍA BLANCO ILZARBE

Posgrado en ingeniería civil, UNAM, Ciudad de México, México

**TUTORES DE TESIS:**

Dr. Rodolfo Silva Casarín




---

**FIRMA**

Dr. Jesús María Blanco Ilzarbe

JESUS MARIA  
BLANCO ILZARBE  
- 29148328Z



Firmado digitalmente por JESUS MARIA BLANCO ILZARBE - 29148328Z  
Nombre de reconocimiento (DN): c=ES, o=LJPV - EHU, ou=Zurbitagi Professional - Certificado Profesional, 2.5.4.97=vATES-Q4818001B, cn=JESUS MARIA BLANCO ILZARBE - 29148328Z, givenName=JESUS MARIA, sn=BLANCO ILZARBE, serialNumber=29148328Z  
Fecha: 2021.10.12 18:19:48 +02'00'

---

**FIRMA**

# Contents

<b>List of figures</b>	<b>1</b>
<b>List of tables</b>	<b>7</b>
<b>Resumen</b>	<b>9</b>
<b>Abstract</b>	<b>12</b>
<b>1 Introduction</b>	<b>14</b>
1.1 Background . . . . .	14
1.2 Wave energy . . . . .	14
1.3 Wave energy technology . . . . .	16
1.3.1 Working principle . . . . .	17
1.3.2 Orientation . . . . .	18
1.3.3 Power take-off mechanism . . . . .	18
1.3.4 Application . . . . .	20
<b>2 Thesis</b>	<b>23</b>
2.1 Motivation . . . . .	23
2.2 General objective . . . . .	24
2.2.1 Specific objectives . . . . .	24
2.3 Thesis outline . . . . .	25
2.4 List of published and submitted articles included in the thesis . . . . .	26
2.4.1 Additional works related to the thesis but not included . . . . .	26
2.5 Comments . . . . .	27
<b>3 Literature review</b>	<b>28</b>
3.1 Oscillating Water Column device . . . . .	28
3.1.1 Background . . . . .	29
3.1.2 Review of research studies . . . . .	32
3.2 Environmental impacts . . . . .	34
3.3 Economics of wave energy . . . . .	35

<b>4</b>	<b>Background theory</b>	<b>44</b>
4.1	Ocean Waves . . . . .	44
4.2	Water Wave Mechanics . . . . .	45
4.2.1	Dispersion Relationship . . . . .	45
4.2.2	Water Wave Motions . . . . .	46
4.3	Review of hydrodynamics . . . . .	47
4.3.1	Conservation of mass . . . . .	47
4.3.2	Conservation of Momentum and Energy . . . . .	48
4.3.3	Velocity Potential . . . . .	49
4.3.4	The Bernoulli equation . . . . .	50
4.4	Linear wave theory . . . . .	51
4.4.1	Governing equation . . . . .	52
4.4.2	Boundary Conditions . . . . .	52
<b>5</b>	<b>The Influence of the Front Wall Thickness on the Hydrodynamic Efficiency of a Land-Fixed OWC Device</b>	<b>57</b>
5.1	Introduction . . . . .	58
5.2	Aims and Methodology . . . . .	62
5.3	The Boundary-Value Problem . . . . .	63
5.4	Solution . . . . .	68
5.5	Results and Discussion . . . . .	74
5.5.1	Front Wall Thickness . . . . .	75
5.5.2	Bottom Profile . . . . .	82
5.6	Conclusions . . . . .	86
<b>6</b>	<b>The Effect of Oblique Waves on the Hydrodynamic Efficiency of a Land-Fixed OWC device</b>	<b>92</b>
6.1	Introduction . . . . .	93
6.2	Problem Formulation . . . . .	97
6.3	Solution method . . . . .	101
6.3.1	Matched Eigenfunction Expansion Method . . . . .	101
6.3.2	Boundary Element Method . . . . .	104
6.4	Convergence study . . . . .	108
6.5	Validation . . . . .	108
6.6	Results and Discussion . . . . .	109
6.6.1	Effect of the angle of incidence . . . . .	110
6.6.2	Effect of the chamber configuration . . . . .	114
6.6.3	Influence of the trapped air inside the OWC chamber . . . . .	114
6.7	Conclusions . . . . .	117

---

<b>7</b>	<b>The Influence of the Chamber Configuration on the Efficiency of a Fixed-Detached OWC Device</b>	<b>124</b>
7.1	Introduction . . . . .	125
7.2	Boundary value problem . . . . .	128
7.3	Solution method . . . . .	130
7.3.1	Matched Eigenfunction Expansion Method . . . . .	130
7.3.2	Boundary Element Method . . . . .	136
7.4	Efficiency relations . . . . .	138
7.5	Convergence and truncation analyses . . . . .	141
7.6	Comparison with experimental results . . . . .	142
7.7	Results and Discussion . . . . .	143
7.7.1	Asymmetric fixed-detached OWC device over a flat bottom . . . . .	143
7.7.2	Asymmetric fixed-detached OWC device over a step . . . . .	149
7.7.3	Asymmetric fixed-detached OWC device near a reflecting wall . . . . .	149
7.8	Conclusions . . . . .	155
<b>8</b>	<b>The Effects of Directional Waves and Chamber Configuration on the Efficiency of an OWC Device</b>	<b>162</b>
8.1	Introduction . . . . .	163
8.2	Boundary value problem . . . . .	167
8.3	Solution method . . . . .	169
8.3.1	Matched Eigenfunction Expansion Method . . . . .	169
8.3.2	Boundary Element Method . . . . .	173
8.4	Efficiency relations . . . . .	176
8.5	Results and Discussion . . . . .	178
8.5.1	Convergence analysis . . . . .	178
8.5.2	Validation . . . . .	179
8.5.3	Effect of the chamber configuration . . . . .	179
8.5.4	Effect of the wave angle of incidence . . . . .	183
8.5.5	Influence of the trapped air inside the OWC chamber . . . . .	185
8.5.6	Case of study: the MWEP . . . . .	185
8.6	Conclusions . . . . .	192
8.7	Appendix . . . . .	193
<b>9</b>	<b>A Three-Dimensional Analysis of the Hydrodynamic Performance of a Land-Fixed OWC Device</b>	<b>200</b>
9.1	Introduction . . . . .	201
9.2	Boundary value problem . . . . .	204
9.3	Efficiency relations . . . . .	207
9.4	Method of solution . . . . .	209
9.4.1	Boundary Element Method . . . . .	209

9.5	Truncation and convergence analyses . . . . .	213
9.6	Comparison with previous results . . . . .	215
9.7	Results and Discussion . . . . .	217
9.8	Conclusions . . . . .	227
<b>10</b>	<b>Conclusion</b>	<b>235</b>
10.1	Overall conclusions . . . . .	235
10.2	Original contributions . . . . .	236
10.3	Recommendations for future work . . . . .	237

# List of Figures

1.1	Global annual mean wave power density (colour) and annual mean best direction (arrows), taken from <a href="#">Gunn and Stock-Williams (2012)</a> . . . . .	15
1.2	Technologies for harnessing wave energy, adapted from <a href="#">Falcão (2010)</a> . . .	16
1.3	Types of WECs depending on their working principle, adapted from <a href="#">Sergiienko (2018)</a> . . . . .	17
1.4	Schematic diagram of the types of WECs depending on their size and orientation relative to the incident wave direction. . . . .	18
1.5	Different main paths for wave energy to electricity conversion, adapted from <a href="#">Pecher and Kofoed (2017b)</a> . . . . .	19
3.1	Schematic layout of oscillating water column system. . . . .	29
3.2	The Kaimei device ( <a href="#">Falcão and Henriques; 2016</a> ). . . . .	30
3.3	Shoreline OWC device on the island of Islay, Scotland ( <a href="#">Falcão and Henriques; 2016</a> ). . . . .	31
3.4	Shoreline and nearshore cost split, adapted from <a href="#">The Carbon Trust (2005)</a> . . . . .	37
4.1	The types of waves that may occur in the ocean, adapted from <a href="#">World Meteorological Organisation (1998)</a> . . . . .	45
4.2	Chart of wave model suitability, adapted from <a href="#">Pecher and Kofoed (2017)</a> . . . . .	46
4.3	Classification of progressive waves based on their wavelength relative to the depth of water through which they are passing, adapted from <a href="#">Garrison (2009)</a> . . . . .	47
4.4	Two-dimensional water waves specified as a BVP, adapted from <a href="#">Dean and Dalrymple (1991)</a> . . . . .	53
5.1	Location and turbo-generators of the MWEP. <b>(a)</b> Location of the harbour at Mutriku (source: Google Maps ( <a href="#">Google Maps 2020; n.d.</a> )). <b>(b)</b> Bird's eye view of Mutriku harbour and the OWC-breakwater system. (source: geoEuskadi ( <a href="#">GeoEuskadi, Infraestructura de Datos Espaciales (IDE) de Euskadi; n.d.</a> )). <b>(c)</b> Mutriku Wells Turbo-generators (source: EVE ( <a href="#">Ente Vasco de la Energía; n.d.</a> )). . . . .	60



5.2	Comparison between the original and the present-day design of the integrated breakwater-OWC system in Mutriku. (a) View of the MWEP in 2008 (Reproduced with permission from <a href="#">Torre-Enciso et al. (2009)</a> ). (b) Mutriku OWC (source: EVE ( <a href="#">Ente Vasco de la Energía</a> ; n.d.)). . . . .	61
5.3	Definition sketch of an OWC device with a thick front wall. . . . .	64
5.4	Schematic diagram of the modeling of the boundary with quadratic elements. . . . .	70
5.5	Boundary element discretization of the composite domain. (a) Separation of the BVP into three regions. (b) Discretization of the three regions. . . . .	75
5.6	Hydrodynamic efficiency versus $Kh$ . (a) For various thickness ratios $w/b$ with $h_a/h = 0.125$ and $b/h = 1.0$ . (b) For different submergence ratios $h_a/h$ with $w/b = 1.0$ and $b/h = 1.0$ . . . . .	76
5.7	The radiation susceptance and radiation conductance coefficients versus $Kh$ . (a) The radiation susceptance coefficient for various thickness ratios $w/b$ with $h_a/h = 0.125$ and $b/h = 1.0$ . (b) The radiation conductance coefficient for various thickness ratios $w/b$ with $h_a/h = 0.125$ and $b/h = 1.0$ . (c) The radiation susceptance coefficient for different submergence ratios $h_a/h$ with $w/b = 1.0$ and $b/h = 1.0$ . (d) The radiation conductance coefficient for different submergence ratios $h_a/h$ with $w/b = 1.0$ and $b/h = 1.0$ . . . . .	79
5.8	Hydrodynamic efficiency versus $Kh$ . (a) For various wall to front barrier spacing ratios $b/h$ with $h_a/h = 0.125$ and $w/b = 1.0$ . (b) For various step to bottom ratios $h_e/h$ with $h_a/h = 0.125$ , $b/h = 1.0$ and $w/b = 1.0$ . . . . .	80
5.9	The radiation susceptance and radiation conductance coefficients versus $Kh$ . (a) The radiation susceptance coefficient for various wall to front barrier spacing ratios $b/h$ with $h_a/h = 0.125$ and $w/b = 1.0$ . (b) The radiation conductance coefficient for various wall to front barrier spacing ratios $b/h$ with $h_a/h = 0.125$ and $w/b = 1.0$ . (c) The radiation susceptance coefficient for various step to bottom ratios $h_e/h$ with $h_a/h = 0.125$ , $b/h = 1.0$ and $w/b = 1.0$ . (d) The radiation conductance coefficient for various step to bottom ratios $h_e/h$ with $h_a/h = 0.125$ , $b/h = 1.0$ and $w/b = 1.0$ . . . . .	81
5.10	Hydrodynamic efficiency versus (a) $Kh$ and (b) $kh$ . (a) Comparison with experimental results obtained by <a href="#">Morris-Thomas et al. (2006)</a> for a thick front wall. (b) Comparison with experimental and numerical results obtained by <a href="#">Wang et al. (2018)</a> . . . . .	82
5.11	Definition sketch of a single chamber in the Mutriku Wave Energy Plant (Dimensions in meters. Chamber width = 4.5 m; HEST = Highest equinoctial spring tide and LEST = Lowest equinoctial spring tide). . . . .	83
5.12	Hydrodynamic efficiency versus period $T$ for different values of linear turbine damping coefficient $\Lambda$ , without considering the step. . . . .	84

5.13	Hydrodynamic efficiency in the cases of HEST and LEST versus $T$ for different bottom profiles. <b>(a)</b> Maximum efficiency versus $T$ with $\varrho = 0$ for various bottom profiles with $h = 7.90$ , $h_a/h = 0.646$ , $b/h = 0.392$ and $w/b = 2.145$ in the case of the HEST. <b>(b)</b> Maximum efficiency versus $T$ for various bottom profiles with $h = 7.90$ , $h_a/h = 0.646$ , $b/h = 0.392$ and $w/b = 2.145$ . in the case of the HEST. <b>(c)</b> Maximum efficiency versus $T$ with $\varrho = 0$ for various bottom profiles with $h = 3.40$ , $h_a/h = 0.176$ , $b/h = 0.392$ and $w/b = 2.145$ in the case of the LEST. <b>(d)</b> Maximum efficiency versus $T$ for various bottom profiles with $h = 3.40$ , $h_a/h = 0.176$ , $b/h = 0.392$ and $w/b = 2.145$ in the case of the LEST. . . . .	85
6.1	Definition sketch of the interaction of an OWC device with oblique waves.	98
6.2	BVP discretization. <b>(a)</b> Two-region domain. <b>(b)</b> Discretization of the two regions. . . . .	107
6.3	Maximum hydrodynamic efficiency versus non-dimensional frequencies $Kh$ with $\theta = 0^\circ$ . Comparison with previous results obtained by <a href="#">Evans and Porter (1995)</a> <b>(a)</b> For $b/h = 1.0$ and $h_a/h = 0.125$ and $0.5$ . <b>(b)</b> For $h_a/h = 0.5$ and $b/h = 0.25$ and $0.5$ . . . . .	109
6.4	Maximum hydrodynamic efficiency versus $Kh$ for different incidence wave angles $\theta$ . <b>(a)</b> For $h_a/h = 0.125$ and $b/h = 1.0$ . <b>(b)</b> For $h_a/h = 0.25$ and $b/h = 0.5$ . <b>(c)</b> For $h_a/h = 0.5$ and $b/h = 0.75$ . . . . .	111
6.5	Maximum hydrodynamic efficiency versus $\theta$ with $Kh = 0.625$ , $1.25$ and $2.50$ . <b>(a)</b> For $h_a/h = 0.125$ and $b/h = 1.0$ . <b>(b)</b> For $h_a/h = 0.25$ and $b/h = 0.5$ . <b>(c)</b> For $h_a/h = 0.5$ and $b/h = 0.75$ . . . . .	112
6.6	Maximum hydrodynamic efficiency as function of $\theta$ and $Kh$ . <b>(a)</b> - <b>(b)</b> For $h_a/h = 0.125$ and $b/h = 1.0$ . <b>(c)</b> - <b>(d)</b> For $h_a/h = 0.25$ and $b/h = 0.5$ . <b>(e)</b> - <b>(f)</b> For $h_a/h = 0.5$ and $b/h = 0.75$ . . . . .	113
6.7	Maximum hydrodynamic efficiency versus $Kh$ for different wall to front barrier spacing ratios $b/h$ and for different submergence ratios $h_a/h$ . <b>(a)</b> For $h_a/h = 0.125$ and $\theta = 45^\circ$ . <b>(b)</b> For $b/h = 1.0$ and $\theta = 45^\circ$ . <b>(c)</b> For $h_a/h = 0.25$ and $\theta = 30^\circ$ . <b>(d)</b> For $b/h = 0.5$ and $\theta = 30^\circ$ . <b>(e)</b> For $h_a/h = 0.5$ and $\theta = 15^\circ$ . <b>(f)</b> For $b/h = 0.75$ and $\theta = 15^\circ$ . . . . .	115
6.8	Maximum hydrodynamic efficiency with $h_a/h = 0.125$ and $b/h = 1.0$ . <b>(a)</b> Versus $Kh$ for different air column ratios $h_c/b$ and $\theta = 45^\circ$ . <b>(b)</b> Versus $Kh$ for different angles of incidence $\theta$ with $h_c/b = 1.0$ . <b>(c)</b> Versus $Kh$ and $\theta$ with $h_c/b = 1.0$ . . . . .	116
7.1	Side view of the interaction of a fixed-detached OWC device with water waves. . . . .	128
7.2	Side view of the interaction of water waves with a fixed-detached OWC device near a vertical wall. . . . .	136

7.3	Meshing and matching of the regions with nodes arranged in an anti-clockwise direction. . . . .	137
7.4	Comparison of the present results for the hydrodynamic efficiency $\eta_{max}$ with the experimental results obtained by He et al. (2016) for a pile-supported OWC device and He and Huang (2016) for an OWC device near a reflecting vertical wall. . . . .	143
7.5	Maximum hydrodynamic efficiency $\eta_{max}$ versus the non-dimensional frequency $Kh$ for different (a) lengths of the OWC chamber $b/h$ , (b) thickness of the rear and front walls, $w_1/h$ and $w_2/h$ , respectively. (c) thickness of the rear wall $w_1/h$ and (d) thickness of the front wall $w_2/h$ . . . . .	144
7.6	Maximum hydrodynamic efficiency $\eta_{max}$ versus the non-dimensional frequency $Kh$ for different (a) submergence depths of the rear and front walls, $a_1/h$ and $a_2/h$ , respectively. (b) submergence depths of the front wall $a_2/h$ and (c) submergence depths of the rear wall $a_1/h$ . . . . .	146
7.7	The influence of chamber length $b/h$ on the (a) radiation susceptance coefficient, (b) radiation conductance coefficient and (c) non-dimensional induced volume flux due to the scattering potential against $Kh$ with $a_1/h = a_2/h = 1/2$ and $w_1/h = w_2/h = 1/8$ . . . . .	147
7.8	Maximum hydrodynamic efficiency $\eta_{max}$ versus the non-dimensional frequency $Kh$ for different (a) lengths of the OWC chamber $b/h$ , (b) thickness of the rear and front walls, $w_1/h$ and $w_2/h$ , respectively. (c) thickness of the rear wall $w_1/h$ and (d) thickness of the front wall $w_2/h$ . . . . .	148
7.9	Maximum hydrodynamic efficiency $\eta_{max}$ versus the non-dimensional frequency $Kh$ for different (a) submergence depths of the rear and front walls, $a_1/h$ and $a_2/h$ , respectively. (b) submergence depths of the front wall $a_2/h$ and (c) submergence depths of the rear wall $a_1/h$ . . . . .	150
7.10	The influence of the thickness in the rear and front walls, $w_1/h$ and $w_2/h$ , respectively, on the (a) radiation susceptance coefficient, (b) radiation conductance coefficient and (c) non-dimensional induced volume flux due to the scattering potential against $Kh$ with $a_1/h = a_2/h = 1/2$ , $b/h = 3/4$ and $h_e/h = 3/4$ . . . . .	151
7.11	Maximum hydrodynamic efficiency $\eta_{max}$ versus the non-dimensional frequency $Kh$ for different (a) lengths of the OWC chamber $b/h$ , (b) thickness of the rear and front walls, $w_1/h$ and $w_2/h$ , respectively. (c) thickness of the rear wall $w_1/h$ and (d) thickness of the front wall $w_2/h$ . . . . .	153
7.12	Maximum hydrodynamic efficiency $\eta_{max}$ versus the non-dimensional frequency $Kh$ for different (a) submergence depths of the rear and front walls, $a_1/h$ and $a_2/h$ , respectively. (b) submergence depths of the front wall $a_1/h$ and (c) submergence depths of the rear wall $a_2/h$ . . . . .	154

7.13	The influence of the length of the gap between the rear and reflecting walls $L/h$ on the maximum hydrodynamic efficiency $\eta_{max}$ versus the non-dimensional frequency $Kh$ with $a_1/h = a_2/h = 1/8$ , $b/h = 1$ and $w_1/h = w_2/h = 1/8$ . . . . .	155
7.14	The influence of the length of the gap between the rear and reflecting walls $L/h$ on the (a) radiation susceptance coefficient, (b) radiation conductance coefficient and (c) non-dimensional induced volume flux due to the scattering potential against $Kh$ with $a_1/h = a_2/h = 1/8$ , $b/h = 1$ and $w_1/h = w_2/h = 1/8$ . . . . .	156
8.1	Definition sketch of the interaction of a thick front barrier OWC device with oblique waves. . . . .	168
8.2	Discretization and matching of the regions. . . . .	175
8.3	Maximum hydrodynamic efficiency versus non-dimensional frequencies $Kh$ compared with previous results obtained by <a href="#">Evans and Porter (1995)</a> and <a href="#">Medina Rodríguez et al. (2020)</a> . (a) For $b/h = 1.0$ , $h_a/h = 0.125$ , $\theta = 0^\circ$ and different $w/b$ ratios. (b) For $h_a/h = 0.5$ , $w/b = 0.01$ and various $b/h$ ratios. . . . .	180
8.4	Maximum hydrodynamic efficiency versus $Kh$ for different incidence wave angles $\theta$ with $h_a/h = 0.125$ and $b/h = 1.0$ . (a) For $w/b = 0.5$ . (b) For $w/b = 1.0$ . (c) For $w/b = 1.5$ . (d) For $w/b = 2.0$ . . . . .	181
8.5	Maximum hydrodynamic efficiency versus $Kh$ for different incidence wave angles $\theta$ with $h_a/h = 0.125$ and $w/b = 1.0$ . (a) For $b/h = 3/4$ . (b) For $b/h = 1/2$ . (c) For $b/h = 1/4$ . (d) For $b/h = 1/8$ . . . . .	182
8.6	Maximum hydrodynamic efficiency versus $Kh$ with $b/h = 1.0$ and $w/b = 1.0$ . (a) For $h_a/h = 1/4$ . (b) For $h_a/h = 1/2$ . (c) For $h_a/h = 3/4$ . . . . .	183
8.7	Maximum hydrodynamic efficiency versus $\theta$ for different non-dimensional frequencies $Kh$ with $h_a/h = 0.125$ and $b/h = 1.0$ . (a) For $w/b = 0.5$ . (b) For $w/b = 1.0$ . (c) For $w/b = 1.5$ . (d) For $w/b = 2.0$ . . . . .	184
8.8	Numerical results for the maximum hydrodynamic efficiency as function of $\theta$ and $Kh$ with $h_a/h = 0.125$ and $b/h = 1.0$ . (a)-(b) For $w/b = 0.01$ . (c)-(d) For $w/b = 0.5$ . (e)-(f) For $w/b = 1.0$ . . . . .	186
8.8	Numerical results for the maximum hydrodynamic efficiency as function of $\theta$ and $Kh$ with $h_a/h = 0.125$ and $b/h = 1.0$ . (g)-(h) For $w/b = 1.5$ . (i)-(j) For $w/b = 2.0$ . . . . .	187
8.9	Maximum hydrodynamic efficiency versus $Kh$ for different air column height to water depth ratios $h_c/h$ with $h_a/h = 0.125$ , $b/h = 1.0$ and $w/b = 1.0$ . (a) For $h_c/h = 0.75$ . (b) For $h_c/h = 1.0$ . (c) For $h_c/h = 1.5$ . (d) For $h_c/h = 2.0$ . . . . .	188

8.10	Sketch of a single chamber in the MWEP for the highest and lowest equinoctial spring tides, HEST (black dimensions) and LEST (gray dimensions), respectively. . . . .	189
8.11	Maximum hydrodynamic efficiency versus $Kh$ for different incidence wave angles $\theta$ in the case of HEST. <b>(a)</b> - <b>(b)</b> For $h_a/h = 0.59$ , $b/h = 0.39$ , $w/h = 0.21$ and $h_c/h = 0$ and $h_c/h = 0.66$ , respectively. <b>(c)</b> - <b>(d)</b> For $h_a/h = 0.65$ , $b/h = 0.39$ , $w/h = 0.84$ and $h_c/h = 0$ and $h_c/h = 0.66$ , respectively. . . . .	190
8.12	Maximum hydrodynamic efficiency versus $Kh$ for different incidence wave angles $\theta$ in the case of LEST. <b>(a)</b> - <b>(b)</b> For $h_a/h = 0.06$ , $b/h = 0.91$ , $w/h = 0.48$ and $h_c/h = 0$ and $h_c/h = 2.85$ , respectively. <b>(c)</b> - <b>(d)</b> For $h_a/h = 0.18$ , $b/h = 0.91$ , $w/h = 1.96$ and $h_c/h = 0$ and $h_c/h = 2.85$ , respectively. . . . .	191
9.1	Definition sketch of the 3D interaction of a land-fixed OWC device with perpendicular incident waves. . . . .	205
9.2	BVP discretization. <b>(a)</b> Discretization of Region 1 which is conformed by the OWC chamber and the gap below the front barrier. <b>(b)</b> Nine-noded quadrilateral element (nodes are ordered in the anticlockwise direction). . . . .	210
9.3	Matching of the regions on the gap at $x = L$ . . . . .	212
9.4	Hydrodynamic efficiency against the length of Region 2 with $a/h = 1/2$ , $b/h = 1$ , $w/h = 1/2$ and $d/h = 1/2$ . . . . .	214
9.5	Hydrodynamic efficiency against the non-dimensional frequency $Kh$ and wave period $T$ . . . . .	216
9.6	Capture width with $a/h = 1/2$ , $b/h = 1$ and $w/h = 1/2$ versus $Kh$ for different chamber width to water depth ratios $d/h(= 1/4, 1/2, 1$ and $2)$ . . . . .	218
9.7	Free surface elevation with $a/h = 1/2$ , $b/h = 1$ , $w/h = 1/2$ and $d/h = 1/2$ at the resonant peak frequency. . . . .	218
9.8	Capture width and radiation conductance and susceptance coefficients with $a/h = 1/2$ , $w/h = 1/2$ and $d/h = 1/2$ versus $Kh$ for different chamber length to water depth ratios $b/h(= 1/4, 1/2, 3/4$ and $1)$ . . . . .	219
9.9	Free surface elevation with $a/h = 1/2$ , $w/h = 1/2$ and $d/h = 1/2$ . . . . .	221
9.10	Capture width and radiation conductance and susceptance coefficients with $b/h = 1$ , $w/h = 1/2$ and $d/h = 1/2$ versus $Kh$ for different front barrier draft to water depth ratios $a/h(= 1/8, 1/4, 1/2$ and $3/4)$ . . . . .	222
9.11	Free surface elevation with $b/h = 1$ , $w/h = 1/2$ and $d/h = 1/2$ . . . . .	224
9.12	Capture width and radiation conductance and susceptance coefficients with $b/h = 1$ , $a/h = 1/2$ and $d/h = 1/2$ versus $Kh$ for different front wall thickness to water depth ratios $w/h(= 1/8, 1/4, 1/2$ and $1)$ . . . . .	225
9.13	Free surface elevation with $b/h = 1$ , $a/h = 1/2$ and $d/h = 1/2$ . . . . .	226

9.14 Capture width with  $b/h = 1$ ,  $w/h = 1/2$  and  $d/h = 1/2$  against  $Kh$  for different ari column height to water depth ratios  $c/h = (1/2, 3/4, 1 \text{ and } 3/2)$ . . . . . 227

9.15 Free surface elevation with  $b/h = 1$ ,  $a/h = 1/2$ ,  $w/h = 1/2$  and  $d/h = 1/2$ . 228

10.1 Numerical wave generation in OpenFOAM **(a)** Velocity magnitude and **(b)** Hydrostatic pressure of the interaction of water waves with a thick front barrier OWC device. . . . . 237

10.2 **(a)** Model scale of a thick front barrier OWC device and **(b)-(c)** testing in the multidirectional wave tank of the Autonomous University of Campeche. 238

# List of Tables

3.1	Interactions between devices and the surrounding environment, with the expected adverse impact intensity: ● No impact, ● Very low, ● Low, ● Medium, ● High, adapted from <a href="#">Mendoza et al. (2019)</a> . . . . .	35
5.1	Values of hydrodynamic efficiency $\eta_{max}$ , radiation susceptance coefficient $\mu$ and radiation conductance coefficient $\nu$ computed for different number of nodes $N$ with $h_a/h = 0.125$ , $b/h = 1.0$ and $w/b = 0.5$ . . . . .	75
6.1	Summary of past investigations on non-cylindrical OWCs. . . . .	94
6.2	Values of the maximum hydrodynamic efficiency $\eta_{max}$ , radiation susceptance coefficient $\mu$ and radiation conductance coefficient $\nu$ computed for different number of evanescent modes $N_{em}$ with $h_a/h = 0.125$ , $b/h = 1.0$ and $\theta = 0^\circ$ . . . . .	108
6.3	Values of the maximum hydrodynamic efficiency $\eta_{max}$ , radiation susceptance coefficient $\mu$ and radiation conductance coefficient $\nu$ computed for different number of nodes $N$ with $h_a/h = 0.125$ , $b/h = 1.0$ and $\theta = 45^\circ$ . . . . .	109
7.1	Convergence of the maximum hydrodynamic efficiency $\eta_{max}$ computed by using the EEM for different number of evanescent modes $N$ with $a_1/h = a_2/h = 0.5$ , $w_1/h = w_2/h = 0.125$ , $b/h = 1.0$ and $h_e/h = 1$ without the reflecting vertical wall. . . . .	141
7.2	Calculation of the maximum hydrodynamic efficiency $\eta_{max}$ by using the BEM for different distances at which the left and right radiation boundaries are truncated $a_1/h = a_2/h = 0.5$ , $w_1/h = w_2/h = 0.125$ , $b/h = 1.0$ and $h_e/h = 1$ without the reflecting vertical wall. . . . .	141
7.3	Convergence of the maximum hydrodynamic efficiency $\eta_{max}$ computed for different numbers of nodes $N_{bem}$ with $a_1/h = a_2/h = 0.5$ , $w_1/h = w_2/h = 0.125$ , $b/h = 1.0$ and $h_e/h = 1$ without the reflecting vertical wall. . . . .	142
8.1	Maximum hydrodynamic efficiency $\eta_{max}$ computed for different number of evanescent modes $N_{em}$ with $h_a/h = 0.125$ , $b/h = 1.0$ , $w/b = 1.0$ and $\theta = 60^\circ$ . . . . .	178

8.2	Maximum hydrodynamic efficiency $\eta_{max}$ computed for different number of nodes $N$ with $h_a/h = 0.125$ , $b/h = 1.0$ , $w/b = 1.0$ and $\theta = 60^\circ$ . . . . .	179
9.1	Maximum hydrodynamic efficiency $\eta_{max}$ , radiation susceptance $\mu$ and radiation conductance $\nu$ computed for different number of nodes $N$ and average distance between two neighbouring nodes $\bar{d}s$ with $a/h = 1/2$ , $b/h = 1$ , $w/h = 1/2$ and $d/h = 1/2$ . . . . .	215
9.2	Maximum hydrodynamic efficiency $\eta_{max}$ , radiation susceptance $\mu$ and radiation conductance $\nu$ computed for different number of nodes $N$ and average distance between two neighbouring nodes $\bar{d}s$ with $a/h = 1/2$ , $b/h = 1$ , $w/h = 1/2$ and $d/h = 2$ . . . . .	215



# Resumen

El cambio climático, como resultado de la contaminación por combustibles fósiles, el crecimiento de la población y el aumento del consumo de energía, requiere la exploración y aprovechamiento de recursos energéticos renovables. Debido a su mayor densidad energética en comparación con otras fuentes renovables, la energía proveniente del oleaje ha sido propuesta como un recurso potencial para mitigar los impactos del calentamiento global. Sin embargo, a pesar de ser una de las fuentes más abundantes de energía renovable, la energía del oleaje permanece en su mayor parte desaprovechada. Esto se debe a una mayor tendencia hacia otras energías renovables, una financiación limitada para su investigación, la inmadurez de las tecnologías actuales y la falta de una tecnología fiable y rentable para su extracción.

En este sentido, el dispositivo de Columna de Agua Oscilante o por sus siglas en inglés OWC (Oscillating Water Column) es un sistema esencial para la extracción de energía del oleaje. Debido a su principio de funcionamiento simple y su adaptabilidad, se puede utilizar como una estructura fija (costera) o flotante (en alta mar). Para un funcionamiento óptimo, la cámara del dispositivo OWC juega un papel importante para lograr un mejor rendimiento. Normalmente, la configuración de la cámara se elige para producir una columna de agua con una frecuencia natural de oscilación que coincida con la del oleaje más común en el área donde se desplegará el sistema. Sin embargo, la variabilidad de las condiciones del mar, como la direccionalidad del oleaje, los cambios en la profundidad debido a las variaciones de las mareas y las altas fuerzas ejercidas por oleaje en condiciones extremas, pueden comprometer el correcto funcionamiento del dispositivo. Por lo tanto, para garantizar un funcionamiento adecuado, la configuración de la cámara OWC debe ajustarse de manera eficiente en relación con su entorno.

El enfoque principal de esta tesis es hacia el análisis de la configuración de la cámara OWC, la dirección del oleaje incidente y la compresibilidad del aire dentro de la cámara con el fin de responder a tres preguntas: (i) ¿Qué influencia tiene el espesor de la pared frontal en la eficiencia hidrodinámica?; (ii) ¿Cómo afecta la dirección del oleaje incidente al rendimiento del sistema?; y considerando estos dos últimos aspectos (iii) ¿Qué efecto tiene la compresibilidad del aire sobre el rendimiento hidrodinámico?

Para explorar estos aspectos, se han desarrollado modelos analíticos y numéricos en el dominio de la frecuencia utilizando técnicas teóricas basadas en la teoría de línea del

oleaje. El primero es el método semi-analítico de expansión de funciones características (eigenfunction expansion method, EEM, por sus siglas en inglés), que utiliza la continuidad del potencial de velocidades y el flujo, así como la propiedad ortogonal de las funciones características, para reducir el problema de valores en la frontera (boundary value problem, BVP, por sus siglas en inglés) a un sistema lineal de ecuaciones algebraicas. El otro es el método del elementos de frontera (boundary element method, BEM, por sus siglas en inglés), que es un enfoque numérico basado en la aplicación de una ecuación integral. En este caso, el BEM con elementos de orden superior se utiliza para obtener la variación de potencial y flujo en las fronteras del dominio.

A lo largo de esta tesis, cinco estudios se describen. En primer lugar, se investigan los efectos en el rendimiento debido al espesor de la pared frontal y los perfiles del fondo de la cámara usando el BEM. Los resultados demuestran que el uso de una barrera frontal gruesa tiene un impacto significativo en la eficiencia hidrodinámica. Esto se explica por el hecho de que la transmisión de energía del oleaje incidente hacia la columna de agua interna debido al movimiento orbital de las partículas de agua se reduce para barreras gruesas. Después, se investiga la interacción de oleaje oblicuo con un dispositivo OWC fijo en tierra. Los resultados en este caso indicaron que al aumentar el ángulo de incidencia del oleaje, la frecuencia a la que se produce la resonancia aumenta, lo que ofrece beneficios para la extracción de energía en dispositivos fijos en condiciones donde la dirección del oleaje varía.

Posteriormente, se lleva a cabo un análisis para investigar los cambios en las curvas de eficiencia y la frecuencia de resonancia causados por diferentes configuraciones de la pared posterior y frontal de un dispositivo OWC asimétrico fijo-flotante. Después, se examinan la oblicuidad del oleaje y el grosor de la barrera frontal para analizar su influencia combinada en el rendimiento de un sistema OWC fijo en tierra. Los resultados muestran que la banda de eficiencia hidrodinámica puede reducirse considerablemente y el valor de la frecuencia resonante puede modificarse. El último aspecto de esta disertación está dedicado a un análisis tridimensional de la interacción de oleaje incidente perpendicular con un dispositivo OWC fijo. Los hallazgos revelan una influencia sustancial en el ancho de banda de captura, la frecuencia de resonancia y la elevación de la superficie libre dentro del dispositivo debido al diseño de la cámara y la compresibilidad del aire.

Para cada caso de estudio, se presentan los detalles de formulación matemática, procedimientos de solución, discusiones y conclusiones. Finalmente, se destacan las conclusiones generales y propuestas para estudios futuros.

# Abstract

Climate change, as a result of fossil fuel pollution, population growth and increased energy consumption, necessitates the exploration and harvesting of renewable energy resources. Due to its higher energy density when compared to other renewable sources, ocean wave energy has been suggested as a potential resource for mitigating the impacts of global warming. However, despite being one of the most abundant sources of renewable energy, ocean energy remains mostly unharnessed. This is owing to a wider tendency towards other clean resources, limited research funding, the unmaturing of current technologies and the lack of a reliable and cost-effective energy extraction technology from sea waves.

In this regard, the Oscillating Water Column (OWC) device is an essential system for extracting wave energy. Due to its simple operation principle and adaptability, it can be utilized as fixed (coastal) or floating structures (offshore) to absorb energy from the waves. For an optimal operation, the OWC chamber plays a significant role to achieve better performance. Typically, the chamber configuration is chosen to produce a water column with a natural frequency of oscillation that matches that of the most common wave at the area where the OWC will be deployed. However, the variability of the sea state conditions, such as wave directionality, changes in water depth due to tidal variations and high loads exerted by extreme waves, can compromise the device's correct operation. Therefore, to ensure appropriate operation, the OWC chamber configuration must be efficiently tuned in relation to the wave environment.

The main focus of this thesis is towards the analysis of the OWC chamber configuration, incident wave direction and linear air compressibility in order to answer three research questions: (i) what influence does the thickness of the front wall have on hydrodynamic efficiency?; (ii) how the incoming wave direction affects the system performance?; and by considering these last two aspects (iii) What effect does air compressibility have on the hydrodynamic performance?

To explore these questions, analytical and numerical frequency domain models have been developed using theoretical techniques based on linear wave theory. The first one is the semi-analytic matched eigenfunction expansion method (EEM), which uses the continuity of velocity potential and flux, as well as the orthogonal property of the eigenfunctions, to reduce the boundary value problem (BVP) to a linear system of

algebraic equations. The other is the boundary element method (BEM), which is a numerical approach based on the application of an integral equation. In this case, the BEM with higher-order elements is utilized to account for the variation of potential and flux on the boundaries.

Throughout this thesis, five case studies are provided. First, the effects of the front wall thickness and chamber bottom profiles on the performance are investigated by means of the BEM. The results demonstrate that using a thick front barrier has a significant impact on hydrodynamic efficiency. This is explained by the fact that the transmission of energy from the incoming wave to the internal water column due to the orbital wave motion is reduced for thick barriers. Then, the interaction of oblique sea waves with a land-fixed OWC device is investigated. The results, in this case, indicated that increasing the wave angle of incidence, increases the wave frequency at which resonance occurs, which offers benefits to wave power extraction in real sea conditions for fixed devices.

Subsequently, an analysis is carried out to investigate changes in efficiency curves and resonance frequency caused by the different rear and front wall configurations of an asymmetric fixed-detached OWC device. Then, the obliquity of the water waves and the thickness of the front barrier are both examined to analyse their combined influence on the performance of a fixed-land OWC system. The results show that the hydrodynamic efficiency band may be considerably reduced and the resonant frequency value modified. The last aspect of this dissertation is devoted to a three-dimensional (3D) analysis of the interaction of perpendicular incident waves with an onshore OWC device. The findings reveal a substantial influence on the captured width bandwidth, resonance frequency and free surface elevation within the chamber due to the chamber design and linear air compressibility.

For each case of study, the details of mathematical formulation, solution procedures, discussions and conclusions are presented. Finally, general conclusions and proposals on the scope of future studies are highlighted.

# Chapter 1

## Introduction

### 1.1 Background

In recent years, electricity needs have grown substantially as a result of the exponential growth of the human population, and the usage of fossil fuels to meet these demands is projected to continue for at least the first half of the century ([González-Santaló; 2009](#)). However, due to the huge quantity of carbon dioxide (CO<sub>2</sub>) emitted into the atmosphere, which contributes to the accumulation of greenhouse gases and is one of the major drivers of climate change, its use is being called into question.

This situation has compelled numerous countries to launch research efforts into obtaining energy from renewable and clean sources such as wind, solar, geothermal, hydrogen, ocean, etc. These sustainable sources provide a huge and nearly endless supply of energy with low global warming emissions and with a variable energetic potential depending on location. In this regard, according to [Vicinanza et al. \(2013\)](#), ocean energy is the cleanest, safest, inexhaustible and predictable of all mentioned sources, and may be considered a vital alternative for sustainable development. Ocean energy is classified into several types based on its energy resources, namely ocean wave energy, ocean thermal energy, energy from ocean currents, and tidal energy. Ocean wave energy, in particular, is abundant across the planet, and in recent years it has witnessed tremendous development and become highly significant because of the enormous energetic potential inherent in the seas.

### 1.2 Wave energy

Ocean wave energy has the potential to produce vast amounts of clean, safe, and reliable renewable energy ([Evans; 1976](#)), but it is now a mostly underexploited resource. The World Energy Council estimates that the yearly quantity of wave energy throughout the world is around 17.5 PWh, which is comparable to the projected annual global energy

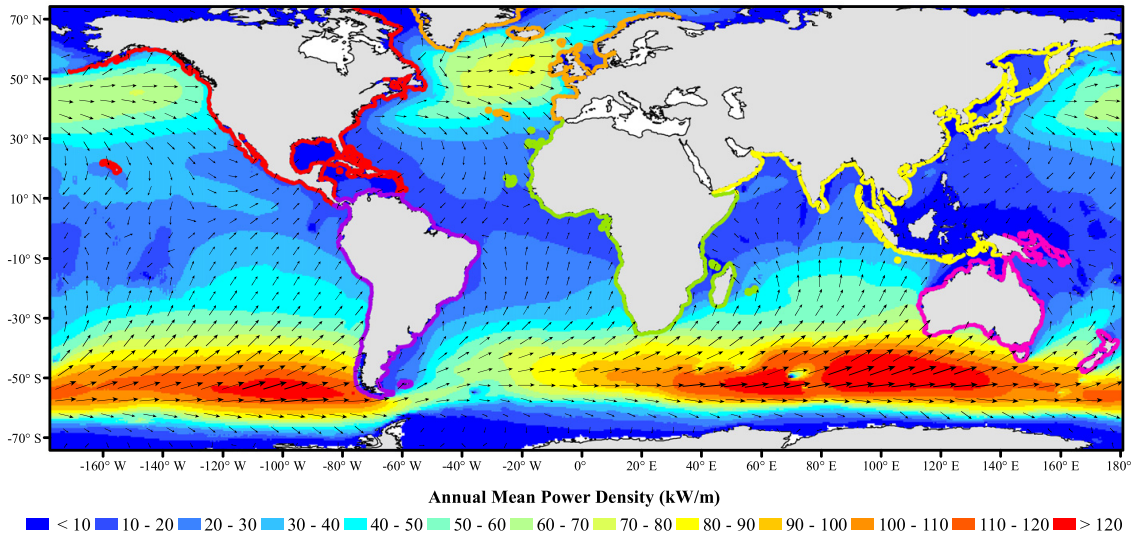


Figure 1.1: Global annual mean wave power density (colour) and annual mean best direction (arrows), taken from [Gunn and Stock-Williams \(2012\)](#).

consumption of 16 PWh ([Boyle; 2012](#)). The global annual mean wave power density and annual mean best direction calculated by [Gunn and Stock-Williams \(2012\)](#) are shown in Fig. 1.1. Thus, if efficiently harnessed, wave energy may supply the majority of the world's electricity requirement by 2030.

Apart from its accessibility, wave power has additional benefits; since much of the world's population lives in the vicinity of coastal regions, it reduces the distance between energy production and consumption; thus, reducing losses and investments in transmission lines. Contrary to alternative sources, such as wind, electricity and solar energy, the installation of wave energy systems does not require the use of highly valuable areas or landscapes ([Fagley et al.; 2013](#)). Furthermore, because wave energy is so capable of providing huge amounts of clean and renewable energy, it is an ideal source of energy efficiency in densely populated coastal areas.

However, considering this kind of energy involves extremely particular research, because water waves generate large amplitudes in certain places only. Moreover, its unpredictability is another disadvantage; nevertheless, it may be moderately controlled. Water waves are therefore a unique phenomenon occurring in each coastal location, with a single difference in the amplitude and time period.

In recent years, scientists and engineers have been working in this field to develop efficient systems for extracting energy from waves. More than a thousand patents had been registered by the 1980s, and the number has grown significantly since then ([McCormick; 2010](#)). Essentially, the development of this type of technology has been based on the research and construction of structures that have the property of converting

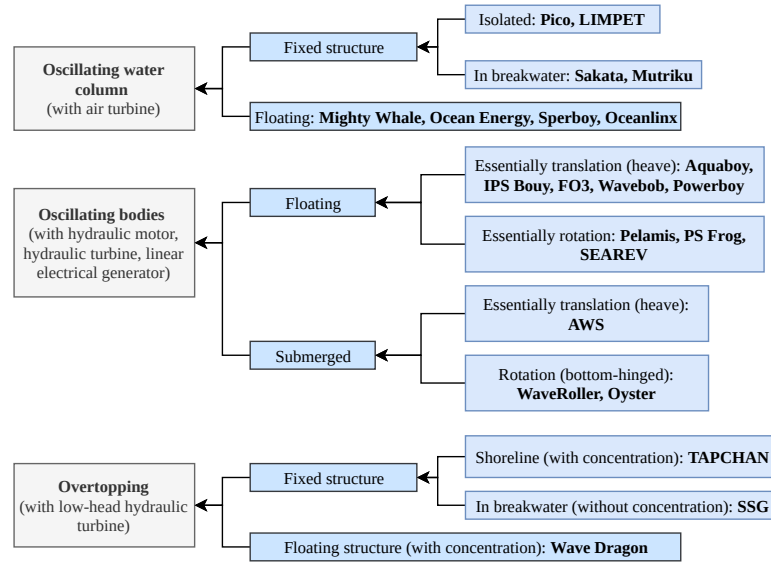


Figure 1.2: Technologies for harnessing wave energy, adapted from Falcão (2010).

wave energy into mechanical and electrical energy. Each system offers benefits and drawbacks that are assessed based on economic feasibility and construction circumstances in a specific location.

In this respect, Vantorre et al. (2004) pointed out that for a given sea state, a successful wave absorber should meet four criteria: first, the frequency to which the converter is most sensitive should coincide with the main frequency in the wave spectrum; second, it should be possible to adapt this frequency of the system to variations of the sea state; third, the converter must be capable of absorbing the energy of other wave components with acceptable efficiency; and fourth, if the performance of the absorber is affected by the wave direction, the same principles apply to the directional distribution.

### 1.3 Wave energy technology

Various studies have offered alternative approaches to classifying wave power systems. They took account of the geometry and direction of the wave energy, position and mode of motion, power take-off (PTO) mechanism, wave-structure interaction, mooring dependency, etc. An example of this is the classification of Falcão (2010), Fig. 1.2, based largely on the working principle of these devices, which focuses on projects where the prototype stage has been achieved or where at least some development work has been done. Another example is the classification based on the most common technologies (IRENA; 2014), which are described below.

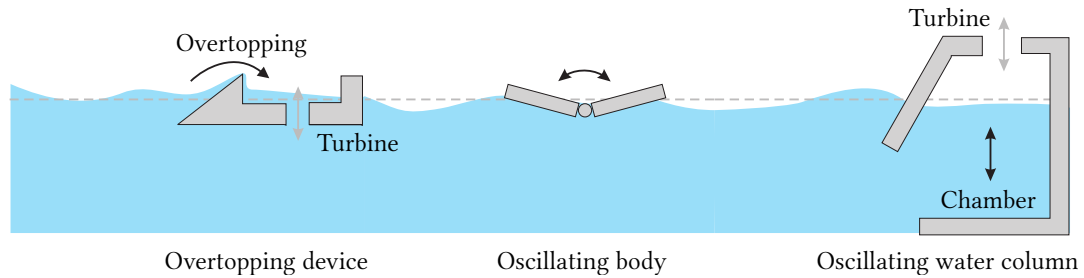


Figure 1.3: Types of WECs depending on their working principle, adapted from [Sergiienko \(2018\)](#).

### 1.3.1 Working principle

The operational principle specifies how energy from an incoming wavefield is extracted through contact with a wave energy converter (WEC). The WEC benefits from the oscillatory or circular motion of the waves to transform the associated kinetic and potential energy into usable mechanical or electrical energy. As shown in Fig. 1.3, WECs are classified into three types: oscillating water columns (OWCs), oscillating bodies, and overtopping devices.

An **OWC** device is a fixed or floating hollow structure which consists of a partially submerged open-end box made of concrete or steel with trapped water and air columns. Due to the incoming incident waves, the water column inside the structure has alternative pressure fluctuations that run the trapped air above the internal free surface through a turbine, which eventually drives the electrical generator to produce electricity. One of the primary benefits of this system is that the PTO mechanism is placed above water level, preventing direct contact with water.

**Oscillating bodies** are articulated, floating structures with a PTO system that absorb wave energy as a result of dynamic fluid-structure interaction ([Lattanzio and Scruggs; 2011](#)). Offshore devices are essentially oscillating bodies that are either floating or (in rare cases) totally submerged. They make use of the stronger wave regimes seen in deeper water (typically more than 40 m water depth). Offshore WECs are more complicated in general because, in addition to mooring issues, access for maintenance and the requirement for long underwater electrical cables have hampered their development, and only recently certain systems have reached the full-scale demonstration stage ([Falcão and Henriques; 2016](#)).

An **overtopping device** is a wave collector that extracts energy from the oceans. Water at the wave crest is captured and introduced into a reservoir, where it is stored at a level higher than the average free-surface level of the surrounding sea. The potential energy of the stored water is transformed into usable energy using conventional low-head hydraulic turbines. The hydrodynamics of overtopping devices are significantly



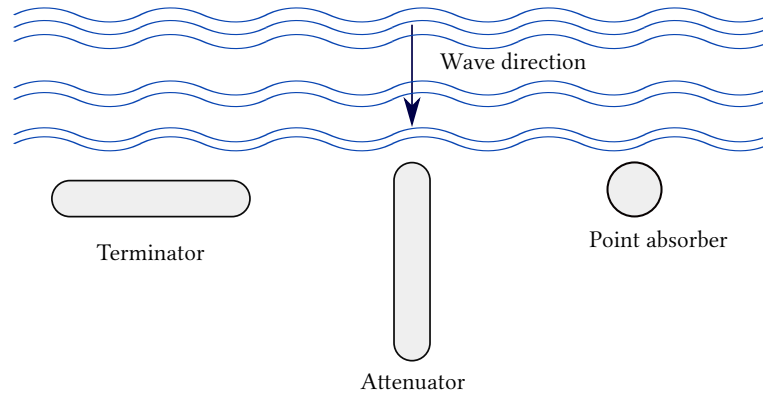


Figure 1.4: Schematic diagram of the types of WECs depending on their size and orientation relative to the incident wave direction.

nonlinear, and their operation is comparable to that of a hydropower plant but applied to an offshore floating platform.

### 1.3.2 Orientation

Depending on the dimensions and orientation with respect to the propagating wave, WECs can be grouped as follows, Fig. 1.4:

- **Terminator** is a kind of device that has its principal axis parallel to the incident wave crest (perpendicular to the predominant wave direction)
- **Attenuator** devices are floating wave energy converters that are oriented parallel to the direction of wave travel.
- **Point absorber** is a floating device that their horizontal dimensions are much smaller than the wavelength and can absorb power regardless of the direction of wave propagation.

### 1.3.3 Power take-off mechanism

The PTO of a WEC is the mechanism with which the absorbed energy by the primary converter (for example, the enclosed chamber for an OWC or a point absorber buoy) is transformed into useable electricity, Fig. 1.5. The PTO system is a critical system within any WEC since it affects not only directly how efficiently the absorbed wave power is converted into electricity but also contributes to the mass, the size and the structural dynamics of the WEC (Pecher and Kofoed; 2017a).

The types of PTO systems can be classified into five main categories and are described as follows:

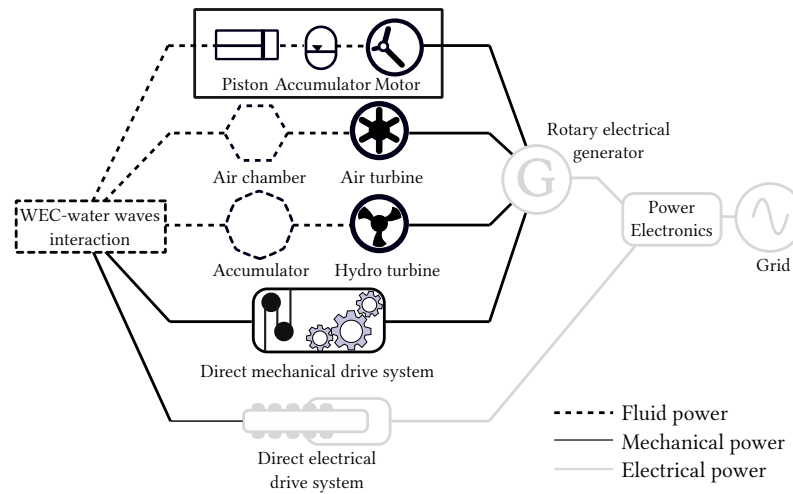


Figure 1.5: Different main paths for wave energy to electricity conversion, adapted from Pecher and Kofoed (2017b).

- **Air turbines** are employed for converting wave power into mechanical power. They are mostly used to equip OWC devices where, due to the oscillating water level induced by the ocean waves, the oscillating air pressure in an enclosed chamber drives a turbine. The main challenge in this system comes from the bidirectional nature of the flow; however, almost all OWC prototypes tested so far have been equipped with self-rectifying air turbines that convert an alternating airflow into a unidirectional rotation.
- A **hydraulic** PTO system is often the solution chosen to interface the WEC with the electrical generator since they are well suited to absorb energy when dealing with large forces at low frequencies. The concept is based on the traditional hydraulic system but, in this particular case, in a reversed motion. Here, the movement of the body feeds energy into a hydraulic motor, which in turn translate the energy to an electrical generator.
- **Hydro turbines** are employed in overtopping devices or hydraulic pump systems using seawater as fluid. In overtopping type of devices, the water reaching over a ramp accumulates in a basin where its potential energy is converted using low-head turbines and generators (Pecher and Kofoed; 2017a). This system has the benefit of being a mature technology that has been employed for many decades for power generation, they can operate at efficiency values of an excess of 90% and require low maintenance.
- A **direct mechanical drive** PTO system consists of translating the mechanical

energy of an oscillating body subjected to waves into electricity by means of an extra mechanical system driving a rotary electrical generator. The mechanical conversion systems can comprise a gearbox, pulleys and cables and a flywheel can be integrated into a rotation-based system so as to accumulate or release energy and thereby smooth out power variations (Yoshida et al.; 2012).

- In a **direct electrical drive** system, the mechanical energy captured by the primary converter is directly coupled to the moving part of a linear electrical generator. For example, a translator, which is equipped with alternating polarity magnets, is coupled to a buoy and the ocean waves induce a heaving motion to this system with respect to a stationary stator equipped with coils, inducing electrical current in the stator.

### 1.3.4 Application

Finally, regarding the location, WEC can be categorized into three groups:

- **Onshore** devices are built and fixed on land which avoids the use of a mooring system and long underwater electrical cables. The location may be on the coastline or integrated into structures such as breakwaters which can reduce the initial, operational and maintenance costs.
- **Nearshore** devices are predominantly fixed on a gently sloping seabed on relatively shallow water. This shallow water typically varies between 10 to 20 m at a distance of between 0.5 and 2.0 km from the coastline.
- **Offshore** devices are generally in deep water, which can be defined as tens of meters water depth, water depth greater than 40 m, or depth exceeding one-third of the wavelength (Drew et al.; 2009). Being deployed in deep water makes these types of devices to be exposed to a greater wave power potential, often making them more cost-effective. However, the deeper the water, the more challenging and costly becomes the construction, the deployment of a mooring system, the sub-sea cables that lay on the seabed and, once in operation, the access for maintenance.

Among the few full-size prototypes that have been built and deployed in open water, most of these are or were located near the coast, and they are sometimes referred to as first-generation devices. In general, these devices are placed on the seabed or attached to a rocky cliff. As mentioned above, these devices designed to operate on the coastline have the advantage of being easier to install and maintain and do not require a deep-water mooring system or long underwater electrical cables. On the shore, they encounter less energetic swell but this may be compensated in part by the natural concentration of wave energy due to refraction and/or diffraction (provided the device is suitably located

for that purpose). In this respect, the most common first-generation device is the OWC device, which is the most studied, best developed and one of the few systems that in multiple times has reached the full-size prototype stage (Falcão; 2010). More details regarding the background and characteristics of this WEC type will be provided in the following chapter.

## Bibliography

- Boyle, G. (2012). *Renewable Energy: Power for a Sustainable Future (3rd ed)*, Oxford University Press and Open University.
- Drew, B., Plummer, A. and Sahinkaya, M. (2009). A review of wave energy converter technology, *Proceedings of The Institution of Mechanical Engineers Part A-journal of Power and Energy* **223**: 887–902.
- Evans, D. V. (1976). A theory for wave-power absorption by oscillating bodies, *Journal of Fluid Mechanics* **77**(1): 1–25.
- Fagley, C., Siegel, S., Seidel, J. and Schmittner, C. (2013). 3d efficiency analysis of cycloidal wave energy converters in oblique wave fields, *Proceedings of the International Conference on Offshore Mechanics and Arctic Engineering OMAE*, Vol. 8.
- Falcão, A. (2010). Wave energy utilization: A review of the technologies, *Renewable and Sustainable Energy Reviews* **14**(3): 899 – 918.
- Falcão, A. and Henriques, J. C. C. (2016). Oscillating-water-column wave energy converters and air turbines: A review, *Renewable Energy* **85**: 1391–1424.
- González-Santaló, J. M. (2009). La generación eléctrica a partir de combustibles fósiles, *Boletín IIE* pp. 143–151.
- Gunn, K. and Stock-Williams, C. (2012). Quantifying the global wave power resource, *Renewable Energy* **44**: 296 – 304.  
**URL:** <http://www.sciencedirect.com/science/article/pii/S0960148112001310>
- IRENA (2014). *Ocean power: Technologies, patents, deployment status and outlook. Report*, International Renewable Energy Agency.
- Lattanzio, S. M. and Scruggs, J. T. (2011). Maximum power generation of a wave energy converter in a stochastic environment, *2011 IEEE International Conference on Control Applications (CCA)*, pp. 1125–1130.

- McCormick, M. E. (2010). *Ocean Engineering Mechanics with Applications*, Cambridge University Press, New York.
- Pecher, A. and Kofoed, J. (2017a). *Handbook of Ocean Wave Energy*.
- Pecher, A. and Kofoed, J. P. (2017b). *Handbook of Ocean Wave Energy*, Ocean Engineering & Oceanography, Springer International Publishing.  
**URL:** <https://books.google.es/books?id=IuTxjwEACAAJ>
- Sergiienko, N. (2018). *Three-tether wave energy converter: Hydrodynamic modelling, performance assessment and control*, PhD thesis.
- Vantorre, M., Banasiak, R. and Verhoeven, R. (2004). Modelling of hydraulic performance and wave energy extraction by a point absorber in heave, *Applied Ocean Research* **26**(1): 61 – 72.  
**URL:** <http://www.sciencedirect.com/science/article/pii/S0141118704000392>
- Vicinanza, D., Nørgaard, J. H., Contestabile, P. and Andersen, T. L. (2013). Wave loadings acting on Overtopping Breakwater for Energy Conversion, *Journal of Coastal Research* (65 (10065)): 1669–1674.
- Yoshida, T., Sanada, M., Morimoto, S. and Inoue, Y. (2012). Study of flywheel energy storage system for power leveling of wave power generation system, *2012 15th International Conference on Electrical Machines and Systems (ICEMS)*, pp. 1–5.

# Chapter 2

## Thesis

### 2.1 Motivation

Due to its adaptability, OWC systems may be designed to be installed on the shore or integrated into ocean structures such as land-fixed or pile-supported breakwaters. The Mutriku Oscillating Water Column Energy Plant, located in Gipuzkoa (northern Spain), is an example of this, where 16 OWC units that are 4.5 m wide, 3.1 m depth, and 10 m high were built on a 100 m boomerang-shaped breakwater. However, the initial performance expectations of the plant have not been fulfilled because the breakwater that houses the OWC units was mainly designed to protect the harbour and not for wave energy harnessing.

Other related factors are that the boomerang-shaped breakwater that houses the OWC power plant is north-northeast oriented, causing each of the sixteen chambers to face the incoming sea waves at a distinct angle. As a result, while the structural design of the chambers remains the same, the pneumatic power produced by each of the 14 Wells turbines in operation varies. Furthermore, the location is frequently lashed by storms, and before completion of the power station, two storms hit the OWC plant and a further storm produced severe structural damage to a number of the OWC chambers. As a consequence, the front face of each chamber was reinforced by employing precast concrete slabs to withstand the wave loads, and its front wall thickness now doubled the length of the chambers. This implementation was done to secure the integrity of the structure without taking into account the influence that this additional design setting may have on device performance. Therefore, motivated by the case of Mutriku, the main focus of this work is the evaluation of the influence that the front wall thickness of an OWC chamber and the wave directionality have on the OWC hydrodynamic performance.

## 2.2 General objective

The main objective of this work is to theoretically model the problem of water wave interaction with an OWC device for different configurations. The mathematical models are based on the linear wave theory. The eigenfunction expansion method and the boundary element method with a second-order discretization are employed to obtain a solution to each two or three-dimensional problem.

### 2.2.1 Specific objectives

To perform these tasks, the following specific objectives were targeted:

- To propose a mathematical model of the water wave-OWC device interaction.
- To determine the appropriate boundary conditions of the BVP.
- To numerically solve the BVPs employing the matched EEM.
- To numerically solve the BVPs using the BEM with quadratic elements.
- To analyze the degree of accuracy of the theoretical solutions.
- To compare and recover the results reported in the literature.
- To analyze the influence of the chamber configuration on the hydrodynamic performance of the OWC device.
- To investigate the effect on the OWC performance of oblique waves.
- To study the impact of air compressibility on the OWC performance.

Such tasks require an understanding of:

- Linear wave theory.
- Hydrodynamics of OWC.
- Eigenfunction expansion method.
- Boundary element method.
- Numerical tools (Fortran, MATLAB and GMSH).

## 2.3 Thesis outline

This thesis is conformed of a compilation of works published or under review, with the exception of Chapters 1–4 and 10. Chapter 3 presents the background and literature review of existing OWC technologies. This includes experimental, numerical and analytical studies, as well as a review of the reported environmental impacts caused by WECs and the economics of wave energy. The critical review of literature specific to the research work presented in this thesis is expanded in Chapters 5–9. Then, in Chapter 4, associated concepts of the linear theory of ocean waves are presented.

In Chapter 5, the effect on the efficiency, added mass and radiation damping of the front barrier thickness of a land-fixed OWC device are analyzed by means of the BEM with quadratic elements. Then based on the physical dimensions of the OWC plant in Mutriku, the influence of four different bottom profiles on the hydrodynamic efficiency are investigated.

The interaction of oblique water waves with a land-fixed OWC device is examined in Chapter 6. Here, both the matched EEM using dual series relations and the BEM with higher-order elements are utilized to solve the associated BVP. The influence of wave directionality and linear air compressibility on the efficiency are discussed.

The influence of the chamber configuration of an asymmetric, fixed-detached OWC device on its performance was investigated in Chapter 7. The solution to the radiation and scattering BVP was obtained by both the matched EEM and BEM, and the effects on device performance of adding a step under the OWC chamber and a reflecting wall in the downstream region were also investigated.

In Chapter 8, the combined effects on the hydrodynamic performance of the wave directionality and the thickness of the front barrier are investigated for a land-fixed OWC device. By means of the matched EEM and BEM, a solution to the BVP was achieved. Furthermore, a case of study for a single chamber of the Mutriku OWC plant considering the above-mentioned aspects is presented.

Then, a 3D BEM with nine-noded quadrilateral elements is presented in Chapter 9 to obtain a solution of the interaction of water waves with an onshore OWC device. The capture width, hydrodynamical coefficients and free surface elevations are analysed for different OWC geometric parameters of the chamber.

Finally, in Chapter 10 the main conclusions and contributions to the research field made throughout this thesis are commented on, and some recommendations for future work are provided.



## 2.4 List of published and submitted articles included in the thesis

1. Medina Rodríguez A.A., Blanco Ilzarbe J.M., Silva Casarín R., Izquierdo Ereño U. (2020). “*The Influence of the Chamber Configuration on the Hydrodynamic Efficiency of Oscillating Water Column Devices*”. **Journal of Marine Science and Engineering**. 8(10): 751. <https://doi.org/10.3390/jmse8100751>.
2. Medina Rodríguez A.A., Martínez Flores A., Blanco Ilzarbe J.M., Silva Casarín R. (2021). “*Interaction of oblique waves with an Oscillating Water Column device*”. **Ocean Engineering**. 228: 108931. <https://doi.org/10.1016/j.oceaneng.2021.108931>.
3. Medina Rodríguez A.A., Silva Casarín R., Blanco Ilzarbe J.M. (2021). “*A theoretical study of the hydrodynamic performance of an asymmetric fixed-detached OWC device*”. **Water**. 13: 2637. <https://doi.org/10.3390/w13192637>.
4. Medina Rodríguez A.A., Silva Casarín R., Blanco Ilzarbe J.M. (2021). “*The influence of oblique waves on the hydrodynamic efficiency of an onshore OWC wave energy converter*”. **Renewable Energy**. Under Review.
5. Medina Rodríguez A.A., Silva Casarín R., Blanco Ilzarbe J.M. (2021). “*A 3D boundary element method for analysing the hydrodynamic performance of a land-fixed oscillating water column device*”. **Engineering Analysis with Boundary Elements**. Under Review.

### 2.4.1 Additional works related to the thesis but not included

1. Medina Rodríguez A.A., Martínez Flores A., Silva Casarín R. (2018). “*The effect of an asymmetric submarine trench on the efficiency of an oscillating water column device in a two-layer fluid*”. **WIT Transactions on Engineering Sciences**. 120: 137–148. <https://doi.org/10.2495/AFM180141>.
2. Medina Rodríguez A.A., Martínez Flores A., Silva Casarín R. (2018). “*The effect of an asymmetric submarine trench on the efficiency of an oscillating water column device in a two-layer fluid*”. **12th International Conference on Advances in Fluid Mechanics**. Ljubljana, Slovenia.
3. Medina Rodríguez A.A., Martínez Flores A., Silva Casarín R. (2018). “*Estudio de la eficiencia de un dispositivo OWC en presencia de una trinchera en un fluido estratificado*”. **XXVIII Congreso Latinoamericano de Hidráulica**. Buenos Aires, Argentina.

4. Medina Rodríguez A.A., Blanco Ilzarbe J.M., Silva Casarín R. (2019). “*The effects of the bottom and front barrier thickness on the efficiency of an owc device*”. **VI Marine Energy Conference**. Bilbao, Spain.
5. Medina Rodríguez A.A., Silva Casarín R. Blanco Ilzarbe J.M., (2021). “*La influencia de los efectos tridimensionales en el rendimiento de los dispositivos de columna de agua oscilante*”. **1er Congreso Internacional CEMIE-Océano**. Online Conference.

## 2.5 Comments

All of the articles in this thesis are identical in content to the original articles that were published or submitted, except for the following points:

- The formatting and referencing have been changed to ensure that the thesis follows a uniform structure throughout.
- To improve readability, the locations of the figures and tables may change from the final published version of the articles.
- Each publication’s table, figure, and equation numbers have been updated to incorporate the chapter number.

# Chapter 3

## Literature review

The goal of this chapter is to provide background information and a literature review of the existing OWC technologies. This covers experimental, numerical, and analytical studies of the parameters influencing their power absorption efficiency, as well as some research studies into the reported environmental impacts produced by WECs and the economics of wave energy.

### 3.1 Oscillating Water Column device

The Oscillating Water Column concept is probably unique among the several suggested systems for wave energy extraction, Fig. 3.1. An OWC device consists of two main parts; a partially or completely submerged collecting chamber, which is a concrete or steel structure, and a PTO mechanism. Due to wave action, the trapped air inside the collecting chamber is alternatively compressed when the water column rises and rarified when the column lowers, forcing the air to flow through a turbine connected to a generator. OWC collectors can also exist in nature, such as blowholes in cliffs, although they lack an optimal shape that can be exploited economically (Heath; 2012).

The system of energy extraction is usually an air turbine (although hydraulic pumps are also an alternative), and for simplification purposes, the type of air turbine normally selected is the self-rectifying one, where it does not matter if the collector breathes or exhales the air inside the chamber because the turbine is driven in the same direction. The combination of a Wells turbine with an induction generator is the most commonly used form of energy extraction (Heath; 2012). Thus, the ease with which the OWC device may be coupled with an air turbine is what makes it an appealing technology.

In practice, an OWC device offers numerous advantages: it contains few moving parts, none of which are submerged; it is a versatile device that may be utilized in a variety of locations, such as a fixed device on the coastline or offshore as a floating device; also, the use of an air turbine eliminates the need for gearboxes; it is reliable; it is relatively easy

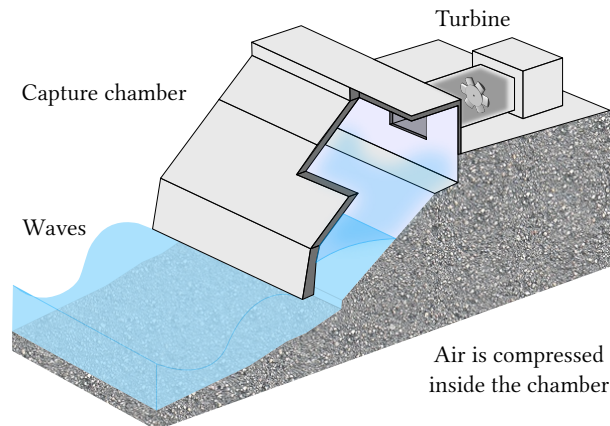


Figure 3.1: Schematic layout of oscillating water column system.

to maintain; and, it uses marine space efficiently. Perhaps, the only drawback of this type of device is that constructions located on and near the coastline can have a negative visual impact. In this regard, the ability to apply the concept of an OWC device in a variety of settings is important as it allows the acceptance and progressive growth of this type of WEC.

### 3.1.1 Background

The whistling buoy, which was employed as a navigational aid, was the earliest known application of the concept of an oscillating water column. This was used as an auditory warning device and was viewed as a replacement to the conventional Bell buoys in the 19th century. Later, J. M. Courtney in New York patented the whistle buoy, and in 1885, in *Scientific American*, it was reported that 34 buoys were functioning throughout the US coast (Heath; 2012; Masuda; 1986). More than half a century later, Yoshio Masuda developed and installed in Japan the first OWC device that drove a turbine to generate electricity (Falcão; 2010). This unit was installed in Osaka Bay and the electricity generated provided power to navigation lights.

In the 1970s, a team led by the International Energy Agency (IEA) investigated OWC devices mounted on a floating barge named Kaimei (Masuda; 1979), Fig. 3.2. The 800-tonne and 80-metre-long barge was moored off the shore of Yura in Yamagata Prefecture, Japan. In the project, thirteen OWC devices were installed on the barge, eight of which had a nominal output of 125 kW (Falcão and Henriques; 2016). Aside from Japan, which acted as the primary partner, contributions were made by the United Kingdom, Canada, Ireland, and the United States.

Subsequently, many OWC devices were developed and tested in Japan, India, China, Norway, Portugal, and the United Kingdom between 1980 and 1990. The largest of



Figure 3.2: The Kaimei device (Falcão and Henriques; 2016).

them was constructed in the Sakata Port, Japan. This five-chamber device was built as part of a breakwater, which was a box-shaped concrete structure that was set in situ before being sunk and filled with ballast. The device was commissioned in 1989 and was equipped with a Wells tandem turbine, generating 60 kW (Ohneda et al.; 1991). For many years, this system was the first case of integrating a WEC with a breakwater, which also assisted in lowering project costs (Falcão and Henriques; 2016).

Furthermore, Queen’s University in Belfast developed an OWC device with a 75 kW turbine located in Islay, Scotland. This plant was connected to the grid and operated between 1991 and 2000, Fig. 3.3. As a continuation of the prototype in Islay, the Queen’s University team designed the LIMPET plant, which was built near the original facility (Heath et al.; 2000). The prototype was built in a relatively sheltered gully, with the LIMPET plant facing south and with a nominal power of 500 kW. At the same time that LIMPET was being developed, the company Eletricidade dos Açores built a 400 kW OWC device on the island of Pico, Portugal (Falcão; 2000). This plant was operated intermittently by the Centro de Energia do Oleagem and supplied crucial data for the further development of OWC devices.

As stated above, floating devices designed by Yoshio Masuda in Japan were the first OWCs deployed in open waters: the navigation buoys and the large barge Kaimei. Masuda realized that the energy conversion of the Kaimei device was extremely poor and designed an alternative geometric system for a floating OWC: the Bent Back Duct Buoy or BBDB. The duct of the BBDB device is bent backwards in relation to the direction of the incident waves, which was considered to be beneficial when compared to the forward-facing form of the duct (Masuda and McCormick; 1987). In this manner, the length of the water column could be increased to achieve resonance while maintaining the depth of the floating construction within acceptable limits. Then, in Ireland, Ocean Energy developed a device similar to the one initially proposed by Masuda (Energy; n.d.), which was designed at a quarter of the original scale and with over 20,000 hours of open-ocean testing.



Figure 3.3: Shoreline OWC device on the island of Islay, Scotland (Falcão and Henriques; 2016).

On the other hand, the Australian company Oceanlinx developed an alternative design of a floating OWC device called the MK3. This model is a one-third scale version of the original 2.5 MW device. Other full-size OWC prototypes were built in Norway (at Toftestallen, near Bergen, 1985 (Bønke and Ambli; 1986)), and India (Vizhinjam, near Trivandrum, Kerala State, 1990 (Ravindran and Koola; 1991)); whereas smaller OWC prototypes were built off the coast of Islay, the United Kingdom, and in China (Whittaker et al.; 1993).

Design and construction are two of the most essential aspects of fixed OWC devices, as well as the most economically influential. Integrating an OWC plant with a breakwater for coastal protection offers numerous advantages: first, construction expenses are shared, and second, access to the power plant for construction, operation, and maintenance is greatly simplified.

This was done successfully for the first time at the port of Sakata, Japan, as previously stated, and subsequently in Mutriku, Basque Country, Spain, where the Basque Energy Agency built an OWC device adopting this same concept (Torre-Enciso et al.; 2009). The wave power plant in Mutriku consists of 16 units that comprise the section of an OWC breakwater and are the first multiple OWC plant that allows researchers to examine the interaction between its components and their complexity in control. Furthermore, it is the only OWC breakwater device now in service that delivers electricity to the electrical grid on a regular basis (Ibarra-Berastegi et al.; 2018).

Furthermore, Boccotti (2007a) presented a new design for an OWC installed in a breakwater, with the collecting chamber being long in the direction of the wave crest and narrow in its cross-section. This section of the OWC is U-shaped, with the outer aperture facing vertically and the design has the benefit of increasing the overall length of the water column without lowering the aperture below the free surface. Currently, this sort of OWC-breakwater device is now being built at the Italian port of Civitavecchia, consisting of 17 caissons and 136 OWCs, and it is expected that this concept will be

adopted in new breakwaters in Italy (Falcão and Henriques; 2016). Finally, in Yongsoo, South Korea, a fixed OWC device with a nominal output of 500 kW was built. This plant is 37 m long and 31.2 m wide and is equipped with two axial flow turbines of 250 kW each (Falcão and Henriques; 2016).

### 3.1.2 Review of research studies

Over the last few decades, a number of analytical, computational, and experimental approaches for studying the hydrodynamic efficiency of an OWC device have been developed. Early theories for OWC devices focused on rigid-body models in an attempt to predict their performance. Evans (1978) demonstrated how rigid-body theory may be applied to a simple OWC model. In his study, he claimed that, at least in long waves, the internal fluid motion could be modelled as a solid mass with the free surface acting as a light rigid piston. By taking into account a spatial variation of the free surface motion, Falcão and Sarmiento (1980) sought to improve this concept of an OWC by allowing for greater pressure at the free surface. Later, Evans (1982) examined an arbitrary number of fixed chambers enclosing an internal free surface that functioned as a system of OWC devices. In 1985, Falnes and McIver (1985) provided a further generalisation of the work by Evans (1982) allowing the possibility of movement of the rigid bodies and designing a wave energy absorption system with an unlimited number of oscillating bodies and internal pressure distributions. These concepts were used by Smith (1983) to a simple 2D model of an OWC and the matched EEM to solve the BVPs was employed. The studies listed above are the fundamental works for developing broad theories on oscillating pressure systems.

Evans and Porter (1995) used the matching EEM and the Galerkin technique to investigate the hydrodynamic performance of an OWC device consisting of a thin rigid surface piercing barrier near a vertical wall. Experimentally, Boccotti (2003) suggested a new wave energy absorber that can be tuned such that the interior water column remains in resonant condition in any sea state by adjusting the air amount in an enclosed chamber. Later, Boccotti (2007c) presented an OWC model with an extra duct that improves performance compared to the standard OWC device for both long and short wind waves. In this sense, Boccotti (2007b) analysed an OWC system that is connected to the sea through a small opening. In this model, waves cannot enter the chamber and the water column oscillations are due to the wave pressure on the small opening. Hong et al. (2004) investigated the motion and the drift force of a floating OWC device in regular waves by the BEM.

The addition of projecting walls in front of the entrance of an OWC device may cause waves to concentrate as a result of refraction, reflection, and diffraction. This idea aims to cause resonance of the harbour area surrounded by the walls (Ikoma et al.; 2016). This modification can improve the frequency bandwidth of the useful power extraction of the device and may be regarded as an alternative for improving its performance. Count and

Evans (1984) developed a theoretical model to predict the hydrodynamic performance of a WEC with projecting sides. Their findings show that adding a harbour causes significant changes, which are intended to be highly beneficial. Malmo and Reitan (1985, 1986a,b) used the matched EEM to examine the performance of a single and several OWC systems near a reflecting wall or in a canal with uniform water depths. McIver and Evans (1988) developed an approximation theory for the performance of a series of OWCs into a reflecting wall of constant depth using the approach of matched asymptotic expansions. Ikoma et al. (2011) presented an OWC device with an artificial harbour enclosed by projecting walls to increase the effectiveness of wave power absorption. Under a random sea state, Daniel Raj et al. (2019) conducted experimental research into the effect of resonant length and opening angle of harbour walls integrated with an OWC system.

Analysing the influence of the OWC geometry and surrounding bathymetry has been the subject of extensive study for many researchers. Wang et al. (2002) investigated the hydrodynamic performance of an OWC device with arbitrary topography near the shoreline by using both numerical and experimental techniques. They found that when the slope of the bottom increases, the peaks of the capture-width ratios move to lower frequency values, and they inferred that the influence of a change in water depth on the hydrodynamic performance is also substantial. A 3D BEM for the numerical modelling of the OWC plant on the Island of Pico/Azores was performed by Brito-Melo and Sarmiento (2002). The influence of front wall geometry on the hydrodynamic efficiency of a fixed OWC device was experimentally examined by Morris-Thomas et al. (2006). They concluded that the overall peak hydrodynamic efficiency is not greatly influenced by the front wall geometry. A theoretical analysis of an OWC device with a gap on its fully submerged front wall was carried out by Şentürk and Özdamar (2012). They showed that it is possible to increase the efficiency with a surface piercing barrier type front wall when appropriate geometrical parameters are considered.

Rezanejad et al. (2013) investigated the role of stepped bottom topography in increasing the efficiency of a nearshore OWC device. The authors reported that significant effects on the efficiency of the device are observed when a step bottom profile is introduced outside of the chamber. In a 2D nonlinear numerical wave flume, Ning et al. (2015) investigated the hydrodynamic performance of a fixed OWC device based on a time-domain higher-order BEM. The hydrodynamic performance of the OWC chamber with and without a bottom slope was examined, and it was shown that the geometric characteristics of the air chamber had a substantial impact on the hydrodynamic efficiency. Iino et al. (2016) conducted research on how variations in motion direction impact the water column in an inclined OWC device.

John Ashlin et al. (2016) experimentally studied the effect of the bottom profile of an OWC device on its hydrodynamic performance. Flat, circular curve and sloping bottom profiles were evaluated in a wave flume, and it was discovered that the OWC device with a circular curve bottom profile performed better in terms of effective wave



energy conversion and wave amplification factor within the chamber. Based on the work by [Boccotti \(2007c\)](#), [Vyzikas et al. \(2017\)](#) proposed a new U-OWC design with a slope. They showed that the proposed modification to the conventional OWC system by including a toe protection unit enhanced the efficiency of the classic model. [Rezanejad et al. \(2017\)](#) numerically and experimentally studied the influence of turbine damping and wave period in the performance of an OWC device in both regular and random wave conditions. The effect of the radius and finite wall thickness of the tubular structure was studied by [Zheng et al. \(2020\)](#). They demonstrated that an OWC device with a thinner chamber wall offers benefits to wave power extraction in terms of a broader primary band of efficiency curves. Using the coupled EEM–BEM, [Koley and Trivedi \(2020\)](#) analyzed the hydrodynamic performance and efficiency of an OWC device placed on an undulated seabed. A 2D BEM model for studying the response of an OWC device in general bathymetry regions was carried out by [Belibassakis et al. \(2020\)](#).

## 3.2 Environmental impacts

One of the primary motivations behind the development of marine energy converters is their environmental advantages over traditional generation methods. WECs do not emit gaseous, liquid or solid pollutants and therefore, under typical working circumstances, its energy is practically a non-polluting source. It should be noted, however, that no power generating technology is exempt from creating environmental impacts, and that limited experience with WECs provides only an incomplete picture of their potential implications ([Thorpe and Unit; 1999](#)).

In this sense, the deployment of WECs can have a variety of environmental effects. Some of these effects may be beneficial, while others may be potentially adverse. As a result, one of the major problems confronting renewable energy generation, particularly wave energy, is assessing the potential environmental impacts that might be created throughout the construction, operation and decommissioning phases of the plant. Specifically, as noted by [Mendoza et al. \(2019\)](#), these may have an influence on hydrodynamics, geomorphology, chemical characteristics of seawater and sediments, biotic interactions, and socioeconomic aspects.

Many of the impacts are largely influenced by their mode of operation and location, [Table 3.1](#). For example, in the case of an onshore OWC device, such as the Mutriku wave power plant, [Mendoza et al. \(2019\)](#) identified the main following biophysical interactions:

- Hydrodynamics: changes in wave energy distribution and water circulation.
- Geomorphological: changes in erosion patterns and sediment properties.
- Chemical: changes in the distribution of gases and nutrients.

Table 3.1: Interactions between devices and the surrounding environment, with the expected adverse impact intensity: ● No impact, ● Very low, ● Low, ● Medium, ● High, adapted from [Mendoza et al. \(2019\)](#).

Interactions	Floating	Submerged	Bottom	Onshore
<i>Far field sediment transport properties</i>	●	●	●	●
<i>Local sediment transport properties</i>	●	●	●	●
<i>Current direction</i>	●	●	●	●
<i>Wave energy distribution</i>	●	●	●	●
<i>Wave turbulence</i>	●	●	●	●
<i>Habitat</i>	●	●	●	●
<i>Ecological interactions</i>	●	●	●	●
<i>Electromagnetism</i>	●	●	●	●
<i>Noise and vibration</i>	●	●	●	●
<i>Nutrients</i>	●	●	●	●
<i>Water quality</i>	●	●	●	●
<i>Fishing</i>	●	●	●	●
<i>Recreation</i>	●	●	●	●
<i>Scenic value and mental health</i>	●	●	●	●

- Biotic: changes in behaviour and population density and ecological connectivity and new habitat creation.
- Socio-economic: landscape disruption, tourism and fisheries impact.

As a result, even though wave energy is a clean source of energy, WECs can locally alter biophysical habitats, and by modifying the surrounding wave environment, changes can be created over a longer distance from the installation. The magnitude of the impacts may be proportional to the scale of the development and may vary depending on the nature of the place chosen ([Frid et al.; 2012](#)). Therefore, proper scientific investigations should accompany the licensing of commercial-scale installations of these devices, reducing the risk of making environmental mistakes owing to a lack of knowledge.

### 3.3 Economics of wave energy

Nowadays, the development of WEC devices to capture ocean energy is still in its early phases, and as a result, they are frequently seen as financially unviable. In fact, due

to this early phase, it is difficult to predict the costs and performance of the devices and the rest of the installation, and the simplicity in most existing economic studies generates uncertainty in investors (Astariz and Iglesias; 2015). However, this renewable energy source, like tidal energy or offshore wind energy, presents an enormous potential for electricity production (Astariz and Iglesias; 2015).

The commercialization of WECs is hampered primarily by two factors: high cost and low energy conversion efficiency (Zhang and Ning; 2019). At the moment, a MWh generated by wave power is more expensive than a MWh generated by conventional sources or most other renewables, therefore wave power plants can only be economically feasible if subsidized (Astariz and Iglesias; 2015). However, the economics of WECs may be improved by enhancing system efficiency, and in this regard, emphasis has been devoted to device hydrodynamic efficiency and annual output power improvement through device shape optimization. Energy production can be maximized if the design of WECs devices, including their form and array, among other factors, is promoted.

The main costs in a wave energy plant are the following: pre-operating cost, construction costs, operational expenditure (OPEX), and decommissioning costs. The pre-operating cost includes the costs of preliminary studies, projects, environmental impact assessment, consenting procedures, etc. It is difficult to determine a generic value for this cost since it mainly depends on the kind of installation, location and particular characteristics of the project (often considered as 10% of the capital expenditure (CAPEX)) (Astariz and Iglesias; 2015). The construction cost includes developing, manufacturing, and installing the device. The cost of operation and maintenance (OPEX) is crucial in the economic analysis, but estimating this cost is a complicated procedure due to a lack of expertise in wave energy installation. Finally, decommissioning expenses include the costs of uninstalling and removing equipment when the WEC has reached the end of its useful life. This is estimated to be 0.5 - 1% of the initial investment (Astariz and Iglesias; 2015).

The levelised cost of electricity (LCoE), which incorporates all expenses associated with the system life-cycle, is one of the most significant indicators for energy investment (Sergiienko; 2018) and is expressed by

$$\text{LCoE} = \frac{\text{CapEx} + \sum_{y=0}^Y \text{PV}(\text{OpEx}_y)}{\sum_{y=0}^Y \text{PV}(\text{AEP}_y)}, \quad (3.1)$$

where PV indicates a present value, AEP is the annual energy production and  $Y$  is a total number of operation years. The LCoE is the ratio of total lifetime expenses versus total expected outputs, expressed in terms of the present value equivalent (Astariz and Iglesias; 2015). This measure allows to properly assess the expenses of a specific energy conversion technology and to be compared with other systems. It should be noted that LCoE is only valid in comparisons of power generation options under comparable economic conditions and should not be used to compare energy-generating projects that

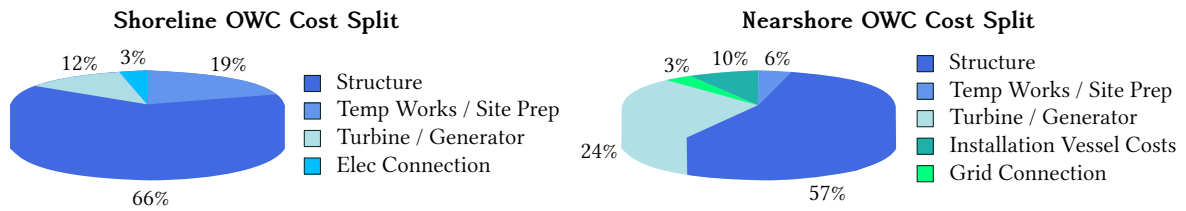


Figure 3.4: Shoreline and nearshore cost split, adapted from [The Carbon Trust \(2005\)](#).

would attract significantly different power purchase prices or tax rates, such as projects in different countries ([Pecher and Kofoed; 2017](#)).

Studies that analyze the economics of installing OWC devices have been conducted by ([The Carbon Trust; 2005](#); [Draycott et al.; 2018](#); [Green et al.; 1983](#)). As a first-generation device, OWCs have the longest track record of deployment of any of the wet renewable technologies ([The Carbon Trust; 2005](#)). Nonetheless, despite the fact that grid-connected facilities have been operating for some years, an OWC market has not been established. The Marine Energy Challenge study ([The Carbon Trust; 2005](#)) indicates that near-shore OWC devices may reach a stage where they can function within the UK framework for renewable power generation without further government funding within a realistic timeframe. However, without a more coherent approach and some financial assistance, the OWC sector will not deliver improvements in performance and cost. In their study, they conducted a comparison between shoreline and nearshore OWC devices, taking into account factors such as cost, site flexibility, production feasibility, and weather condition susceptibility, among others, Fig. 3.4. They found that shoreline OWC technology will never achieve as low a power price as nearshore OWC systems, but it can still play a role in serving isolated communities where there is power price premium.

On the other hand, [Draycott et al. \(2018\)](#) carried out a coupled techno-macro-economic model to assess the macro-economic benefit of installing a 5.25 MW farm of OWC in selected areas in Scotland and Portugal. According to their analysis, the project development will immediately boost various sectors related to the construction, installation, and operation of the devices, as well as those related to insurance and project management. Furthermore, their coupled techno-macro-economic model emphasizes the benefit of this type of projects and provides additional information to investors, policymakers and funding agencies.

As previously stated, the technology in the OWC devices has shown to be available and effective; nevertheless, there has not been much acceptance since, despite its effectiveness, this sort of technology is still somewhat expensive. Among the numerous reasons for this are that projects are frequently small, thus project costs are disproportionately expensive; limited volumes entail high equipment costs; and, finally, weak power grids in suitable coastal areas need high connection costs. The challenge for the industry is to get to the point where these constraints no longer apply and these

sorts of projects are truly commercial. The governments involved have acknowledged this issue, and in Scotland and Portugal, in particular, there are substantial support tariffs for power generated by this sort of technology. Being a renewable energy system, the main constraint to the acceptance of WECs in commercial operations is the cost of the energy generated, which is now being addressed. The combination of early public support and industry commitment to improve competitiveness indicates that OWC devices will be part of future clean energy generation systems.

## Bibliography

- Astariz, S. and Iglesias, G. (2015). The economics of wave energy: A review, *Renewable and Sustainable Energy Reviews* **45**: 397 – 408.  
URL: <http://www.sciencedirect.com/science/article/pii/S1364032115000714>
- Belibassakis, K., Magkouris, A. and Rusu, E. (2020). A BEM for the hydrodynamic analysis of oscillating water column systems in variable bathymetry, *Energies* **13(13)**: 3403.
- Bønke, K. and Ambli, N. (1986). Prototype wave power stations in norway, *Proceedings of International Symposium on Utilization of Ocean Waves-Wave to Energy Conversion. La Jolla, CA, ASCE*, pp. 34–45.
- Boccotti, P. (2003). On a new wave energy absorber, *Ocean Engineering* **30**: 1191–1200.
- Boccotti, P. (2007a). Caisson breakwaters embodying an owc with a small opening-part i: Theory, *Ocean Engineering* **34(5-6)**: 806–819.
- Boccotti, P. (2007b). Caisson breakwaters embodying an owc with a small opening—part i: Theory, *Ocean Engineering* **34**: 806–819.
- Boccotti, P. (2007c). Comparison between a u-owc and a conventional owc, *Ocean Engineering* **34**: 799–805.
- Brito-Melo, A. and Sarmento, A. (2002). Numerical modelling of owc wave-power plants of the oscillating water column type.
- Count, B. M. and Evans, D. V. (1984). The influence of projecting sidewalls on the hydrodynamic performance of wave-energy devices, *Journal of Fluid Mechanics* **145**: 361–376.
- Daniel Raj, D., Sundar, V. and Sannasiraj, S. A. (2019). Enhancement of hydrodynamic performance of an oscillating water column with harbour walls, *Renewable Energy*

- 132:** 142 – 156.  
**URL:** <http://www.sciencedirect.com/science/article/pii/S0960148118308863>
- Draycott, S., Szadkowska, I. and Ingram, D. (2018). Assessing the macro-economic benefit of installing a farm of oscillating water columns in scotland and portugal, *Energies* **11**.
- Şentürk, U. and Özdamar, A. (2012). Wave energy extraction by an oscillating water column with a gap on the fully submerged front wall, *Applied Ocean Research* **37**: 174 – 182.  
**URL:** <http://www.sciencedirect.com/science/article/pii/S0141118712000405>
- Evans, D. and Porter, R. (1995). Hydrodynamic characteristics of an oscillating water column device, *Applied Ocean Research* **17**(3): 155 – 164.  
**URL:** <http://www.sciencedirect.com/science/article/pii/0141118795000089>
- Evans, D. V. (1978). The Oscillating Water Column Wave-energy Device, *IMA Journal of Applied Mathematics* **22**(4): 423–433.  
**URL:** <https://doi.org/10.1093/imamat/22.4.423>
- Evans, D. V. (1982). Wave-power absorption by systems of oscillating surface pressure distributions, *Journal of Fluid Mechanics* **114**: 481–499.
- Falcão, A. (2000). The shoreline owc wave power plant at the azores, *Proceedings of 4th European Wave Energy Conference, Aalborg, Denmark*, pp. 42–47.
- Falcão, A. (2010). Wave energy utilization: A review of the technologies, *Renewable and Sustainable Energy Reviews* **14**(3): 899 – 918.
- Falcão, A. and Henriques, J. C. C. (2016). Oscillating-water-column wave energy converters and air turbines: A review, *Renewable Energy* **85**: 1391–1424.
- Falcão, J. and Sarmiento, A. J. N. A. (1980). Wave generation by a periodic surface pressure and its application in wave-energy extraction, *15th International Congress on Theoretical Applied Mechanics. Toronto*.
- Falnes, J. and McIver, P. (1985). Surface wave interactions with systems of oscillating bodies and pressure distributions, *Applied Ocean Research* **7**(4): 225–234.  
**URL:** <https://www.sciencedirect.com/science/article/pii/014111878590029X>

- Frid, C., Andonegi, E., Depestele, J., Judd, A., Rihan, D., Rogers, S. I. and Kenchington, E. (2012). The environmental interactions of tidal and wave energy generation devices, *Environmental Impact Assessment Review* **32**(1): 133 – 139.
- Green, W. L., Campo, J. J., Parker, J., Miller, J. A. and Miles, J. B. (1983). Wave energy conversion with an oscillating water column on a fixed offshore platform, Vol. 105, pp. 487–490.
- Heath, T. (2012). A review of oscillating water columns, *Philosophical Transactions of the Royal Society A* **370**: 235–45.
- Heath, T., Whittaker, T. J. T. and Boake, C. B. (2000). The design, construction and operation of the limpet wave energy converter (islay, scotland), *Proceedings of 4th European Wave Energy Conference*, pp. 49–55.
- Hong, D., Hong, S. and Hong, S. (2004). Numerical study of the motions and drift force of a floating owc device, *Ocean Engineering* **31**(2): 139–164.  
**URL:** <https://www.sciencedirect.com/science/article/pii/S0029801803001185>
- Ibarra-Berastegi, G., Sáenz, J., Ulazia, A., Serras, P., Esnaola, G. and Garcia-Soto, C. (2018). Electricity production, capacity factor, and plant efficiency index at the mutriku wave farm (2014–2016), *Ocean Engineering* **147**: 20 – 29.  
**URL:** <http://www.sciencedirect.com/science/article/pii/S0029801817306157>
- Iino, M., Miyazaki, T., Segawa, H. and Iida, M. (2016). Effect of inclination on oscillation characteristics of an oscillating water column wave energy converter, *Ocean Engineering* **116**: 226 – 235.  
**URL:** <http://www.sciencedirect.com/science/article/pii/S0029801816001219>
- Ikoma, T., Masuda, K., Omori, H., Osawa, H. and Maeda, H. (2016). Improvement of performance of wave power conversion due to the projecting walls for owc type wec, *Journal of Offshore Mechanics and Arctic Engineering* **138**.
- Ikoma, T., Osawa, H., Masuda, K. and Maeda, H. (2011). Expected values of wave power absorption around the japanese islands using owc types with projecting walls, *Proceedings of the International Conference on Offshore Mechanics and Arctic Engineering - OMAE*, Vol. 5.
- John Ashlin, S., Sundar, V. and Sannasiraj, S. (2016). Effects of bottom profile of an oscillating water column device on its hydrodynamic characteristics, *Renewable Energy* **96**: 341 – 353.

- URL:** <http://www.sciencedirect.com/science/article/pii/S0960148116303937>
- Koley, S. and Trivedi, K. (2020). Mathematical modeling of oscillating water column wave energy converter devices over the undulated sea bed, *Engineering Analysis with Boundary Elements* **117**: 26 – 40.
- URL:** <http://www.sciencedirect.com/science/article/pii/S0955799720300801>
- Malmo, O. and Reitan, A. (1985). Wave-power absorption by an oscillating water column in a channel, *Journal of Fluid Mechanics* **158**: 153–175.
- Malmo, O. and Reitan, A. (1986a). Wave-power absorption by a finite row of oscillating water columns in a reflecting wall, *Applied Ocean Research* **8**(2): 105–109.
- URL:** <https://www.sciencedirect.com/science/article/pii/S0141118786800050>
- Malmo, O. and Reitan, A. (1986b). Wave-power absorption by an oscillating water column in a reflecting wall, *Applied Ocean Research* **8**(1): 42–48.
- URL:** <https://www.sciencedirect.com/science/article/pii/S014111878680030X>
- Masuda, Y. (1979). Experimental full-scale results of wave power machine kaimei in 1978, *Proceedings of the First Symposium on Wave Energy Utilization, Gothenburg, Sweden*.
- Masuda, Y. (1986). An experience of wave power generator through tests and improvement, in D. V. Evans and A. F. O. de Falcão (eds), *Hydrodynamics of Ocean Wave-Energy Utilization*, Springer Berlin Heidelberg, Berlin, Heidelberg, pp. 445–452.
- Masuda, Y. and McCormick, M. (1987). Experiences in pneumatic wave energy conversion in japan, *Utilization of ocean waves-wave to energy conversion. New York: ASCE* pp. 1–33.
- McIver, P. and Evans, D. (1988). An approximate theory for the performance of a number of wave-energy devices set into a reflecting wall, *Applied Ocean Research* **10**(2): 58–65.
- URL:** <https://www.sciencedirect.com/science/article/pii/S0141118788800324>
- Mendoza, E., Lithgow, D., Flores, P., Felix, A., Simas, T. and Silva, R. (2019). A framework to evaluate the environmental impact of ocean energy devices, *Renewable and Sustainable Energy Reviews* **112**: 440–449.



- Morris-Thomas, M. T., Irvin, R. J. and Thiagarajan, K. P. (2006). An Investigation Into the Hydrodynamic Efficiency of an Oscillating Water Column, *Journal of Offshore Mechanics and Arctic Engineering* **129**(4): 273–278.  
URL: <https://doi.org/10.1115/1.2426992>
- Ning, D.-Z., Shi, J., Zou, Q.-P. and Teng, B. (2015). Investigation of hydrodynamic performance of an owc (oscillating water column) wave energy device using a fully nonlinear hoberm (higher-order boundary element method), *Energy* **83**: 177 – 188.  
URL: <http://www.sciencedirect.com/science/article/pii/S0360544215001644>
- Ohneda, H., Igarashi, S., Shinbo, O., Sekihara, S., Suzuki, K., Kubota, H. and Morita, H. (1991). Construction procedure of a wave power extracting caisson breakwater, *Proceedings of 3rd Symposium on Ocean Energy Utilization*, pp. 171–179.
- Pecher, A. and Kofoed, J. P. (2017). *Handbook of Ocean Wave Energy*, Ocean Engineering & Oceanography, Springer International Publishing.  
URL: <https://books.google.es/books?id=IuTxjwEACAAJ>
- Ravindran, M. and Koola, P. M. (1991). Energy from sea waves-the indian wave energy programme, *Current Science* **60**(12): 676–680.
- Rezanejad, K., Bhattacharjee, J. and Guedes Soares, C. (2013). Stepped sea bottom effects on the efficiency of nearshore oscillating water column device, *Ocean Engineering* **70**: 25 – 38.  
URL: <http://www.sciencedirect.com/science/article/pii/S0029801813002229>
- Rezanejad, K., Guedes Soares, C., López, I. and Carballo, R. (2017). Experimental and numerical investigation of the hydrodynamic performance of an oscillating water column wave energy converter, *Renewable Energy* **106**: 1 – 16.  
URL: <http://www.sciencedirect.com/science/article/pii/S0960148117300034>
- Sergiienko, N. (2018). *Three-tether wave energy converter: Hydrodynamic modelling, performance assessment and control*, PhD thesis.
- Smith, C. M. (1983). *Some problems in linear water waves*, PhD thesis, University of Bristol, Bristol, UK.
- The Carbon Trust (2005). *Marine Energy Challenge: Oscillating Water Column Wave Energy Converter. Evaluation Report*.

- Thorpe, T. W. and Unit, H. L. E. T. S. (1999). *A Brief Review of Wave Energy*, Harwell Laboratory, Energy Technology Support Unit.
- Torre-Enciso, Y., Ortubia, I., Aguilera, L. and Marqués, J. (2009). Mutriku wave power plant: From the thinking out to the reality, *Proceedings of the 8th European Wave and Tidal Energy Conference* pp. 319–329.
- Energy, O. (n.d.). Accessed on 2nd February 2019, <http://www.oceanenergy.ie/>.
- Vyzikas, T., Deshoulières, S., Barton, M., Giroux, O., Greaves, D. and Simmonds, D. (2017). Experimental investigation of different geometries of fixed oscillating water column devices, *Renewable Energy* **104**: 248 – 258.  
**URL:** <http://www.sciencedirect.com/science/article/pii/S096014811631045X>
- Wang, D., Katory, M. and Li, Y. (2002). Analytical and experimental investigation on the hydrodynamic performance of onshore wave-power devices, *Ocean Engineering* **29**(8): 871 – 885.  
**URL:** <http://www.sciencedirect.com/science/article/pii/S0029801801000580>
- Whittaker, T. J. T., McIwaine, S. J. and Raghunathan, S. (1993). A review of the islay shoreline wave power station, *Proceedings of First European Wave Energy Symposium*, pp. 283–286.
- Zhang, C. and Ning, D. (2019). Hydrodynamic study of a novel breakwater with parabolic openings for wave energy harvest, *Ocean Engineering* **182**: 540 – 551.  
**URL:** <http://www.sciencedirect.com/science/article/pii/S0029801819301854>
- Zheng, S., Zhu, G., Simmonds, D., Greaves, D. and Iglesias, G. (2020). Wave power extraction from a tubular structure integrated oscillating water column, *Renewable Energy* **150**: 342 – 355.  
**URL:** <http://www.sciencedirect.com/science/article/pii/S0960148120300094>

# Chapter 4

## Background theory

This chapter summarizes the fundamental aspects of water waves and hydrodynamics that are the conceptual basis for the development of the theoretical models of the present work. First, a brief explanation of the type of ocean waves is given, then the governing equations for fluid flow are listed and a short description of the velocity potential and the Bernoulli equation are explained; finally, the governing equations and boundary conditions that constitute the linear wave theory are presented.

### 4.1 Ocean Waves

The waves on the ocean surface can be caused by a mix of several disturbing and restoring factors, see Fig. 4.1. Thus, in general, tides might be thought of as very long period waves, and disturbances such as earthquakes that generate tsunamis could also be considered waves. However, the waves used by WECs are often created by wind blowing over the surface of the ocean (Pecher and Kofoed; 2017).

Water waves always begin as little ripples and grow in size owing to the sustained energy input from the wind. As long as the wind blows, the waves reach a limit beyond which they do not grow owing to energy losses such as white-capping that balance out the energy input from the wind. In this scenario, the waves are considered to be fully developed. The extent to which a sea develops is determined by both the wind speed and the distance, or fetch, across which the wind has been blowing. However, after the wind stops blowing, the waves continue to exist and can travel over extremely long distances with little energy loss. In this state, they are typically known as swell waves because the wind that caused them is no longer present.

It is common to divide waves into wind waves generated by local winds and swell waves formed by no longer blowing winds. While the distinction between wind and swell waves is useful for debate, they are basically two extremes of a wave continuum. In fact, all waves are both created by the effect of previous wind and affected by the local wind.

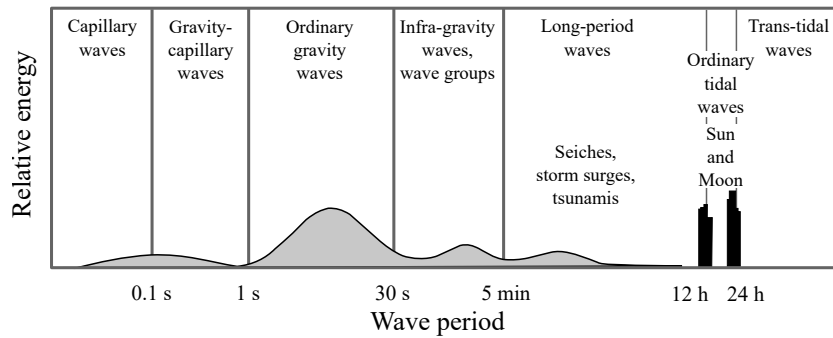


Figure 4.1: The types of waves that may occur in the ocean, adapted from [World Meteorological Organisation \(1998\)](#).

Although separating waves into wind and swell waves may be a helpful tool for describing the conditions of a particular location in the ocean, this is only an abstraction, as the hydrodynamics of wind and swell waves are identical.

## 4.2 Water Wave Mechanics

A basic ocean wave is typically regarded as a sinusoidal variation at the water surface and can be defined by its height,  $H$ , which is the vertical distance from the wave crest to the wave trough, a wavelength,  $\lambda$ , which is the distance between two similar points of the wave and the wave period,  $T$ , which is the time taken for the wave to repeat. Other useful wave parameters are wave steepness ( $s = H/\lambda$ ), which is often used to distinguish between linear and non-linear waves, wave number ( $k = 2\pi/\lambda$ ) and wave frequency ( $\omega = 2\pi/T$ ).

The suitability of the different wave theories based on the wave steepness ( $H/gT^2$ ) and the relative water depth ( $h/gT^2$ ) is shown in Fig. 4.2. It is worth mentioning that it is extremely complex to apply any theory, except linear theory, to irregular waves and it is usual to apply linear wave theory beyond the boundaries illustrated in Fig. 4.2, while acknowledging that it is not fully accurate.

### 4.2.1 Dispersion Relationship

One of the most distinguishing characteristics of ocean waves is that they are generally dispersive, which indicates that the energy in the wave does not travel at the same velocity as the wave profile ([Dean and Dalrymple; 1991](#); [Pecher and Kofoed; 2017](#)). For example, the effect of dispersion can be observed when the wave paddles in a wave tank stop generating waves. Due to the wave energy, waves appear to be left behind the main

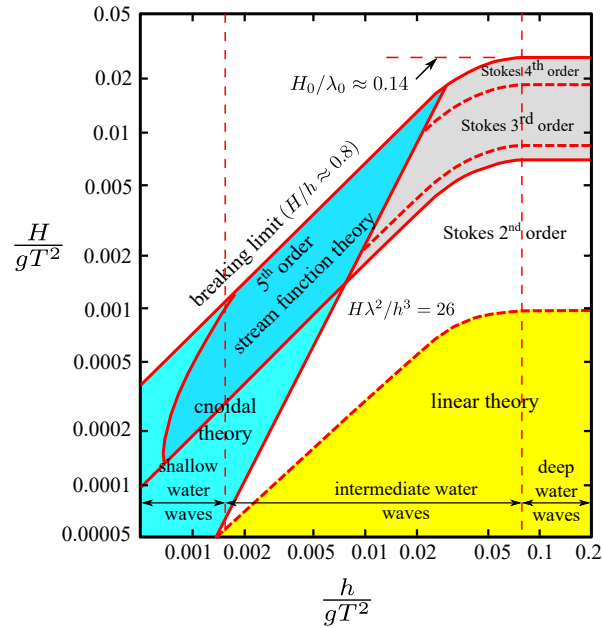


Figure 4.2: Chart of wave model suitability, adapted from Pecher and Kofoed (2017).

wave and travel at a slower pace than the wave crests. The velocity of a wave crest is called the wave celerity,  $c$ , and the velocity of the energy propagation is typically called the group velocity,  $c_g$ , defined by

$$c_g = \frac{1}{2} \left( 1 + \frac{4\pi h/\lambda}{\sinh(4\pi h/\lambda)} \right) c, \quad (4.1)$$

while wave celerity is given by

$$c = \frac{\lambda}{T} = \frac{gT}{2\pi} \tanh\left(\frac{2\pi h}{\lambda}\right), \quad (4.2)$$

which is called the dispersion equation and defines the wavelength based on the wave period and water depth.

### 4.2.2 Water Wave Motions

The variation in water surface elevation is the consequence of the elliptical movement of the water particles which extends far below the water surfaces, with the amplitude of motion diminishing exponentially with depth, as shown in Fig. 4.3. The water particle movements in deep water are circular, but as the water depth decreases, they become

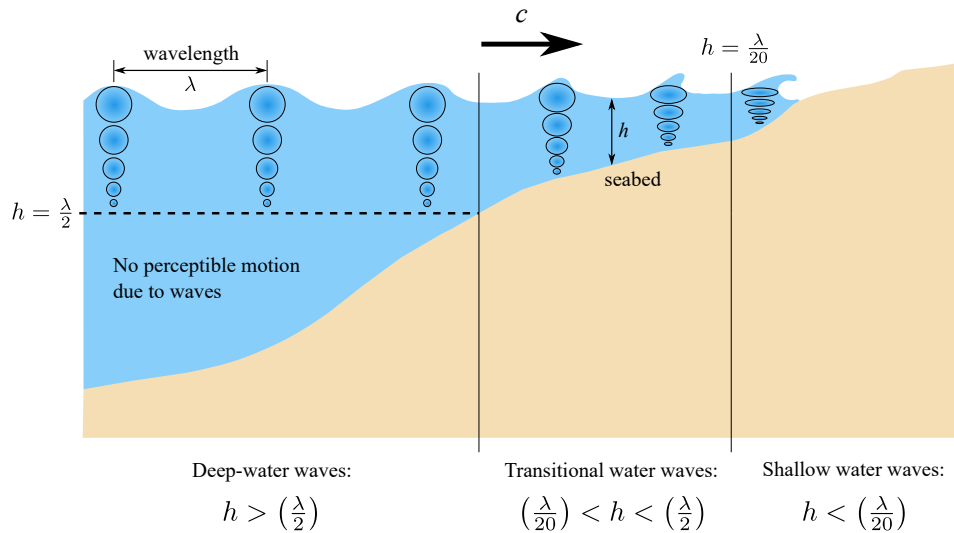


Figure 4.3: Classification of progressive waves based on their wavelength relative to the depth of water through which they are passing, adapted from Garrison (2009).

more elliptical. In particular, the variation in water particle motion is dependent on the water depth relative to the wavelength, and this is frequently used to define three regions of water depth:

- deep water, where the seabed has no effect on the waves and where the water depth is usually higher than half the wavelength;
- shallow water requires a water depth of less than 1/20th of a wavelength and has no change in horizontal water particle motion with water depth;
- intermediate depth that exists between these two extremes.

However, it is important to note that these limits are somewhat arbitrary, and because they are dependent on the wavelength, the concept of water depth is not fixed. As a result, extreme caution should be taken in determining which reference wavelength should be utilized to establish the relative depth.

## 4.3 Review of hydrodynamics

### 4.3.1 Conservation of mass

The conservation of mass applied to fluid flow is expressed by the equation of continuity. This equation expresses the fact that the internal time rate of decrease of mass within a

control volume equals the net flux of mass through the surface area of the volume. The equation can be written in differential form as

$$\frac{\partial \rho}{\partial t} + \nabla \cdot (\rho V) = 0, \quad (4.3)$$

where the nabla operator is defined in Cartesian coordinates by

$$\nabla \equiv \frac{\partial}{\partial x} \mathbf{i} + \frac{\partial}{\partial y} \mathbf{j} + \frac{\partial}{\partial z} \mathbf{k}, \quad (4.4)$$

the fluid velocity vector is

$$V = u\mathbf{i} + v\mathbf{j} + w\mathbf{k} \quad (4.5)$$

and  $\rho$  is the density of the medium. In water, for a  $1 \times 10^6 \text{ Nm}^{-2}$  increase in pressure results in a 0.05% change in density of water. Therefore, it will be assumed henceforth that water is incompressible. From Eq. (4.3), the conservation of mass equation for an incompressible fluid can be stated simply as

$$\frac{\partial u}{\partial x} + \frac{\partial v}{\partial y} + \frac{\partial w}{\partial z} = 0, \quad (4.6)$$

which must be true at every location in the fluid. This equation is also referred to as the *continuity* equation, and the flow field satisfying Eq. (4.6) is termed a non-divergent flow.

### 4.3.2 Conservation of Momentum and Energy

Newton's second law of motion applied to fluid motion can be paraphrased as the time-rate of change of linear momentum of the fluid is equal to the sum of the external forces acting on the fluid (McCormick; 2010). For incompressible flow, this statement can be expressed mathematically by

$$m \frac{DV}{Dt} = m \left( \frac{\partial V}{\partial t} + V \cdot \nabla V \right) = \sum F, \quad (4.7)$$

where  $m$  is the mass of the fluid in a control volume and  $F$  is an external force acting on the mass in the control volume. The term  $DV/Dt$  is used to represent the total time derivative of the velocity. In Eq. (4.7) there are two types of fluid acceleration: the first ( $\partial V/\partial t$ ) is called the local acceleration and exists only if there is a velocity variation in time and; the second, ( $V \cdot \nabla V$ ) is called the convective acceleration, and exists because of a change in flow geometry.

On the other hand, the external forces acting on the fluid are body forces, such as the gravitational force ( $-\rho g \mathbf{k}$ ), and surface forces, which include those due to pressure

gradient ( $-\nabla P$ ) and shear stress ( $\mu\nabla^2 V$ ), where  $g$  is the gravitational constant,  $p$  the pressure and  $\mu$  the dynamic viscosity.

Applied to incompressible flow, the expression in Eq. (4.7) is

$$\rho \left( \frac{\partial V}{\partial t} + V \cdot \nabla V \right) = -\rho g \mathbf{k} - \nabla P + \mu \nabla^2 V. \quad (4.8)$$

This expression is a form of the Navier-Stokes equations. It represents three equations, one in each of the component directions and due to the convective acceleration term, Eq. (4.8) is nonlinear, without an existing general solution so far.

When the viscous forces are neglected ( $\mu = 0$ ), the flow is said to be inviscid. For an inviscid flow, the Navier-Stokes equations reduce to a form called Euler's equations, which is expressed as follows

$$\rho \left( \frac{\partial V}{\partial t} + V \cdot \nabla V \right) = -\rho g \mathbf{k} - \nabla P. \quad (4.9)$$

However, like the Navier-Stokes equations, Euler's equations are nonlinear because of the convective acceleration and, therefore, there is no general solution to Euler's equations.

### 4.3.3 Velocity Potential

Let us define the value of the line integral of  $V$  as  $\phi$ :

$$\phi = \oint V \cdot dl = \oint (u dx + v dy + w dz), \quad (4.10)$$

where the quantity  $V \cdot dl$  is a measure of the fluid velocity in the direction of the contour at each point,  $\phi$  is related to the product of the velocity and length along the path between two points.

For the value of  $\phi$  to be independent of path, that is, for the flow rate between two points to be the same no matter how the integration is carried out, the terms in the integral must be an exact differential  $d\phi$

$$\phi = \oint d\phi = \oint \left( \frac{\partial \phi}{\partial x} dx + \frac{\partial \phi}{\partial y} dy + \frac{\partial \phi}{\partial z} dz \right), \quad (4.11)$$

where where  $d\phi$  is the exact differential of  $\phi$  and, therefore, by equating Eq. (4.10) and (4.11) results

$$u = \frac{\partial \phi}{\partial x}, \quad (4.12a)$$

$$v = \frac{\partial \phi}{\partial y}, \quad (4.12b)$$



$$w = \frac{\partial \phi}{\partial z}. \quad (4.12c)$$

To ensure that this scalar function must be zero:

$$\nabla \times V = 0 = \left( \frac{\partial w}{\partial y} - \frac{\partial v}{\partial z} \right) \mathbf{i} + \left( \frac{\partial u}{\partial z} - \frac{\partial w}{\partial x} \right) \mathbf{j} + \left( \frac{\partial v}{\partial x} - \frac{\partial u}{\partial y} \right) \mathbf{k}, \quad (4.13)$$

where the curl of the velocity vector is referred to as the vorticity  $\boldsymbol{\omega}$ .

Therefore, the velocity vector  $V$  can be conveniently represented as

$$V = \nabla \phi, \quad (4.14)$$

and expresses the vector quantity by the gradient of a scalar function  $\phi$  for a flow with no vorticity.

### 4.3.4 The Bernoulli equation

Basically, the Bernoulli equation is an integrated form of Euler equations of motion and provides a relationship between the pressure field and kinematics. Retaining our assumptions of irrotational motion and incompressible fluid, the governing equations of motion in the fluid for the  $x - z$  plane are the Euler equations (4.9)

$$\frac{\partial u}{\partial t} + u \frac{\partial u}{\partial x} + w \frac{\partial u}{\partial z} = -\frac{1}{\rho} \frac{\partial p}{\partial x}, \quad (4.15a)$$

$$\frac{\partial w}{\partial t} + u \frac{\partial w}{\partial x} + w \frac{\partial w}{\partial z} = -\frac{1}{\rho} \frac{\partial p}{\partial z} - g. \quad (4.15b)$$

From Eq. (4.13) the irrotationality condition gives

$$\frac{\partial u}{\partial z} = \frac{\partial w}{\partial x}. \quad (4.16)$$

Thus, the Eqs. (4.15) can be rewritten as

$$\frac{\partial u}{\partial t} + \frac{\partial (u^2/2)}{\partial x} + \frac{\partial (w^2/2)}{\partial x} = -\frac{1}{\rho} \frac{\partial p}{\partial x}, \quad (4.17a)$$

$$\frac{\partial w}{\partial t} + \frac{\partial (u^2/2)}{\partial z} + \frac{\partial (w^2/2)}{\partial z} = -\frac{1}{\rho} \frac{\partial p}{\partial z} - g. \quad (4.17b)$$

Now, since a velocity potential exists for the fluid, we have

$$u = \frac{\partial \phi}{\partial x}, \quad w = \frac{\partial \phi}{\partial z}. \quad (4.18)$$

Therefore, if we substitute these definitions into Eqs. (4.17), we obtain

$$\frac{\partial}{\partial x} \left[ \frac{\partial \phi}{\partial t} + \frac{1}{2} (u^2 + w^2) + \frac{p}{\rho} \right] = 0, \quad (4.19a)$$

$$\frac{\partial}{\partial z} \left[ \frac{\partial \phi}{\partial t} + \frac{1}{2} (u^2 + w^2) + \frac{p}{\rho} \right] = -g, \quad (4.19b)$$

where it has been assumed that the density is uniform throughout the fluid. Integrating the  $x$  equation yields

$$\frac{\partial \phi}{\partial t} + \frac{1}{2} (u^2 + w^2) + \frac{p}{\rho} = C'(z, t), \quad (4.20)$$

where the constant of integration  $C'(z, t)$ , varies only with  $z$  and  $t$ . Similarly, integrating the  $z$  equation yields

$$\frac{\partial \phi}{\partial t} + \frac{1}{2} (u^2 + w^2) + \frac{p}{\rho} = -gz + C(x, t). \quad (4.21)$$

Examining these two equations, which have the same quantity on the left-hand sides, shows clearly that

$$C'(z, t) = -gz + C(x, t). \quad (4.22)$$

Thus  $C$  cannot be a function of  $x$ , as neither  $C'$  nor  $(gz)$  depend on  $x$ . Therefore,  $C'(z, t) = -gz + C(t)$ , and the resulting equation is

$$\frac{\partial \phi}{\partial t} + \frac{1}{2} (u^2 + w^2) + \frac{p}{\rho} + gz = C(t), \quad (4.23)$$

where the function  $C(t)$  is referred to as the Bernoulli term and is a constant for steady flows.

## 4.4 Linear wave theory

Linear wave theory is the core theory of ocean surface waves used in ocean and coastal engineering. This theory is a mathematical formulation of the propagation of gravity waves on the surface of an ideal fluid. It assumes that the water depth is uniform, and the fluid flow is incompressible, irrotational and inviscid. Furthermore, it considers that wave height is small compared to the wavelength. Although the theory is somewhat basic, the kinematic wave properties derived from the theory agree quite well with those actually observed. In this section, the governing differential equation, and the relevant linearized boundary conditions are presented.

### 4.4.1 Governing equation

Under the assumption of irrotational motion and incompressible fluid, a velocity potential exists which should satisfy the continuity equation (4.6)

$$\nabla \cdot V = \nabla \cdot \nabla \phi = 0, \quad (4.24)$$

and where the divergence of a gradient leads to the Laplace equation, which must hold throughout the fluid, Fig. 4.4,

$$\nabla^2 \phi = \frac{\partial^2 \phi}{\partial x^2} + \frac{\partial^2 \phi}{\partial y^2} + \frac{\partial^2 \phi}{\partial z^2} = 0. \quad (4.25)$$

### 4.4.2 Boundary Conditions

#### Kinematic boundary conditions

The mathematical expression for the kinematic boundary condition may be derived from an equation that describes a surface that constitutes a boundary. A fixed or moving surface can be expressed in terms of a mathematical expression of the form  $F(x, y, z, t) = 0$ . If the surface varies with time, like the water surface, then the total derivative of the surface with respect to time would be zero on the surface

$$\frac{DF(x, y, z, t)}{Dt} = 0 = \frac{\partial F}{\partial t} + u \frac{\partial F}{\partial x} + v \frac{\partial F}{\partial y} + w \frac{\partial F}{\partial z} \quad (4.26)$$

or

$$-\frac{\partial F}{\partial t} = V \cdot \nabla F = V \cdot \mathbf{n} |\nabla F|, \quad (4.27)$$

where the unit vector normal to the surface is given by  $\mathbf{n} = \nabla F / |\nabla F|$ .

Rearranging Eq. (4.27):

$$V \cdot \mathbf{n} = \frac{-\frac{\partial F}{\partial t}}{|\nabla F|}, \quad (4.28)$$

where

$$|\nabla F| = \sqrt{\left(\frac{\partial F}{\partial x}\right)^2 + \left(\frac{\partial F}{\partial y}\right)^2 + \left(\frac{\partial F}{\partial z}\right)^2}.$$

This condition requires that the component of the fluid velocity normal to the surface be related to the local velocity of that surface. For a surface with no time variation, then  $V \cdot \mathbf{n} = 0$ , which means that the velocity component normal to the surface is zero.

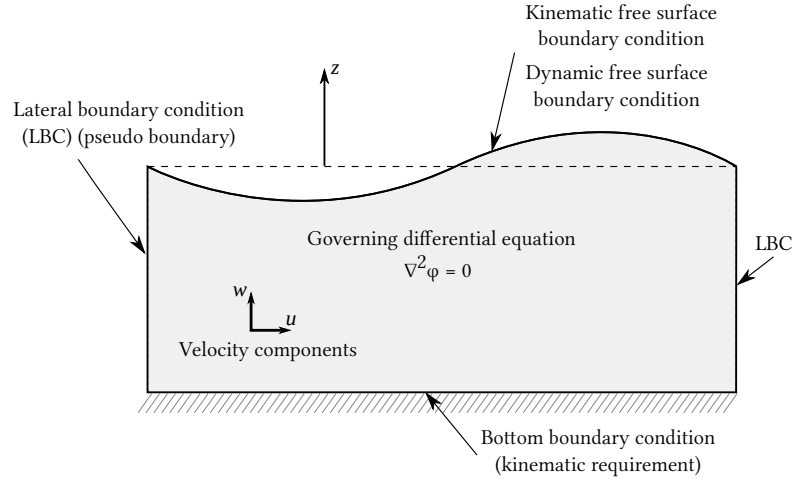


Figure 4.4: Two-dimensional water waves specified as a BVP, adapted from [Dean and Dalrymple \(1991\)](#).

### The bottom boundary condition

In general, the lower boundary of our region of interest is the bed profile described as  $z = h(x)$  for a two-dimensional case where the origin is located at the still water level and  $h$  represents the depth. For an impermeable bottom,  $V \cdot \mathbf{n} = 0$  as the bottom does not move with time; however, there exist some cases where it does, such as earthquake motions. Thus, the surface equation for the bottom is  $F(x, y) = z + h(x) = 0$ , therefore

$$V \cdot \mathbf{n} = 0, \quad (4.29)$$

where

$$\mathbf{n} = \frac{\nabla F}{|\nabla F|} = \frac{\frac{dh}{dx}\mathbf{i} + \mathbf{k}}{\sqrt{\left(\frac{dh}{dx}\right)^2 + 1}} \quad (4.30)$$

and simplifying we obtain

$$u \frac{dh}{dx} + w = 0 \quad \text{on} \quad z = -h(x). \quad (4.31)$$

In terms of the velocity potential,  $\phi(x, z, t)$ , the above equation is written as

$$\frac{\partial \phi}{\partial x} \frac{dh}{dx} + \frac{\partial \phi}{\partial z} = 0 \quad \text{on} \quad z = -h(x). \quad (4.32)$$

### Kinematic free surface boundary condition

In this case, the free surface of a wave can be described as  $F(x, y, z, t) = z - \eta(x, y, t) = 0$ , where  $\eta(x, y, t)$  is the displacement of the free surface about the horizontal plane,  $z = 0$ .

Substituting  $F$  on Eq. (4.28), the kinematic boundary condition at the free surface is

$$V \cdot \mathbf{n} = \frac{\frac{\partial \eta}{\partial t}}{\sqrt{\left(\frac{\partial \eta}{\partial x}\right)^2 + \left(\frac{\partial \eta}{\partial y}\right)^2 + 1}} \quad \text{on } z = \eta(x, y, t), \quad (4.33)$$

where

$$\mathbf{n} = \frac{-\frac{\partial \eta}{\partial x} \mathbf{i} - \frac{\partial \eta}{\partial y} \mathbf{j} + \mathbf{k}}{\sqrt{\left(\frac{\partial \eta}{\partial x}\right)^2 + \left(\frac{\partial \eta}{\partial y}\right)^2 + 1}}. \quad (4.34)$$

Carrying out the dot product yields

$$w = \frac{\partial \eta}{\partial t} + u \frac{\partial \eta}{\partial x} + v \frac{\partial \eta}{\partial y} \quad \text{on } z = \eta(x, y, t). \quad (4.35)$$

Finally, substituting the velocity potential, we obtain

$$\frac{\partial \phi}{\partial z} = \frac{\partial \eta}{\partial t} + \frac{\partial \phi}{\partial x} \frac{\partial \eta}{\partial x} + \frac{\partial \phi}{\partial y} \frac{\partial \eta}{\partial y} \quad \text{on } z = \eta(x, y, t). \quad (4.36)$$

### Dynamic free surface boundary condition

Free surfaces, such as the air-water interface, cannot support variations in pressure across the interface and hence must respond in order to maintain the pressure as uniform. An additional condition, termed as a dynamic boundary condition, is thus required on any free surface or interface, to prescribe the pressure distribution on this boundary.

As the dynamic free surface boundary condition is a requirement that the pressure on the free surface is uniform along with the waveform, the unsteady Bernoulli equation (4.23) with  $p = \text{constant}$  is applied on the free surface  $z = \eta(x, t)$

$$\frac{\partial \phi}{\partial t} + \frac{1}{2} (u^2 + w^2) + \frac{p}{\rho} + gz = C(t), \quad (4.37)$$

where  $p$  is a constant and usually taken as gauge pressure,  $p = 0$ . The integration constant  $C(t)$  does not play an essential role and can be eliminated by redefining the velocity potential by

$$\frac{\partial \Phi}{\partial t} = \frac{\partial \phi}{\partial t} - C(t).$$

Summarising, in terms of the velocity potential  $\Phi$  the governing equation for irrotational wave motion is expressed as

$$\frac{\partial^2 \Phi}{\partial x^2} + \frac{\partial^2 \Phi}{\partial y^2} + \frac{\partial^2 \Phi}{\partial z^2} = 0 \quad \text{on } -h(x) \leq z \leq \eta(x, y, t) \quad (4.38)$$

and the three boundary conditions

$$\frac{\partial \Phi}{\partial t} + \frac{1}{2} \left[ \left( \frac{\partial \Phi}{\partial x} \right)^2 + \left( \frac{\partial \Phi}{\partial z} \right)^2 \right] + g\eta = 0 \quad \text{on} \quad z = \eta(x, y, t), \quad (4.39a)$$

$$\frac{\partial \Phi}{\partial z} = \frac{\partial \eta}{\partial t} + \frac{\partial \Phi}{\partial x} \frac{\partial \eta}{\partial x} + \frac{\partial \Phi}{\partial y} \frac{\partial \eta}{\partial y} \quad \text{on} \quad z = \eta(x, y, t), \quad (4.39b)$$

$$\frac{\partial \Phi}{\partial x} \frac{dh}{dx} + \frac{\partial \Phi}{\partial z} = 0 \quad \text{on} \quad z = -h(x). \quad (4.39c)$$

Finally, linearization is performed on Eqs. (4.39a)-(4.39b) by evaluating them on  $z = \eta(x, t)$  and expanding the value of the condition at  $z = 0$  (a known location) by the truncated Taylor series (see Dean and Dalrymple (1991); Dingemans (1997) for a detail explanation). Thus, the linear equations for water waves are given below for two-dimensional horizontal wave propagation over an uneven bottom:

$$\nabla^2 \Phi = 0 \quad \text{on} \quad -h(x) \leq z \leq 0, \quad (4.40a)$$

$$\frac{\partial \Phi}{\partial t} + g\eta = 0 \quad \text{on} \quad z = 0, \quad (4.40b)$$

$$\frac{\partial \Phi}{\partial z} = \frac{\partial \eta}{\partial t} \quad \text{on} \quad z = 0, \quad (4.40c)$$

$$\frac{\partial \Phi}{\partial x} \frac{dh}{dx} + \frac{\partial \Phi}{\partial z} = 0 \quad \text{on} \quad z = -h(x). \quad (4.40d)$$

## Bibliography

- Dean, R. G. and Dalrymple, R. A. (1991). *Water wave mechanics for engineers and scientists*, World Scientific, Singapore.
- Dingemans, M. W. (1997). *Water wave propagation over uneven bottoms. Advanced series on ocean engineering, 13*, World Scientific Publishing Co Pte Ltd.
- Garrison, T. (2009). *Oceanography: An Invitation to Marine Science*, Cengage Learning.  
**URL:** <https://books.google.com.mx/books?id=jUMJzgEACAAJ>
- McCormick, M. E. (2010). *Ocean Engineering Mechanics with Applications*, Cambridge University Press, New York.

Pecher, A. and Kofoed, J. P. (2017). *Handbook of Ocean Wave Energy*, Ocean Engineering & Oceanography, Springer International Publishing.

**URL:** <https://books.google.es/books?id=IuTxjwEACAAJ>

World Meteorological Organisation (1998). *Guide to wave analysis and forecasting*, (WMO 702), 2nd edn. WMO.

## Chapter 5

# The Influence of the Front Wall Thickness on the Hydrodynamic Efficiency of a Land-Fixed OWC Device

The focus of this chapter is on the effect of the chamber configuration on the OWC hydrodynamic efficiency by using a numerical approach. In practice, the OWC chamber design plays a key role in achieving better efficiency. The geometrical shape of the chamber is often selected to generate a column whose natural frequency of oscillation matches that of the most frequently occurring wave at the site where the OWC will be deployed. In this regard, the unpredictability of sea state conditions might have an impact on OWC feasibility since, once built, the size and shape of the structure are difficult to change.

However, whereas other parameters such as chamber length, submergence, and inclination have been researched, the thickness of the front wall in land-fixed OWC devices has not been extensively investigated. The fundamental idea of this chapter is that using a thick front barrier can have a significant impact on hydrodynamic efficiency. As a result, this chapter gives insights into the performance of a land-fixed OWC device and answers the following research question: What effect does the thickness of the front barrier have on maximum hydrodynamic efficiency curves of land-fixed OWC devices?

This chapter consists of the published journal article:

Medina Rodríguez A.A., Blanco Ilzarbe J.M., Silva Casarín R., Izquierdo Ereño U. (2020). “*The Influence of the Chamber Configuration on the Hydrodynamic Efficiency of Oscillating Water Column Devices*”. **Journal of Marine Science and Engineering**. 8(10): 751. <https://doi.org/10.3390/jmse8100751>.



**The Influence of the Chamber Configuration on the Hydrodynamic  
Efficiency of Oscillating Water Column Devices**

Ayrton Alfonso Medina Rodríguez, Jesús María Blanco Ilzarbe, Rodolfo Silva Casarín  
and Urko Izquierdo Ereño

**Abstract**

Based on the two-dimensional linear wave theory, the effects of the front wall thickness and the bottom profile of an Oscillating Water Column (OWC) device on its efficiency were analyzed. Using the potential flow approach, the solution of the associated boundary value problem was obtained via the boundary element method (BEM). Numerical results for several physical parameters and configurations were obtained. The effects of the front wall thickness on the efficiency are discussed in detail, then, various configurations of the chamber bottom are presented. A wider efficiency band was obtained with a thinner front wall. In a real scenario having a thinner front wall means that such a structure could have less capacity to withstand the impact of storm waves. Applying the model for the case of the Mutriku Wave Energy Plant (MWEP), findings showed that the proposed bottom profiles alter the efficiency curve slightly; higher periods of the incoming water waves were found. This could increase the efficiency of the device in the long-wave regime. Finally, the numerical results were compared with those available in the literature, and were found to be in good agreement.

## 5.1 Introduction

It has been suggested that wave power has the potential to provide most of the world's electricity needs in the short term (Izquierdo et al.; 2019). A wide variety of systems have been proposed, of which only a few have reached full-scale prototype deployments (Ahamed et al.; 2020). Among the deployed systems, the OWC system has been shown to be one of the most promising devices. It is probably the system that has been most studied and is one of the few to have been tested at full-scale. OWCs can be located offshore, near-shore or on the shoreline, and placed on the seabed or fixed to a rocky cliff (Falcão and Henriques; 2016). Since the design and construction of OWCs are strongly site-dependent, their location and anchorage points are of the most critical aspects, as well as the most influential in economic terms.

In light of this, installing an OWC device into a breakwater was seen as a means to provide many benefits and thus encourage further development of OWC technology (Vicinanza et al.; 2019). The breakwater provides shelter and contributes to coastal protection by reducing wave reflection. An OWC power plant within a breakwater has the advantage of being relatively easy to install and maintain, having no mooring systems and underwater electric cables. With construction and maintenance costs shared, and the operation of the power plant being easier, energy extraction is more cost-effective. Although the waves found near the coast are less energetic, this can, in part, be compensated by the natural concentration of wave energy due to shoaling, refraction and diffraction (Polinder and Scuotto; 2005).

## CHAPTER 5. THE INFLUENCE OF THE FRONT WALL THICKNESS ON THE HYDRODYNAMIC EFFICIENCY OF A LAND-FIXED OWC DEVICE

---

The first integrated breakwater-OWC system was built in the port of Sakata, Japan, in 1990 (Torre-Enciso et al.; 2009). Subsequently, the Basque Energy Agency (Ente Vasco de la Energía or EVE for its acronym in Spanish) employed this concept in Mutriku, The Basque Country, Spain, opening the Mutriku Wave Energy Plant in July 2011, Fig. 5.1. This plant consists of 16 units built onsite that are 4.5 m wide, 3.1 m depth, and 10 m high (above Maximum Equinoctial Spring Tide Low Water). For each unit, a hole of 0.75 m diameter leads to a Wells turbine and electrical generator of 18.5 kW (Garrido et al.; 2015), yielding the total 296 kW with a 100 m breakwater. The MWEP section of the breakwater is the first multiple OWC plant in the world and is currently the only OWC device in operation that regularly supplies power to the grid. However, regarding its performance, the initial expectations have not been met because of the poor design in some of the chambers that provide moderately different pressure at the inlet of their turbines (Ibarra-Berastegi et al.; 2018). This is because the breakwater that houses the Wells turbines was mainly designed to maximizing the protection of Mutriku harbour and not for wave energy harnessing.

In this context, another factor contributing to the plant's reduced electricity output could be the changes made to the front face of the original design. The area is regularly affected by severe storms and during the construction of the power plant, three storms hit the MWEP producing severe structural damage to a number of the OWC chambers (Medina-Lopez et al.; 2015). As a consequence, the front face of the chambers was reinforced to withstand the wave loads, using prefabricated concrete slabs, so that now the thickness of the front wall has doubled the length of the chambers, Fig. 5.2. This alteration was made to save the structure of the plant, but without considering the effect that this would have on the device performance. The main focus of this work is, therefore, the evaluation of the influence that the front wall thickness of an OWC-breakwater system has on its hydrodynamic performance as an OWC.

It is important to note that the success of the OWC system will depend on the coupling between the chamber and the power take-off (PTO) system. In this sense, a good turbine design, an effective control strategy and the matching of the turbine to the OWC collector to ensure efficient collector operation are essential (Heath; 2012). Furthermore, the peak performance of most OWC systems occurs at resonance, which takes place when the incident wave frequency coincides with the natural frequency of the converter. Therefore, to operate optimally at resonance, the OWC chamber design plays a significant role to obtain higher efficiencies. Typically the chamber geometrical configuration is chosen to produce a column whose natural frequency of oscillation coincides with that of the most occurring wave at the location where the OWC will be installed (Delmonte et al.; 2016). In this sense, the variability of sea state conditions can influence the OWC feasibility, because, once installed, the size and shape of the structure can be hardly modified.

Over the last years, a variety of analytical, numerical and experimental techniques have been employed to study the effects of the geometrical configuration of an OWC on its hydrodynamic efficiency. Wang et al. (2002) studied the hydrodynamic performance, both numerically and theoretically, of an OWC device with arbitrary topography near the shoreline. They reported that as the bottom slope increases, the peaks in capture-width ratios become lower frequency values, concluding that a change in water depth at the shoreline has a significant effect on the hydrodynamic performance of an OWC. The effect of front wall geometry on OWC

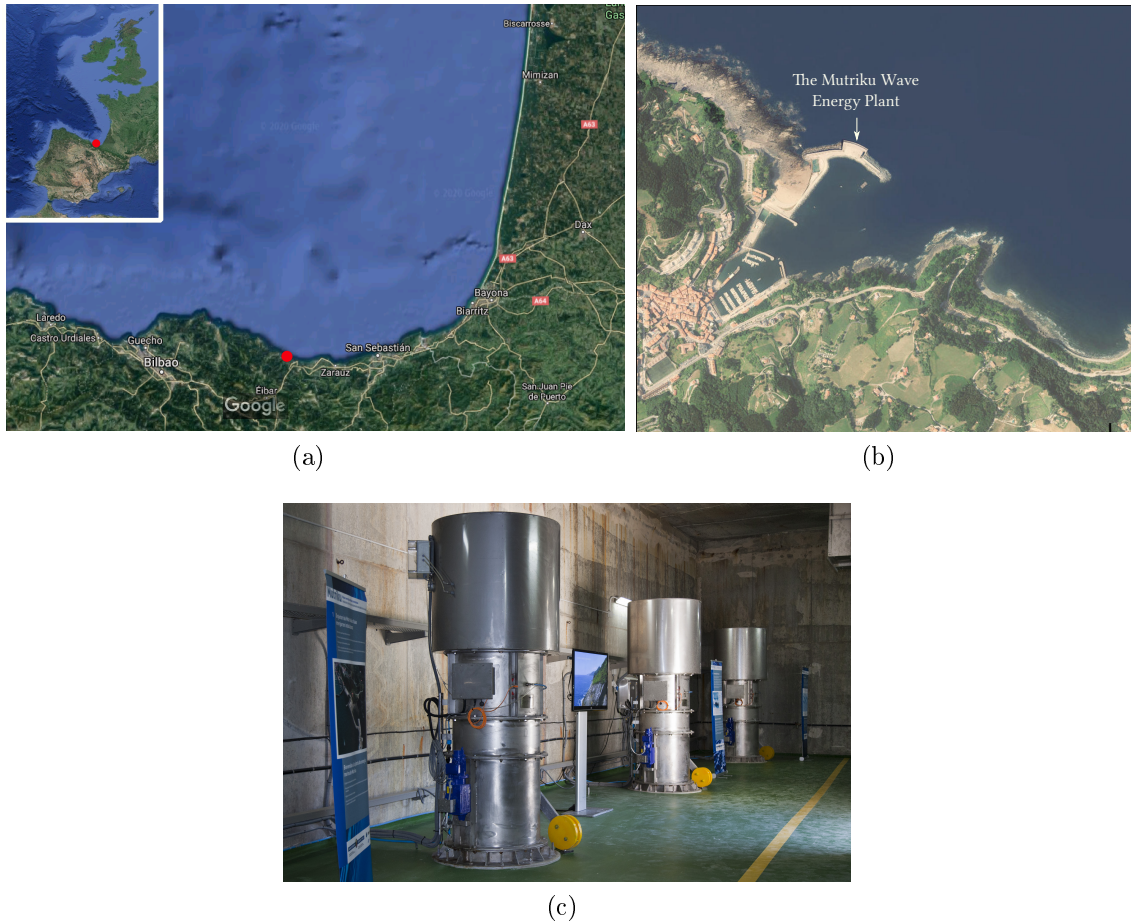


Figure 5.1: Location and turbo-generators of the MWEP. (a) Location of the harbour at Mutriku (source: Google Maps (*Google Maps 2020*; n.d.)). (b) Bird's eye view of Mutriku harbour and the OWC-breakwater system. (source: geoEuskadi (*GeoEuskadi, Infraestructura de Datos Espaciales (IDE) de Euskadi*; n.d.)). (c) Mutriku Wells Turbo-generators (source: EVE (*Ente Vasco de la Energía*; n.d.)).



Figure 5.2: Comparison between the original and the present-day design of the integrated breakwater-OWC system in Mutriku. (a) View of the MWEP in 2008 (Reproduced with permission from Torre-Enciso et al. (2009)). (b) Mutriku OWC (source: EVE (*Ente Vasco de la Energía*; n.d.)).

hydrodynamic efficiency was analyzed by Morris-Thomas et al. (2006). Their experimental study concluded that the overall peak in hydrodynamic efficiency is not influenced greatly by the front wall geometry. Martins-rivas and Mei (2009) presented a theoretical model for a cylindrical OWC installed on a cliff coast. It was found that air compressibility helps optimize the power absorption efficiency while the angle of incidence significantly affects the waves outside the chamber but not the averaged response inside or the capture length of energy absorption. Şentürk and Özdamar (2012) carried out a theoretical analysis of an OWC which had a gap in its fully-submerged front wall. They showed that it is possible to increase the efficiency of an OWC with a surface piercing, barrier-type front wall when appropriate geometrical parameters are taken into consideration.

Rezanejad et al. (2013) analyzed the impact of stepped bottom topography in the efficiency of a nearshore OWC device. They reported that there are significant effects when there is a stepped bottom profile outside of the chamber. Ning et al. (2015) studied the performance of a fixed OWC device based on a time-domain higher-order BEM in a 2D fully nonlinear numerical wave flume. They investigated the hydrodynamic performance, with, and without, a bottom slope in the OWC chamber, and reported that the geometric parameters of the air chamber have a significant influence on hydrodynamic efficiency. The configuration of the bottom profile on the hydrodynamic performance of the OWC was investigated experimentally by John Ashlin et al. (2016). Flat, circular, curved and sloped bottom profiles were tested in a wave flume. It was found that the OWC with a circular curved bottom profile was more effective in wave energy conversion, as was the wave amplification factor inside the chamber. The effects of the incident wave amplitude and geometric parameters on the hydrodynamic efficiency of a fixed OWC were investigated by Ning, Wang, Zou and Teng (2016). They concluded that the incident wave amplitude and the bottom slope have a small influence on the resonant

frequency, while the optimal hydrodynamic efficiency increases with an increase of bottom slope. A theoretical model based on linear potential flow theory to study the performance of a circular cylindrical OWC along a vertical coast/breakwater without the thin-wall restriction was proposed by [Zheng, Zhang and Iglesias \(2019\)](#). The authors concluded that the incident wave direction and the thickness of the circular chamber wall both play an important role in the wave power captured by the OWC. By employing the eigenfunction matching method, [Zheng, Antonini, Zhang, Greaves, Miles and Iglesias \(2019\)](#) developed a theoretical model to evaluate the hydrodynamic performance of multiple circular cylinder OWCs installed along a vertical straight coast. It was found that due to the effects of constructive wave interference from the OWCs array and the coast, the hydrodynamic performance of the OWC devices was enhanced significantly for a certain range of wave conditions. [Zheng et al. \(2020\)](#) studied the effect of the radius of the entrance to the chamber and the finite wall thickness of the tubular-structure. They demonstrated that wave power extraction is greater with a thinner chamber wall thickness, mainly in terms of a broader primary band of efficiency curves. Using a coupled eigenfunction expansion—BEM, [Koley and Trivedi \(2020\)](#) analyzed the hydrodynamic performance and efficiency of an OWC device placed on an undulated seabed. They concluded that the OWC structural design and bottom profile can significantly increase the hydrodynamic efficiency. A 2D BEM model for analyzing the OWC's response in general bathymetry regions was carried out by [Belibassakis et al. \(2020\)](#). They showed that the effects of the bottom slope and curvature on the OWC performance could be important, especially when the wave climate leads the site-specific optimal design to low resonance frequencies.

## 5.2 Aims and Methodology

In the specialized literature, there still remains a lot to be investigated regarding the improvement of the OWC efficiency by modifying its structural configuration. To the authors' knowledge, a numerical study for analyzing the interaction of water waves with an OWC-breakwater system considering a wide front barrier has not been examined in the past. The fundamental hypothesis of the present work is that the hydrodynamic efficiency can be highly affected when a thick front barrier is employed. This reduction to the efficiency could be explained by the fact that the transfer of energy from the incoming wave to the internal free surface due to the orbital wave motion is reduced. A reduction in energy transmission then may lead to a decrease in the internal free surface oscillation for driving the air column, which consequently diminishes the output power.

Furthermore, by following the same idea of a wide front barrier but now considering the physical dimensions of a chamber in the MWEP, three different bottom profiles inside the chamber are then proposed to analyze their influence on the hydrodynamic efficiency. These proposed varying bottom profiles are a slope, a cycloid and an ellipse. This proposal is motivated by the fact that a curve bottom profile can exhibit better performance in terms of wave energy conversion and wave amplification inside the chamber, as it was experimentally studied by [John Ashlin et al. \(2016\)](#). For this purpose, a numerical study for analyzing these curved profiles inside the chamber is also proposed.

Thus, this work examines the two-dimensional hydrodynamic interaction of ocean waves with an OWC device. Linear wave theory for a constant sea depth is employed and the viscous effects and the nonlinear air compressibility are neglected. The associated Boundary Value Problem (BVP) is then solved by the BEM employing three noded quadratic elements. The present formulation is novel in addressing the influence of a wide front wall and the use of BEM with a second-order discretization. The main interest of this work a) lies on the analysis of the bandwidth reduction on the efficiency curves due to an increment on the front wall thickness, and then, b) based on the geometric dimensions of the MWEF, to study alternatives for increasing the efficiency by considering a modification in the bottom profile inside the OWC chamber. Numerical estimates for the hydrodynamic efficiency and the radiation susceptance and radiation conductance coefficients are presented for a range of different parameters. Furthermore, numerical results for particular cases are validated with the previous results obtained by [Evans and Porter \(1995\)](#) for a thin vertical surface-piercing barrier next to a vertical wall, and [Şentürk and Özdamar \(2012\)](#) for an OWC with a gap on a fully submerged front wall.

### 5.3 The Boundary-Value Problem

For the present study, the Cartesian coordinate system was chosen, with the  $x$ -axis corresponding to the opposite direction of the wave propagation and the  $z$ -axis corresponding to the upward direction. The origin of the coordinate system lies on the undisturbed free surface and the left-vertical wall inside the chamber. The OWC is this rigid wall, situated at  $x = 0$ , extending down to the sea bottom and complemented by a vertical, surface-piercing barrier, at  $x = b$ , with a thickness  $w$  and a draft  $h_a$ , as shown in Fig. 5.3. The front barrier is denoted by  $L_b = \{(x, z) : (x = b, -h_a \leq z \leq 0) \cup (b < x < b + w, z = -h_a) \cup (x = b + w, -h_a \leq z \leq 0)\}$ , at the left side of the chamber entrance, the vertical length of the gap between the immersed tip of the barrier and the bottom is defined by  $L_g = \{(x, z) : x = b, -h_e \leq z \leq -h_a\}$ , the rigid vertical wall by  $S_w = \{(x, z) : x = 0, -h < z < 0\}$ , the internal free surface inside the water column by  $S_i = \{(x, z) : 0 \leq x \leq b, z = 0\}$ , the external free surface by  $S_f = \{(x, z) : b + w \leq x \leq \infty, z = 0\}$  and the bottom by  $S_b = \{(x, z) : (0 < x < b, z = -h) \cup (x = b, -h < z < -h_e) \cup (b < x < b + w, z = -h_e) \cup (x = b + w, -h < z < -h_e) \cup (b + w < x < \infty, z = -h)\}$ .

The fluid is assumed to be inviscid and incompressible and linear wave theory is applied, ignoring the effect of surface tension. By assuming an irrotational flow and simple harmonic in time with angular frequency  $\omega$ , there is thus a velocity potential  $\Phi(x, z, t)$  with  $\Phi(x, z, t) = \text{Re}\{\phi(x, z)e^{-i\omega t}\}$ , where  $\text{Re}\{\}$  denotes the real part of a complex expression and  $t$  is the time. The spatial velocity potential  $\phi$  then satisfies the Laplace equation

$$\frac{\partial^2 \phi}{\partial x^2} + \frac{\partial^2 \phi}{\partial z^2} = 0, \quad (5.1)$$

along with the no-flow boundary condition on the solid boundaries such as the barrier, the rigid vertical wall and the bottom described by

$$\frac{\partial \phi}{\partial n} = 0 \quad \text{for } (x, z) \in S_b, S_w \text{ and } L_b, \quad (5.2)$$

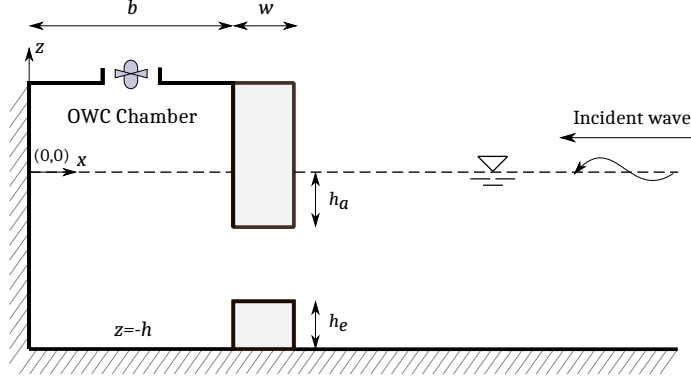


Figure 5.3: Definition sketch of an OWC device with a thick front wall.

together with the continuity of pressure and horizontal velocity given by

$$\phi_- = \phi_+ \quad \text{and} \quad \frac{\partial \phi}{\partial x_-} = -\frac{\partial \phi}{\partial x_+} \quad \text{for} \quad (x, z) \in L_g \quad \text{on} \quad \begin{cases} x = b, \\ x = b + w. \end{cases} \quad (5.3)$$

Inside the chamber, by imposing a pressure distribution over the internal free surface  $P(t)$  and after considering simple harmonic motions for the free surface  $\bar{\eta} = \text{Re}\{\zeta e^{-i\omega t}\}$  and  $P(t) = \text{Re}\{p e^{-i\omega t}\}$ , the dynamic and kinematic free surface boundary conditions are

$$\phi + \frac{ig}{\omega} \zeta = -\frac{i}{\rho\omega} p \quad \text{on} \quad z = 0, \quad 0 < x < b, \quad (5.4a)$$

$$\frac{\partial \phi}{\partial z} + i\omega \zeta = 0 \quad \text{on} \quad z = 0, \quad 0 < x < b, \quad (5.4b)$$

and on the external free surface with  $p = 0$

$$\phi + \frac{ig}{\omega} \zeta = 0 \quad \text{on} \quad z = 0, \quad b < x < \infty, \quad (5.5a)$$

$$\frac{\partial \phi}{\partial z} + i\omega \zeta = 0 \quad \text{on} \quad z = 0, \quad b < x < \infty. \quad (5.5b)$$

Thus, by combining Eqs. (5.4) and (5.5), the internal and external linearized free surface boundary conditions are

$$\frac{\partial \phi}{\partial z} - K\phi = \begin{cases} \frac{i\omega p}{\rho g} & \text{on} \quad z = 0, \quad 0 < x < b, \\ 0 & \text{on} \quad z = 0, \quad b < x < \infty, \end{cases} \quad (5.6)$$

respectively, where  $K = \omega^2/g$ , with  $g$  being the gravitational constant and  $\rho$  the seawater density.

CHAPTER 5. THE INFLUENCE OF THE FRONT WALL THICKNESS ON THE  
HYDRODYNAMIC EFFICIENCY OF A LAND-FIXED OWC DEVICE

---

Here, as described by [Evans and Porter \(1995\)](#), the potential is decomposed into two parts as follows

$$\phi(x, z) = \phi^S + \frac{i\omega p}{\rho g} \phi^R. \quad (5.7)$$

The scattered potential  $\phi^S$  represents the solution of the scattering of an incident wave coming from  $x = +\infty$  in the absence of an imposed pressure on the internal free surface inside the chamber, satisfying Eqs. (5.1)–(5.6) with  $p = 0$ ; while the radiated potential  $\phi^R$  represents the solution of the radiation problem due to the pressure imposed on the internal free surface and satisfies Eqs. (5.1)–(5.6) with Eq. (5.6) replaced by

$$\frac{\partial \phi^R}{\partial z} - K \phi^R = 1 \quad \text{on} \quad z = 0, \quad 0 < x < b, \quad (5.8)$$

which is due to an oscillating pressure distribution on the internal free surface in the absence of incoming waves.

The Sommerfeld radiation condition describes the far field boundary condition for the diffraction and radiation problems as follows:

$$\frac{\partial \phi^{D,R}}{\partial x} - ik \phi^{D,R} = 0 \quad \text{as} \quad x \rightarrow +\infty, \quad (5.9)$$

where  $\phi^D$  represents the diffracted potential that together with the incident potential  $\phi^I$  composed the scattered potential  $\phi^S$ , while  $k$  represents the wave number and is the real root of the wave dispersion relation given by

$$\omega^2 = gk \tanh kh, \quad (5.10)$$

whose solution of this expression can be easily determined by a root-finding algorithm.

On the other hand, the time harmonic induced volume flux across the internal free surface,  $Q(t) = \text{Re}\{qe^{-i\omega t}\}$  (see [Evans and Porter \(1995\)](#)) is given by

$$q = \int_{S_i} \frac{\partial \phi}{\partial z} dx = q^S + \frac{i\omega p}{\rho g} q^R, \quad (5.11)$$

where  $q^S$  and  $q^R$  are the volume fluxes across  $S_i$  in the scattering and radiation problems, respectively. Thus, by using the continuity of volume flux across the internal free surface and the gap between the barrier tip and the sea bottom, we obtain

$$q^{S,R} = \int_{S_i} \frac{\partial \phi^{S,R}}{\partial z} dx = - \int_{L_g} \frac{\partial \phi^{S,R}}{\partial x} dz. \quad (5.12)$$

Finally, the volume flux  $q^R$  for the radiation problem is separated into real and imaginary parts as follows

$$\frac{i\omega p}{\rho g} q^R = - \left( \tilde{B} - i\tilde{A} \right) p = -Zp, \quad (5.13)$$

where  $Z = \tilde{B} - i\tilde{A}$  is a complex admittance and  $\tilde{A}$  and  $\tilde{B}$  are analogous to the added mass and the radiation damping coefficients of the forced oscillation of a rigid body system immersed in



an ideal fluid and, following [Evans and Porter \(1995\)](#), are called the radiation susceptance and the radiation conductance parameters, respectively, described by

$$\tilde{A} = \frac{\omega}{\rho g} \operatorname{Re}\{q^R\}, \quad (5.14a)$$

$$\tilde{B} = \frac{\omega}{\rho g} \operatorname{Im}\{q^R\}, \quad (5.14b)$$

where  $\operatorname{Im}\{\}$  denotes the imaginary part of a complex expression.

## Efficiency Relations

Since in practice it may be easier to control the volume flux through the turbines than the pressure drop across it ([Evans; 1982](#)), a linear relationship between these two without a phase lag is assumed,

$$q = (\Lambda - i\rho) p, \quad (5.15)$$

where  $\Lambda$  is a real control parameter, related to the damping induced to the airflow by the linear turbine and  $\rho = \omega V_0 / (\gamma p_a)$  represents the effect of compressibility of air in the chamber with  $V_0$  being the air volume inside the chamber,  $\gamma$  the specific heat ratio of air equal to 1.4 and  $p_a$  the atmospheric air pressure ([Rezanejad et al.; 2017](#)). The sign in  $\Lambda$  is taken to be positive since, in contrast to Eq. (5.13), the pressure forces and volume fluxes are both measured vertically upwards. Equation (5.15) assumes that the pressure inside the chamber is uniform and the air exits to the atmosphere through the turbine, a characteristic of Wells turbines that has been widely investigated for OWC devices. Using Eqs. (5.11), (5.13) and (5.15) an expression for the pressure in the chamber can be found

$$p = \frac{q^S}{\Lambda + Z - i\rho}. \quad (5.16)$$

The total rate of working of the pressure forces inside the OWC is basically  $Q(t) \times P(t)$ . By averaging this over one period, the mean power absorbed per unit width of pressure distribution is obtained

$$W = \frac{1}{2} \operatorname{Re}\{p^* q\}, \quad (5.17)$$

where  $*$  denotes complex conjugate. Now, by using Eqs. (5.11) and (5.13) on this last expression, we obtain

$$W = \frac{1}{2} \operatorname{Re}\{p^* (q^S - Zp)\} = \frac{1}{2} \left( \operatorname{Re}\{p^* q^S\} - \tilde{B}|p|^2 \right). \quad (5.18)$$

The expression (5.18) can be re-written in the form

$$W = \frac{1}{8} q^{S*} q^S \tilde{B}^{-1} - \frac{1}{2} \tilde{B} \left( p - \frac{q^S}{2\tilde{B}} \right)^* \left( p - \frac{q^S}{2\tilde{B}} \right) = \frac{|q^S|^2}{8\tilde{B}} - \frac{\tilde{B}}{2} \left| p - \frac{q^S}{2\tilde{B}} \right|^2, \quad (5.19)$$

where if  $\tilde{B}^{-1}$  exists, the maximum work is

$$W_{max} = \frac{|q^S|^2}{8\tilde{B}}, \quad (5.20)$$

when

$$p = \frac{q^S}{2\tilde{B}}, \quad (5.21)$$

showing that  $\Lambda = (Z - i\rho)^*$  for maximum power.

By combining previous Eqs. (5.16) and (5.19), it is finally obtained Eq. (5.22):

$$W = \frac{|q^S|^2}{8\tilde{B}} \left[ 1 - \left( \frac{|\Lambda - Z + i\rho|}{|\Lambda + Z - i\rho|} \right)^2 \right]. \quad (5.22)$$

Now, in order to optimize the power conversion efficiency, the last term in the square brackets must be minimized. As in Şentürk and Özdamar (2012), this can be done by finding the optimum value of  $\Lambda$ , which can be evaluated by applying zero value to the derivative for the squared-right term inside the brackets of Eq. (5.22) with respect to  $\Lambda$ , and thus obtaining

$$\Lambda_{opt} = |Z - i\rho| = \left( \tilde{B}^2 + (\tilde{A} + \rho)^2 \right)^{1/2}. \quad (5.23)$$

Therefore, the maximum value of extracted work at this condition becomes,

$$W_{opt} = \frac{|q^S|^2}{8\tilde{B}} \left[ 1 - \frac{\Lambda_{opt} - \tilde{B}}{\Lambda_{opt} + \tilde{B}} \right], \quad (5.24)$$

where  $\tilde{A}$ ,  $\tilde{B}$  and  $\Lambda$  are function of the angular frequency  $\omega$  which means that for each wave frequency, the turbine parameter must be altered appropriately to satisfy Eq. (5.23).

Thus, the expression for maximum efficiency is expressed as

$$\eta_{max} = \frac{W_{opt}}{W_{max}} = \frac{2\tilde{B}}{\Lambda_{opt} + \tilde{B}}, \quad (5.25)$$

where the maximum hydrodynamic efficiency is bounded by  $0 \leq \eta_{max} \leq 1$ . From expression (5.23), it is clear that when the radiation susceptance parameter is zero and the air compressibility term is neglected, it results in  $\Lambda_{opt} = \tilde{B}$ ,  $W_{opt} = W_{max}$  and  $\eta_{max} = 1$ , thus implying that the device has effectively absorbed all of the incident wave energy. In this situation, the free surface inside the OWC chamber is characterized by a piston-like resonant mode and the PTO damping optimization is satisfied (Michele et al.; 2019). To remain at this condition, the rate of energy extraction must equate to the rate of radiation damping while the internal free surface must remain in a state of resonance. Physically, this requires that the radiated waves, resulting from the oscillatory heave motion of the internal free surface, superpose and cancel the incident and scattered waves; in this instance, the device has thereby captured all of the incident wave energy (Morris-Thomas et al.; 2006).

Now, as in [Evans and Porter \(1995\)](#) the non-dimensionalised quantities  $\mu$  and  $\nu$  to represent the radiation susceptance and radiation conductance coefficients are defined as

$$\mu = \frac{\rho g}{\omega b} \tilde{A}, \quad (5.26a)$$

$$\nu = \frac{\rho g}{\omega b} \tilde{B}, \quad (5.26b)$$

respectively, where the radiation conductance coefficient  $\nu$  is related to the transfer of energy into the system, while the radiation susceptance coefficient  $\mu$  to the energy that remains uncaptured ([Rezanejad et al.; 2013](#)).

Therefore, by substituting these coefficients into Eq. (5.25), the efficiency  $\eta_{max}$  is

$$\eta_{max} = \frac{2}{\left(1 + \left(\frac{\mu}{\nu}\right)^2\right)^{1/2} + 1}, \quad (5.27)$$

which is independent of the incident wave power and only depends on the radiation solution of the volume flux  $q$ .

## 5.4 Solution

In this section, the BEM is used to solve the BVP in the frequency domain. In order to solve the governing equation together with the appropriated boundary conditions, a quadratic distribution of variables along each element is considered. The integral representation of the solution for the Laplace equation (5.1) at any point source  $\bar{P}$  inside the domain  $\Omega$  in terms of the boundary values of  $\phi$  and  $\partial\phi/\partial n$  is given by

$$\alpha(\bar{P})\phi(\bar{P}) + \int_{\Gamma} \phi(\bar{q}) \frac{\partial\psi(\bar{P}, \bar{q})}{\partial n_{\bar{q}}} d\Gamma_{\bar{q}} = \int_{\Gamma} \psi(\bar{P}, \bar{q}) \frac{\partial\phi(\bar{q})}{\partial n_{\bar{q}}} d\Gamma_{\bar{q}}, \quad (5.28)$$

where  $\phi$  is the unknown flow potential;  $\partial\phi/\partial n$  is the derivative of the potential relative to normal unit vector on the boundary  $\Gamma$ ;  $d\Gamma$  is the length of an infinitesimal piece of  $\Gamma$ ;  $\bar{q}$  an arbitrary point; while  $\psi$  and  $\partial\psi/\partial n$  are the fundamental solution of Laplace equation and its normal derivative at point  $\bar{q}$  of the boundary, respectively; and  $\alpha = \theta/2\pi$ , where  $\theta$  is the internal angle of the corner in radians ([Katsikadelis; 2002](#)).

The fundamental solution of Laplace equation is given by

$$\psi = \frac{1}{2\pi} \ln r, \quad (5.29)$$

where  $r$  is the distance between the source  $\bar{P}$  and the arbitrary point  $\bar{q}$ .

Now, discretizing the boundary into a series of  $NE$  elements, Eq. (5.28) can be written as

$$\alpha^i \phi^i + \sum_{j=1}^{NE} \int_{\Gamma} \phi \frac{\partial\psi}{\partial n} d\Gamma = \sum_{j=1}^{NE} \int_{\Gamma} \psi \frac{\partial\phi}{\partial n} d\Gamma. \quad (5.30)$$

CHAPTER 5. THE INFLUENCE OF THE FRONT WALL THICKNESS ON THE  
HYDRODYNAMIC EFFICIENCY OF A LAND-FIXED OWC DEVICE

---

In order to define the values of  $\phi$  and  $\partial\phi/\partial n$  on each element, three noded quadratic elements are employed, Fig. 5.4. The variables  $\phi$  and  $\partial\phi/\partial n$  are thus written in terms of interpolation functions,  $\hat{\varphi}_{1,2,3}$ , which are function of a homogeneous coordinate  $\xi$  as follows

$$\phi(\xi) = \hat{\varphi}_1\phi^1 + \hat{\varphi}_2\phi^2 + \hat{\varphi}_3\phi^3, \quad (5.31a)$$

$$\frac{\partial\phi(\xi)}{\partial n} = \hat{\varphi}_1\frac{\partial\phi^1}{\partial n} + \hat{\varphi}_2\frac{\partial\phi^2}{\partial n} + \hat{\varphi}_3\frac{\partial\phi^3}{\partial n}, \quad (5.31b)$$

where the superscript indicates the number of the node, while the interpolation functions are given by

$$\hat{\varphi}_1 = \frac{1}{2}\xi(\xi - 1), \quad (5.32a)$$

$$\hat{\varphi}_2 = \frac{1}{2}(1 - \xi)(1 + \xi), \quad (5.32b)$$

$$\hat{\varphi}_3 = \frac{1}{2}\xi(1 + \xi), \quad (5.32c)$$

with the dimensionless coordinate  $\xi$  varying from  $-1$  to  $1$ . Now, carrying out the integrals from Eq. (5.30) over an element  $j$ , these can be written as

$$\int_{\Gamma_j} \phi \frac{\partial\psi}{\partial n} d\Gamma = \left[ \int_{\Gamma_j} \hat{\varphi}_1 \frac{\partial\psi}{\partial n} d\Gamma, \int_{\Gamma_j} \hat{\varphi}_2 \frac{\partial\psi}{\partial n} d\Gamma, \int_{\Gamma_j} \hat{\varphi}_3 \frac{\partial\psi}{\partial n} d\Gamma \right] \cdot \begin{Bmatrix} \phi^1 \\ \phi^2 \\ \phi^3 \end{Bmatrix}, \quad (5.33)$$

and

$$\int_{\Gamma_j} \psi \frac{\partial\phi}{\partial n} d\Gamma = \left[ \int_{\Gamma_j} \hat{\varphi}_1 \psi d\Gamma, \int_{\Gamma_j} \hat{\varphi}_2 \psi d\Gamma, \int_{\Gamma_j} \hat{\varphi}_3 \psi d\Gamma \right] \cdot \begin{Bmatrix} \frac{\partial\phi^1}{\partial n} \\ \frac{\partial\phi^2}{\partial n} \\ \frac{\partial\phi^3}{\partial n} \end{Bmatrix}. \quad (5.34)$$

Here, it is observed that in order to solve the integrals Eqs. (5.33) and (5.34), the calculation of the Jacobian is required since they are a function of the boundary  $\Gamma$  in the  $x - z$  plane, while the interpolation functions are a function of  $\xi$ . This transformation is given by

$$d\Gamma = \left[ \sqrt{\left(\frac{dx}{d\xi}\right)^2 + \left(\frac{dz}{d\xi}\right)^2} \right] d\xi = |J|d\xi, \quad (5.35)$$

where  $J$  indicates the Jacobian and can then be substituted into Eqs. (5.33) and (5.34). Additionally, in order to calculate the value of Eq. (5.35), the variation of the  $x$  and  $z$  coordinates in terms of  $\xi$  must be also known. This can be carried out in the same way as the variables  $\phi$  and  $\partial\phi/\partial n$ , with the use of the quadratic interpolation defined by

$$x = \hat{\varphi}_1x^1 + \hat{\varphi}_2x^2 + \hat{\varphi}_3x^3, \quad (5.36a)$$

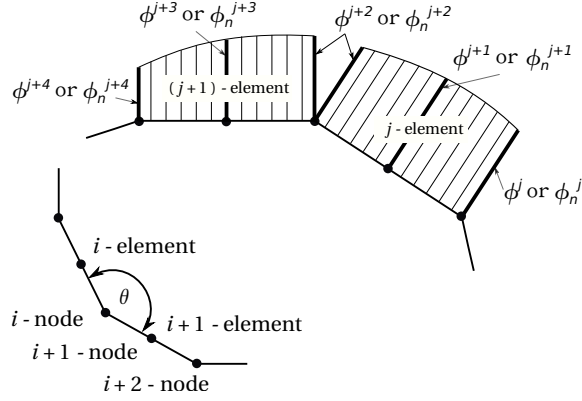


Figure 5.4: Schematic diagram of the modeling of the boundary with quadratic elements.

$$z = \hat{\varphi}_1 z^1 + \hat{\varphi}_2 z^2 + \hat{\varphi}_3 z^3, \quad (5.36b)$$

where again the superscript indicates the number of the node. Thus, Eq. (5.30) can be written as

$$\alpha^i \phi^i + \sum_{j=1}^{NE} [h_1^{ij}, h_2^{ij}, h_3^{ij}] \cdot \begin{Bmatrix} \phi^1 \\ \phi^2 \\ \phi^3 \end{Bmatrix}^j = \sum_{j=1}^{NE} [g_1^{ij}, g_2^{ij}, g_3^{ij}] \cdot \begin{Bmatrix} \phi_n^1 \\ \phi_n^2 \\ \phi_n^3 \end{Bmatrix}^j, \quad (5.37)$$

where

$$h_k^{ij} = \int_{-1}^1 \hat{\varphi}_k(\xi) \frac{\partial \psi}{\partial n} |J| d\xi, \quad (5.38a)$$

$$g_k^{ij} = \int_{-1}^1 \hat{\varphi}_k(\xi) \psi |J| d\xi, \quad (5.38b)$$

with  $k = 1, 2$  and  $3$  and  $h_k^{ij}$  and  $g_k^{ij}$  are estimated by using a Gauss integration method with ten points to account for the quadratic variation of the element geometry, the potential and flux. More details regarding the numerical procedure for solving these integrals can be found in Dominguez (1993); Brebbia and Dominguez (1992).

Furthermore, as explained by Dominguez (1993), in order to consider the possibility of having different values of  $\phi_n$  at node 3 of an element and at node 1 of the next adjoining element, the fluxes are arranged in a  $3 \times NE$  array where a position is held for each nodal value of every element. However, in the case of the potential  $\phi$ , its value is always considered unique in the connection between two elements. Therefore, the values of  $\phi$  can be arranged in an  $N$  array, where  $N$  is the number of nodes equal to  $2NE$  for closed boundaries. Thus, Eq. (5.37)

can be written as

$$\alpha^i \phi^i + [\hat{H}^{i1}, \dots, \hat{H}^{iN}] \cdot \begin{Bmatrix} \phi^1 \\ \vdots \\ \phi^N \end{Bmatrix}^j = [G^{i1}, \dots, G^{iNE}] \cdot \begin{Bmatrix} \begin{Bmatrix} \phi_n^1 \\ \phi_n^2 \\ \phi_n^3 \end{Bmatrix}^1 \\ \vdots \\ \begin{Bmatrix} \phi_n^1 \\ \phi_n^2 \\ \phi_n^3 \end{Bmatrix}^{NE} \end{Bmatrix}^j, \quad (5.39)$$

with  $\hat{H}^{ij}$  being equal to the  $h_1$  term of an element plus the  $h_3$  term of the previous element for odd nodes and equal to the  $h_2$  term of the corresponding element for the central nodes. On the other hand,  $G^{ij}$  are  $1 \times 3$  matrices with the elements  $[g_1^{ij}, g_2^{ij}, g_3^{ij}]$ . Therefore, the whole system of equations can be simply written as follows

$$\mathbf{H}\Phi = \mathbf{G}\Phi_{\mathbf{n}}, \quad (5.40)$$

where  $\mathbf{H}$  is a square matrix  $N \times N$ ,  $\Phi$  is an  $N \times 1$  vector,  $\mathbf{G}$  is a rectangular matrix  $N \times 3NE$  and  $\Phi_{\mathbf{n}}$  is an  $3NE \times 1$  vector.

Furthermore, as previously described by [Rezanejad et al. \(2013\)](#), in order to avoid the numerical errors arising from the cases where a very thin front wall of the device is considered, the method of subdomains is used to solve the BVP by applying the BEM separately to each of its regions ([Katsikadelis; 2002](#); [Becker; 1992](#)). The domain is then divided into three separate regions which have a common interface boundary on both lateral sides of the front wall as shown in [Fig. 5.5a](#). For each subdomain the following vectors are defined: in region R1

- $\Phi_1^1, \Phi_{\mathbf{n}1}^1$  Nodal values on  $\Gamma_1$  of the external boundary.
- $\Phi_{12}^1, \Phi_{\mathbf{n}12}^1$  Nodal values on the interface  $\Gamma_{12}$ ,

where the superscript denotes the region, while the subscript denotes the corresponding external boundary or interface. The number of the nodal points on  $\Gamma_1$  and  $\Gamma_{12}$  are  $N_1$  and  $N_{12}$ , respectively. In region R2

- $\Phi_2^2, \Phi_{\mathbf{n}2}^2$  Nodal values on  $\Gamma_2$  of the external boundary.
- $\Phi_{12}^2, \Phi_{\mathbf{n}12}^2$  Nodal values on the interface  $\Gamma_{12}$ .
- $\Phi_{23}^2, \Phi_{\mathbf{n}23}^2$  Nodal values on the interface  $\Gamma_{23}$ ,

where the number of the nodal points on  $\Gamma_2, \Gamma_{12}$  and  $\Gamma_{23}$  are  $N_2, N_{12}$  and  $N_{23}$ , respectively. In region R3

- $\Phi_3^3, \Phi_{\mathbf{n}3}^3$  Nodal values on  $\Gamma_3$  of the external boundary.
- $\Phi_{23}^3, \Phi_{\mathbf{n}23}^3$  Nodal values on the interface  $\Gamma_{23}$ ,

CHAPTER 5. THE INFLUENCE OF THE FRONT WALL THICKNESS ON THE  
HYDRODYNAMIC EFFICIENCY OF A LAND-FIXED OWC DEVICE

---

with  $N_3$  and  $N_{23}$  being the number of the nodal points on  $\Gamma_3$  and  $\Gamma_{23}$ , respectively.

Since  $\phi$  is unknown on either side of the interfaces  $\Gamma_{12}$  and  $\Gamma_{23}$ , the number of boundary unknowns in each subdomain is:

- Region 1:  $N_1$  on  $\Gamma_1$  and  $N_{12}$  on  $\Gamma_{12}$ .
- Region 2:  $N_2$  on  $\Gamma_2$ ,  $N_{12}$  on  $\Gamma_{12}$  and  $N_{23}$  on  $\Gamma_{23}$ .
- Region 3:  $N_3$  on  $\Gamma_3$  and  $N_{23}$  on  $\Gamma_{23}$ .

On the other hand, for  $\phi_n$ , which is defined on the three nodes of each element, it is given by:

- Region 1:  $M_1 = 3NE_1$  on  $\Gamma_1$  and  $M_{12} = 3NE_{12}$  on  $\Gamma_{12}$ .
- Region 2:  $M_2 = 3NE_2$  on  $\Gamma_2$ ,  $M_{12} = 3NE_{12}$  on  $\Gamma_{12}$  and  $M_{23} = 3NE_{23}$  on  $\Gamma_{23}$ .
- Region 3:  $M_3 = 3NE_3$  on  $\Gamma_3$  and  $M_{23} = 3NE_{23}$  on  $\Gamma_{23}$ ,

where  $NE_j$  denotes the number of elements depending on the boundary or interface.

Furthermore, in order to match the regions and to obtain the same number of unknowns and equations, the physical consideration of continuity of the potential and flux at the interfaces Eq. (5.3) should be made. Thus, assuming that the nodes in  $\Gamma_{12}$  of  $R1$  and  $R2$ , and the nodes in  $\Gamma_{23}$  of  $R2$  and  $R3$  are in perfect contact, Fig. 5.5b, the following physical consideration at the interfaces can be made:

- Continuity of the potential: The values of the potential on each side of the interface separating two subdomains must be equal

$$\begin{cases} \Phi_{12}^1 = \Phi_{12}^2, \\ \Phi_{23}^2 = \Phi_{23}^3. \end{cases} \quad (5.41)$$

- Continuity of the flux: The outgoing flux from one subdomain is equal to the incoming flux in the adjacent subdomain. Thus, the flux along the normal of the interface requires

$$\begin{cases} \Phi_{n12}^1 = -\Phi_{n12}^2, \\ \Phi_{n23}^2 = -\Phi_{n23}^3, \end{cases} \quad (5.42)$$

where the minus signs in the right hand side of Eq. (5.42) indicate that the two flux vectors at the common interface of adjacent subdomains are in opposite directions.

Therefore, the matrix equation for each boundary subdomain is as follows: for the boundary subdomain  $R1$

$$\begin{bmatrix} [H]_1^1 & [H]_{12}^1 \end{bmatrix} \begin{bmatrix} \Phi_1^1 \\ \Phi_{12}^1 \end{bmatrix} = \begin{bmatrix} [G]_1^1 & [G]_{12}^1 \end{bmatrix} \begin{bmatrix} \Phi_{n1}^1 \\ \Phi_{n12}^1 \end{bmatrix}, \quad (5.43)$$

while for the boundary subdomain  $R2$

$$\begin{bmatrix} [H]_{12}^2 & [H]_2^2 & [H]_{23}^2 \end{bmatrix} \begin{bmatrix} \Phi_{12}^2 \\ \Phi_2^2 \\ \Phi_{23}^2 \end{bmatrix} = \begin{bmatrix} [G]_{12}^2 & [G]_2^2 & [G]_{23}^2 \end{bmatrix} \begin{bmatrix} \Phi_{n12}^2 \\ \Phi_{n2}^2 \\ \Phi_{n23}^2 \end{bmatrix}, \quad (5.44)$$

and for the boundary subdomain  $R3$

$$\begin{bmatrix} [H]_3^3 & [H]_{23}^3 \end{bmatrix} \begin{bmatrix} \Phi_3^3 \\ \Phi_{23}^3 \end{bmatrix} = \begin{bmatrix} [G]_3^3 & [G]_{23}^3 \end{bmatrix} \begin{bmatrix} \Phi_{n3}^3 \\ \Phi_{n23}^3 \end{bmatrix}. \quad (5.45)$$

Equations (5.43)–(5.45) of the three subdomains may then be combined in a single matrix equation as

$$\begin{bmatrix} [H]_1^1 & [H]_{12}^1 & 0 & 0 & 0 & 0 & 0 \\ 0 & 0 & [H]_2^2 & [H]_{12}^2 & [H]_{23}^2 & 0 & 0 \\ 0 & 0 & 0 & 0 & 0 & [H]_3^3 & [H]_{23}^3 \end{bmatrix} \begin{bmatrix} \Phi_1^1 \\ \Phi_{12}^1 \\ \Phi_2^2 \\ \Phi_{12}^2 \\ \Phi_{23}^2 \\ \Phi_3^3 \\ \Phi_{23}^3 \end{bmatrix} = \begin{bmatrix} [G]_1^1 & [G]_{12}^1 & 0 & 0 & 0 & 0 & 0 \\ 0 & 0 & [G]_2^2 & [G]_{12}^2 & [G]_{23}^2 & 0 & 0 \\ 0 & 0 & 0 & 0 & 0 & [G]_3^3 & [G]_{23}^3 \end{bmatrix} \begin{bmatrix} \Phi_{n1}^1 \\ \Phi_{n12}^1 \\ \Phi_{n2}^2 \\ \Phi_{n12}^2 \\ \Phi_{n23}^2 \\ \Phi_{n3}^3 \\ \Phi_{n23}^3 \end{bmatrix}, \quad (5.46)$$

where the left-hand side matrix and vector have dimensions of  $N \times N$  and  $N \times 1$ , respectively, with  $N = N_1 + N_2 + N_3 + 2N_{12} + 2N_{23}$ , while the right-hand side matrix and vector of  $N \times 3NE$  and  $3NE \times 1$ , respectively, with  $3NE = M_1 + M_2 + M_3 + 2M_{12} + 2M_{23}$ . Now, since the nodes on  $\Gamma_{12}$  and  $\Gamma_{23}$  are in perfect contact, the matrices can be further arranged by combining the



coefficients of the related variables as follows

$$\begin{bmatrix} [H]_1^1 & [H]_{12}^1 & 0 & 0 & 0 & 0 & 0 \\ 0 & [H]_{12}^2 & [H]_2^2 & 0 & [H]_{23}^2 & 0 & 0 \\ 0 & 0 & 0 & 0 & [H]_{23}^3 & [H]_3^3 & 0 \end{bmatrix} \begin{bmatrix} \Phi_1^1 \\ \Phi_{12}^1 \\ \Phi_2^2 \\ 0 \\ \Phi_{23}^2 \\ \Phi_3^3 \\ 0 \end{bmatrix} = \begin{bmatrix} [G]_1^1 & [G]_{12}^1 & 0 & 0 & 0 & 0 & 0 \\ 0 & -[G]_{12}^2 & [G]_2^2 & 0 & [G]_{23}^2 & 0 & 0 \\ 0 & 0 & 0 & 0 & -[G]_{23}^3 & [G]_3^3 & 0 \end{bmatrix} \begin{bmatrix} \Phi_{n1}^1 \\ \Phi_{n12}^1 \\ \Phi_{n2}^2 \\ 0 \\ \Phi_{n23}^2 \\ \Phi_{n3}^3 \\ 0 \end{bmatrix}. \quad (5.47)$$

Finally, after inserting the boundary conditions specified in Eqs. (5.2), (5.6), (5.8) and (5.9), and shifting the known variables to the right-hand side and the unknowns to the left-hand side, a matrix of the following form is obtained

$$[A] \{X\} = \{B\}, \quad (5.48)$$

where  $\{X\}$  is a vector consisting of all the unknown values on the external boundary and on the interfaces of dimension  $N \times 1$ ;  $[A]$  is known square coefficient matrix of dimensions  $N \times N$  whose columns are columns of  $H$  and columns of  $G$  after a change of sign or sum of two consecutive columns of  $G$  with the opposite sign when the unknown is the unique flux at the interfaces at a node connecting two elements (Dominguez; 1993); while  $\{B\}$  is a known vector of dimension  $N \times 1$ .

## 5.5 Results and Discussion

In this section, numerical results based on the BEM discussed in the previous section are presented. First, by considering a thick front wall and ignoring the influence of the air compressibility (i.e.,  $\varrho = 0$ ), the effect of the chamber configuration on the hydrodynamic efficiency, radiation susceptance and radiation conductance coefficients is analyzed. Then, based on the physical dimensions of a single chamber of the MWEP, the effects of three different bottom profiles and the air compressibility on the efficiency are studied. It should be mentioned here that in order to minimize the effect of local disturbances at the far-field boundary, for the boundary discretization the distance between the front wall and the far-field boundary was considered to be 4 times the water depth  $h$ .

On the other hand, before performing the rest of the numerical calculations, a convergence analysis was carried out. In Table 5.1, the results of the hydrodynamic efficiency  $\eta$ , radiation

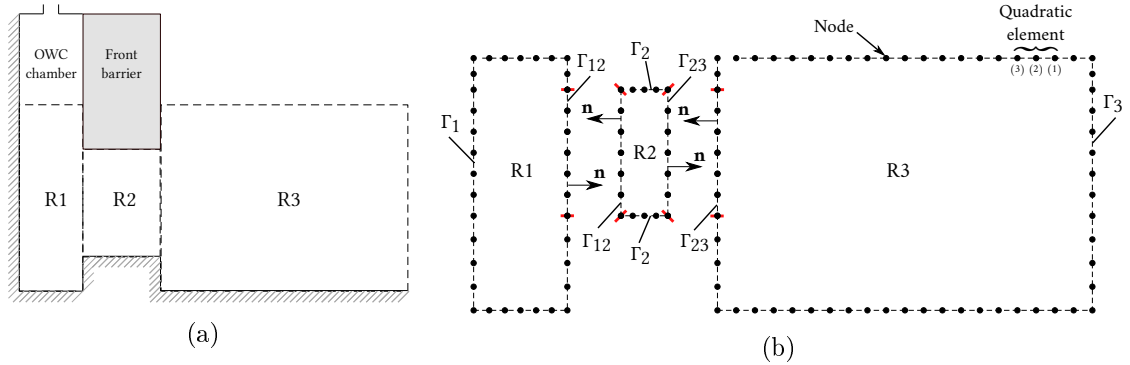


Figure 5.5: Boundary element discretization of the composite domain. (a) Separation of the BVP into three regions. (b) Discretization of the three regions.

Table 5.1: Values of hydrodynamic efficiency  $\eta_{max}$ , radiation susceptance coefficient  $\mu$  and radiation conductance coefficient  $\nu$  computed for different number of nodes  $N$  with  $h_a/h = 0.125$ ,  $b/h = 1.0$  and  $w/b = 0.5$ .

$N$	$Kh = 3.8329$			$Kh = 2.2657$			$Kh = 1.2054$			$Kh = 0.5074$		
	$\eta$	$\mu$	$\nu$	$\eta$	$\mu$	$\nu$	$\eta$	$\mu$	$\nu$	$\eta$	$\mu$	$\nu$
560	0.2808	-0.2926	0.0484	0.4335	-0.3595	0.1035	0.8621	-0.6287	0.7299	0.9425	0.6507	1.2787
480	0.2814	-0.2940	0.0488	0.4337	-0.3598	0.1037	0.8622	-0.6295	0.7312	0.9425	0.6519	1.2806
400	0.2822	-0.2957	0.0492	0.4340	-0.3602	0.1039	0.8624	-0.6305	0.7329	0.9424	0.6534	1.2830
328	0.2833	-0.2982	0.0499	0.4343	-0.3608	0.1042	0.8626	-0.6318	0.7352	0.9423	0.6556	1.2861
256	0.2848	-0.3018	0.0508	0.4349	-0.3616	0.1046	0.8629	-0.6338	0.7386	0.9422	0.6587	1.2906
200	0.2856	-0.3071	0.0519	0.4370	-0.3644	0.1061	0.8636	-0.6373	0.7451	0.9418	0.6649	1.2978

susceptance  $\mu$  and radiation conductance  $\nu$  for four different  $Kh$  values are given. It is observed that around 480 nodes (240 quadratic elements) are enough to ensure convergence of the numerical results within three decimal places and also to avoid numerical instabilities that arise when the front wall thickness  $w$  tends to zero. Therefore, in the present calculations, all the BVPs are discretized through 480 nodes.

### 5.5.1 Front Wall Thickness

To validate the numerical method described here, the numerical results for the limiting case of [Evans and Porter \(1995\)](#) were used. In the case of  $h_a/h = 0.125$ ,  $b/h = 1$ , while  $w$  and  $h_e$  tending to zero, the efficiency obtained by the present formulation was compared with the corresponding results of [Evans and Porter \(1995\)](#) for an OWC device with a horizontal topography, as shown in Fig. 5.6a. The circles in Fig. 5.6a depict the results of [Evans and Porter \(1995\)](#), whereas the line represents the results calculated by the present method. It can be seen that both results are in good agreement.

The numerical results of the efficiency  $\eta_{max}$  versus  $Kh$  for different thickness ratios

CHAPTER 5. THE INFLUENCE OF THE FRONT WALL THICKNESS ON THE HYDRODYNAMIC EFFICIENCY OF A LAND-FIXED OWC DEVICE

$w/b$  ( $= 2.0, 1.5, 1.0, 0.5$ , and  $0.01$ ) in a flat bottom (without considering  $h_e$ ) are shown in Fig. 5.6a. In this figure, it is seen that by increasing the thickness of the front barrier, the bandwidth of the efficiency curves is reduced and their first peak frequency value is shifted to lower values of the non-dimensional frequency  $Kh$ . This reduction in the efficiency is explained by the fact that the energy transfer due to the wave motion over small periods is reduced when the front barriers are greater in thickness. However, in a real scenario, during severe storm events, or during times of high water levels, the front barrier is subjected to high loads, due to direct wave action (Viviano et al.; 2016; Pawitan et al.; 2019; Viviano et al.; 2019; Pawitan et al.; 2020), and a slender front wall cannot offer protection to the whole system, as occurred at the MWEP (Medina-Lopez et al.; 2015). Therefore, special consideration should be given to this structural aspect.

On the other hand, Fig. 5.6b shows the effect on efficiency of different submergence ratios  $h_a/h$  ( $= 0.125, 0.250, 0.500$ , and  $0.750$ ), together with a front barrier of the same thickness as the OWC chamber (i.e.,  $w/b = 1.0$ ). In this figure, it is observed that the effective area of efficiency, under the curve, and the magnitude of the first natural frequency, both increase when the front wall  $h_a/h$  decreases. Nevertheless, for a relatively small  $h_a/h$ , and considering that changes in water depth due to tidal variations and extreme waves may take place, a small draft may mean that the trough of a wave propagates below the front wall. This should be considered at the design stage, since in this situation the pressure within the chamber would be equivalent to the atmospheric pressure, causing the power available inside the OWC device to be zero and thus decreasing the efficiency.

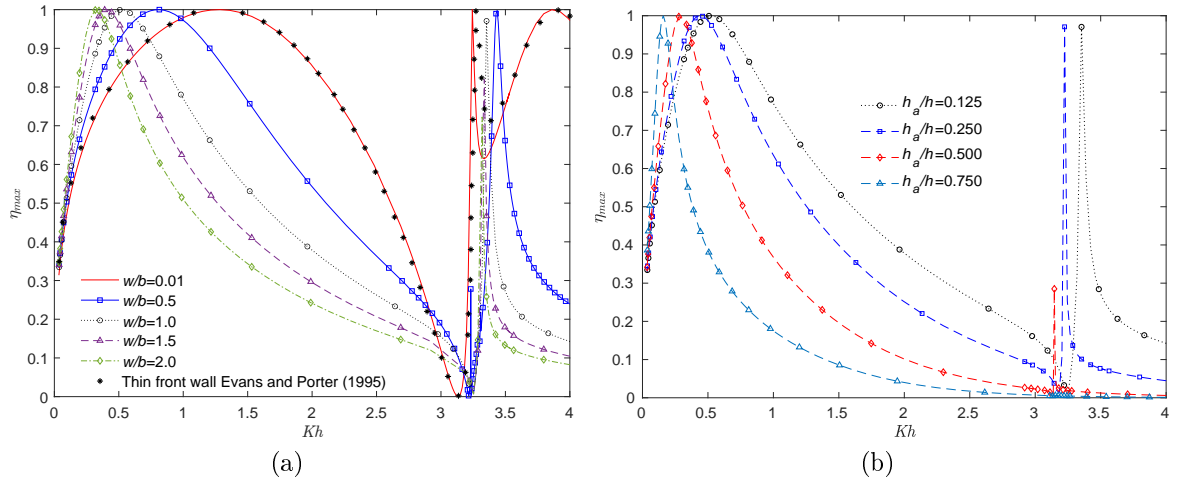


Figure 5.6: Hydrodynamic efficiency versus  $Kh$ . (a) For various thickness ratios  $w/b$  with  $h_a/h = 0.125$  and  $b/h = 1.0$ . (b) For different submergence ratios  $h_a/h$  with  $w/b = 1.0$  and  $b/h = 1.0$ .

The variation of the radiation susceptance and radiation conductance coefficients versus  $Kh$  when  $h_a/h = 0.125$  and  $b/h = 1.0$  for different values of  $w/b$  ( $= 2.0, 1.5, 1.0, 0.5$ , and  $0.01$ ) is shown in Figs. 5.7a and 5.7b, respectively. In Fig. 5.7a it is observed that the frequencies for

which  $\mu$  is zero are related to the peaks of maximum efficiency shown in Fig. 5.6a, which is also evident from the maximum efficiency Eq. (5.27). Figure 5.7a also shows that when the thickness ratio  $w/b$  increases, the range of the non-dimensional frequency  $Kh$  for which  $\mu$  is negative also increases. As previously mentioned, the radiation susceptance  $\mu$  is related to  $\dot{A}$  which is analogous to the added mass of the forced oscillation of a rigid body system. In this sense, the above-mentioned negative values in  $\mu$  are may be due to the relevance of the free-surface effects of the internal free surface enclosed by the rigid wall and the surface-piercing front barrier. Negative values in the added mass are a common phenomenon in the theory of submerged and floating moving bodies in a fluid, such as when one or more elements of a structure enclose a portion of the free surface or two-dimensional cylinders are close to the free surface (McIver and Evans; 1984; McIver and McIver; 2016). Furthermore, as demonstrated by Falnes (1983), negative added mass occurs when an oscillating body produces a water motion where the associated potential energy is greater than the associated kinetic energy.

Figure 5.7b shows that the peaks in the radiation conductance  $\nu$  are associated with those observed in Fig. 5.6a. Together with Fig. 5.7a, this shows that by increasing the radiation conductance coefficient  $\nu$ , with respect to the radiation susceptance coefficient  $\mu$ , an increase in the power extraction capacity can be attained. In this sense, the radiation conductance coefficient  $\nu$  indicates the degree to which the system absorbs energy at different frequencies.

Figures 5.7c and 5.7d show the numerical results of the radiation susceptance and radiation conductance coefficients, respectively, versus  $Kh$  with  $w/b = 1.0$ ,  $b/h = 1.0$  and for different submergence ratios  $h_a/h (= 0.125, 0.250, 0.500, \text{ and } 0.750)$ . In Fig. 5.7c it is observed that by increasing the front wall draft  $h_a$  with respect to  $h$ , the value of  $Kh$  for which  $\mu$  first become zero decreases, which is associated with the first resonance frequency inside the chamber, while the range of  $Kh$  for negative values of  $\mu$  increases. On the other hand, Fig. 5.7d shows that a larger draft decreases the frequency at which this resonance occurs. It can also be observed that the peak resonance become more prominent the further the barrier is submerged. With a large draft, conditions are similar to those in a closed tank with parallel sides, where a second resonance mechanism occurs when the incident wave frequency is such that the fluid inside the chamber is excited into an antisymmetric sloshing mode (Evans and Porter; 1995). In this case, the sloshing frequencies occur at values of the dimensionless wave number  $kb = n\pi$ , with  $n$  being the sloshing mode. For the case presented in Fig. 5.7d, it is observed that the second peaks in  $\nu$  due to the first sloshing frequency take place close to  $Kh \approx \pi$ .

Figure 5.8a plots the numerical results of the efficiency  $\eta_{max}$  versus  $Kh$  for various wall to front barrier spacing ratios  $b/h (= 1.0, 0.5, 0.25, \text{ and } 0.125)$  with  $h_a/h = 0.125$  and  $w/b = 1.0$  with in a flat bottom. As reported by Evans and Porter (1995); Rezanejad et al. (2013), large motions inside the chamber occur when the fluid between the front barrier and the back wall is excited by the incident wave into a resonant piston-like motion inside the OWC. An estimation of this natural frequency of oscillation can be obtained for small values of  $b/h$  and so the water contained between the walls can be regarded as a solid body. By employing simple hydrostatic modelling gives that the expected resonance occurs at  $Kh \approx h/h_a$ . In the present case, this resonance would occur at  $Kh = 8$ , which is seemed to be approached for smaller values of  $b/h$ . On the other hand, for a longer chamber, the frequency at which this resonance occurs is smaller. Physically, this is due to the fact that by increasing the length of the device, the

horizontal distance a typical fluid particle must travel during a period of motion increases. This can also be obtained in the vertical direction by increasing the draft of the front wall. As a consequence, a decrease in the value of  $Kh$  at which resonance occurs is caused, and since an increase in  $b/h$  allows more local fluid motion inside the chamber, this leads to a breakdown in the solid-body model of resonance, and the amplitude of oscillation decreases.

Figure 5.8b illustrates the condition when a step, as long as the front wall, is placed below the latter with  $h_a/h = 0.125$ ,  $b/h = 1.0$  and  $w/b = 1.0$ . First, a comparison of the present formulation with the limiting case of Şentürk and Özdamar (2012) of an OWC device with a gap in its fully submerged thin front wall, together with the nondimensional parameters  $h_a/h = 0.125$ ,  $h_e/h = 0.625$ ,  $b/h = 1.0$  and  $w/b = 0.01$ , is shown in Fig. 5.8b. It can be seen that both results agree very well. Then, it can be observed that the smaller the distance between the front wall and the step, the lower the magnitude of the non-dimensional frequency  $Kh$  at which resonance occurs. This is similar to the trend observed when the draft of the front wall is increased without considering the step, Fig. 5.6b. A larger gap leads to a wider range of frequency bandwidth as it increases the transference of energy due to wave motion.

The numerical results for the radiation susceptance and radiation conductance coefficients versus  $Kh$  when  $h_a/h = 0.125$  and  $w/b = 1.0$  for different values of  $b/h$  (= 1.0, 0.5, 0.25, and 0.125) are shown in Figs. 5.9a and 5.9b, respectively. In Fig. 5.9a, it is observed that when the wall to front barrier spacing is sufficiently small, compared to the depth  $h$ , the range of the non-dimensional frequency  $Kh$  for which the radiation susceptance is negative decreases. Thus, when a small draft is considered, the  $b/h$  ratio is important for the occurrence of negative values of the radiation susceptance coefficient. On the other hand, Fig. 5.9b shows that when the length of chamber  $b$  increases with respect to the depth  $h$ , the radiation conductance coefficient peaks are maximum for longer periods. Consequently, since  $\nu$  is a measure of the transfer of energy into the system, it may be beneficial to design the chamber length of the OWC device so that the range of frequency bandwidth in the radiation conductance coincides with the most occurring wave period of a particular location and thus exploit the available wave energy as much as possible.

Figures 5.9c and 5.9d show the radiation susceptance and radiation conductance coefficients, respectively, versus  $Kh$  for various step to bottom ratios  $h_e/h$  with  $h_a/h = 0.125$ ,  $b/h = 1.0$  and  $w/b = 1.0$ . On one hand, Fig. 5.9c shows that the variation from positive to negative in the radiation susceptance increases when the vertical spacing between the step and the front wall decreases. On the other hand, Fig. 5.9d shows an increasing and narrowing peak for the radiation conductance coefficient, as the gap is reduced, decreasing the magnitude of the resonance frequency.

Figures 5.10a and 5.10b show a comparison of the present formulation with the experimental results obtained by Morris-Thomas et al. (2006) and Wang et al. (2018), respectively. First, in the case of a thick front wall considered by Morris-Thomas et al. (2006), the OWC dimensions employed in the calculations are  $h = 0.92$  m,  $b = 0.64$  m,  $h_a = 0.15$  m and  $w = 0.08$  m, while in the case of comparison with Wang et al. (2018), the dimensions are  $h = 0.80$  m,  $b = 0.55$  m,  $h_a = 0.14$  m and  $w = 0.04$  m. From Figs. 5.10a and 5.10b, it is observed that by comparing the maximum theoretical efficiency and the experimental efficiency, the discrepancy is significant. The numerical solutions overpredict the hydrodynamic efficiency since it neglects

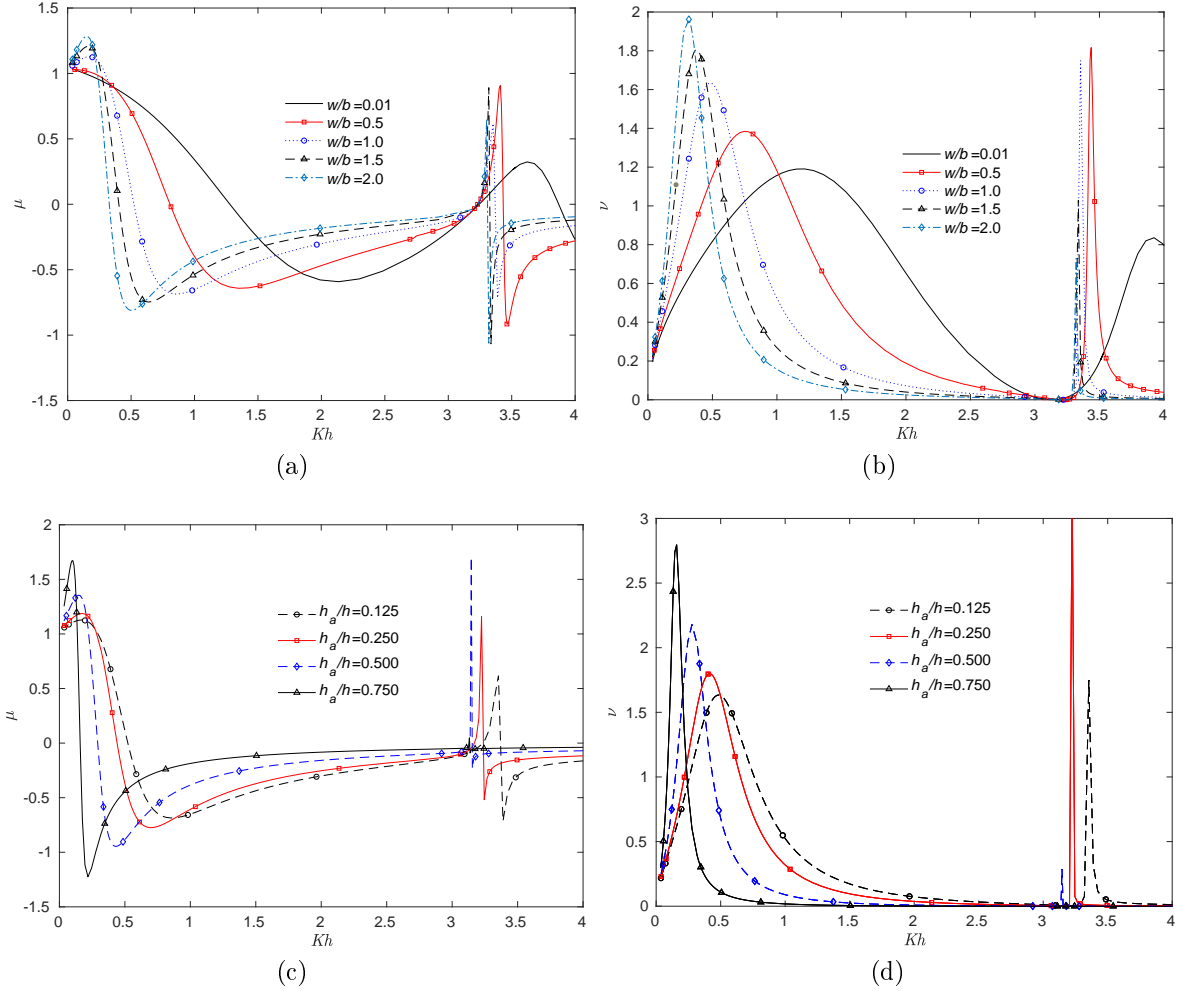


Figure 5.7: The radiation susceptance and radiation conductance coefficients versus  $Kh$ . **(a)** The radiation susceptance coefficient for various thickness ratios  $w/b$  with  $h_a/h = 0.125$  and  $b/h = 1.0$ . **(b)** The radiation conductance coefficient for various thickness ratios  $w/b$  with  $h_a/h = 0.125$  and  $b/h = 1.0$ . **(c)** The radiation susceptance coefficient for different submergence ratios  $h_a/h$  with  $w/b = 1.0$  and  $b/h = 1.0$ . **(d)** The radiation conductance coefficient for different submergence ratios  $h_a/h$  with  $w/b = 1.0$  and  $b/h = 1.0$ .

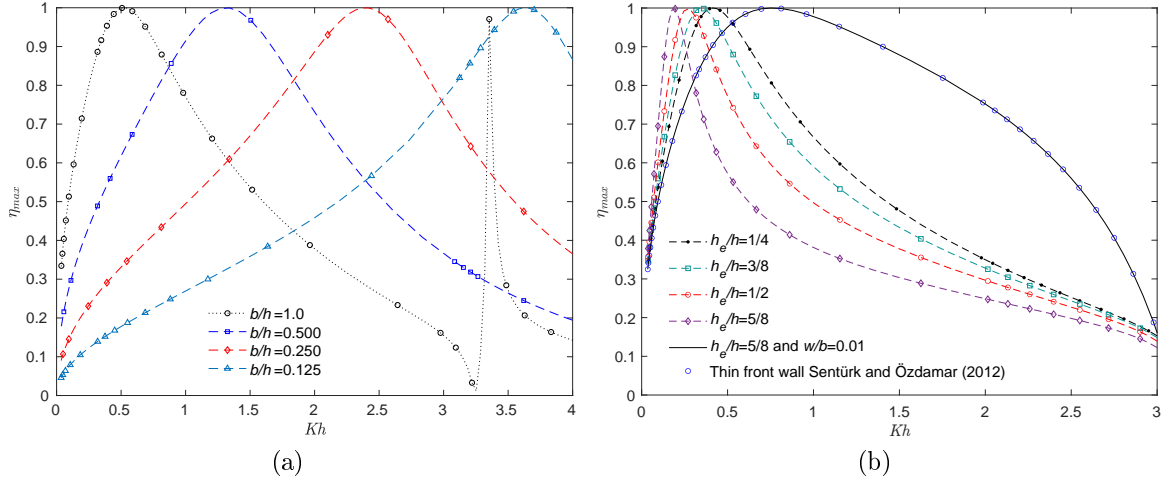


Figure 5.8: Hydrodynamic efficiency versus  $Kh$ . (a) For various wall to front barrier spacing ratios  $b/h$  with  $h_a/h = 0.125$  and  $w/b = 1.0$ . (b) For various step to bottom ratios  $h_e/h$  with  $h_a/h = 0.125$ ,  $b/h = 1.0$  and  $w/b = 1.0$ .

the wave nonlinearity and the viscous dissipation, but the resonant frequencies and the shapes of the hydrodynamic efficiency curves predicted by the present numerical method agree well with each experiment (Ning et al.; 2015; Ning, Wang, Zou and Teng; 2016). It should be pointed out that the present formulation is based on the assumption of an ideal fluid and, therefore, viscous effects and flow separation due to the front wall are apparently the main cause of difference between the experimental and numerical results. Furthermore, another factor contributing to this discrepancy may be attributed to the rate of energy extraction modelled by the PTO system and the energy loss through it by viscous dissipation during the experiments.

In this sense, it is worth mentioning that  $\eta_{max} = 1$  theoretically means that the OWC device effectively captures all the incident wave energy, a condition that in practice is not feasible, due to the radiated wave generated by the oscillatory motion of the internal free surface, the scattering waves by the device and various viscous damping previously mentioned (Ning et al.; 2015). Thus, in a real scenario, a value of  $\eta_{max} = 1$  could never be achieved because of the energy loss through viscous dissipation as the fluid flow interacts with the chamber geometry and the PTO modelling. It should be mentioned that the effect of vortex and flow separation, which occur near the front wall, can be simulated well by introducing an artificial viscous damping term to the dynamic free surface boundary condition inside the OWC chamber and thus, to account for the energy loss due to vortex shedding and flow separation as previously reported by Ning et al. (2015); Ning, Wang, Zou and Teng (2016); Ning, Wang, Gou, Zhao and Teng (2016); Wang et al. (2018); Wang and Ning (2020).

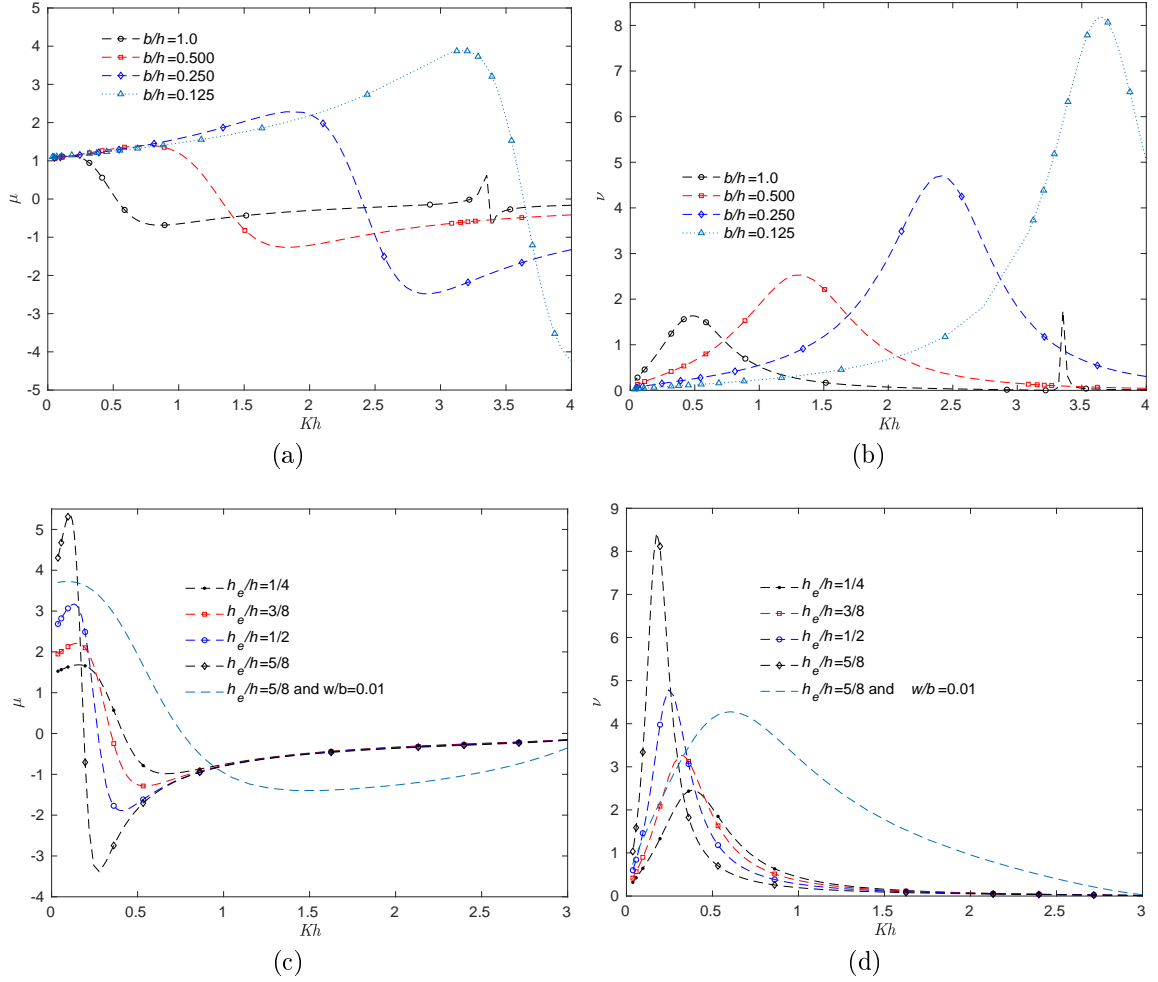


Figure 5.9: The radiation susceptance and radiation conductance coefficients versus  $Kh$ . (a) The radiation susceptance coefficient for various wall to front barrier spacing ratios  $b/h$  with  $h_a/h = 0.125$  and  $w/b = 1.0$ . (b) The radiation conductance coefficient for various wall to front barrier spacing ratios  $b/h$  with  $h_a/h = 0.125$  and  $w/b = 1.0$ . (c) The radiation susceptance coefficient for various step to bottom ratios  $h_e/h$  with  $h_a/h = 0.125$ ,  $b/h = 1.0$  and  $w/b = 1.0$ . (d) The radiation conductance coefficient for various step to bottom ratios  $h_e/h$  with  $h_a/h = 0.125$ ,  $b/h = 1.0$  and  $w/b = 1.0$ .



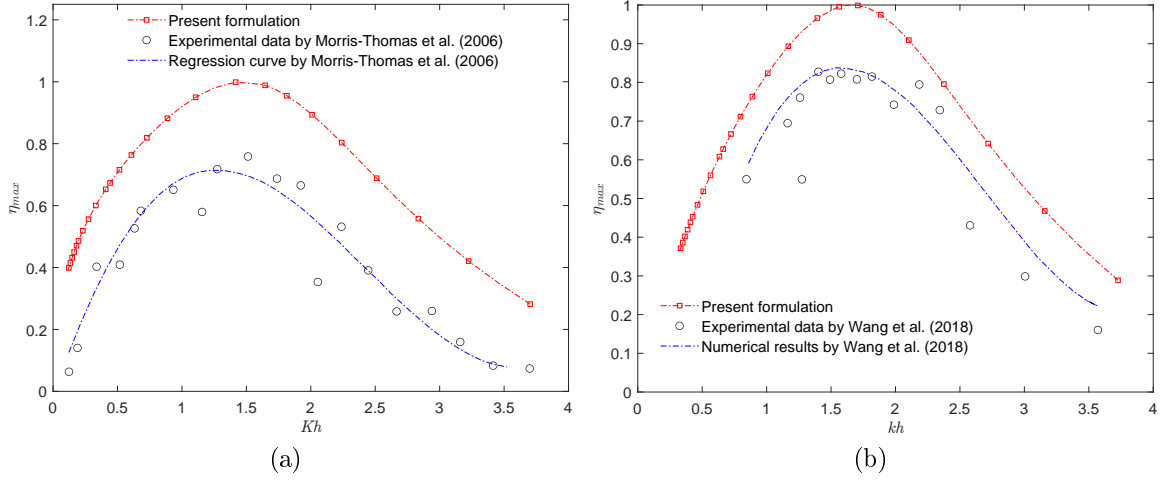


Figure 5.10: Hydrodynamic efficiency versus (a)  $Kh$  and (b)  $kh$ . (a) Comparison with experimental results obtained by [Morris-Thomas et al. \(2006\)](#) for a thick front wall. (b) Comparison with experimental and numerical results obtained by [Wang et al. \(2018\)](#).

### 5.5.2 Bottom Profile

In this subsection, an analysis is made, based on the physical dimensions of the MWEF and on the highest and lowest tidal levels, Fig. 5.11. The influence of different bottom profiles, the linear turbine damping and the linearized air compressibility inside the chamber on the hydrodynamic efficiency are evaluated. However, it should be noted that in this study the effect of the non-linear phenomena that occur in the interaction between the waves, the OWC device and the trapped air inside the chamber, such as viscous flow separation, turbulence, wave breaking and thermodynamic processes, are not taken into account. These aspects may play an important role in the performance of the OWC when variations in the bottom chamber are considered.

The varying bottom profiles proposed are defined in the interval  $0 \leq x \leq b$  and given by:

$$z = -h(x) = \begin{cases} \left(\frac{h_a - h}{b}\right)x - h_a, & \text{Sloped bottom,} \\ \left(\frac{h - h_a}{b}\right)\sqrt{b^2 - x^2} - h, & \text{Elliptical bottom,} \end{cases} \quad (5.49)$$

while the cycloidal bottom is given by the parametric equation

$$x(\hat{\theta}) = \hat{r} \left( \hat{\theta} + \sin \hat{\theta} - \pi \right) + b, \quad (5.50a)$$

$$z(\hat{\theta}) = \hat{r} \left( \cos \hat{\theta} + 1 \right) - h, \quad (5.50b)$$

with  $0.56416 \leq \hat{\theta} \leq \pi$  and  $\hat{r} = 1.51759$  m.

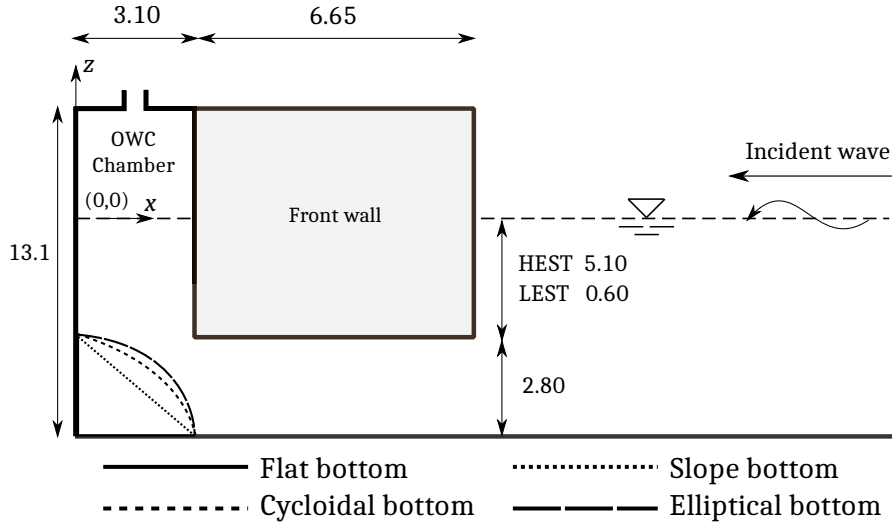


Figure 5.11: Definition sketch of a single chamber in the Mutriku Wave Energy Plant (Dimensions in meters. Chamber width = 4.5 m; HEST = Highest equinoctial spring tide and LEST = Lowest equinoctial spring tide).

In Fig. 5.12, the numerical results for 1:1 sloped bottom profile with different linear turbine damping coefficients,  $\Lambda$ , are compared with the experimental results obtained by John Ashlin et al. (2016) for a wave steepness  $H_w/\lambda$  varying from 0.0320 to 0.0371. Regarding the numerical results presented here, it is worth noting that these are independent of the wave height since linear wave theory was employed for the formulation of the BVP. In order to perform the calculations, the OWC dimensions are those used by John Ashlin et al. (2016) in their experiments; these are  $h = 0.500$  m,  $h_a = 0.200$  m,  $b = 0.300$  m,  $w = 0.012$  m, a chamber width of  $l = 0.471$  m and a distance from the internal free surface to the top of the chamber of  $s = 0.400$  m. In order to see better the agreement between the results, the least-squares method was applied to the experimental data presented by John Ashlin et al. (2016) to obtain a best-fit second-order polynomial curve. Figure 5.12 shows that the numerical solution and the experimental results of John Ashlin et al. (2016) are in good agreement for a linear turbine damping coefficient  $\Lambda = 5 \times 10^{-4}$  m<sup>4</sup>·s/kg. However, it is observed that by comparing the maximum theoretical efficiency obtained from Eq. (5.27) and the experimental efficiency, the discrepancy is high. Therefore, special attention should be paid to turbine damping, as well as non-linear effects, in order to make an adequate estimation of the power absorption of an OWC device.

Figures 5.13a–d show the numerical results of the maximum  $\eta_{max}$  versus the incoming wave period  $T$  for the cases when the HEST and LEST take place and the linearized air compressibility is considered. The range of wave period used in these figures is related to mean wave periods reported by Ibarra-Berastegi et al. (2018). In Figs. 5.13a and 5.13c the maximum efficiency was obtained from Eq. (5.25) with  $\varrho = 0$ , while in Figs. 5.13b and 5.13d, the optimum value of the damping coefficient ( $\Lambda_{opt}$ ), calculated from Eq. (5.23), was employed to obtain the

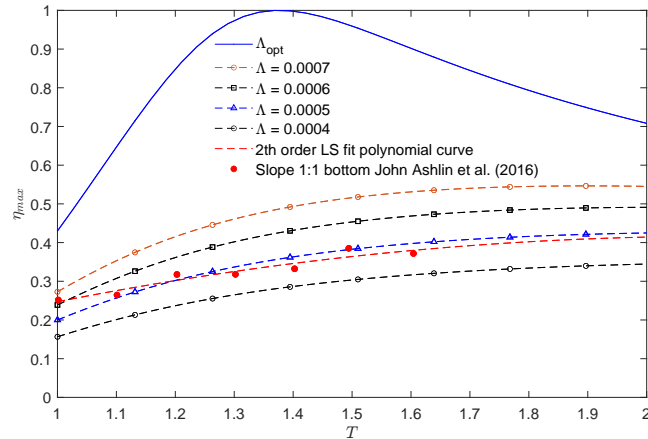


Figure 5.12: Hydrodynamic efficiency versus period  $T$  for different values of linear turbine damping coefficient  $\Lambda$ , without considering the step.

hydrodynamic efficiency by considering the linearized air compressibility inside the chamber. In all the figures it can be seen that the efficiency band shifts slightly to the right as the bottom of the chamber becomes steeper, generating a slightly higher efficiency for higher periods. Figures 5.13a and 5.13b show that for incoming wave periods of less than 8 s, the flat bottom inside the chamber gives maximum efficiency. As reported by John Ashlin et al. (2016), this is due to the higher reflection generated by the curved bottom, together with the energy reflection caused by the front and back walls of the OWC device, for shorter wavelengths. The cycloidal and elliptical bottoms decrease the efficiency because these profiles reduce the section of the entrance of fluid particles, obstructing the waves and leading to a decrease in the internal free surface oscillation which drives the air column. This consequently diminishes the output power. The natural frequency of the system is seen to alter slightly for the different bottom profile configurations. Figures 5.13c and 5.13d show the efficiency in the case of the lowest equinoctial spring tide. As expected, compared with the HEST, the period at which resonance takes place is reduced due to the lower front wall draft,  $h_a = 0.60$  m. Furthermore, as observed in Fig. 5.6b, Fig. 5.13c shows that the efficiency effective area under the curve increases with a shorter front wall draft. However, in the case of Mutriku, where significant wave heights of 4 m are common (Ibarra-Berastegi et al.; 2018), this small draft increases the possibility that the wave trough propagates below the front wall, and thus reduces efficiency. Regarding the effect of the volume of air inside the chamber, compared with Fig. 5.13b, Fig. 5.13d shows that efficiency is significantly reduced when the air volume is larger. Comparing Fig. 5.13d to Fig. 5.13c shows that the period at which resonance occurs is independent of the damping condition and is mostly determined by the natural frequency of the water column.

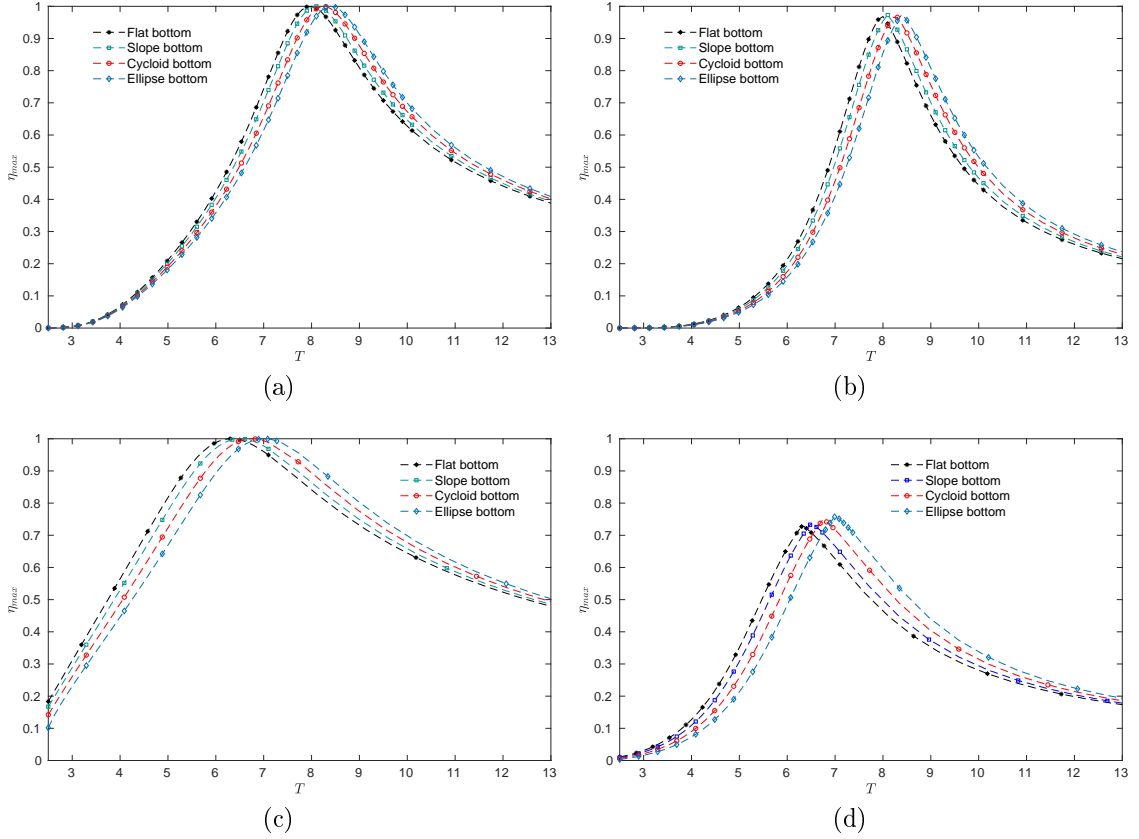


Figure 5.13: Hydrodynamic efficiency in the cases of HEST and LEST versus  $T$  for different bottom profiles. (a) Maximum efficiency versus  $T$  with  $\varrho = 0$  for various bottom profiles with  $h = 7.90$ ,  $h_a/h = 0.646$ ,  $b/h = 0.392$  and  $w/b = 2.145$  in the case of the HEST. (b) Maximum efficiency versus  $T$  for various bottom profiles with  $h = 7.90$ ,  $h_a/h = 0.646$ ,  $b/h = 0.392$  and  $w/b = 2.145$ . in the case of the HEST. (c) Maximum efficiency versus  $T$  with  $\varrho = 0$  for various bottom profiles with  $h = 3.40$ ,  $h_a/h = 0.176$ ,  $b/h = 0.392$  and  $w/b = 2.145$  in the case of the LEST. (d) Maximum efficiency versus  $T$  for various bottom profiles with  $h = 3.40$ ,  $h_a/h = 0.176$ ,  $b/h = 0.392$  and  $w/b = 2.145$  in the case of the LEST.

## 5.6 Conclusions

The effects of the chamber configuration of an OWC device on efficiency were numerically analyzed, using the BEM, employing quadratic elements. Comparisons were made of these numerical results with theoretical limiting cases obtained by [Evans and Porter \(1995\)](#) and [Şentürk and Özdamar \(2012\)](#) for a thin front wall and very good agreement was achieved. Numerical estimates for the hydrodynamic efficiency and the radiation susceptance and radiation conductance coefficients were then obtained for different physical configurations. Experimental results reported by [Morris-Thomas et al. \(2006\)](#) and [Wang et al. \(2018\)](#) were compared with those obtained by the present formulation; resonance frequencies and shapes of the hydrodynamic efficiency curves were found to be in good agreement. The main conclusions drawn from this study are as follows:

- By increasing the thickness of the front barrier, the bandwidth on the efficiency curves is reduced. This reduction in efficiency could be related to the fact that the transfer of energy from the incoming wave to the internal free surface, due to the orbital wave motion, is reduced for short wave periods when the front barrier is thicker.
- For a thick front barrier, a further reduction in the efficiency effective area under the curve is obtained when the front wall draft is increased.
- When the OWC chamber length-water depth ratio  $b/h$  is decreased, the period of maximum hydrodynamic efficiency is shorter. Consequently, an OWC chamber in which the range of frequency bandwidth in  $\eta_{max}$  coincides with the predominant wave period of a particular location, will mean the available wave power will be made better use of.
- It was observed that the incorporation of a step below the front wall reduces the bandwidth on the efficiency. This step gives a similar effect as that observed when the draft of the front wall is increased in an OWC with a completely flat bottom.
- It was also observed that when the wall to front barrier spacing is sufficiently small, compared to the depth, the range of the non-dimensional frequency  $Kh$ , for which the radiation susceptance coefficient is negative, is significantly reduced.
- By comparing the maximum theoretical efficiency with the experimental efficiency reported by [John Ashlin et al. \(2016\)](#) for a wave steepness  $H/\lambda$  varying from 0.0320 to 0.0371, the discrepancy is seen to be high. Therefore, special attention should be paid to turbine damping, as well as to non-linear effects, in order to make an adequate estimation of the power absorption of an OWC.
- When sloped, cycloidal or elliptical bottom profiles in a chamber of the MWEP were considered, it was seen that the efficiency band slightly shifts to longer periods, as the bottom of the chamber becomes steeper, generating slightly higher efficiency for longer wavelengths.

- For small periods, it was found that compared with the flat bottom, the sloped, cycloidal and elliptical bottoms diminish the hydrodynamic efficiency. This is due to the reduction of the part of the chamber entrance for the fluid particles, obstructing the waves and leading to a decrease in the internal free surface oscillation which drives the air column.
- It was observed that in the case of LEST in the MWEP, the efficiency band becomes wider as the draft is reduced. However, when the air volume inside the chamber is greater, the efficiency is significantly reduced.
- By comparing the different bottom profiles, it was found that the period in which resonance occurs is almost independent of the bottom geometrical configuration and it is mostly determined by the natural frequency of the water column.

This paper is only a numerical investigation on the hydrodynamic performance of an OWC device based on the linear wave theory. Experimental investigations that include the nonlinearities on the air compressibility and the turbine damping should be carried out in the future. Finally, it is hoped that the results of this study may provide valuable information for the clean and efficient harnessing of marine renewable energy.

## Bibliography

- Ahamed, R., McKee, K. and Howard, I. (2020). Advancements of wave energy converters based on power take off (pto) systems: A review, *Ocean Engineering* **204**: 107248.  
**URL:** <https://www.sciencedirect.com/science/article/pii/S0029801820302985>
- Becker, A. (1992). *The Boundary Element Method in Engineering: A Complete Course*, McGraw-Hill.  
**URL:** <https://books.google.com.mx/books?id=Co9YAAAAYAAJ>
- Belibassakis, K., Magkouris, A. and Rusu, E. (2020). A BEM for the hydrodynamic analysis of oscillating water column systems in variable bathymetry, *Energies* **13(13)**: 3403.
- Brebbia, C. and Dominguez, J. (1992). *Boundary Elements: An Introductory Course*, Computational Mechanics Publications.  
**URL:** [https://books.google.com.mx/books?id=X\\_ceAQAAIAAJ](https://books.google.com.mx/books?id=X_ceAQAAIAAJ)
- Delmonte, N., Barater, D., Giuliani, F., Cova, P. and Buticchi, G. (2016). Review of oscillating water column converters, *IEEE Transactions on Industry Applications* **52(2)**: 1698–1710.
- Dominguez, J. (1993). *Boundary Elements in Dynamics*, Computational Engineering, Computational Mechanics Publications.  
**URL:** <https://books.google.com.mx/books?id=N4ghw092NIMC>
- Ente Vasco de la Energía* (n.d.). <http://www.eve.es>. Accessed: 15 August 2020.

CHAPTER 5. THE INFLUENCE OF THE FRONT WALL THICKNESS ON THE HYDRODYNAMIC EFFICIENCY OF A LAND-FIXED OWC DEVICE

---

- Şentürk, U. and Özdamar, A. (2012). Wave energy extraction by an oscillating water column with a gap on the fully submerged front wall, *Applied Ocean Research* **37**: 174 – 182.  
**URL:** <http://www.sciencedirect.com/science/article/pii/S0141118712000405>
- Evans, D. and Porter, R. (1995). Hydrodynamic characteristics of an oscillating water column device, *Applied Ocean Research* **17**(3): 155 – 164.  
**URL:** <http://www.sciencedirect.com/science/article/pii/0141118795000089>
- Evans, D. V. (1982). Wave-power absorption by systems of oscillating surface pressure distributions, *Journal of Fluid Mechanics* **114**: 481–499.
- Falcão, A. F. and Henriques, J. C. (2016). Oscillating-water-column wave energy converters and air turbines: A review, *Renewable Energy* **85**: 1391 – 1424.  
**URL:** <http://www.sciencedirect.com/science/article/pii/S0960148115301828>
- Falnes, J. (1983). *Added-Mass Matrix and Energy Stored in the “Near Field”*; Internal Report, Division of Experimental Physics, University of Trondheim: Trondheim, Norway.
- Garrido, A., Otaola, E., Garrido, I., Lekube, J., Maseda, F., Liria, P. and Mader, J. (2015). Mathematical modeling of oscillating water columns wave-structure interaction in ocean energy plants, *Mathematical Problems in Engineering* **2015**: 1–11.
- GeoEuskadi, Infraestructura de Datos Espaciales (IDE) de Euskadi* (n.d.). <http://www.geo.euskadi.eus>. Accessed: 10 July 2020.
- Google Maps 2020* (n.d.). <https://www.google.es/maps>. Accessed: 10 July 2020.
- Heath, T. (2012). A review of oscillating water columns, *Philosophical Transactions of the Royal Society A* **370**: 235–45.
- Ibarra-Berastegi, G., Sáenz, J., Ulazia, A., Serras, P., Esnaola, G. and Garcia-Soto, C. (2018). Electricity production, capacity factor, and plant efficiency index at the mutriku wave farm (2014–2016), *Ocean Engineering* **147**: 20 – 29.  
**URL:** <http://www.sciencedirect.com/science/article/pii/S0029801817306157>
- Izquierdo, U., Esteban, G. A., Blanco, J. M., Albaina, I. and Peña, A. (2019). Experimental validation of a cfd model using a narrow wave flume, *Applied Ocean Research* **86**: 1 – 12.  
**URL:** <http://www.sciencedirect.com/science/article/pii/S0141118718304772>
- John Ashlin, S., Sundar, V. and Sannasiraj, S. (2016). Effects of bottom profile of an oscillating water column device on its hydrodynamic characteristics, *Renewable Energy* **96**: 341 – 353.  
**URL:** <http://www.sciencedirect.com/science/article/pii/S0960148116303937>
- Katsikadelis, J. (2002). *Boundary Elements. Theory and Applications*, Elsevier.

CHAPTER 5. THE INFLUENCE OF THE FRONT WALL THICKNESS ON THE HYDRODYNAMIC EFFICIENCY OF A LAND-FIXED OWC DEVICE

---

- Koley, S. and Trivedi, K. (2020). Mathematical modeling of oscillating water column wave energy converter devices over the undulated sea bed, *Engineering Analysis with Boundary Elements* **117**: 26 – 40.  
**URL:** <http://www.sciencedirect.com/science/article/pii/S0955799720300801>
- Martins-rivas, H. and Mei, C. C. (2009). Wave power extraction from an oscillating water column along a straight coast, *Ocean Engineering* **36**(6): 426 – 433.  
**URL:** <http://www.sciencedirect.com/science/article/pii/S002980180900002X>
- McIver, M. and McIver, P. (2016). The added mass for two-dimensional floating structures, *Wave Motion* **64**: 1–12.  
**URL:** <https://www.sciencedirect.com/science/article/pii/S016521251600024X>
- McIver, P. and Evans, D. (1984). The occurrence of negative added mass in free-surface problems involving submerged oscillating bodies, *Journal of Engineering Mathematics* **18**: 7–22.
- Medina-Lopez, E., Allsop, W., Dimakopoulos, A. and Bruce, T. (2015). *Conjectures on the Failure of the OWC Breakwater at Mutriku*, pp. 592–603.  
**URL:** <https://ascelibrary.org/doi/abs/10.1061/9780784480304.063>
- Michele, S., Renzi, E., Perez-Collazo, C., Greaves, D. and Iglesias, G. (2019). Power extraction in regular and random waves from an owc in hybrid wind-wave energy systems, *Ocean Engineering* **191**: 106519.  
**URL:** <http://www.sciencedirect.com/science/article/pii/S0029801819306572>
- Morris-Thomas, M. T., Irvin, R. J. and Thiagarajan, K. P. (2006). An Investigation Into the Hydrodynamic Efficiency of an Oscillating Water Column, *Journal of Offshore Mechanics and Arctic Engineering* **129**(4): 273–278.  
**URL:** <https://doi.org/10.1115/1.2426992>
- Ning, D.-Z., Shi, J., Zou, Q.-P. and Teng, B. (2015). Investigation of hydrodynamic performance of an owc (oscillating water column) wave energy device using a fully nonlinear hoberm (higher-order boundary element method), *Energy* **83**: 177 – 188.  
**URL:** <http://www.sciencedirect.com/science/article/pii/S0360544215001644>
- Ning, D.-Z., Wang, R.-Q., Gou, Y., Zhao, M. and Teng, B. (2016). Numerical and experimental investigation of wave dynamics on a land-fixed owc device, *Energy* **115**: 326 – 337.  
**URL:** <http://www.sciencedirect.com/science/article/pii/S0360544216312324>
- Ning, D.-Z., Wang, R.-Q., Zou, Q.-P. and Teng, B. (2016). An experimental investigation of hydrodynamics of a fixed owc wave energy converter, *Applied Energy* **168**: 636 – 648.  
**URL:** <http://www.sciencedirect.com/science/article/pii/S0306261916300952>
- Pawitan, K. A., Dimakopoulos, A. S., Vicinanza, D., Allsop, W. and Bruce, T. (2019). A loading model for an owc caisson based upon large-scale measurements, *Coastal Engineering* **145**: 1 – 20.  
**URL:** <http://www.sciencedirect.com/science/article/pii/S0378383918302114>



CHAPTER 5. THE INFLUENCE OF THE FRONT WALL THICKNESS ON THE  
HYDRODYNAMIC EFFICIENCY OF A LAND-FIXED OWC DEVICE

---

- Pawitan, K. A., Vicinanza, D., Allsop, W. and Bruce, T. (2020). Front wall and in-chamber impact loads on a breakwater-integrated oscillating water column, *Journal of Waterway, Port, Coastal, and Ocean Engineering* **146**(5): 04020037.  
**URL:** <https://ascelibrary.org/doi/abs/10.1061/%28ASCE%29WW.1943-5460.0000595>
- Polinder, H. and Scuotto, M. (2005). Wave energy converters and their impact on power systems, *2005 International Conference on Future Power Systems*, pp. 9 pp.-9.
- Rezanejad, K., Bhattacharjee, J. and Guedes Soares, C. (2013). Stepped sea bottom effects on the efficiency of nearshore oscillating water column device, *Ocean Engineering* **70**: 25 – 38.  
**URL:** <http://www.sciencedirect.com/science/article/pii/S0029801813002229>
- Rezanejad, K., Guedes Soares, C., López, I. and Carballo, R. (2017). Experimental and numerical investigation of the hydrodynamic performance of an oscillating water column wave energy converter, *Renewable Energy* **106**: 1 – 16.  
**URL:** <http://www.sciencedirect.com/science/article/pii/S0960148117300034>
- Torre-Enciso, Y., Ortubia, I., Aguilera, L. and Marqués, J. (2009). Mutriku wave power plant: From the thinking out to the reality, *Proceedings of the 8th European Wave and Tidal Energy Conference* pp. 319–329.
- Vicinanza, D., Lauro, E. D., Contestabile, P., Gissoni, C., Lara, J. L. and Losada, I. J. (2019). Review of innovative harbor breakwaters for wave-energy conversion, *Journal of Waterway, Port, Coastal, and Ocean Engineering* **145**(4): 03119001.  
**URL:** <https://ascelibrary.org/doi/abs/10.1061/%28ASCE%29WW.1943-5460.0000519>
- Viviano, A., Musumeci, R. E., Vicinanza, D. and Foti, E. (2019). Pressures induced by regular waves on a large scale owc, *Coastal Engineering* **152**: 103528.  
**URL:** <http://www.sciencedirect.com/science/article/pii/S0378383919301589>
- Viviano, A., Naty, S., Foti, E., Bruce, T., Allsop, W. and Vicinanza, D. (2016). Large-scale experiments on the behaviour of a generalised oscillating water column under random waves, *Renewable Energy* **99**: 875 – 887.  
**URL:** <http://www.sciencedirect.com/science/article/pii/S0960148116306826>
- Wang, D., Katory, M. and Li, Y. (2002). Analytical and experimental investigation on the hydrodynamic performance of onshore wave-power devices, *Ocean Engineering* **29**(8): 871 – 885.  
**URL:** <http://www.sciencedirect.com/science/article/pii/S0029801801000580>
- Wang, R.-Q. and Ning, D.-Z. (2020). Dynamic analysis of wave action on an owc wave energy converter under the influence of viscosity, *Renewable Energy* **150**: 578 – 588.  
**URL:** <http://www.sciencedirect.com/science/article/pii/S0960148120300082>
- Wang, R.-Q., Ning, D.-Z., Zhang, C.-W., Zou, Q.-P. and Liu, Z. (2018). Nonlinear and viscous effects on the hydrodynamic performance of a fixed owc wave energy converter, *Coastal*

CHAPTER 5. THE INFLUENCE OF THE FRONT WALL THICKNESS ON THE  
HYDRODYNAMIC EFFICIENCY OF A LAND-FIXED OWC DEVICE

---

*Engineering* **131**: 42 – 50.

**URL:** <http://www.sciencedirect.com/science/article/pii/S0378383917300637>

Zheng, S., Antonini, A., Zhang, Y., Greaves, D., Miles, J. and Iglesias, G. (2019). Wave power extraction from multiple oscillating water columns along a straight coast, *Journal of Fluid Mechanics* **878**: 445–480.

Zheng, S., Zhang, Y. and Iglesias, G. (2019). Coast/breakwater-integrated owc: A theoretical model, *Marine Structures* **66**: 121 – 135.

**URL:** <http://www.sciencedirect.com/science/article/pii/S0951833918304180>

Zheng, S., Zhu, G., Simmonds, D., Greaves, D. and Iglesias, G. (2020). Wave power extraction from a tubular structure integrated oscillating water column, *Renewable Energy* **150**: 342 – 355.

**URL:** <http://www.sciencedirect.com/science/article/pii/S0960148120300094>

## Chapter 6

# The Effect of Oblique Waves on the Hydrodynamic Efficiency of a Land-Fixed OWC device

It has been revealed in the previous chapter, that the chamber configuration strongly influences the OWC hydrodynamic performance when water waves propagate normally to the device. However, in real sea conditions, the direction of the water waves is not always perpendicular to the OWC chamber transverse axis. The most well-known example is the Wave Energy Plant in Mutriku, Spain, where the direction of the water waves is mostly oblique with respect to the combined OWC-breakwater system. In this example, the breakwater that houses the OWC power plant has a boomerang-shaped design oriented to the north-northeast, which causes the chambers to face the predominantly north-western arriving sea waves at varied angles. Thus, although the chambers' structural design is identical, the power that the turbines generate varies.

In this chapter, in order to investigate the influence of oblique waves on hydrodynamic efficiency, two theoretical approaches are presented to provide possibilities to study the performance of integrated OWC-breakwater systems in various sea states. Thus, the purpose of the present chapter is to provide some insight into the following research question: Is the direction of the incoming water waves important for the hydrodynamic efficiency of a land-fixed OWC device?

This chapter consists of the published journal article:

Medina Rodríguez A.A., Martínez Flores A., Blanco Ilzarbe J.M., Silva Casarín R. (2021). “*Interaction of oblique waves with an Oscillating Water Column device*”. **Ocean Engineering**. 228: 108931. <https://doi.org/10.1016/j.oceaneng.2021.108931>.

**Interaction of Oblique Waves with an Oscillating Water Column Device**

Ayrton Alfonso Medina Rodríguez, Alejandro Martínez Flores, Jesús María Blanco Ilzarbe  
and Rodolfo Silva Casarín

**Abstract**

The interaction of oblique water waves with a land-fixed Oscillating Water Column (OWC) type wave energy converter is examined. Two-dimensional linear wave theory is used to formulate the mathematical problem. The matched eigenfunction expansion method (EEM) using dual series relations and the Boundary Element Method (BEM) with quadratic elements are utilized to solve the associated boundary value problem (BVP). The novelty of the present work lies on addressing the influence of oblique water waves on the OWC efficiency and the use of dual series relations to solve this type of BVP. Variations of the hydrodynamic efficiency with the wave angle of incidence, and with the chamber length and front barrier draft to water depth ratios are discussed. Both analytical and numerical results were found to be in good agreement. Findings revealed that by increasing the angle of incidence, a broader hydrodynamic efficiency band and a higher wave frequency at which resonance occurs are both obtained. This aspect may offer benefits to wave power extraction in real sea conditions for fixed OWC devices. Finally, cases published in the specialized literature were recovered and very good agreement was achieved.

## 6.1 Introduction

In order to attenuate the effect of global warming and meet the electricity demands of the rapidly increasing world population, a prompt conversion from fossil fuel energy systems to renewable energy technologies is required. In this sense, wave energy has been suggested as a potential renewable source to provide most of the world electricity needs in the short term (Izquierdo et al.; 2019). A wide variety of technologies have been proposed over the past few decades, among which the OWC device has been proven to be one of the most promising systems for ocean wave energy harvesting. The OWC device is a unique system among wave energy converters (WECs) since it only consists of two main parts: a partially submerged collecting chamber and a power take-off (PTO) mechanism which is located above sea level and thus evades direct exposure to the seawater. It also poses a simple working principle where due to the wave action, the water column inside the collecting chamber vertically oscillates, driving the confined air volume back and forth through a turbine coupled to a generator (Falcão and Henriques; 2016).

However, despite its simplicity, one of the greatest issues of this kind of WEC is the economical aspect (Lin et al.; 2015). For the sake of encouraging the development of OWC technology, its installation into a breakwater has been extensively investigated in the last few decades (Vicinanza et al.; 2019). This integration provides several benefits: with an OWC power plant integrated into a breakwater, energy extraction becomes more cost-effective since installation and maintenance costs are shared, the operation of the power plant becomes easier

*CHAPTER 6. THE EFFECT OF OBLIQUE WAVES ON THE HYDRODYNAMIC EFFICIENCY OF A LAND-FIXED OWC DEVICE*

Table 6.1: Summary of past investigations on non-cylindrical OWCs.

Researchers	Wave incidence direction	Type of OWC	Solution method used
Evans and Porter (1995)	Perpendicular	Land-fixed	EEM and Galerkin method
Wang et al. (2002)	Perpendicular	Onshore	BEM and Experimental
Morris-Thomas et al. (2006)	Perpendicular	Onshore	Experimental
Şentürk and Özdamar (2012)	Perpendicular	Onshore	EEM and Galerkin method
Rezanejad et al. (2013)	Perpendicular	Nearshore	BEM and EEM
Ning et al. (2015)	Perpendicular	Land-fixed	Higher-order BEM
John Ashlin et al. (2016)	Perpendicular	Land-fixed	Experimental
Ning, Wang, Zou and Teng (2016)	Perpendicular	Land-fixed	Experimental
Rezanejad et al. (2017)	Perpendicular	Shoreline fixed	BEM and Experimental
Malara et al. (2017)	Perpendicular and Oblique	Land-fixed	BEM and EEM
Koley and Trivedi (2020)	Perpendicular	Land-fixed	Coupled EEM - BEM
Belibassakis et al. (2020)	Perpendicular	Land-fixed	BEM

and the utilization of mooring systems and underwater electric cables is avoided. Additionally, due to the energy absorption into the OWC chamber, both the hydraulic performance of the breakwater to coastal protection by reducing the wave reflection and the disturbance in the navigation of vessels at harbour entrances are improved. Taking into account these aspects, integrated OWC-breakwater systems for wave-power conversion can turn into a reliable wave-energy technology with the potential to become commercially successful shortly. For this purpose, further research should be carried out to attain a better understanding of the relationship among OWC structural design, the control strategy of the PTO mechanism, wave climate and hydraulic performance and thus to demonstrate the economic potential of OWC-breakwater systems by achieving competitive costs and high reliability.

In the specialized literature, most studies on OWC systems focus on their interaction considering that waves propagate normally towards the device (Evans and Porter; 1995; Morris-Thomas et al.; 2006; Şentürk and Özdamar; 2012; Rezanejad et al.; 2013; Koley and Trivedi; 2020), Table 6.1. However, in real sea conditions, water waves direction is not always perpendicular with respect to the OWC chamber transverse axis (Jin et al.; 2012). For instance, this is the case of the Mutriku Wave Energy Plant (MWEP), where the water waves direction is mainly oblique with respect to the integrated OWC-breakwater system. In this particular case, the breakwater that houses the OWC power plant is oriented to the north-northeast and follows a boomerang-shaped design, which makes the chambers to face the mostly north-western incoming sea waves at a varying angle and to interact with different waves due to changes in the nearby bathymetry (Ibarra-Berastegi et al.; 2018). The total pressure generated at the chambers is therefore relatively different and a distinct incoming airflow on each of the 14 working Wells turbines is thus generated. As a consequence, even though the structural design is the same among the chambers, the electricity generated by the turbines varies. Thus, motivated by the aforementioned points, this work investigates the influence of the wave angle of incidence on the hydrodynamic performance of an integrated OWC-breakwater system.

Previous studies have investigated the influence of the OWC structural characteristics on its hydrodynamic performance with the aid of analytical, experimental and numerical techniques (Wang et al.; 2002; Morris-Thomas et al.; 2006; Martins-rivas and Mei; 2009; Şentürk and

Özdamar; 2012; Rezanejad et al.; 2013; Ning et al.; 2015; John Ashlin et al.; 2016; Ning, Wang, Zou and Teng; 2016; Zheng, Zhang and Iglesias; 2019; Zheng, Antonini, Zhang, Greaves, Miles and Iglesias; 2019; Zheng et al.; 2020; Koley and Trivedi; 2020; Belibassakis et al.; 2020; Medina Rodríguez et al.; 2020). By using a numerical approach, the hydrodynamic performance of an OWC device with arbitrary topography near the shoreline was analyzed by Wang et al. (2002). In their work, the authors showed that a modification in water depth at the shoreline has a significant effect on the OWC hydrodynamic performance. Morris-Thomas et al. (2006) experimental studied the effect of front wall geometry on the OWC hydrodynamic efficiency and concluded that the peak values of the hydrodynamic efficiency are not significantly influenced by the front barrier geometry. Martins-rivas and Mei (2009) developed a theoretical model for a vertical OWC installed on a straight and cliff-like coast. The authors found that the shore reflection roughly doubles the energy absorption, while the considered PTO produces a higher efficiency over a broad frequency band.

By using the EEM and a Galerkin approximation, the hydrodynamic efficiency of an OWC with a gap in its fully-submerged front wall was analyzed by Şentürk and Özdamar (2012). The authors showed that by selecting the appropriate geometrical parameters, it is possible to obtain improvements on the OWC hydrodynamic efficiency. The impact of stepped bottom topography on the efficiency of a nearshore OWC device was analyzed by Rezanejad et al. (2013). In their work, it was found that significant effects on the OWC hydrodynamic performance occur when a stepped bottom profile outside of the chamber is considered. Ning et al. (2015) carried out a time-domain analysis of the performance of a fixed OWC device based on a higher-order BEM in a 2D fully nonlinear numerical wave flume. The authors investigated the influence of the bottom slope on the hydrodynamic efficiency and concluded that the chamber geometric configuration has a significant effect on the hydrodynamic performance. John Ashlin et al. (2016) experimentally investigated the influence of the bottom profile configuration on the OWC hydrodynamic performance. By testing four different bottom profiles (flat, circular, curved and sloped) in a wave flume, the authors found that the circular curved bottom profile inside the chamber was more effective for wave energy conversion. Ning, Wang, Zou and Teng (2016) investigated the effects of the incident wave amplitude and the geometric parameters on the hydrodynamic efficiency of a fixed OWC. The authors reported that an increase in the bottom slope can increase the optimal hydrodynamic efficiency while the incident wave amplitude and the bottom slope have a minor effect on the resonant frequency. An analysis of the three-dimensional effects affecting the U-OWC performance was developed by Malara et al. (2017). The authors showed that 3D effects are significant when the device width is smaller than 20 m, resulting in an improvement in power output per unit width. Zheng, Zhang and Iglesias (2019) carried out a theoretical model to study the performance of a circular cylindrical OWC along a vertical coast/breakwater considering the thickness of the chamber wall. It was found that the angle of incidence and the thickness of the chamber wall both affect the wave power captured by the OWC. Zheng, Antonini, Zhang, Greaves, Miles and Iglesias (2019) employed the EEM to develop a theoretical model for the evaluation of the hydrodynamic performance of multiple circular cylinder OWCs located along a vertical straight coast. The authors found that the hydrodynamic performance of the OWC devices was enhanced significantly for a certain range of wave conditions due to the constructive wave interference from the OWCs array and the

coast. [Zheng et al. \(2020\)](#) analyzed the influence of the entrance radius of the OWC chamber and the wall thickness of the tubular-structure. They showed that a thinner chamber wall thickness results in a higher wave power extraction in terms of a broader bandwidth of efficiency curves. [Koley and Trivedi \(2020\)](#) employed a coupled EEM-BEM to analyze the hydrodynamic performance of an OWC device located on an undulated seabed and concluded that the OWC structural configuration and bottom profile play a significant role in the hydrodynamic efficiency. [Belibassakis et al. \(2020\)](#) employed a 2D BEM model for analyzing the OWC's response in general bathymetry regions and found that the bottom slope and curvature can be relevant to the OWC performance. By using the BEM, the effects of the front wall thickness and the bottom profile of an OWC device on its efficiency were analyzed by [Medina Rodríguez et al. \(2020\)](#). The authors showed that by increasing the thickness of the front barrier, the bandwidth on the efficiency curves is significantly reduced.

The EEM to obtain dual series relations that are then solved by applying the least square method has been successfully employed to analyze the scattering and radiation of water waves by segmented breakwaters or vertical barriers ([Dalrymple and Martin; 1990](#); [Losada et al.; 1992](#); [Abul-Azm; 1996](#); [Lee and Chwang; 2000](#); [Sahoo et al.; 2000](#); [Choudhary and Martha; 2016, 2017](#)). The latter method was developed by [Kelman and Koper \(1973\)](#) to solve dual series relations, and its convergence was approached theoretically by [Feinerman and Kelman \(1974\)](#). By using variational methods and the EEM, [Dalrymple and Martin \(1990\)](#) determined the reflection and transmission coefficients due to the interaction of water waves with a long linear array of offshore breakwaters. [Losada et al. \(1992\)](#) analysed the propagation of oblique incident waves through a rigid vertical thin barrier in water of uniform finite depth. They matched the horizontal components of the velocity at the right and left sides of the thin barrier and at the gap to obtain the corresponding dual series relations. [Abul-Azm \(1996\)](#) investigated the wave reflection and dynamic displacement of a submerged flexible breakwater and showed that the proposed submerged breakwaters are generally less effective in reflecting waves than the surface-piercing breakwaters. The scattering and radiation of surface waves by several types of permeable vertical porous barriers in finite water depth were studied by [Lee and Chwang \(2000\)](#). [Sahoo et al. \(2000\)](#) studied the wave trapping by vertical porous barriers and the wave generation by vertical porous wavemakers in front of the end-wall of a semi-infinitely long channel. With the help of a perturbation analysis, the scattering of water waves by bottom undulation in the presence of different kinds of thin vertical barriers was solved by [Choudhary and Martha \(2016\)](#).

The objective of this paper is to extend the work done by [Evans and Porter \(1995\)](#) on the OWC–water wave interaction by considering oblique incidental waves. This is in order to analyse its influence on the efficiency bandwidth and thus provide further possibilities to improve the performance and design of integrated OWC-breakwater systems in various sea states. To the authors' knowledge, both theoretical and numerical studies for analysing the interaction of oblique water waves with a 2D integrated OWC-breakwater system have not been examined in the past. The fundamental hypothesis of the present work is that the angle of incidence has a significant influence on the hydrodynamic efficiency band as important as the length of the chamber and front barrier's draft. Therefore, this work examines the two-dimensional hydrodynamic interaction of oblique water waves with an OWC device.

Under the potential flow approach, linear wave theory is employed and the viscous effects and the nonlinear air compressibility are neglected. Two different mathematical techniques are presented to solve the associated BVP. The first one is the well-known semi-analytic matched EEM which leads to dual series relations to obtain the correct matching conditions at the front barrier. These relations are solved by a least-squares technique to find the amplitudes of the propagating and evanescent wave modes both upwave and down-wave. The second one is the BEM, which is a numerical technique based on an integral equation formulation. The BEM with a second-order discretization will be employed in this work and is used to compare the results with the ones found from the semi-analytic method. The main objectives of this work lie a) on the analysis of the bandwidth modification on the efficiency curves due to oblique incident waves interacting with an OWC device and b) the reduction on the maximum hydrodynamic efficiency due to the trapped air column inside the chamber. Analytical and numerical calculations for the hydrodynamic efficiency are presented for a range of different parameters. Furthermore, analytical and numerical outcomes for particular cases are compared with previous results obtained by [Evans and Porter \(1995\)](#).

## 6.2 Problem Formulation

The Cartesian coordinate system was chosen with the  $x - y$  plane on the mean position of the free surface and the  $z$ -axis pointing upwards. The origin of the coordinate system is situated on the undisturbed free surface and the left-rigid vertical wall. The OWC consists of this left-rigid wall, located at  $x = 0$ , and complemented by a vertical, surface-piercing barrier at  $x = b$ , with a draft  $h_a$ , as shown in Fig. 6.1. The 2-dimensional case is considered, with the OWC being infinitely long and parallel to the incoming wave crest. The domain considered was separated into two regions: Region 1 ( $0 \leq x \leq b, -h \leq z \leq 0$ ) and Region 2 ( $b \leq x < \infty, -h \leq z \leq 0$ ). The front wall is denoted by  $L_b = \{(x, z) : (x = b, -h_a \leq z \leq 0)\}$ , the gap between the immersed tip of the front barrier and the sea bottom is given by  $L_g = \{(x, z) : x = b, -h \leq z \leq -h_a\}$ , the left-rigid wall by  $S_w = \{(x, z) : x = 0, -h < z < 0\}$ , the free surface inside chamber by  $S_i = \{(x, z) : 0 \leq x \leq b, z = 0\}$ , the external free surface by  $S_f = \{(x, z) : b \leq x \leq \infty, z = 0\}$  and the flat bottom by  $S_b = \{(x, z) : (0 < x < \infty, z = -h)\}$ .

The fluid was assumed to be inviscid and incompressible, and the wave motion was considered to be represented adequately by the linearized wave theory, disregarding surface tension effects. The wave incidence angle ( $\theta$ ) is defined by the angle between  $x$ -axis and the direction of wave propagation. By assuming an irrotational flow, we define a simple harmonic in time velocity potential  $\Phi(x, z, t) = \text{Re}\{\phi(x, z)e^{-i\omega t + i\kappa y}\}$ , where  $\text{Re}\{\}$  denotes the real part of a complex expression,  $\omega$  is the angular frequency,  $\kappa = k \sin \theta$ ,  $k$  is the wavenumber of the plane progressive wave and  $t$  is the time. The spatial velocity potential  $\phi$  then satisfies the Helmholtz equation

$$\frac{\partial^2 \phi}{\partial x^2} + \frac{\partial^2 \phi}{\partial z^2} - \kappa^2 \phi = 0, \quad (6.1)$$

along with the no-flow boundary condition on the solid boundaries such as the bottom, the



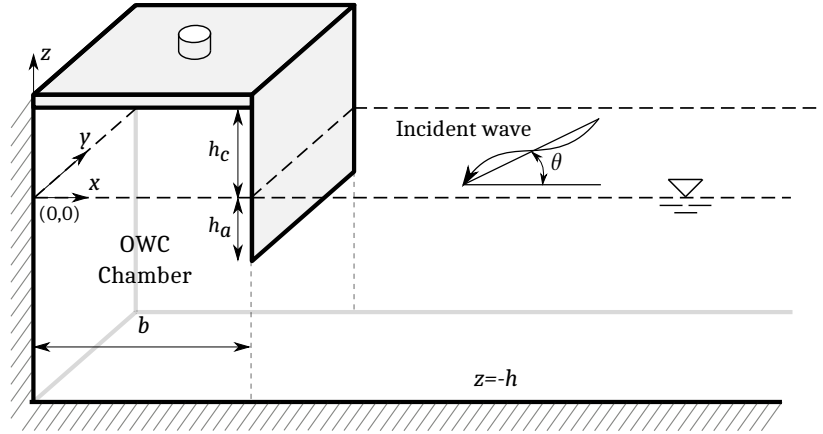


Figure 6.1: Definition sketch of the interaction of an OWC device with oblique waves.

front barrier and the left-rigid vertical wall described by

$$\frac{\partial \phi}{\partial n} = 0 \quad \text{for } (x, z) \in S_b, L_b \text{ and } S_w. \quad (6.2)$$

Together with the continuity of pressure and horizontal velocity across the vertical plane separating the fluid regions

$$\phi_- = \phi_+ \quad \text{and} \quad \frac{\partial \phi}{\partial x_-} = \frac{\partial \phi}{\partial x_+} \quad \text{on } x = b, \quad -h \leq z \leq -h_a. \quad (6.3)$$

A pressure distribution  $P(t)$  over the internal free surface is imposed and after considering simple harmonic motions for the pressure and the free surface  $(P(t), \bar{\eta}(t)) = \text{Re}\{(p, \zeta) e^{-i\omega t}\}$ , the internal and external linearized free surface boundary conditions are

$$\frac{\partial \phi}{\partial z} - K\phi = \begin{cases} \frac{i\omega p}{\rho g} & \text{on } z = 0, \quad 0 < x < b, \\ 0 & \text{on } z = 0, \quad b < x < \infty, \end{cases} \quad (6.4)$$

respectively, with  $K = \omega^2/g$ ,  $\rho$  being the seawater density and  $g$  the gravitational constant.

The potential is then decomposed into a scattered and a radiated potential as in [Evans and Porter \(1995\)](#) as follows

$$\phi(x, z) = \phi^S + \frac{i\omega p}{\rho g} \phi^R, \quad (6.5)$$

where the  $\phi^S$  is the solution of the scattering of an incident wave coming from  $x = +\infty$  in the absence of an imposed pressure on the internal free surface, satisfying Eqs. (6.1)–(6.4) with  $p = 0$ ; while  $\phi^R$  represents the solution of the radiation problem due to an oscillating pressure distribution imposed on the internal free surface in the absence of incoming waves and satisfies Eqs. (6.1)–(6.4) with Eq. (6.4) replaced by

$$\frac{\partial \phi^R}{\partial z} - K\phi^R = 1 \quad \text{on } z = 0, \quad 0 < x < b. \quad (6.6)$$

CHAPTER 6. THE EFFECT OF OBLIQUE WAVES ON THE HYDRODYNAMIC  
EFFICIENCY OF A LAND-FIXED OWC DEVICE

---

Additionally, for the diffraction and radiation problems, the Sommerfeld radiation condition is applied at the right end of the domain as follows:

$$\frac{\partial \phi^{D,R}}{\partial x} - ik \cos \theta \phi^{D,R} = 0 \quad \text{as} \quad x \rightarrow +\infty, \quad (6.7)$$

with  $\phi^D$  being the diffracted potential that together with the incident potential  $\phi^I$  composed the scattered potential  $\phi^S$ , while  $k$  is the wavenumber and real root of the wave dispersion relation given by

$$\omega^2 = gk \tanh kh. \quad (6.8)$$

Similar to the velocity potential, the time harmonic induced volume flux across the internal free surface,  $Q(t) = \text{Re}\{qe^{-i\omega t}\}$  is decomposed into scattering and radiation volume fluxes  $q^S$  and  $q^R$ , respectively, across  $S_i$  as follows

$$q = \int_{S_i} \frac{\partial \phi}{\partial z} dx = q^S + \frac{i\omega p}{\rho g} q^R, \quad (6.9)$$

and since the continuity of volume flux should be ensured across the internal free surface and the gap below the barrier tip, we obtain

$$q^{S,R} = \int_{S_i} \frac{\partial \phi^{S,R}}{\partial z} dx = \int_{L_g} \frac{\partial \phi^{S,R}}{\partial x} dz. \quad (6.10)$$

Furthermore, the radiation volume flux  $q^R$  is decomposed into real and imaginary parts as follows

$$\frac{i\omega p}{\rho g} q^R = -(\tilde{B} - i\tilde{A})p = -Zp, \quad (6.11)$$

with  $Z = \tilde{B} - i\tilde{A}$  being a complex admittance, while the real coefficients  $\tilde{A}$  and  $\tilde{B}$  are related to the added mass and the radiation damping coefficients in a rigid body system, respectively (Evans and Porter; 1995). These coefficients are then called the radiation susceptance and the radiation conductance parameters (Evans and Porter; 1995) described by

$$\tilde{A} = \frac{\omega}{\rho g} \text{Re}\{q^R\}, \quad (6.12a)$$

$$\tilde{B} = \frac{\omega}{\rho g} \text{Im}\{q^R\}, \quad (6.12b)$$

respectively, with  $\text{Im}\{\}$  denoting the imaginary part of a complex expression.

Now, by assuming a linear relationship between the volume flux through the turbine and the pressure drop across it (Evans; 1982), we have

$$q = (\Lambda - i\varrho)p, \quad (6.13)$$

where  $\Lambda$  is a real control parameter, associated with the linear turbine damping induced to the airflow. Air compressibility is modelled assuming a linearized isentropic relationship, with the trapped air within the chamber being an ideal gas and where the compression-expansion process

CHAPTER 6. THE EFFECT OF OBLIQUE WAVES ON THE HYDRODYNAMIC EFFICIENCY OF A LAND-FIXED OWC DEVICE

---

is adiabatic and reversible. Thus, the quantity  $\varrho = \omega V_0 / (\gamma p_a)$  represents the compressibility of the trapped air with  $V_0$  being the air volume,  $\gamma$  the specific heat ratio of air equal to 1.4 and  $p_a$  the atmospheric air pressure (Rezanejad et al.; 2017). After combining Eqs. (6.9), (6.11) and (6.13), the imposed internal pressure yields

$$p = \frac{q^S}{\Lambda + Z - i\varrho}. \quad (6.14)$$

By averaging over one wave period the total rate of work done by the pressure forces inside the OWC,  $Q(t) \times P(t)$ , it gives

$$W = \frac{1}{2} \text{Re}\{\bar{p}q\}, \quad (6.15)$$

where the horizontal bar ( $\bar{\phantom{x}}$ ) denotes the complex conjugate. Now, after using Eqs. (6.9) and (6.11) in Eq. (6.15) and simplifying, we obtain

$$W = \frac{1}{2} \text{Re}\{\bar{p}(q^S - Zp)\} = \frac{1}{2} \left( \text{Re}\{\bar{p}q^S\} - \tilde{B}|p|^2 \right) = \frac{|q^S|^2}{8\tilde{B}} - \frac{\tilde{B}}{2} \left| p - \frac{q^S}{2\tilde{B}} \right|^2, \quad (6.16)$$

where if  $\tilde{B}^{-1}$  exists, the maximum work results

$$W_{max} = \frac{|q^S|^2}{8\tilde{B}}, \quad \text{when} \quad p = \frac{q^S}{2\tilde{B}}, \quad (6.17)$$

with  $\Lambda = \overline{(Z - i\varrho)}$  for maximum power.

Combining Eqs. (6.14) and (6.16) gives

$$W = \frac{|q^S|^2}{8\tilde{B}} \left[ 1 - \left( \frac{|\Lambda - Z + i\varrho|}{|\Lambda + Z - i\varrho|} \right)^2 \right]. \quad (6.18)$$

To optimize the power conversion efficiency, the optimum value of  $\Lambda$  must be determined. This value is obtained by applying zero value to the derivative for the squared-right term inside the brackets of Eq. (6.18) with respect to  $\Lambda$  (Şentürk and Özdamar; 2012), yielding

$$\Lambda_{opt} = |Z - i\varrho| = \left( \tilde{B}^2 + (\tilde{A} + \varrho)^2 \right)^{1/2} \quad (6.19)$$

and substituting the above expression into Eq. (6.18) gives

$$W_{opt} = \frac{|q^S|^2}{8\tilde{B}} \left[ 1 - \frac{\Lambda_{opt} - \tilde{B}}{\Lambda_{opt} + \tilde{B}} \right], \quad (6.20)$$

with  $\tilde{A}$ ,  $\tilde{B}$  and  $\Lambda$  being function of the angular frequency  $\omega$ .

Hence, the expression for the maximum hydrodynamic efficiency is of the form

$$\eta_{max} = \frac{W_{opt}}{W_{max}} = \frac{2\tilde{B}}{\Lambda_{opt} + \tilde{B}}, \quad (6.21)$$

with  $\eta_{max}$  in the range of 0 to 1. In the ideal case of  $\eta_{max} = 1$ , it indicates that the OWC device has effectively captured all of the incident wave energy, the internal free surface is excited in a piston-type resonant mode and the PTO damping optimization is satisfied (Michele et al.; 2019). Such condition will remain if the rate of energy extraction equates to the rate of radiation damping while the state of resonance in the internal free surface is preserved, which requires that the radiated waves, superpose and cancel the incident and scattered waves (Morris-Thomas et al.; 2006).

Following Evans and Porter (1995), we now define the non-dimensionalised quantities  $\mu$  and  $\nu$  as follows

$$\mu = \frac{\rho g}{\omega b} \tilde{A}, \quad (6.22a)$$

$$\nu = \frac{\rho g}{\omega b} \tilde{B}, \quad (6.22b)$$

which represent the radiation susceptance and radiation conductance coefficients, respectively. The radiation conductance coefficient  $\nu$  represents the energy transfer into the system, while the radiation susceptance coefficient  $\mu$  the energy that remains un-captured (Rezanejad et al.; 2013).

Finally, after substituting the above coefficients into Eq. (6.21), the hydrodynamic efficiency  $\eta_{max}$  gives

$$\eta_{max} = \frac{2}{\left[1 + \left(\frac{\mu}{\nu} + \frac{\rho g}{\omega b} \frac{\rho}{\nu}\right)^2\right]^{1/2} + 1}. \quad (6.23)$$

This last expression is independent of the incident wave power and only depends on the radiated volume flux  $q^R$ . Now, by neglecting the effect of the air compressibility, i.e.,  $\rho = 0$ , it gives rise to the expression previously reported by Evans and Porter (1995)

$$\eta_{max} = \frac{2}{\left[1 + \left(\frac{\mu}{\nu}\right)^2\right]^{1/2} + 1}. \quad (6.24)$$

## 6.3 Solution method

### 6.3.1 Matched Eigenfunction Expansion Method

In this subsection, the solution method for the radiation and the scattering problems are described. First, for the radiation problem, the spatial velocity potentials in the two regions are expanded in terms of the appropriate eigenfunctions as given by

$$\phi_1^R(x, z) = B_0^R \cos k_x x \Psi_0(z) + \sum_{n=1}^{\infty} B_n^R \cosh k_{nx} x \Psi_n(z) - \frac{1}{K}, \quad (6.25a)$$

$$\phi_2^R(x, z) = A^R e^{ik_x(x-b)} \Psi_0(z) + \sum_{n=1}^{\infty} A_n^R e^{-k_{nx}(x-b)} \Psi_n(z), \quad (6.25b)$$

CHAPTER 6. THE EFFECT OF OBLIQUE WAVES ON THE HYDRODYNAMIC  
EFFICIENCY OF A LAND-FIXED OWC DEVICE

---

for Region 1 and 2, respectively, and where the term  $-1/K$  on  $\phi_2^R(x, z)$  is included to satisfy Eq. (6.6), while  $k_x = \sqrt{k^2 - \kappa^2}$  and  $k_{nx} = \sqrt{k_n^2 + \kappa^2}$  for  $n = 1, 2, \dots$ . Additionally, the eigenfunction  $\Psi_n$  for  $n = 0, 1, \dots$  is given by

$$\Psi_n(z) = \frac{1}{\sqrt{N_n}} \cos k_n(z + h), \quad \text{for } n = 0, 1, 2, \dots, \quad (6.26)$$

where

$$N_n = \frac{1}{2} \left[ 1 + \frac{\sin 2k_n h}{2k_n h} \right], \quad \text{for } n = 0, 1, 2, \dots \quad (6.27)$$

Wavenumber  $k$  indicates the positive real root, and  $ik_n$  for  $n \geq 1$  indicates the purely imaginary roots of the dispersion relation in  $k$  given by Eq. (6.8). The coefficients  $A^R$ ,  $A_n^R$  for  $n = 1, 2, \dots$  and  $B_n^R$  for  $n = 0, 1, \dots$  are the unknown constants to be determined. The eigenfunction  $\Psi_n$  is orthonormal with respect to the inner product

$$\langle \Psi_n, \Psi_m \rangle = \frac{1}{h} \int_{-h}^0 \Psi_n(z) \Psi_m(z) dz = \delta_{nm}, \quad (6.28)$$

with  $\delta_{nm}$  being the Kronecker delta.

On the other hand, regarding the scattering problem, as described previously for the radiation problem, the velocity potentials are also expanded in terms of appropriate eigenfunctions. These are expressed as follows

$$\phi_1^S(x, z) = B_0^R \cos k_x x \Psi_0(z) + \sum_{n=1}^{\infty} B_n^R \cosh k_{nx} x \Psi_n(z), \quad (6.29a)$$

$$\phi_2^S(x, z) = \left( e^{-ik_x(x-b)} + R e^{ik_x(x-b)} \right) \Psi_0(z) + \sum_{n=1}^{\infty} A_n^R e^{-k_{nx}(x-b)} \Psi_n(z), \quad (6.29b)$$

where the associated eigenvalue and eigenfunction are the same as defined above.

The far-field behaviour of the radiated and scattered potentials are respectively of the form

$$\phi^R \sim A^R e^{ik_x(x-b)} \Psi_0(z), \quad \text{as } x \rightarrow +\infty, \quad (6.30)$$

$$\phi^S \sim \left( e^{-ik_x(x-b)} + R e^{ik_x(x-b)} \right) \Psi_0(z), \quad \text{as } x \rightarrow +\infty, \quad (6.31)$$

where  $A^R$  represents the radiated wave amplitude due to the forcing on the internal free surface, while  $R$  being the scattered wave amplitude with  $|R| = 1$  since due to the OWC structure all the incident wave energy is reflected (Evans and Porter; 1995).

Application of the second matching condition Eq. (6.3) at  $x = b$  with the velocity potentials described by Eqs. (6.25a) and (6.25b), together with the boundary condition at the barrier, Eq. (6.2), applied to both velocity potentials, adding their corresponding results and exploiting the orthonormality of the eigenfunctions as defined in Eq. (6.28), results

$$A^R = iB_0^R \sin k_x b, \quad (6.32a)$$

$$A_m^R = -B_m^R \sinh k_{mx}b, \quad \text{for } m \geq 1. \quad (6.32b)$$

Next, by using the upstream potential, Eq. (6.25b), Eq. (6.2) at  $L_b$  is:

$$ik_x A^R \Psi_0(z) - \sum_{n=1}^{\infty} k_{nx} A_n^R \Psi_n(z) dz = 0 \quad \text{at the barrier} \quad (6.33)$$

and after substituting Eqs. (6.25a) and (6.25b) into the first matching condition Eq. (6.3) and making use of Eqs. (6.32a) and (6.32b), yields

$$(1 + i \cot k_x b) A^R \Psi_0(z) + \sum_{n=1}^{\infty} A_n^R (1 + \coth k_{nx} b) \Psi_n(z) + \frac{1}{K} = 0. \quad (6.34)$$

Equations (6.33) and (6.34) are known as dual series relations (Sneddon; 1966) and can be combined to make a single mixed boundary condition. This condition is expressed as  $F(z) = 0$  for  $-h \leq z \leq 0$ , where

$$F(z) = \begin{cases} ik_x A^R \Psi_0(z) - \sum_{n=1}^{\infty} k_{nx} A_n^R \Psi_n(z) dz & \text{for } -h_a \leq z \leq 0, \\ (1 + i \cot k_x b) A^R \Psi_0(z) + \sum_{n=1}^{\infty} A_n^R (1 + \coth k_{nx} b) \Psi_n(z) + \frac{1}{K} & \text{for } -h \leq z < -h_a. \end{cases} \quad (6.35)$$

To determine the  $A^R$  and  $A_n^R$ , different techniques such as collocation and least squares can be employed (Dalrymple and Martin; 1990). Here, the method of minimal squares is implemented, which requires:

$$\int_{-h}^0 |F(z)|^2 dz \quad \text{to be minimum.} \quad (6.36)$$

Minimizing the above with respect to the  $A_n^R$  leads to the following expression

$$\int_{-h}^0 \bar{F} \frac{\partial F(z)}{\partial A_n^R} dz = 0, \quad \text{for } m \geq 0, \quad (6.37)$$

where  $\bar{F}$  is the complex conjugate of  $F$ . This condition of minimum integral can also expanded as:

$$\int_{-h}^{-h_a} \bar{F} \frac{\partial F(z)}{\partial A_n^R} dz + \int_{-h_a}^0 \bar{F} \frac{\partial F(z)}{\partial A_n^R} dz = 0, \quad \text{for } m \geq 0, \quad (6.38)$$

where from Eq. (6.35), we obtain

$$\frac{\partial F(z)}{\partial A^R} = ik_x \Psi_0(z), \quad \frac{\partial F(z)}{\partial A_n^R} = -k_{nx} \Psi_n(z), \quad \text{for } -h_a \leq z \leq 0, \quad (6.39a)$$

$$\frac{\partial F(z)}{\partial A^R} = (1 + i \cot k_x b) \Psi_0(z), \quad \frac{\partial F(z)}{\partial A_n^R} = (1 + i \coth k_{nx} b) \Psi_n(z), \quad \text{for } -h \leq z < -h_a. \quad (6.39b)$$

CHAPTER 6. THE EFFECT OF OBLIQUE WAVES ON THE HYDRODYNAMIC  
EFFICIENCY OF A LAND-FIXED OWC DEVICE

---

After substituting Eqs. (6.39) and the conjugate of  $F(z)$  from Eq. (6.35), into Eq. (6.38), the following expressions are then obtained:

$$\begin{aligned} \overline{A^R} \left[ \left(1 + \cot^2 k_x b\right) \int_{-h}^{-h_a} \Psi_0(z) \Psi_0(z) dz + k_x^2 \int_{-h_a}^0 \Psi_0(z) \Psi_0(z) dz \right] + \\ \sum_{n=1}^{\infty} \overline{A_n^R} \left[ \left(1 + i \cot k_x b\right) \left(1 + \coth k_{nx} b\right) \int_{-h}^{-h_a} \Psi_n(z) \Psi_0(z) dz + i k_x k_{nx} \int_{-h_a}^0 \Psi_n(z) \Psi_0(z) dz \right] + \\ \frac{1}{K} \left(1 + i \cot k_x b\right) \int_{-h}^{-h_a} \Psi_0(z) dz = 0, \quad (6.40a) \end{aligned}$$

$$\begin{aligned} \overline{A^R} \left[ \left(1 + i \cot k_x b\right) \left(1 + \coth k_{mx} b\right) \int_{-h}^{-h_a} \Psi_0(z) \Psi_m(z) dz - i k_x k_{mx} \int_{-h_a}^0 \Psi_0(z) \Psi_m(z) dz \right] + \\ \sum_{n=1}^{\infty} \overline{A_n^R} \left[ \left(1 + \coth k_{nx} b\right) \left(1 + \coth k_{mx} b\right) \int_{-h}^{-h_a} \Psi_n(z) \Psi_m(z) dz + k_{nx} k_{mx} \int_{-h_a}^0 \Psi_n(z) \Psi_m(z) dz \right] + \\ \frac{1}{K} \left(1 + \cot k_{mx} b\right) \int_{-h}^{-h_a} \Psi_m(z) dz = 0, \quad \text{for } m \geq 1. \quad (6.40b) \end{aligned}$$

By truncating Eqs. (6.40) to  $N_{em}$  terms and solving for the  $N_{em}$  values of  $A_n^R$  simultaneously, a complex  $(N_{em} + 1) \times (N_{em} + 1)$  system of equations for the determination of the unknowns is then obtained. Finally, a similar solution procedure as described above can be used for the scattering problem.

### 6.3.2 Boundary Element Method

#### Boundary integral equation

In this subsection, our focus is the BEM to solve the associated BVP in the frequency domain. The boundary integral equation for the representation of the Helmholtz expression (Eq. 6.1) is given by

$$\alpha(\bar{P})\phi(\bar{P}) + \int_{\Gamma} \phi(\bar{q}) \frac{\partial \psi(\bar{P}, \bar{q})}{\partial n_{\bar{q}}} d\Gamma_{\bar{q}} = \int_{\Gamma} \psi(\bar{P}, \bar{q}) \frac{\partial \phi(\bar{q})}{\partial n_{\bar{q}}} d\Gamma_{\bar{q}}, \quad (6.41)$$

with  $\phi$  being the unknown velocity potential;  $\partial\phi/\partial n$  is the derivative of the potential relative to normal unit vector on the boundary  $\Gamma$ ;  $\bar{P}(x, z)$  and  $\bar{q}(\hat{\xi}, \hat{\eta})$  are, respectively, the source and field points inside the domain  $\Omega$ ;  $d\Gamma$  is the length of an infinitesimal piece of  $\Gamma$ ;  $\psi$  and  $\partial\psi/\partial n$  represent, respectively, the fundamental solution of Helmholtz equation and its normal derivative at point  $\bar{q}$  of the boundary; and the parameter  $\alpha = \vartheta/2\pi$ , with  $\vartheta$  being the angle in radians between points  $\bar{P}$  and  $\bar{q}$  (Katsikadelis; 2002).

The fundamental solution of Helmholtz equation is

$$\psi = \frac{K_0(kr \sin \theta)}{2\pi}, \quad (6.42)$$

where  $K_0$  being the zeroth-order modified Bessel function of the second kind and  $r = \sqrt{(x - \hat{\xi})^2 + (z - \hat{\eta})^2}$  is the distance between the source  $\bar{P}$  and the arbitrary point  $\bar{q}$ . This expression satisfies Eq. (6.1) and it could also have been written in terms of Hankel functions (Brebbia and Dominguez; 1992).

For the case of normal incidence, the spatial velocity potential  $\phi$  satisfies the Laplace equation

$$\frac{\partial^2 \phi}{\partial x^2} + \frac{\partial^2 \phi}{\partial z^2} = 0, \quad (6.43)$$

whose fundamental solution is given by

$$\psi = \frac{1}{2\pi} \ln r. \quad (6.44)$$

### Discretization of the boundary integral equation

By subdividing the boundary of the computational domain into  $NE$  boundary elements, Eq. (6.41) can then be discretized as

$$\alpha^i \phi^i + \sum_{j=1}^{NE} \int_{\Gamma} \phi \frac{\partial \psi}{\partial n} d\Gamma = \sum_{j=1}^{NE} \int_{\Gamma} \psi \frac{\partial \phi}{\partial n} d\Gamma. \quad (6.45)$$

with  $i$  indicating the boundary node, while  $j$  the boundary element. In the above expression, the values of  $\phi$  and  $\partial\phi/\partial n$  are assumed to have a three-noded quadratic variation on each element. For this purpose, these variables are written in terms of interpolation functions,  $\hat{\varphi}_{1,2,3}$ , as a function of a homogeneous coordinate  $\xi$ , thus

$$\phi(\xi) = \hat{\varphi}_1 \phi^1 + \hat{\varphi}_2 \phi^2 + \hat{\varphi}_3 \phi^3, \quad (6.46a)$$

$$\frac{\partial \phi(\xi)}{\partial n} = \hat{\varphi}_1 \frac{\partial \phi^1}{\partial n} + \hat{\varphi}_2 \frac{\partial \phi^2}{\partial n} + \hat{\varphi}_3 \frac{\partial \phi^3}{\partial n}, \quad (6.46b)$$

whilst the variation of the  $x$  and  $z$  coordinates in terms of  $\xi$  is given by

$$x = \hat{\varphi}_1 x^1 + \hat{\varphi}_2 x^2 + \hat{\varphi}_3 x^3, \quad (6.47a)$$

$$z = \hat{\varphi}_1 z^1 + \hat{\varphi}_2 z^2 + \hat{\varphi}_3 z^3, \quad (6.47b)$$

and the interpolation functions are of the form

$$\hat{\varphi}_1 = \frac{1}{2}\xi(\xi - 1), \quad \hat{\varphi}_2 = \frac{1}{2}(1 - \xi)(1 + \xi), \quad \hat{\varphi}_3 = \frac{1}{2}\xi(1 + \xi), \quad (6.48)$$

with  $\xi$  varying from -1 to 1 and where the superscript indicates the number of the node. After using Eqs. (6.46a) and (6.46b), the integrals from Eq. (6.45) can be written as

$$\int_{\Gamma_j} \phi \frac{\partial \psi}{\partial n} d\Gamma = \left[ \int_{\Gamma_j} \hat{\varphi}_1 \frac{\partial \psi}{\partial n} d\Gamma, \quad \int_{\Gamma_j} \hat{\varphi}_2 \frac{\partial \psi}{\partial n} d\Gamma, \quad \int_{\Gamma_j} \hat{\varphi}_3 \frac{\partial \psi}{\partial n} d\Gamma \right] \cdot \begin{Bmatrix} \phi^1 \\ \phi^2 \\ \phi^3 \end{Bmatrix}, \quad (6.49)$$



and

$$\int_{\Gamma_j} \psi \frac{\partial \phi}{\partial n} d\Gamma = \left[ \int_{\Gamma_j} \hat{\varphi}_1 \psi d\Gamma, \int_{\Gamma_j} \hat{\varphi}_2 \psi d\Gamma, \int_{\Gamma_j} \hat{\varphi}_3 \psi d\Gamma \right] \cdot \left\{ \begin{array}{c} \frac{\partial \phi^1}{\partial n} \\ \frac{\partial \phi^2}{\partial n} \\ \frac{\partial \phi^3}{\partial n} \end{array} \right\}. \quad (6.50)$$

To compute the above integrals, the calculation of the Jacobian is required since they are a function of  $\Gamma$ , while the interpolation functions are  $\xi$ -dependent. Thus, we have

$$d\Gamma = \left[ \sqrt{\left(\frac{dx}{d\xi}\right)^2 + \left(\frac{dz}{d\xi}\right)^2} \right] d\xi = |J|d\xi, \quad (6.51)$$

where the Jacobian  $J$  can now be inserted into Eqs. (6.49)-(6.50).

Hence, the discretized boundary integral expression (Eq. 6.45) can be written as

$$\alpha^i \phi^i + \sum_{j=1}^{NE} \left[ h_1^{ij}, h_2^{ij}, h_3^{ij} \right] \cdot \left\{ \begin{array}{c} \phi^1 \\ \phi^2 \\ \phi^3 \end{array} \right\}^j = \sum_{j=1}^{NE} \left[ g_1^{ij}, g_2^{ij}, g_3^{ij} \right] \cdot \left\{ \begin{array}{c} \phi_n^1 \\ \phi_n^2 \\ \phi_n^3 \end{array} \right\}^j, \quad (6.52)$$

with

$$h_k^{ij} = \int_{-1}^1 \hat{\varphi}_k(\xi) \frac{\partial \psi}{\partial n} |J| d\xi, \quad (6.53a)$$

$$g_k^{ij} = \int_{-1}^1 \hat{\varphi}_k(\xi) \psi |J| d\xi, \quad (6.53b)$$

where  $k = 1, 2$  and  $3$ , whilst the integrals  $h_k^{ij}$  and  $g_k^{ij}$  are computed by applying a 10-point Gaussian quadrature rule. Details of the above theory can be found in Dominguez (1993).

We now define the arrangement for fluxes and potentials on each element. As in Dominguez (1993), fluxes hold a unique nodal value on every element so the possibility of having different values between adjoining elements is considered, while velocity potentials always hold a unique value in the connection between two adjoining elements. Hence, fluxes are arranged in a  $3 \times NE$  array while velocity potentials in an  $N$  array, where  $N$  is the number of nodes equal to  $2NE$  for closed boundaries. This leads to the following representation of Eq. (6.52) as

$$\alpha^i \phi^i + \left[ \hat{H}^{i1}, \dots, \hat{H}^{iN} \right] \cdot \left\{ \begin{array}{c} \phi^1 \\ \vdots \\ \phi^N \end{array} \right\}^j = \left[ G^{i1}, \dots, G^{iNE} \right] \cdot \left\{ \begin{array}{c} \left[ \begin{array}{c} \phi_n^1 \\ \phi_n^2 \\ \phi_n^3 \end{array} \right]^1 \\ \vdots \\ \left[ \begin{array}{c} \phi_n^1 \\ \phi_n^2 \\ \phi_n^3 \end{array} \right]^{NE} \end{array} \right\}^j, \quad (6.54)$$

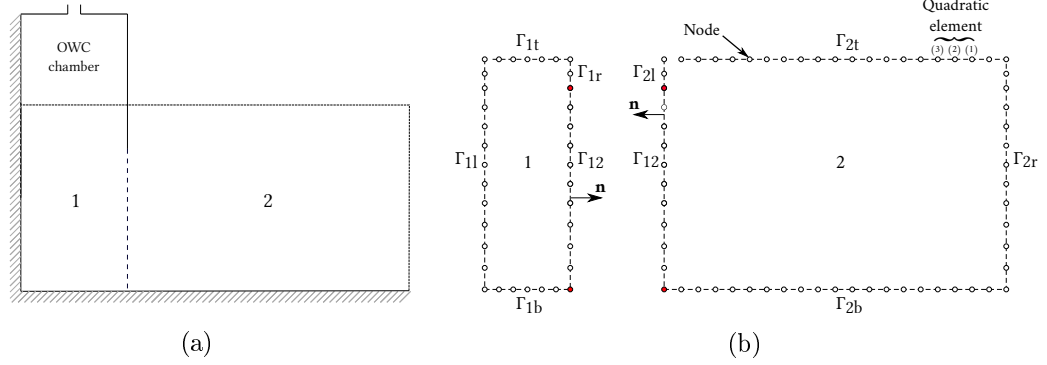


Figure 6.2: BVP discretization. (a) Two-region domain. (b) Discretization of the two regions.

where the coefficients  $\hat{H}^{ij}$  are equal to the  $h_1$  term of a  $j$ -element plus the  $h_3$  term of the  $(j - 1)$ -element for odd nodes, while for central nodes the coefficients  $\hat{H}^{ij}$  are equal to the  $h_2$  term of the corresponding  $j$  element. The coefficients  $G^{ij}$  are  $1 \times 3$  matrices defined by  $\begin{bmatrix} g_1^{ij} & g_2^{ij} & g_3^{ij} \end{bmatrix}$ . Then, Eq. (6.54) can be simplified as

$$\mathbf{H}\Phi = \mathbf{G}\Phi_{\mathbf{n}}, \quad (6.55)$$

with  $\mathbf{H}$  and  $\mathbf{G}$  being square ( $N \times N$ ) and rectangular ( $N \times 3NE$ ) matrixes, respectively, while  $\Phi$  and  $\Phi_{\mathbf{n}}$  are vectors with dimensions  $N \times 1$  and  $3NE \times 1$ , respectively.

### Matching of the subdomains

The two-region domain with a common boundary on the gap below the front barrier is shown in Fig. 6.2a. Following Rezanejad et al. (2013), the method of subdomains is used to match the regions and to avoid numerical instabilities associated with the considered thin front wall of the OWC device. Thus, aiming to match the regions, the continuity of velocity potential and flux at the common interface should be made (Katsikadelis; 2002; Becker; 1992). For this purpose, the nodes in the common interface  $\Gamma_{12}$  of Regions 1 and 2 are assumed to be in perfect contact, Fig. 6.2b. These continuity velocity potential and flux conditions are

$$\Phi_{12}^1 = \Phi_{12}^2. \quad (6.56a)$$

$$\Phi_{\mathbf{n}12}^1 = -\Phi_{\mathbf{n}12}^2, \quad (6.56b)$$

respectively.

Then, boundary conditions defined by Eqs. (6.2), (6.4), (6.6) and (6.7), are inserted into Eq. (6.52) and the known variables are shifted to the right-hand side while the unknowns to the left-hand side. Thus, the following matrix is obtained

$$[A]\{X\} = \{B\}, \quad (6.57)$$

CHAPTER 6. THE EFFECT OF OBLIQUE WAVES ON THE HYDRODYNAMIC EFFICIENCY OF A LAND-FIXED OWC DEVICE

Table 6.2: Values of the maximum hydrodynamic efficiency  $\eta_{max}$ , radiation susceptance coefficient  $\mu$  and radiation conductance coefficient  $\nu$  computed for different number of evanescent modes  $N_{em}$  with  $h_a/h = 0.125$ ,  $b/h = 1.0$  and  $\theta = 0^\circ$ .

$N_{em}$	$Kh = 0.5$			$Kh = 1.5$			$Kh = 2.5$			$Kh = 3.5$		
	$\eta_{max}$	$\mu$	$\nu$	$\eta_{max}$	$\mu$	$\nu$	$\eta_{max}$	$\mu$	$\nu$	$\eta_{max}$	$\mu$	$\nu$
5	0.8324	0.7625	0.7753	0.9884	-0.2205	1.0109	0.5842	-0.4923	0.2230	0.8294	0.0989	0.0993
10	0.8332	0.7657	0.7811	0.9868	-0.2391	1.0282	0.5761	-0.4948	0.2189	0.8042	0.1336	0.1214
20	0.8336	0.7670	0.7837	0.9862	-0.2480	1.0421	0.5728	-0.4964	0.2175	0.7909	0.1726	0.1493
30	0.8343	0.7644	0.7835	0.9864	-0.2474	1.0445	0.5750	-0.4955	0.2185	0.8016	0.1687	0.1518
40	0.8337	0.7672	0.7843	0.9863	-0.2492	1.0505	0.5732	-0.4972	0.2181	0.7945	0.1957	0.1715
50	0.8337	0.7672	0.7843	0.9863	-0.2490	1.0509	0.5733	-0.4976	0.2182	0.7923	0.1990	0.1729
60	0.8337	0.7672	0.7841	0.9864	-0.2484	1.0512	0.5735	-0.4973	0.2184	0.7901	0.2017	0.1739
70	0.8336	0.7671	0.7839	0.9865	-0.2479	1.0513	0.5738	-0.4974	0.2185	0.7890	0.2027	0.1741

where  $[A]$  is a square matrix of dimensions  $N \times N$ ;  $\{X\}$  is a  $N \times 1$  vector containing the unknown values of the velocity potential or fluxes on the boundaries and the common interface; and  $\{B\}$  is a known vector of dimension  $N \times 1$  (Dominguez; 1993).

## 6.4 Convergence study

Before performing the numerical calculations, a convergence analysis for both EEM and BEM was carried out. First, in Table 6.2, the results obtained by the matched EEM for the maximum hydrodynamic efficiency  $\eta_{max}$ , radiation susceptance  $\mu$  and radiation conductance  $\nu$  for different values of the non-dimensional frequency  $Kh (= 0.5, 1.5, 2.5$  and  $3.5)$  are given. The choice of the number of evanescent modes  $N_{em}$  must be done carefully, as small values for  $N_{em}$  lead to truncation errors especially when large incidence wave angles are considered. From Table 6.2 it is observed that around 50-60 evanescent modes are enough to ensure convergence of the analytical results within three decimal places. Thus, in the present calculations,  $N_{em}$  in a range between 50-60 is employed. Then, in Table 6.3, the results of  $\eta_{max}$ ,  $\mu$  and  $\nu$  for the same  $Kh$  values are given for different number of nodes  $N$ . In this case, around 528 nodes (264 quadratic elements) ensure enough convergence of the numerical results within three decimal places. Therefore, 528 nodes are selected to discretize the BVP.

## 6.5 Validation

To validate the analytical and numerical methods described here, the numerical results for the limiting case of Evans and Porter (1995) were used. In Figs. 6.3a and 6.3b, in the case of  $b/h = 1.0$  for  $h_a/h (= 0.125, 0.5)$  and  $h_a/h = 0.5$  for  $b/h (= 0.25, 0.5)$ , respectively, the hydrodynamic efficiency results obtained by the present formulations were compared with the corresponding results of Evans and Porter (1995) for an OWC device with a horizontal topography and normal wave propagation. The black dots in Figs. 6.3 depict the results of Evans and Porter (1995), whereas the blue dashed line represents the results calculated by the

CHAPTER 6. THE EFFECT OF OBLIQUE WAVES ON THE HYDRODYNAMIC EFFICIENCY OF A LAND-FIXED OWC DEVICE

Table 6.3: Values of the maximum hydrodynamic efficiency  $\eta_{max}$ , radiation susceptance coefficient  $\mu$  and radiation conductance coefficient  $\nu$  computed for different number of nodes  $N$  with  $h_a/h = 0.125$ ,  $b/h = 1.0$  and  $\theta = 45^\circ$ .

$N$	$Kh = 0.5$			$Kh = 1.5$			$Kh = 2.5$			$Kh = 3.5$		
	$\eta_{max}$	$\mu$	$\nu$	$\eta_{max}$	$\mu$	$\nu$	$\eta_{max}$	$\mu$	$\nu$	$\eta_{max}$	$\mu$	$\nu$
400	0.6911	1.0190	0.6335	0.9774	0.4341	1.4103	0.9283	-0.6068	1.0516	0.5964	-0.5430	0.2549
432	0.6914	1.0151	0.6317	0.9776	0.4309	1.4058	0.9277	-0.6063	1.0455	0.5950	-0.5404	0.2526
464	0.6917	1.0118	0.6302	0.9777	0.4281	1.4021	0.9271	-0.6058	1.0403	0.5938	-0.5382	0.2507
496	0.6920	1.0090	0.6290	0.9779	0.4258	1.3988	0.9267	-0.6054	1.0358	0.5927	-0.5363	0.2490
528	0.6922	1.0066	0.6279	0.9780	0.4238	1.3960	0.9263	-0.6050	1.0320	0.5919	-0.5346	0.2476
560	0.6924	1.0045	0.6270	0.9781	0.4220	1.3936	0.9259	-0.6046	1.0287	0.5911	-0.5332	0.2464

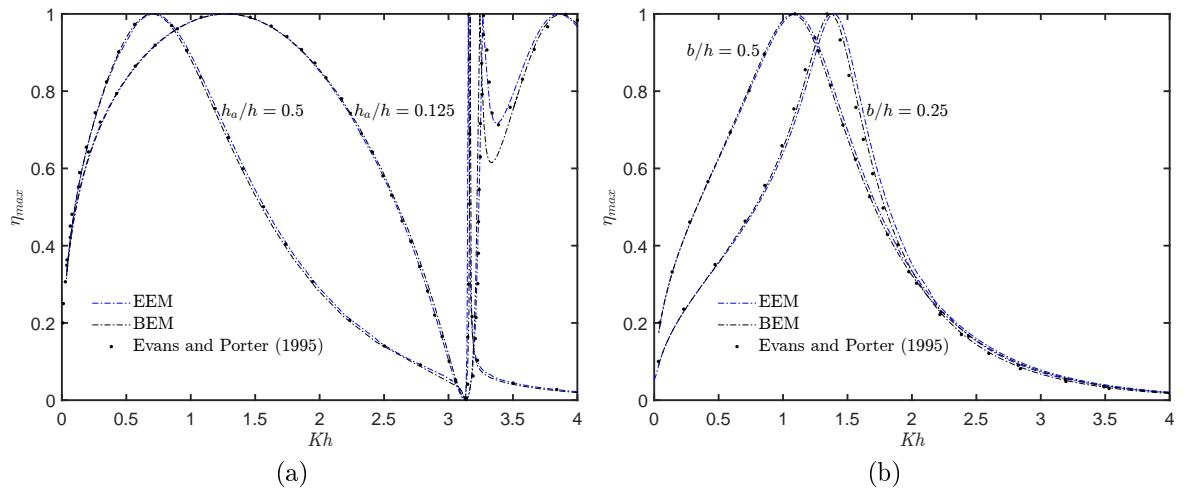


Figure 6.3: Maximum hydrodynamic efficiency versus non-dimensional frequencies  $Kh$  with  $\theta = 0^\circ$ . Comparison with previous results obtained by [Evans and Porter \(1995\)](#) (a) For  $b/h = 1.0$  and  $h_a/h = 0.125$  and  $0.5$ . (b) For  $h_a/h = 0.5$  and  $b/h = 0.25$  and  $0.5$ .

EEM and the black dashed line the results obtained by the BEM. It can be seen that in both figures the results are in good agreement.

## 6.6 Results and Discussion

In this section, numerical results based on previously discussed EEM and BEM are presented. The effects of the incidence wave angle, the chamber configuration and the linearized air compressibility on the maximum hydrodynamic efficiency are commented. In the case of the BEM, to minimize the effect of local disturbances at the far-field boundary, a distance of 4 times the water depth  $h$  between the front barrier and the far-field boundary was considered. In both formulations, the water depth was 7.90 m as in [Medina Rodríguez et al. \(2020\)](#) with a wave period  $T$  bounded by  $2.50 \leq T \leq 30$  s.

### 6.6.1 Effect of the angle of incidence

The analytical and numerical results of the maximum hydrodynamic efficiency  $\eta_{max}$  versus the non-dimensional frequency  $Kh$  for different angles of incidence  $\theta$  ( $= 15^\circ, 30^\circ, 45^\circ, 60^\circ$  and  $75^\circ$ ) are shown in Figs. 6.4a–c. In these figures, it is observed that the greater the angle of incidence  $\theta$ , the smaller the incoming wave period at which the OWC resonates. It is also observed that with an increase in  $\theta$ , the bandwidth of the efficiency curves is increased. This aspect of the efficiency curves may be beneficial when selecting the location of an integrated OWC-breakwater system. In practice, an OWC device with a range of frequency bandwidth coincident with the most predominant wave period and direction of a particular location can make better use of the available wave energy. On the other hand, it is observed that, in general, the analytical and numerical results are in good agreement, especially for small frequencies and when a short wave angle of incidence is considered.

The variations of the maximum hydrodynamic efficiency versus the angle of incidence  $\theta$  in the range of  $0^\circ \leq \theta \leq 90^\circ$  for different values of  $Kh$  ( $= 0.625, 1.25$  and  $2.50$ ) are shown in Figs. 6.5a–c. It is observed that for small frequencies,  $\eta_{max}$  drops as  $\theta$  tends to  $90^\circ$ , while for large values of  $Kh$ , the curves first increase up to a peak and then drop. Furthermore, as expected, the maximum hydrodynamic efficiency becomes zero when  $\theta = 90^\circ$  due to the null excitation of the inside water column by the parallel incident waves.

The analytical results of  $\eta_{max}$  versus the non-dimensional frequency  $Kh$  and the angle of incidence  $\theta$  are shown in Figs. 6.6a–f. In these figures, the previous results from Figs. 6.4 and 6.5 are also shown with their corresponding curves and labels. First, in Figs. 6.6a–b, two zones with high values of the hydrodynamic efficiency are observed. The first one, with a boomerang-shaped, is due to large motions in the internal water column that occur when the fluid is excited by the incident wave into a resonant piston-like motion (Evans and Porter; 1995). This red-big zone of peak hydrodynamic efficiency may provide valuable information for the efficient harnessing of wave energy of OWC devices since, as previously mentioned, an integrated OWC-breakwater system can be designed to coincide with the prevailing wave climate of a particular location and thus to optimize the use of the available wave energy resource. On the other hand, the second red zone, located on the left corner for relatively small angles of incidence ( $0^\circ \leq \theta \leq 40^\circ$ ), is due to the excitation into an antisymmetric sloshing mode on the internal free surface produced by the incident wave frequency. In this situation, the sloshing frequencies occur at values of the dimensionless wavenumber  $kb = n\pi$ , with  $n$  being the sloshing mode. For this case, it is observed that this peak in  $\eta_{max}$  due to the first sloshing frequency occurs close to  $Kh \approx \pi$ .

Then, in Figs. 6.6c–d for  $h_a/h = 0.25$  with  $b/h = 0.5$  and Figs. 6.6e–f for  $h_a/h = 0.5$  with  $b/h = 0.75$  a single red zone of high maximum hydrodynamic efficiency is observed. In comparison with the one observed in Figs. 6.6a–b, these two red areas are smaller. This is because a higher front wall draft to water depth ratios  $h_a/h$  were considered, and a smaller gap leads to a narrower range of frequency bandwidth as it reduces the energy transfer near the free surface due to wave motion.

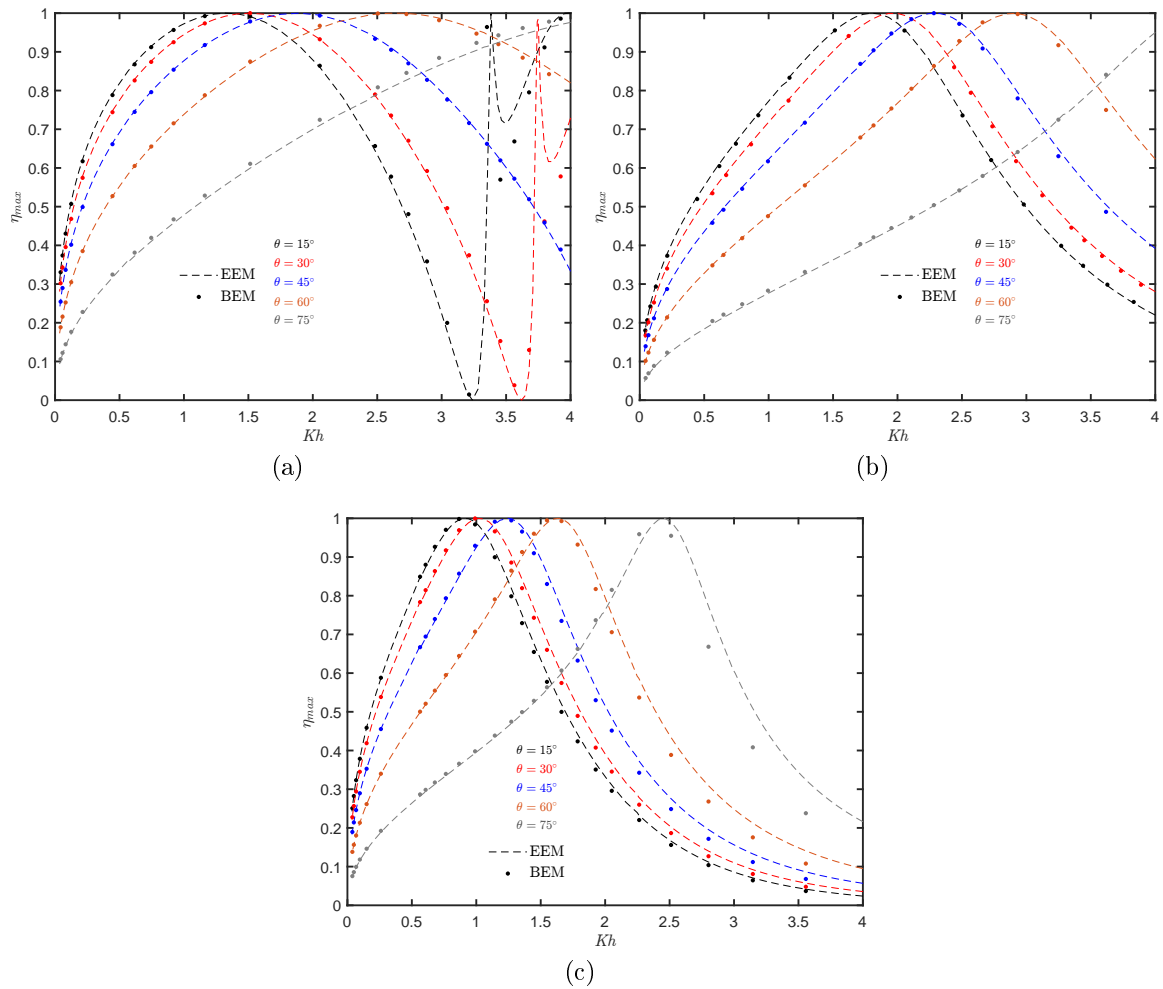


Figure 6.4: Maximum hydrodynamic efficiency versus  $Kh$  for different incidence wave angles  $\theta$ . (a) For  $h_a/h = 0.125$  and  $b/h = 1.0$ . (b) For  $h_a/h = 0.25$  and  $b/h = 0.5$ . (c) For  $h_a/h = 0.5$  and  $b/h = 0.75$ .

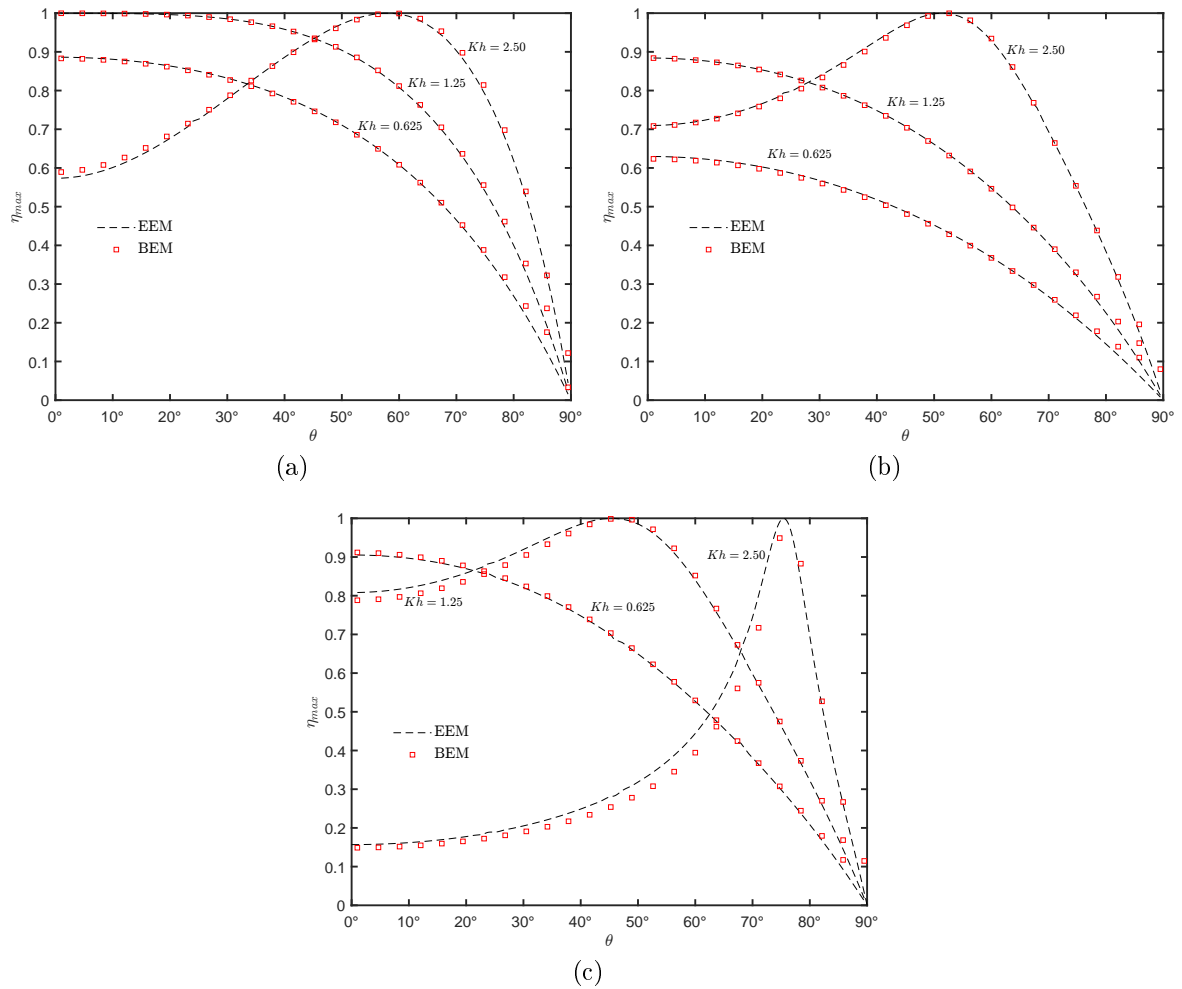


Figure 6.5: Maximum hydrodynamic efficiency versus  $\theta$  with  $Kh = 0.625, 1.25$  and  $2.50$ . (a) For  $h_a/h = 0.125$  and  $b/h = 1.0$ . (b) For  $h_a/h = 0.25$  and  $b/h = 0.5$ . (c) For  $h_a/h = 0.5$  and  $b/h = 0.75$ .

CHAPTER 6. THE EFFECT OF OBLIQUE WAVES ON THE HYDRODYNAMIC EFFICIENCY OF A LAND-FIXED OWC DEVICE

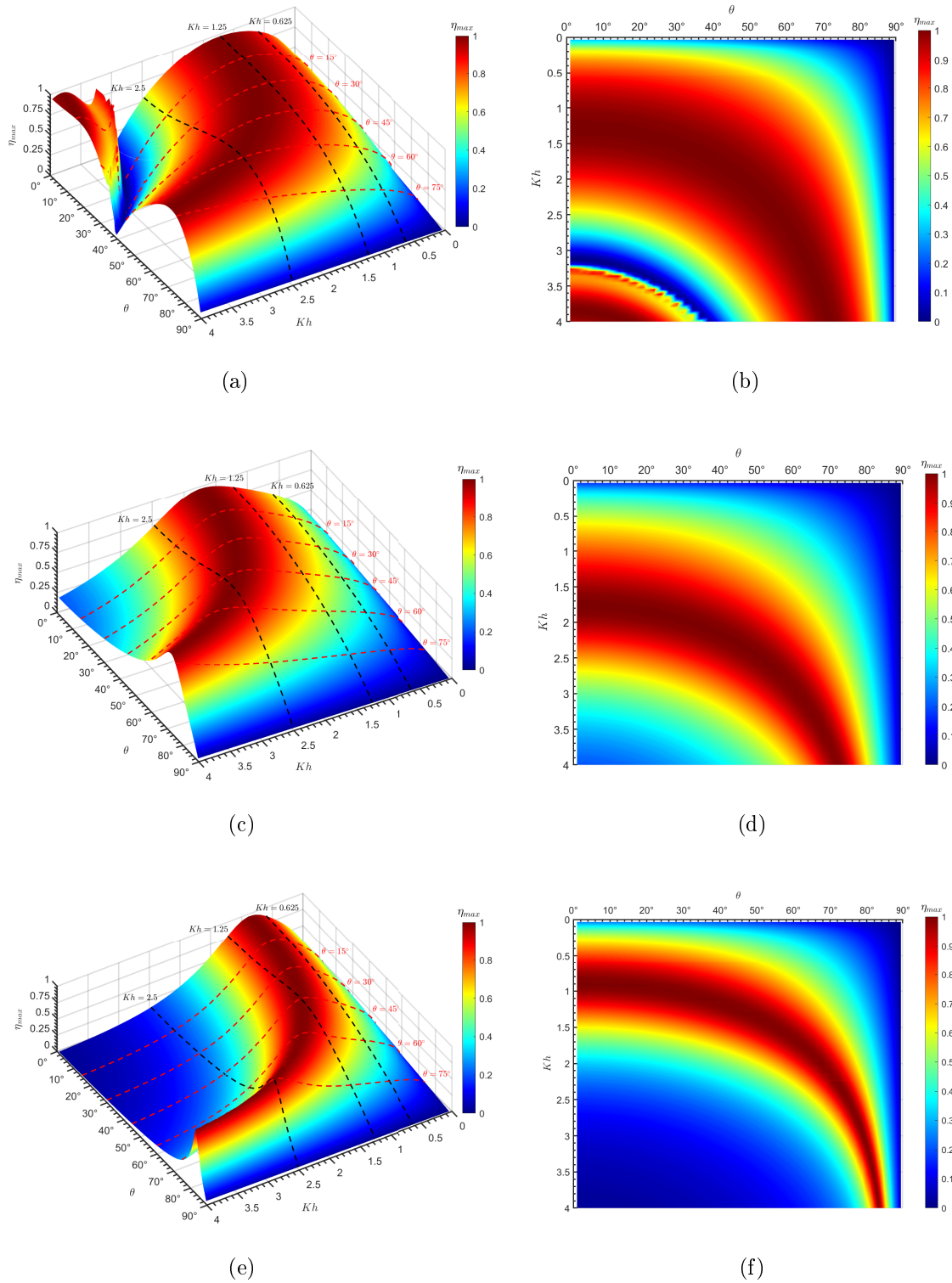


Figure 6.6: Maximum hydrodynamic efficiency as function of  $\theta$  and  $Kh$ . (a)-(b) For  $h_a/h = 0.125$  and  $b/h = 1.0$ . (c)-(d) For  $h_a/h = 0.25$  and  $b/h = 0.5$ . (e)-(f) For  $h_a/h = 0.5$  and  $b/h = 0.75$ .



### 6.6.2 Effect of the chamber configuration

Figures 6.7a, c and e plot the results of  $\eta_{max}$  versus the non-dimensional frequency  $Kh$  for various wall-to-front barrier spacing ratios  $b/h$  ( $= 1, 1/2, 1/4$  and  $1/8$ ). Similar to the case when normal wave incidence is considered (Evans and Porter; 1995), in these plots, it is observed that for a longer chamber relative to the water depth, the frequency at which resonance occurs is smaller. This is because, with an increase in the OWC chamber length, the water particle motions inside the chamber during one period of motion also increase, thus decreasing the value of the non-dimensional frequency  $Kh$  at which resonance occurs. As previously reported by Evans and Porter (1995) and Rezanejad et al. (2013), large heaving motions inside the chamber occur when the internal water column is excited by the incident wave into a resonant piston-type motion. For normal incidence, the natural frequency of these large oscillations can be reasonably estimated for small values of  $b/h$ , so the water contained inside the chamber can be regarded as a solid body. By using a simple hydrostatic approach, it results that the expected resonance occurs at  $Kh \approx h/h_a$ . These resonances are supposed to occur at  $Kh = 8$ ,  $Kh = 4$  and  $Kh = 2$ , for Figs. 6.7a, c and e, respectively. On the other hand, Figs. 6.7b, d and f show the results of  $\eta_{max}$  versus the non-dimensional frequency  $Kh$  for different submergence ratios  $h_a/h$  ( $= 0.125, 0.25, 0.5$  and  $0.75$ ). Similar to the case when  $b/h$  increases, when the front wall draft to water depth ratio  $h_a/h$  increases, it allows a larger fluid motion inside the chamber and the vertical distance a water fluid particle must travel during a period of oscillation increases; therefore, the frequency at which resonance occurs is smaller.

### 6.6.3 Influence of the trapped air inside the OWC chamber

The analytical and numerical results for the maximum hydrodynamic efficiency versus  $Kh$  for different air column height to chamber length ratio  $h_c/b$  ( $= 0.5, 1.0$  and  $1.5$ ) are shown in Fig. 6.8a. For the calculation of the trapped air volume  $V_0$ , the chamber width was kept fixed during the calculations and, based on the physical dimensions of a single chamber of the MWEP (Medina Rodríguez et al.; 2020), a value of 1.5 times  $b$  was considered. In Fig. 6.8a, it is found that as  $h_c/b$  increases, the overall hydrodynamic efficiency decreases; in other words, as air compressibility (accounted for by the isentropic model) is taken into account, less energy from the waves is absorbed. This can also be clearly inferred from Eq. (6.23), where it is seen that as the air volume inside the chamber increases, the optimum damping induced to the airflow by the linear turbine also increases, and hence  $\eta_{max}$  decreases.

Since air compressibility in the OWC chamber is known to greatly affect the power output of full-sized devices, it must be addressed in all the preliminary stages of OWC system design (Falcão and Henriques; 2019). The effect of air compressibility is known to increase with chamber height above the water free surface, so it should not be neglected in full-scale devices with chamber heights of several meters (Sarmiento and Falcão; 1985) since significant errors in determining the device performance may result (López et al.; 2020). However, as explained by Sarmiento and Falcão (1985), it should be pointed out that due to viscous losses in the flow through the turbine, air compression and expansion are more complicated and likely to deviate considerably from an isentropic process, as considered in this work.

CHAPTER 6. THE EFFECT OF OBLIQUE WAVES ON THE HYDRODYNAMIC EFFICIENCY OF A LAND-FIXED OWC DEVICE

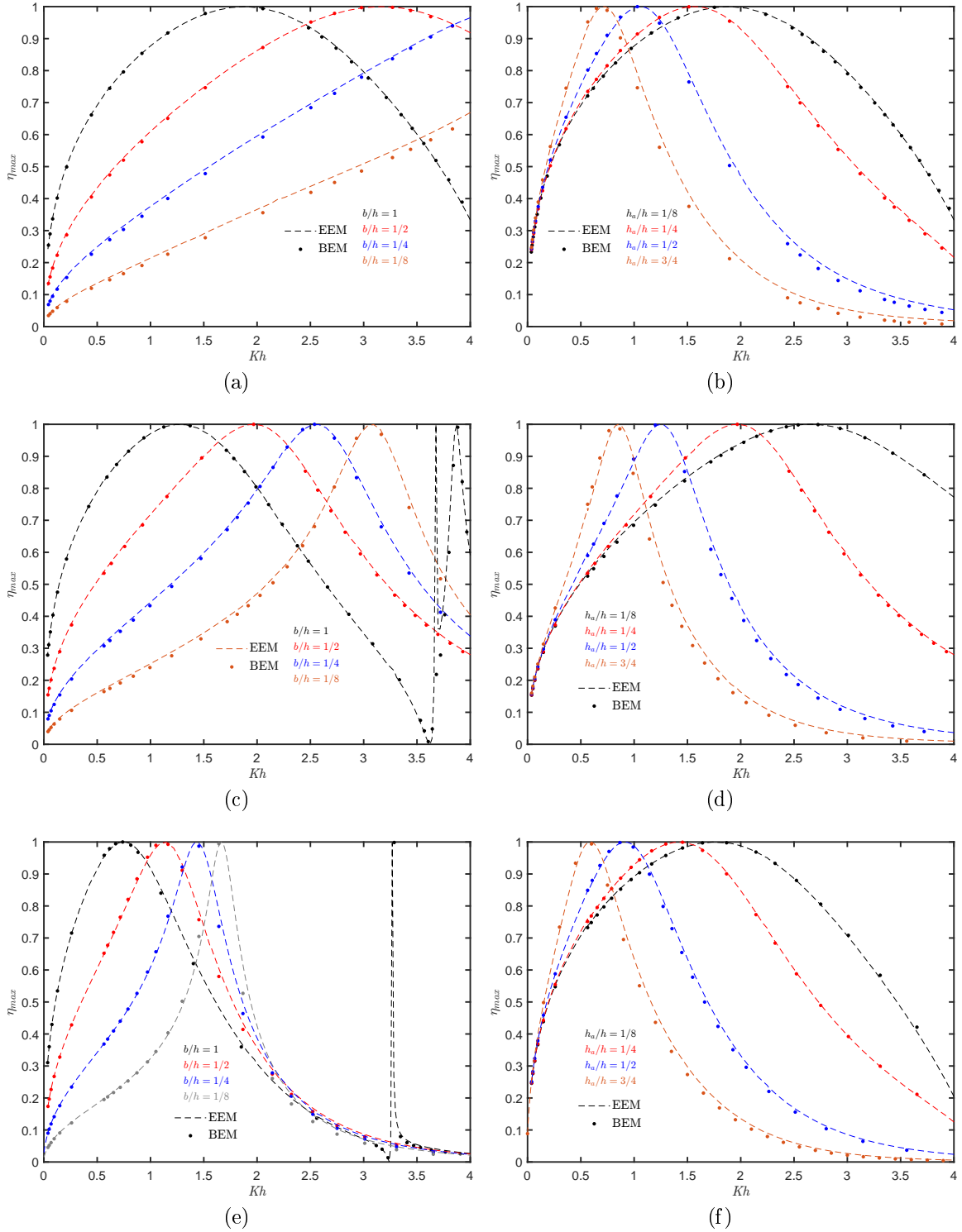


Figure 6.7: Maximum hydrodynamic efficiency versus  $Kh$  for different wall to front barrier spacing ratios  $b/h$  and for different submergence ratios  $h_a/h$ . (a) For  $h_a/h = 0.125$  and  $\theta = 45^\circ$ . (b) For  $b/h = 1.0$  and  $\theta = 45^\circ$ . (c) For  $h_a/h = 0.25$  and  $\theta = 30^\circ$ . (d) For  $b/h = 0.5$  and  $\theta = 30^\circ$ . (e) For  $h_a/h = 0.5$  and  $\theta = 15^\circ$ . (f) For  $b/h = 0.75$  and  $\theta = 15^\circ$ .

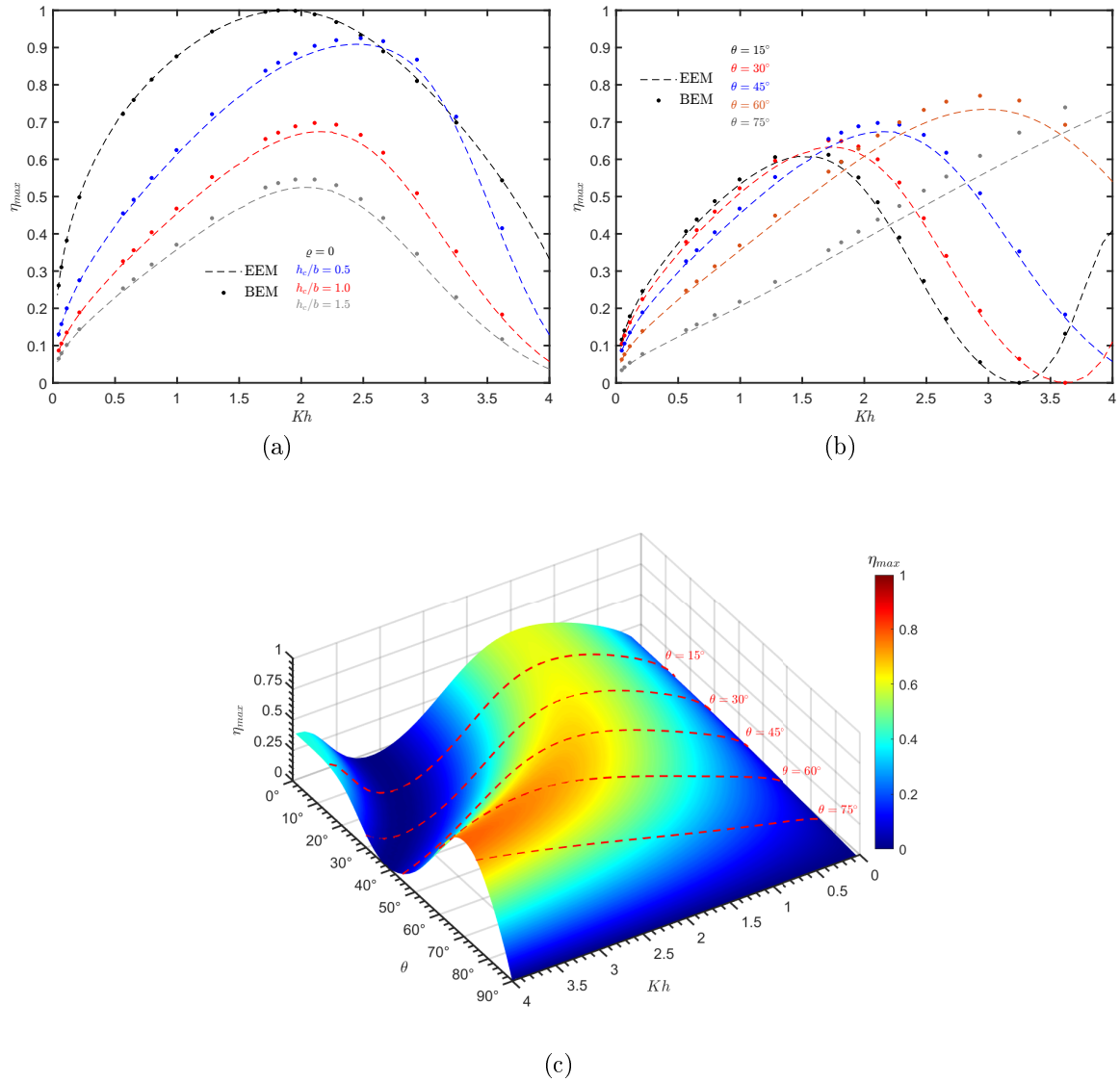


Figure 6.8: Maximum hydrodynamic efficiency with  $h_a/h = 0.125$  and  $b/h = 1.0$ . (a) Versus  $Kh$  for different air column ratios  $h_c/b$  and  $\theta = 45^\circ$ . (b) Versus  $Kh$  for different angles of incidence  $\theta$  with  $h_c/b = 1.0$ . (c) Versus  $Kh$  and  $\theta$  with  $h_c/b = 1.0$ .

On the other hand, in Fig. 6.8b, the hydrodynamic efficiency versus  $Kh$  for different values of the wave angle of incidence  $\theta$  ( $= 15^\circ, 30^\circ, 45^\circ, 60^\circ$  and  $75^\circ$ ) with  $h_c/b = 1.0$  is shown. As in Fig. 6.4a, it is observed that the efficiency band increases when  $\theta$  increases, with a positive sloped trend for very high angles. Additionally, under the influence of linear air compressibility, numerical and analytical results in Fig. 6.8b show that the maximum hydrodynamic efficiency peak value decreases when less oblique water waves interact with the OWC chamber. Finally, Fig. 6.8c shows the analytical results for the variation of the maximum hydrodynamic efficiency as a function of the angle of incidence  $\theta$  and the non-dimensional frequency  $Kh$ , together with the curves from Fig. 6.8b for  $h_c/b = 1.0$ . Compared with Fig. 6.6a, in Fig. 6.8c it is easier to observe the damping effect of the linearised air compressibility on the efficiency since the peaks on  $\eta_{max}$  are significantly reduced when the phenomena of resonance due to the excitation of the OWC and sloshing occur.

As mentioned before, a theoretical value of  $\eta_{max} = 1$  means that the OWC device successfully captures all the incident wave energy. However, this is not achievable in practice, since dissipative energy processes such as the generation of radiated waves by the oscillatory water motion inside the chamber, the scattering of waves produced by the water waves-OWC device interaction, viscous dampings, among others, occur (Ning et al.; 2015). In this sense, investigations such as those carried out by Ning et al. (2015); Ning, Wang, Zou and Teng (2016); Ning, Wang, Gou, Zhao and Teng (2016); Wang et al. (2018); Wang and Ning (2020) have satisfactorily accounted for the energy losses due to vortex shedding and flow separation, which occurs near the front wall, by introducing an artificial viscous damping term into the dynamic free surface boundary condition inside the OWC chamber.

## 6.7 Conclusions

The effects on the maximum hydrodynamic efficiency due to the wave angle of incidence and the chamber configuration of an OWC device were analyzed. The matched EEM using dual series relations and the BEM with three-noded quadratic elements were employed to solve the associated BVP. Comparisons were performed between these two methods and an optimal agreement was achieved, especially for relatively small angles of incidence. Apart from its simplicity, the use of the least-squares technique for solving the dual series relations demonstrates to be an efficient method for the calculation of the hydrodynamic efficiency of an OWC device when a thin front wall is considered. However, the choice of evanescent modes in the EEM must be done carefully, as a small number of them may lead to truncation errors when large angles of incidence at high frequencies are considered. Furthermore, the theoretical cases addressed by Evans and Porter (1995) for a thin front wall in the case of normal wave incidence were satisfactorily recovered by both analytical and numerical formulations. Analytical and numerical calculations for the maximum hydrodynamic efficiency were then obtained and analyzed for different physical configurations.

The results revealed that by increasing the wave angle of incidence, the bandwidth of the efficiency curves and the wave frequency at which resonance occurs both increase. This can be an important characteristic for the wave energy extraction since in a real scenario OWC

devices receive incoming waves at varying angle. As expected, it was observed that for water wave propagation parallel with respect to the OWC chamber, the maximum hydrodynamic efficiency is zero due to the null excitation of the internal water column by the parallel incident waves. Furthermore, it was observed a significant area of high hydrodynamic efficiency that provides the possibility of a more efficient wave energy extraction depending on the diverse incoming wave directions and frequencies of a particular site. The effect of the air volume inside the chamber was analyzed by modifying the trapped air volume and it was found that the maximum hydrodynamic efficiency is reduced when the air volume increases. For oblique waves, when the OWC chamber length-water depth ratio ( $b/h$ ) is decreased, the wave period of maximum hydrodynamic efficiency is shorter, a similar trend to that reported by [Evans and Porter \(1995\)](#) for normal wave incidence. Regarding the effect of the front wall draft, the maximum hydrodynamic efficiency bandwidth significantly increases when the front wall draft to water depth ratio ( $h_a/h$ ) decreases.

Additionally, special consideration should be given to the fact that a thin front barrier was considered in this work. In practice, thin front barriers cannot provide protection to OWC systems since they are continuously subjected to high loads due to direct wave action, especially during severe storm events and times of high water levels ([Viviano et al.; 2016](#); [Pawitan et al.; 2019](#); [Viviano et al.; 2019](#); [Pawitan et al.; 2020](#); [Medina-Lopez et al.; 2015](#)). This paper is only an analytical and numerical investigation on the OWC hydrodynamic performance based on linear wave theory. Further theoretical investigations and experimental campaigns that include other geometrical aspects, energy losses through viscous dissipation, non-linearities on the air compressibility and the turbine damping should be carried out in the future. Finally, it is hoped that the results of this work may encourage the further study of the OWC technology and provide valuable information for efficient wave energy harnessing.

## Bibliography

- Abul-Azm, A. (1996). Wave diffraction through submerged flexible breakwaters, *Ocean Engineering* **23**(5): 403–422.  
**URL:** <http://www.sciencedirect.com/science/article/pii/0029801895000453>
- Becker, A. (1992). *The Boundary Element Method in Engineering: A Complete Course*, McGraw-Hill.  
**URL:** <https://books.google.com.mx/books?id=Co9YAAAAYAAJ>
- Belibassakis, K., Magkouris, A. and Rusu, E. (2020). A BEM for the hydrodynamic analysis of oscillating water column systems in variable bathymetry, *Energies* **13**(13): 3403.
- Brebbia, C. and Dominguez, J. (1992). *Boundary Elements: An Introductory Course*, Computational Mechanics Publications.  
**URL:** [https://books.google.com.mx/books?id=X\\_ceAQAAIAAJ](https://books.google.com.mx/books?id=X_ceAQAAIAAJ)
- Choudhary, A. and Martha, S. (2016). Diffraction of surface water waves by an undulating bed

CHAPTER 6. THE EFFECT OF OBLIQUE WAVES ON THE HYDRODYNAMIC EFFICIENCY OF A LAND-FIXED OWC DEVICE

---

- topography in the presence of vertical barrier, *Ocean Engineering* **122**: 32–43.  
**URL:** <http://www.sciencedirect.com/science/article/pii/S0029801816301925>
- Choudhary, A. and Martha, S. (2017). Approximate solutions of some problems of scattering of surface water waves by vertical barriers, *Sādhanā* **42**: 759–768.
- Dalrymple, R. A. and Martin, P. A. (1990). Wave diffraction through offshore breakwaters, *Journal of Waterway, Port, Coastal, and Ocean Engineering* **116**(6): 727–741.  
**URL:** <https://ascelibrary.org/doi/abs/10.1061/%28ASCE%290733-950X%281990%29116%3A6%28727%29>
- Dominguez, J. (1993). *Boundary Elements in Dynamics*, Computational Engineering, Computational Mechanics Publications.  
**URL:** <https://books.google.com.mx/books?id=N4ghw092NIMC>
- Şentürk, U. and Özdamar, A. (2012). Wave energy extraction by an oscillating water column with a gap on the fully submerged front wall, *Applied Ocean Research* **37**: 174 – 182.  
**URL:** <http://www.sciencedirect.com/science/article/pii/S0141118712000405>
- Evans, D. and Porter, R. (1995). Hydrodynamic characteristics of an oscillating water column device, *Applied Ocean Research* **17**(3): 155 – 164.  
**URL:** <http://www.sciencedirect.com/science/article/pii/0141118795000089>
- Evans, D. V. (1982). Wave-power absorption by systems of oscillating surface pressure distributions, *Journal of Fluid Mechanics* **114**: 481–499.
- Falcão, A. F. and Henriques, J. C. (2016). Oscillating-water-column wave energy converters and air turbines: A review, *Renewable Energy* **85**: 1391 – 1424.  
**URL:** <http://www.sciencedirect.com/science/article/pii/S0960148115301828>
- Falcão, A. F. and Henriques, J. C. (2019). The spring-like air compressibility effect in oscillating-water-column wave energy converters: Review and analyses, *Renewable and Sustainable Energy Reviews* **112**: 483–498.  
**URL:** <https://www.sciencedirect.com/science/article/pii/S1364032119302527>
- Feinerman, R. P. and Kelman, R. B. (1974). The convergence of least squares approximations for dual orthogonal series, *Glasgow Mathematical Journal* **15**(1): 82–84.
- Ibarra-Berastegi, G., Sáenz, J., Ulazia, A., Serras, P., Esnaola, G. and Garcia-Soto, C. (2018). Electricity production, capacity factor, and plant efficiency index at the mutriku wave farm (2014–2016), *Ocean Engineering* **147**: 20 – 29.  
**URL:** <http://www.sciencedirect.com/science/article/pii/S0029801817306157>
- Izquierdo, U., Esteban, G. A., Blanco, J. M., Albaina, I. and Peña, A. (2019). Experimental validation of a cfd model using a narrow wave flume, *Applied Ocean Research* **86**: 1 – 12.  
**URL:** <http://www.sciencedirect.com/science/article/pii/S0141118718304772>

CHAPTER 6. THE EFFECT OF OBLIQUE WAVES ON THE HYDRODYNAMIC EFFICIENCY OF A LAND-FIXED OWC DEVICE

---

- Jin, J., Liu, Z., Hyun, B.-S. and Hong, K. (2012). Effects of wave direction on performance of oscillating water column type wave energy convertor, *Proceedings of the International Offshore and Polar Engineering Conference* pp. 582–587.
- John Ashlin, S., Sundar, V. and Sannasiraj, S. (2016). Effects of bottom profile of an oscillating water column device on its hydrodynamic characteristics, *Renewable Energy* **96**: 341 – 353.  
URL: <http://www.sciencedirect.com/science/article/pii/S0960148116303937>
- Katsikadelis, J. (2002). *Boundary Elements. Theory and Applications*, Elsevier.
- Kelman, R. B. and Koper, C. A. (1973). Least squares approximations for dual trigonometric series, *Glasgow Mathematical Journal* **14**(2): 111–119.
- Koley, S. and Trivedi, K. (2020). Mathematical modeling of oscillating water column wave energy converter devices over the undulated sea bed, *Engineering Analysis with Boundary Elements* **117**: 26 – 40.  
URL: <http://www.sciencedirect.com/science/article/pii/S0955799720300801>
- Lee, M. M. and Chwang, A. T. (2000). Scattering and radiation of water waves by permeable barriers, *Physics of Fluids* **12**(1): 54–65.  
URL: <https://doi.org/10.1063/1.870284>
- Lin, Y., Bao, J., Liu, H., Li, W., Tu, L. and Zhang, D. (2015). Review of hydraulic transmission technologies for wave power generation, *Renewable & Sustainable Energy Reviews* **50**: 194 – 203.  
URL: <http://www.sciencedirect.com/science/article/pii/S1364032115004116>
- Losada, I. J., Losada, M. A. and Roldán, A. J. (1992). Propagation of oblique incident waves past rigid vertical thin barriers, *Applied Ocean Research* **14**(3): 191 – 199.  
URL: <http://www.sciencedirect.com/science/article/pii/014111879290014B>
- López, I., Carballo, R., Taveira-Pinto, F. and Iglesias, G. (2020). Sensitivity of owc performance to air compressibility, *Renewable Energy* **145**: 1334–1347.  
URL: <https://www.sciencedirect.com/science/article/pii/S0960148119309048>
- Malara, G., Gomes, R., Arena, F., Henriques, J., Gato, L. and Falcão, A. (2017). The influence of three-dimensional effects on the performance of u-type oscillating water column wave energy harvesters, *Renewable Energy* **111**: 506 – 522.  
URL: <http://www.sciencedirect.com/science/article/pii/S0960148117303452>
- Martins-rivas, H. and Mei, C. C. (2009). Wave power extraction from an oscillating water column along a straight coast, *Ocean Engineering* **36**(6): 426 – 433.  
URL: <http://www.sciencedirect.com/science/article/pii/S002980180900002X>
- Medina-Lopez, E., Allsop, W., Dimakopoulos, A. and Bruce, T. (2015). *Conjectures on the Failure of the OWC Breakwater at Mutriku*, pp. 592–603.  
URL: <https://ascelibrary.org/doi/abs/10.1061/9780784480304.063>

CHAPTER 6. THE EFFECT OF OBLIQUE WAVES ON THE HYDRODYNAMIC EFFICIENCY OF A LAND-FIXED OWC DEVICE

---

- Medina Rodríguez, A. A., Blanco Ilzarbe, J. M., Silva Casarín, R. and Izquierdo Ereño, U. (2020). The influence of the chamber configuration on the hydrodynamic efficiency of oscillating water column devices, *Journal of Marine Science and Engineering* **8**(10): 751.
- Michele, S., Renzi, E., Perez-Collazo, C., Greaves, D. and Iglesias, G. (2019). Power extraction in regular and random waves from an owc in hybrid wind-wave energy systems, *Ocean Engineering* **191**: 106519.  
**URL:** <http://www.sciencedirect.com/science/article/pii/S0029801819306572>
- Morris-Thomas, M. T., Irvin, R. J. and Thiagarajan, K. P. (2006). An Investigation Into the Hydrodynamic Efficiency of an Oscillating Water Column, *Journal of Offshore Mechanics and Arctic Engineering* **129**(4): 273–278.  
**URL:** <https://doi.org/10.1115/1.2426992>
- Ning, D.-Z., Shi, J., Zou, Q.-P. and Teng, B. (2015). Investigation of hydrodynamic performance of an owc (oscillating water column) wave energy device using a fully nonlinear hobem (higher-order boundary element method), *Energy* **83**: 177 – 188.  
**URL:** <http://www.sciencedirect.com/science/article/pii/S0360544215001644>
- Ning, D.-Z., Wang, R.-Q., Gou, Y., Zhao, M. and Teng, B. (2016). Numerical and experimental investigation of wave dynamics on a land-fixed owc device, *Energy* **115**: 326 – 337.  
**URL:** <http://www.sciencedirect.com/science/article/pii/S0360544216312324>
- Ning, D.-Z., Wang, R.-Q., Zou, Q.-P. and Teng, B. (2016). An experimental investigation of hydrodynamics of a fixed owc wave energy converter, *Applied Energy* **168**: 636 – 648.  
**URL:** <http://www.sciencedirect.com/science/article/pii/S0306261916300952>
- Pawitan, K. A., Dimakopoulos, A. S., Vicinanza, D., Allsop, W. and Bruce, T. (2019). A loading model for an owc caisson based upon large-scale measurements, *Coastal Engineering* **145**: 1 – 20.  
**URL:** <http://www.sciencedirect.com/science/article/pii/S0378383918302114>
- Pawitan, K. A., Vicinanza, D., Allsop, W. and Bruce, T. (2020). Front wall and in-chamber impact loads on a breakwater-integrated oscillating water column, *Journal of Waterway, Port, Coastal, and Ocean Engineering* **146**(5): 04020037.  
**URL:** <https://ascelibrary.org/doi/abs/10.1061/%28ASCE%29WW.1943-5460.0000595>
- Rezanejad, K., Bhattacharjee, J. and Guedes Soares, C. (2013). Stepped sea bottom effects on the efficiency of nearshore oscillating water column device, *Ocean Engineering* **70**: 25 – 38.  
**URL:** <http://www.sciencedirect.com/science/article/pii/S0029801813002229>
- Rezanejad, K., Guedes Soares, C., López, I. and Carballo, R. (2017). Experimental and numerical investigation of the hydrodynamic performance of an oscillating water column wave energy converter, *Renewable Energy* **106**: 1 – 16.  
**URL:** <http://www.sciencedirect.com/science/article/pii/S0960148117300034>



CHAPTER 6. THE EFFECT OF OBLIQUE WAVES ON THE HYDRODYNAMIC EFFICIENCY OF A LAND-FIXED OWC DEVICE

---

- Sahoo, T., Lee, M. M. and Chwang, A. T. (2000). Trapping and generation of waves by vertical porous structures, *Journal of Engineering Mechanics* **126**(10): 1074–1082.  
**URL:** <https://ascelibrary.org/doi/abs/10.1061/%28ASCE%290733-9399%282000%29126%3A10%281074%29>
- Sarmiento, A. J. N. A. and Falcão, A. F. d. O. (1985). Wave generation by an oscillating surface-pressure and its application in wave-energy extraction, *Journal of Fluid Mechanics* **150**: 467–485.
- Sneddon, I. (1966). *Mixed boundary value problems in potential theory*, North Holland Publishing Co. Amsterdam, The Netherlands,.
- Vicinanza, D., Lauro, E. D., Contestabile, P., Gissoni, C., Lara, J. L. and Losada, I. J. (2019). Review of innovative harbor breakwaters for wave-energy conversion, *Journal of Waterway, Port, Coastal, and Ocean Engineering* **145**(4): 03119001.  
**URL:** <https://ascelibrary.org/doi/abs/10.1061/%28ASCE%29WW.1943-5460.0000519>
- Viviano, A., Musumeci, R. E., Vicinanza, D. and Foti, E. (2019). Pressures induced by regular waves on a large scale owc, *Coastal Engineering* **152**: 103528.  
**URL:** <http://www.sciencedirect.com/science/article/pii/S0378383919301589>
- Viviano, A., Naty, S., Foti, E., Bruce, T., Allsop, W. and Vicinanza, D. (2016). Large-scale experiments on the behaviour of a generalised oscillating water column under random waves, *Renewable Energy* **99**: 875 – 887.  
**URL:** <http://www.sciencedirect.com/science/article/pii/S0960148116306826>
- Wang, D., Katory, M. and Li, Y. (2002). Analytical and experimental investigation on the hydrodynamic performance of onshore wave-power devices, *Ocean Engineering* **29**(8): 871 – 885.  
**URL:** <http://www.sciencedirect.com/science/article/pii/S0029801801000580>
- Wang, R.-Q. and Ning, D.-Z. (2020). Dynamic analysis of wave action on an owc wave energy converter under the influence of viscosity, *Renewable Energy* **150**: 578 – 588.  
**URL:** <http://www.sciencedirect.com/science/article/pii/S0960148120300082>
- Wang, R.-Q., Ning, D.-Z., Zhang, C.-W., Zou, Q.-P. and Liu, Z. (2018). Nonlinear and viscous effects on the hydrodynamic performance of a fixed owc wave energy converter, *Coastal Engineering* **131**: 42 – 50.  
**URL:** <http://www.sciencedirect.com/science/article/pii/S0378383917300637>
- Zheng, S., Antonini, A., Zhang, Y., Greaves, D., Miles, J. and Iglesias, G. (2019). Wave power extraction from multiple oscillating water columns along a straight coast, *Journal of Fluid Mechanics* **878**: 445–480.
- Zheng, S., Zhang, Y. and Iglesias, G. (2019). Coast/breakwater-integrated owc: A theoretical model, *Marine Structures* **66**: 121 – 135.  
**URL:** <http://www.sciencedirect.com/science/article/pii/S0951833918304180>

CHAPTER 6. THE EFFECT OF OBLIQUE WAVES ON THE HYDRODYNAMIC  
EFFICIENCY OF A LAND-FIXED OWC DEVICE

---

Zheng, S., Zhu, G., Simmonds, D., Greaves, D. and Iglesias, G. (2020). Wave power extraction from a tubular structure integrated oscillating water column, *Renewable Energy* **150**: 342 – 355.

**URL:** <http://www.sciencedirect.com/science/article/pii/S0960148120300094>

## Chapter 7

# The Influence of the Chamber Configuration on the Efficiency of a Fixed-Detached OWC Device

As discussed in the previous chapters, employing a narrow front barrier in a fixed OWC device is more beneficial in terms of a broader frequency range for wave energy absorption. However, during severe storm events, the front barrier is subjected to large stresses owing to direct wave action, and a narrow front wall cannot offer protection to the entire system. This structural element should thus be carefully studied to enable efficient wave energy harvesting and coastal protection, especially when OWC systems are proposed to be incorporated into maritime structures such as breakwaters.

The incorporation of an OWC device into a fixed-detached breakwater (hereafter referred to as a fixed-detached OWC device) has several advantages: construction and maintenance costs are shared; energy absorption into the OWC collecting chamber contributes to coastal protection; allows the exchange of water and sediment between their seaside and lee side; and is less sensitive to water depth than that of conventional systems. For these reasons, this chapter seeks to find an answer to the following research question: How does the configuration of the front and back walls impact the performance of a fixed-detached OWC device?

This chapter consists of the published journal article:

Medina Rodríguez A.A., Silva Casarín R., Blanco Ilzarbe J.M. (2021). “*A theoretical study of the hydrodynamic performance of an asymmetric fixed-detached OWC device*”. **Water**. 13: 2637. <https://doi.org/10.3390/w13192637>.

**A theoretical study of the hydrodynamic performance of an asymmetric  
fixed-detached OWC device**

Ayrton Alfonso Medina Rodríguez, Rodolfo Silva Casarín and Jesús María Blanco Ilzarbe

**Abstract**

The chamber configuration of an asymmetric, fixed-detached Oscillating Water Column (OWC) device was investigated theoretically to analyze its effects on hydrodynamic performance. Two-dimensional linear wave theory was used, and the solutions for the associated radiation and scattering boundary value problems (BVPs) were derived through the matched eigenfunction expansion method (EEM), and the boundary element method (BEM). The results for the hydrodynamic efficiency and other important hydrodynamic properties were computed and analyzed for various cases. Parameters, such as the length of the chamber and the thickness and submergence of the rear and front walls were varied. The effects on device performance of adding a step under the OWC chamber and reflecting wall in the downstream region were also investigated. A good agreement between the analytical and numerical results was found. Thinner walls and low submergence of the chamber were seen to increase the efficiency bandwidth. The inclusion of a step slightly reduced the frequency at which resonance occurs, and when a downstream reflecting wall is included, the hydrodynamic efficiency is noticeably reduced at low frequencies due to the near trapped waves in the gap between the OWC device and the rigid vertical wall.

## 7.1 Introduction

Ocean wave energy is renewable and pollution-free, resource with the potential to mitigate the effects of global warming and contribute to meet the world's growing demand for electricity. This globally available energy source is estimated at about 2.1 TW (Gunn and Stock-Williams; 2012), or 18 400 TWh per year, approximately 80% of the 2018 world's demand for electricity (Calheiros-Cabral et al.; 2020). By use of wave energy converters (WECs), this energy source can be collected and transformed into electricity. In recent decades a broad range of WEC technologies has been proposed, with the Oscillating Water Column (OWC) device emerging as one of the most successful systems for wave energy harvesting.

The OWC differs from other technologies in its simple operating principle and adaptability for a range of locations (on the coastline, in the nearshore region or offshore). Thus, OWC systems have been researched most often, with full-scale prototypes being developed a number of times (Falcão; 2010). The system essentially consists of two components: a partially submerged hollow structure into which water enters through a bottom opening, and a Power Take-Off (PTO) mechanism, which converts the wave energy into electrical energy. Typically, the PTO system is a Wells turbine, which is the only moving element of the mechanism and which is above the level of the seawater to avoid direct exposure. The hollow chamber has a water column and an air column. The working principle is analogous to a piston in a cylinder; the trapped water inside is forced to oscillate up and down by the wave action. This alternately

## CHAPTER 7. THE INFLUENCE OF THE CHAMBER CONFIGURATION ON THE EFFICIENCY OF A FIXED-DETACHED OWC DEVICE

---

compresses and rarefies the air, trapped above the water column, and drives the airflow back and forth across the turbine in a duct that is coupled to a generator (Falcão and Henriques; 2016).

In an OWC system, wave energy is absorbed by a hydrodynamic mechanism involving relatively complex diffraction and radiation wave processes (Falcão; 2010). In recent years, many researchers have studied the hydrodynamic performance of the OWC device using theoretical analysis, experimental tests and numerical simulations. Pioneering studies of wave energy absorbers based on rigid body models were performed by Evans (1976, 1981); Mei (1976); Falnes and McIver (1985). Earlier, studies of the parameters affecting the hydrodynamic efficiency of land fixed OWC devices were conducted by Evans and Porter (1995, November 1997); Wang et al. (2002); Morris-Thomas et al. (2006); Şentürk and Özdamar (2012); Rezanejad et al. (2013).

Pile-supported OWC structures, with hydrodynamic behavior similar to fixed-detached devices, have been widely studied as a means of extracting wave energy for electricity generation and reducing wave transmission, mainly through the mechanisms of wave reflection (Sarmiento; 1992; Iturrioz et al.; 2014, 2015; He and Huang; 2016; He et al.; 2016, 2019; Sundar and Sannasiraj; 2021). The performance of pile-supported and land-fixed OWC devices were analyzed in experiments by Sarmiento (1992). A pile-supported OWC-type breakwater was experimentally investigated by He et al. (2016). They found that greater pneumatic damping increased energy extraction, but that with less pneumatic damping energy dissipation was more efficient in vortex-induced energy loss. He and Huang (2016) investigated the hydrodynamic performance of a pile-supported OWC structure in front of a vertical wall, demonstrating that this system can serve as a wave absorber to reduce the wave reflection from vertical walls. He et al. (2019) employed the matched EEM to investigate the hydrodynamics of a pile-supported OWC breakwater. Their results showed that by adjusting PTO damping for maximum power, adequate power extraction and wave transmission is possible, whereas optimizing PTO damping for minimal wave transmission significantly lowers power extraction. The combined effect of the chamber geometry and wave conditions on the performance of fixed-detached and asymmetric OWC devices was investigated by Simonetti et al. (2017). Qu et al. (2021) performed experimental tests to study an integrated OWC-pile-supported permeable breakwater and found that, compared with a non-permeable scheme, wave power generation and environmental protection performance were better.

Extensive investigations have been conducted on offshore fixed OWC system performance (Elhanafi, Fleming, Macfarlane and Leong; 2017a; Elhanafi, Macfarlane, Fleming and Leong; 2017; Elhanafi, Fleming, Macfarlane and Leong; 2017b; Elhanafi and Kim; 2018; Zabihi et al.; 2019). Elhanafi, Macfarlane, Fleming and Leong (2017) performed both experimental test and numerical simulations of a 3D offshore stationary OWC device subjected to regular waves. They showed that the total power extraction efficiency of an offshore OWC is considerably overestimated by 2D and wave flume modelling, especially for wave frequencies greater than the chamber resonant frequency. Elhanafi, Fleming, Macfarlane and Leong (2017b) investigated the effects of the underwater front and rear lips on the hydrodynamic performance of an offshore stationary OWC, using a computational fluid dynamics (CFD) model. They concluded that by selecting an appropriate submergence ratio of the asymmetric lips and lip thickness,

## CHAPTER 7. THE INFLUENCE OF THE CHAMBER CONFIGURATION ON THE EFFICIENCY OF A FIXED-DETACHED OWC DEVICE

---

the total hydrodynamic efficiency is considerably increased for a broad bandwidth frequency. Experimental tests were carried out by [Zabihi et al. \(2019\)](#) on a fixed offshore OWC model to study the effect of the wave spectrum shape on its efficiency. An analytical model to analyze the effects of a skirt on an OWC device integrated into an offshore wind turbine monopile was carried out by [Michele et al. \(2019\)](#). Through both experimental tests and numerical simulations, [Deng et al. \(2019\)](#) studied the hydrodynamic performance of an offshore-stationary OWC device with an immersed horizontal bottom plate. By means of the EEM, [Deng et al. \(2020\)](#) made a theoretical study of an asymmetric, offshore-stationary OWC device with an outstretched bottom plate. They found that the bottom plate provides an additional resonance mechanism that can be adjusted to offer a wider bandwidth with high performance.

There is still a lot to be investigated regarding the improvement of the hydrodynamic efficiency of fixed-detached OWC devices by modifying the geometric parameters of the chamber. To the best of the authors' knowledge, a theoretical study into the interaction of water waves with a fixed-detached OWC device with asymmetric thick rear and front walls, with a step and a reflecting wall, has not been reported. Apart from absorption of wave energy, fixed-detached OWC devices can be used to protect maritime structures and human activities from wave attack, as well as to enable water exchange and sediment transport ([He et al.; 2016](#)). They may, however, be affected by severe storms, which can cause serious structural damage, as was the case with the Mutriku Wave Energy Plant ([Medina-Lopez et al.; 2015](#)). Therefore, the thickness of the back and front barriers that comprise the OWC chamber must be designed to withstand wave loads and save the structure, while the effect that this would have on the device performance must be also considered.

Compared to experimental and CFD approaches, this theoretical investigation has the advantage of quickly evaluating different parameters of a fixed-detached OWC device. The main objectives of this analysis were to examine modifications in bandwidth on the efficiency curves, and the shifting of the peak resonant frequency due to different rear and front wall configurations, chamber size and the length of the gap between the OWC chamber and the reflecting wall.

The present study is organized as follows: Section 7.2 defines the physical problems corresponding to the water wave radiation and scattering by a fixed-detached OWC device, based on the potential flow theory. In Section 7.3 the methodologies for solving the BVPs are presented. First, the matched EEM is described, where the eigenfunction expansions along with their orthogonal properties, the continuity of velocity potential and flux are used to reduce the BVP into a linear system of algebraic equations. Then the BEM, which is a numerical technique based on an integral equation formulation and boundary discretization, is presented. In this work, the BEM with three-noded elements is used to account for the variation of the potential and flux on the boundaries. Section 7.4 describes the procedure for obtaining the energy relations. In Sections 7.5 and 7.6, convergence and truncation analyses are carried out, respectively, and a comparison is made with the experimental results of [He et al. \(2016\)](#); [He and Huang \(2016\)](#). Section 7.7 shows the results for various modelled cases. Finally, in Section 7.8, the main conclusions of this study are drawn.

## 7.2 Boundary value problem

Figure 7.1 shows the fixed-detached OWC device, the fluid and the Cartesian coordinate system, with the vertical coordinate,  $z$ , measured positively upwards and the undisturbed free surface located at  $z = 0$ . The waves approach the device from the positive  $x$  direction. The device is composed of two partially immersed front and rear walls, separated by distance  $b$ . The rear wall is located at  $x = -w_1$ , with a draft,  $a_1$ , and a thickness,  $w_1$ , while the front wall is located at  $x = b$ , with draft  $a_2$  and thickness  $w_2$ . A step under the OWC device is considered with a height  $h - h_e$ . There is assumed to be a turbine connecting the trapped air inside the chamber and the atmosphere.

The BVP is divided into five regions, as shown in Figure 7.1 and the boundaries are denoted by:

- The rear wall by  $B_r = \{(x, z) : (x = -w_1, -a_1 \leq z \leq 0) \cup (-w_1 < x < 0, z = -a_1) \cup (x = 0, -a_1 \leq z \leq 0)\}$ .
- The front wall by  $B_f = \{(x, z) : (x = b, -a_2 \leq z \leq 0) \cup (b < x < f_w, z = -a_2) \cup (x = f_w, -a_2 \leq z \leq 0)\}$  where  $f_w = b + w_2$ .
- The internal free surface inside the chamber by  $F_i = \{(x, z) : (0 \leq x \leq b, z = 0)\}$ .
- The external free surface by  $F_e = \{(x, z) : (-\infty < x < -w_1, z = 0) \cup (f_w < x < \infty, z = 0)\}$ .
- The bottom by  $B_d = \{(x, z) : (-\infty < x < -w_1, z = -h) \cup (x = -w_1, -h \leq z \leq -h_e) \cup (-w_1 < x < f_w, z = -h_e) \cup (x = f_w, -h \leq z \leq -h_e) \cup (f_w < x < \infty, z = -h)\}$ .

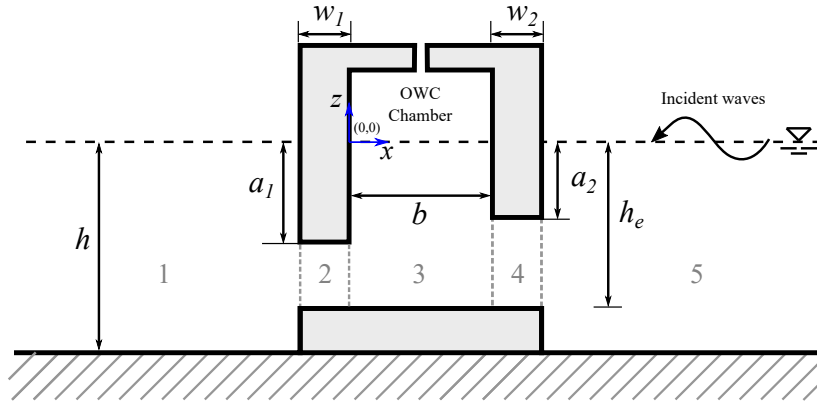


Figure 7.1: Side view of the interaction of a fixed-detached OWC device with water waves.

The fluid is inviscid and incompressible, and the velocity potential theory is applied. The wave motion is represented by linearized wave theory, disregarding surface tension effects. A

CHAPTER 7. THE INFLUENCE OF THE CHAMBER CONFIGURATION ON  
THE EFFICIENCY OF A FIXED-DETACHED OWC DEVICE

---

simple harmonic flow with angular frequency  $\omega$  is assumed, where the velocity potential is defined by  $\Phi(x, z, t)$  with  $\Phi(x, z, t) = \text{Re}\{\phi(x, z)e^{-i\omega t}\}$ , with  $\text{Re}\{\}$  denoting the real part of a complex expression. Under these assumptions, the spatial velocity potential  $\phi$  satisfies the Laplace equation

$$\left(\frac{\partial^2}{\partial x^2} + \frac{\partial^2}{\partial z^2}\right)\phi = 0. \quad (7.1)$$

The no-flow boundary conditions are applied at the bottom and the two barriers as

$$\frac{\partial\phi}{\partial n} = 0 \quad \text{for } (x, z) \in B_d, B_r \text{ and } B_f, \quad (7.2)$$

The continuity of pressure and horizontal velocity on the common interfaces of the five regions are given by

$$\phi_1 = \phi_2 \quad \text{and} \quad \frac{\partial\phi_1}{\partial x} = \frac{\partial\phi_2}{\partial x} \quad \text{on } x = -w_1 \quad \text{and} \quad -h_e \leq z \leq -a_1, \quad (7.3a)$$

$$\phi_2 = \phi_3 \quad \text{and} \quad \frac{\partial\phi_2}{\partial x} = \frac{\partial\phi_3}{\partial x} \quad \text{on } x = 0 \quad \text{and} \quad -h_e \leq z \leq -a_1, \quad (7.3b)$$

$$\phi_3 = \phi_4 \quad \text{and} \quad \frac{\partial\phi_3}{\partial x} = \frac{\partial\phi_4}{\partial x} \quad \text{on } x = b \quad \text{and} \quad -h_e \leq z \leq -a_2, \quad (7.3c)$$

$$\phi_4 = \phi_5 \quad \text{and} \quad \frac{\partial\phi_4}{\partial x} = \frac{\partial\phi_5}{\partial x} \quad \text{on } x = f_w \quad \text{and} \quad -h_e \leq z \leq -a_2. \quad (7.3d)$$

The linearized internal and external free surface boundary conditions are

$$\frac{\partial\phi}{\partial z} - K\phi = \begin{cases} \frac{i\omega p}{\rho g} & \text{on } F_i, \\ 0 & \text{on } F_e, \end{cases} \quad (7.4)$$

respectively, where  $p$  is the harmonic pressure distribution in the internal free surface,  $K = \omega^2/g$ , where  $g$  is the gravitational constant and  $\rho$  the seawater density.

The velocity potential is separated into a scattered potential  $\phi^S$  and a radiated potential  $\phi^R$ , as proposed by Evans (1982),

$$\phi(x, z) = \phi^S + \frac{i\omega p}{\rho g}\phi^R, \quad (7.5)$$

where  $\phi^S$  satisfies Eqs. (7.1)–(7.4) with  $p = 0$  inside the chamber; while  $\phi^R$  satisfies Eqs. (7.1)–(7.4) with Eq. (7.4) replaced by

$$\frac{\partial\phi^R}{\partial z} - K\phi^R = 1 \quad \text{on } F_i. \quad (7.6)$$

The Sommerfeld radiation condition is imposed at the left and right-hand ends ( $x \rightarrow \pm\infty$ ) of the domain

$$\frac{\partial\phi^{D,R}}{\partial x} \mp ik\phi^{D,R} = 0 \quad \text{as } x \rightarrow \pm\infty, \quad (7.7)$$



where  $\phi^D$  represents the diffracted potential, which together with the incident potential  $\phi^I$ , composed the scattered potential  $\phi^S$ , while the wavenumber  $k = 2\pi/\lambda$  is the positive real root of the wave dispersion relation given by

$$\omega^2 = gk \tanh kh, \quad (7.8)$$

and  $\lambda$  is the wavelength.

The time harmonic induced volume flux across  $F_i$  is also decomposed into scattering and radiation volume fluxes,  $q^S$  and  $q^R$ , respectively, as follows

$$q = \int_{F_i} \frac{\partial \phi}{\partial z} dx = q^S + \frac{i\omega p}{\rho g} q^R. \quad (7.9)$$

## 7.3 Solution method

### 7.3.1 Matched Eigenfunction Expansion Method

#### Definition of velocity potentials

The solution technique for the radiation and scattering problems based on the matched EEM is explained in this subsection. For the radiation problem, the method of separation of variables is used to determine the velocity potentials in the five regions represented by the eigenfunctions expansions as

$$\phi_1^R(x, z) = B^R e^{-ik(x+w_1)} \Psi_0(z) + \sum_{n=1}^{\infty} B_n^R e^{k_n(x+w_1)} \Psi_n(z), \quad (7.10a)$$

$$\phi_2^R(x, z) = \left[ C_0^R + D_0^R \frac{x}{w_1} \right] \hat{\chi}_0(z) + \sum_{n=1}^{\infty} \left[ C_n^R \frac{\cosh \hat{\gamma}_n x}{\cosh \hat{\gamma}_n w_1} + D_n^R \frac{\sinh \hat{\gamma}_n x}{\sinh \hat{\gamma}_n w_1} \right] \hat{\chi}_n(z), \quad (7.10b)$$

$$\phi_3^R(x, z) = \left( F_0^R \cos \hat{k}x + G_0^R \sin \hat{k}x \right) \hat{\Psi}_0(z) + \sum_{n=1}^{\infty} \left[ F_n^R \cosh \hat{k}_n x + G_n^R \sinh \hat{k}_n x \right] \hat{\Psi}_n(z) - \frac{1}{K}, \quad (7.10c)$$

$$\phi_4^R(x, z) = \left[ H_0^R + I_0^R \frac{(f_w - x)}{w_2} \right] \tilde{\chi}_0(z) + \sum_{n=1}^{\infty} \left[ H_n^R \frac{\cosh \tilde{\gamma}_n (f_w - x)}{\cosh \tilde{\gamma}_n w_2} + I_n^R \frac{\sinh \tilde{\gamma}_n (f_w - x)}{\sinh \tilde{\gamma}_n w_2} \right] \tilde{\chi}_n(z), \quad (7.10d)$$

$$\phi_5^R(x, z) = A^R e^{ik(x-f_w)} \Psi_0(z) + \sum_{n=1}^{\infty} A_n^R e^{-k_n(x-f_w)} \Psi_n(z), \quad (7.10e)$$

CHAPTER 7. THE INFLUENCE OF THE CHAMBER CONFIGURATION ON  
THE EFFICIENCY OF A FIXED-DETACHED OWC DEVICE

for regions 1 to 5, respectively, where  $\hat{\gamma}_n = n\pi/(h_e - a_1)$  and  $\tilde{\gamma}_n = n\pi/(h_e - a_2)$  for  $n = 0, 1, \dots$ . Additionally, the term  $-1/K$  on  $\phi_1^R$  was introduced to satisfy Eq. (7.6) and the coefficients  $A^R$  and  $B^R$ ,  $A_n^R$  and  $B_n^R$  for  $n = 1, 2, \dots$  and  $C_n^R$ ,  $D_n^R$ ,  $F_n^R$ ,  $G_n^R$ ,  $H_n^R$  and  $I_n^R$  for  $n = 0, 1, \dots$  are the unknown constants to be determined. The eigenfunctions  $\Psi$ ,  $\hat{\chi}$ ,  $\hat{\Psi}$  and  $\tilde{\chi}$  are defined by

$$\Psi_n(z) = \frac{1}{\sqrt{N_n}} \cos k_n(z + h), \quad \text{for } n = 0, 1, 2, \dots, \quad (7.11a)$$

$$\hat{\Psi}_n(z) = \frac{1}{\sqrt{\hat{N}_n}} \cos \hat{k}_n(z + h_e), \quad \text{for } n = 0, 1, 2, \dots, \quad (7.11b)$$

$$\hat{\chi}_n(z) = \frac{1}{\sqrt{\hat{W}_n}} \cos n\pi \left( \frac{z + h_e}{h_e - a_1} \right), \quad \text{for } n = 0, 1, 2, \dots, \quad (7.11c)$$

$$\tilde{\chi}_n(z) = \frac{1}{\sqrt{\tilde{W}_n}} \cos n\pi \left( \frac{z + h_e}{h_e - a_2} \right), \quad \text{for } n = 0, 1, 2, \dots, \quad (7.11d)$$

where

$$N_n = \frac{1}{2} \left[ 1 + \frac{\sin 2k_n h}{2k_n h} \right], \quad \text{for } n = 0, 1, 2, \dots, \quad (7.12a)$$

$$\hat{N}_n = \frac{1}{2} \left[ 1 + \frac{\sin 2\hat{k}_n h_e}{2\hat{k}_n h_e} \right], \quad \text{for } n = 0, 1, 2, \dots, \quad (7.12b)$$

$$\hat{W}_0 = \left[ 1 - \frac{a_1}{h_e} \right], \quad (7.12c)$$

$$\hat{W}_n = \frac{1}{2} \left[ 1 - \frac{a_1}{h_e} \right], \quad \text{for } n = 1, 2, \dots \quad (7.12d)$$

$$\tilde{W}_0 = \left[ 1 - \frac{a_2}{h_e} \right], \quad (7.12e)$$

$$\tilde{W}_n = \frac{1}{2} \left[ 1 - \frac{a_2}{h_e} \right], \quad \text{for } n = 1, 2, \dots \quad (7.12f)$$

with  $k_0 = -ik$  and  $\hat{k}_0 = -i\hat{k}$ , where  $ik_n$  and  $i\hat{k}_n$  for  $n \geq 1$  indicate the imaginary roots of the dispersion relation given by Eq. (7.8), while for  $\hat{k}$  this is given by

$$\omega^2 = g\hat{k} \tanh \hat{k} h_e. \quad (7.13)$$

The eigenfunctions in Eqs. (7.10) are orthonormal with respect to the inner product

$$\langle \Psi_n, \Psi_m \rangle = \frac{1}{h} \int_{-h}^0 \Psi_n(z) \Psi_m(z) dz = \delta_{nm}, \quad (7.14a)$$

$$\langle \hat{\Psi}_n, \hat{\Psi}_m \rangle = \frac{1}{h_e} \int_{-h_e}^0 \hat{\Psi}_n(z) \hat{\Psi}_m(z) dz = \delta_{nm}, \quad (7.14b)$$

$$\langle \hat{\chi}_n, \hat{\chi}_m \rangle = \frac{1}{h_e} \int_{-h_e}^{-a_1} \hat{\chi}_n(z) \hat{\chi}_m(z) dz = \delta_{nm}, \quad (7.14c)$$

$$\langle \tilde{\chi}_n, \tilde{\chi}_m \rangle = \frac{1}{h_e} \int_{-h_e}^{-a_2} \tilde{\chi}_n(z) \tilde{\chi}_m(z) dz = \delta_{nm}, \quad (7.14d)$$

where  $\delta_{nm}$  is the Kronecker delta.

As described for the radiation problem earlier, the velocity potentials for the scattering problem are also expressed by the appropriate eigenfunctions. The expansion of velocity potential  $\phi_2^R$  and  $\phi_4^R$  remain the same as in the case of the radiation problem, while for velocity potentials in regions 1, 3 and 5, these are expressed as follows

$$\phi_1^S(x, z) = T e^{-ik(x+w_1)} \Psi_0(z) + \sum_{n=1}^{\infty} B_n^S e^{k_n(x+w_1)} \Psi_n(z), \quad (7.15a)$$

$$\phi_3^S(x, z) = \left( F_0^S \cos \hat{k}x + G_0^S \sin \hat{k}x \right) \hat{\Psi}_0(z) + \sum_{n=1}^{\infty} \left( F_n^S \cosh \hat{k}_n x + G_n^S \sinh \hat{k}_n x \right) \hat{\Psi}_n(z), \quad (7.15b)$$

$$\phi_5^S(x, z) = \left( e^{-ik(x-f_w)} + R e^{ik(x-f_w)} \right) \Psi_0(z) + \sum_{n=1}^{\infty} A_n^S e^{-k_n(x-f_w)} \Psi_n(z), \quad (7.15c)$$

where the associated eigenvalues and eigenfunctions are the same as defined above.

The far-field behaviour of the scattered and radiated potentials is given by

$$\phi^R \sim B^R e^{-ik(x+w_1)} \Psi_0(z), \quad \text{as } x \rightarrow -\infty, \quad (7.16a)$$

$$\phi^R \sim A^R e^{ik(x-f_w)} \Psi_0(z), \quad \text{as } x \rightarrow +\infty, \quad (7.16b)$$

$$\phi^S \sim T e^{-ik(x+w_1)} \Psi_0(z), \quad \text{as } x \rightarrow -\infty \quad (7.17a)$$

$$\phi^S \sim \left( e^{-ik(x-f_w)} + R e^{ik(x-f_w)} \right) \Psi_0(z), \quad \text{as } x \rightarrow +\infty \quad (7.17b)$$

where  $A^R$  and  $B^R$  represents the amplitude of the radiated wave to  $\pm\infty$ , respectively, while  $R$  and  $T$  are the amplitude of the reflected and transmitted waves in the scattering problem, respectively.

### Matching of regions

Applying of the second matching condition Eq. (7.3a) at  $x = -w_1$  on the velocity potentials described by Eqs. (7.10a) and (7.10b), together with the boundary condition Eq. (7.2) at  $x = -w_1$  and  $-h \leq z \leq -h_e$  and  $-a_1 \leq z \leq 0$  applied to the velocity potential Eq. (7.10a), adding their results, exploiting the orthonormality of the eigenfunctions as defined in Eq. (7.14a) and truncating the infinite series up to  $N$  terms, we have

$$B_m^R = \left( \frac{1}{\hat{k}_m h w_1} \right) D_0^R \int_{-h_e}^{-a_1} \hat{\chi}_0(z) \Psi_m(z) dz - \left( \frac{1}{\hat{k}_m h} \right) \sum_{n=1}^N \hat{\gamma}_n \left[ C_n^R \tanh \hat{\gamma}_n w_1 - D_n^R \coth \hat{\gamma}_n w_1 \right] \times \int_{-h_e}^{-a_1} \hat{\chi}_n(z) \Psi_m(z) dz, \quad \text{for } m \geq 0, \quad (7.18)$$

Next, by using the first matching condition of Eq. (7.3a) at  $x = -w_1$  with the velocity potentials, Eqs. (7.10a) and (7.10b), exploiting the orthonormality of the eigenfunctions as defined in Eq. (7.14c) and truncating the infinite series, we obtain

$$B_0^R \int_{-h_e}^{-a_1} \Psi_0(z) \hat{\chi}_m(z) dz + \sum_{n=1}^N B_n^R \int_{-h_e}^{-a_1} \Psi_n(z) \hat{\chi}_m(z) dz - \left[ C_m^R - D_m^R \right] h = 0, \quad \text{for } m \geq 0. \quad (7.19)$$

By applying the second matching condition of Eq. (7.3b) at  $x = 0$  in the velocity potentials of Regions 2 and 3, Eqs. (7.10b) and (7.10c), respectively, in conjunction with the application of boundary condition Eq. (7.2) at  $x = 0$  and  $-a_1 \leq z \leq 0$  in the velocity potential Eq. (7.10c), adding their results, making use of the orthonormality of the eigenfunctions as given by Eq. (7.14b) and truncating the infinite series up to  $N$  terms, gives

$$G_0^R - \left( \frac{1}{\hat{k} h_e w_1} \right) D_0^R \int_{-h_e}^{-a_1} \hat{\chi}_0(z) \hat{\Psi}_0(z) dz - \left( \frac{1}{\hat{k} h_e} \right) \sum_{n=1}^N D_n^R \left[ \frac{\hat{\gamma}_n}{\sinh \hat{\gamma}_n w_1} \right] \times \int_{-h_e}^{-a_1} \hat{\chi}_n(z) \hat{\Psi}_0(z) dz = 0, \quad \text{for } m = 0 \quad (7.20a)$$

$$G_m^R - \left( \frac{1}{\hat{k}_m h_e w_1} \right) D_0^R \int_{-h_e}^{-a_1} \hat{\chi}_0(z) \hat{\Psi}_m(z) dz - \left( \frac{1}{\hat{k}_m h_e} \right) \sum_{n=1}^N D_n^R \left[ \frac{\hat{\gamma}_n}{\sinh \hat{\gamma}_n w_1} \right] \times \int_{-h_e}^{-a_1} \hat{\chi}_n(z) \hat{\Psi}_m(z) dz = 0, \quad \text{for } m \geq 1 \quad (7.20b)$$

Next, by applying the first matching condition of Eq. (7.3b) at  $x = 0$  on Eqs. (7.10b) and (7.10c), multiplying by  $\hat{\chi}_m$ , integrating from  $-h_e$  to  $-a_1$ , and using the orthonormal properties

of the eigenfunction  $\hat{\chi}_m$  (Eq. 7.14c), we obtain

$$C_0^R - F_0^R \int_{-h_e}^{-a_1} \hat{\Psi}_0(z) \hat{\chi}_m(z) dz - \sum_{n=1}^N F_n^R \int_{-h_e}^{-a_1} \hat{\Psi}_n(z) \hat{\chi}_m(z) dz + \frac{1}{K} \int_{-h_e}^{-a_1} \hat{\chi}_m(z) dz = 0, \quad \text{for } m = 0. \quad (7.21a)$$

$$C_m^R \left[ \frac{h_e}{\cosh \hat{\gamma}_n w_1} \right] - F_0^R \int_{-h_e}^{-a_1} \hat{\Psi}_0(z) \hat{\chi}_m(z) dz - \sum_{n=1}^N F_n^R \int_{-h_e}^{-a_1} \hat{\Psi}_n(z) \hat{\chi}_m(z) dz + \frac{1}{K} \int_{-h_e}^{-a_1} \hat{\chi}_m(z) dz = 0, \quad \text{for } m \geq 1. \quad (7.21b)$$

Then, applying the second matching condition of Eq. (7.3c) at  $x = b$  in the velocity potentials Eqs. (7.10c) and (7.10d), together with the application of boundary condition Eq. (7.2) at  $x = b$  and  $-a_2 \leq z \leq 0$  in the velocity potential Eq. (7.10c), adding their results, making use of the orthonormality of the eigenfunctions as given by Eq. (7.14b) and truncating the infinite series up to  $N$  terms, we obtain

$$- \hat{k} h_e \left[ F_0^R \sin \hat{k} b - G_0^R \cos \hat{k} b \right] + \frac{1}{w_2} I_0^R \int_{-h_e}^{-a_2} \tilde{\chi}_0(z) \hat{\Psi}_0(z) dz + \sum_{n=1}^N \tilde{\gamma}_n \left[ H_n^R \tanh \tilde{\gamma}_n w_2 + I_n^R \coth \tilde{\gamma}_n w_2 \right] \int_{-h_e}^{-a_2} \tilde{\chi}_n(z) \hat{\Psi}_0(z) dz = 0, \quad \text{for } m = 0, \quad (7.22a)$$

$$\hat{k}_m h_e \left[ F_m^R \sin \hat{k} b + G_m^R \cos \hat{k} b \right] + \frac{1}{w_2} I_0^R \int_{-h_e}^{-a_2} \tilde{\chi}_0(z) \hat{\Psi}_m(z) dz + \sum_{n=1}^N \tilde{\gamma}_n \left[ H_n^R \tanh \tilde{\gamma}_n w_2 + I_n^R \coth \tilde{\gamma}_n w_2 \right] \int_{-h_e}^{-a_2} \tilde{\chi}_n(z) \hat{\Psi}_m(z) dz = 0, \quad \text{for } m \geq 1. \quad (7.22b)$$

By using the first matching condition of Eq. (7.3c) at  $x = b$  with the velocity potentials, Eqs. (7.10c) and (7.10d), exploiting the orthonormality of the eigenfunctions, as defined in Eq. (7.14d), and truncating the infinite series, we have

$$\left[ F_0^R \cos \hat{k} b + G_0^R \sin \hat{k} b \right] \int_{-h_e}^{-a_2} \hat{\Psi}_0(z) dz \tilde{\chi}_m(z) dz + \sum_{n=1}^N \left[ F_n^R \cosh \hat{k} b + G_n^R \sinh \hat{k} b \right] \times \int_{-h_e}^{-a_2} \hat{\Psi}_n(z) dz \tilde{\chi}_m(z) dz - \left[ H_m^R + I_m^R \right] h_e + \frac{1}{K} \int_{-h_e}^{-a_2} \tilde{\chi}_m(z) dz = 0, \quad \text{for } m \geq 0, \quad (7.23)$$

Then, by applying the second matching condition of Eq. (7.3d) at  $x = f_w$  on the velocity potentials of Regions 4 and 5, Eqs. (7.10d) and (7.10e), respectively, in conjunction with the

application of boundary condition Eq. (7.2) at  $x = f_w$  and  $-h \leq z \leq -h_e$  and  $-a_2 \leq z \leq 0$  on the velocity potential Eq. (7.10e), adding their results, making use of the orthonormality of the eigenfunctions as given by Eq. (7.14a) and truncating the infinite series, we obtain

$$A_m^R = \left( \frac{1}{k_m h w_2} \right) \int_{-h_e}^{-a_2} \tilde{\chi}_0(z) \Psi_m(z) dz + \left( \frac{1}{k_m h} \right) \sum_{n=1}^N I_n^R \left[ \frac{\tilde{\gamma}_n}{\sinh \tilde{\gamma}_n w_2} \right] \times \int_{-h_e}^{-a_2} \tilde{\chi}_n(z) \Psi_m(z) dz, \quad \text{for } m \geq 0, \quad (7.24)$$

Finally, by using the first matching condition of Eq. (7.3d) at  $x = f_w$  with the velocity potentials, Eqs. (7.10d) and (7.10e), exploiting the orthonormality of the eigenfunctions as defined in Eq. (7.14d), and truncating the infinite series, yields

$$A^R \int_{-h_e}^{-a_2} \Psi_0(z) \tilde{\chi}_m(z) dz + \sum_{n=1}^N A_n^R \int_{-h_e}^{-a_2} \Psi_n(z) \tilde{\chi}_m(z) dz - h_e H_0^R = 0, \quad \text{for } m = 0. \quad (7.25a)$$

$$A^R \int_{-h_e}^{-a_2} \Psi_0(z) \tilde{\chi}_m(z) dz + \sum_{n=1}^N A_n^R \int_{-h_e}^{-a_2} \Psi_n(z) \tilde{\chi}_m(z) dz - \left[ \frac{h_e}{\cosh \tilde{\gamma}_n w_2} \right] H_m^R = 0, \quad \text{for } m \geq 1. \quad (7.25b)$$

Thus, Eqs. (7.18)–(7.25b) provide a linear system of algebraic equations for solving the unknowns. The procedure for solving the scattering problem is similar to that of the radiation problem described above.

### Fixed-detached OWC device near a reflecting wall

In this subsection, the interaction of water waves with a detached OWC device near a rigid, vertical wall is analyzed. For this case, the OWC device is at a finite distance,  $L$ , from the reflecting wall, as shown in Figure 7.2. The velocity potentials in 2, 3, 4 and 5, Eqs. (7.10b)–(7.10e), and the boundary conditions, remain the same as in the previous subsection, except for the radiation condition at the left-hand end, which is now given by

$$\frac{\partial \phi_1}{\partial x} = 0 \quad \text{on } x = -w_1 - L \quad \text{and} \quad -h \leq z \leq 0, \quad (7.26)$$

and the velocity potential  $\phi_1$  now has the following form

$$\phi_1^R(x, z) = B^R \frac{\cos k(x + w_1 + L)}{\cos kL} \Psi_0(z) + \sum_{n=1}^{\infty} B_n^R \frac{\cosh k_n(x + w_1 + L)}{\cosh k_n L} \Psi_n(z), \quad (7.27)$$

Through the application of the matching conditions, as in Eqs. (7.3a)–(7.3d), along with the orthogonality conditions defined in Eqs. (7.14a)–(7.14d), a system of equations to determine

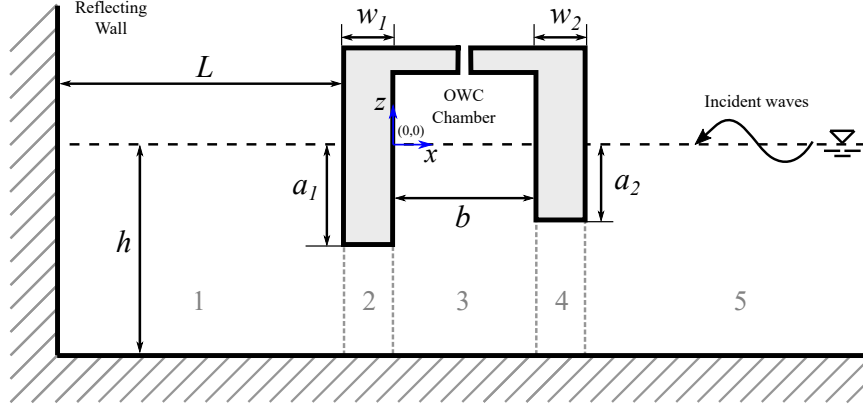


Figure 7.2: Side view of the interaction of water waves with a fixed-detached OWC device near a vertical wall.

of the unknowns is obtained. This is similar to that shown in Eqs. (7.18)–(7.25a), with only a difference in Eq. (7.18), which now takes the following form:

$$B_m^R = \left( \frac{1}{k_m h w_1 \tanh k_n L} \right) D_0^R \int_{-h_e}^{-a_1} \hat{\chi}_0(z) \Psi_m(z) dz - \left( \frac{1}{k_m h \tanh k_n L} \right) \sum_{n=1}^N \hat{\gamma}_n \left[ C_n^R \tanh \hat{\gamma}_n w_1 - D_n^R \coth \hat{\gamma}_n w_1 \right] \int_{-h_e}^{-a_1} \hat{\chi}_n(z) \Psi_m(z) dz, \quad \text{for } m \geq 0. \quad (7.28)$$

### 7.3.2 Boundary Element Method

#### Boundary integral equation

The Laplace equation, (7.1), in its boundary integral representation is given by

$$\alpha(X)\phi(X) + \int_{\Gamma} \phi(Y) \frac{\partial \psi(X, Y)}{\partial n_Y} d\Gamma_Y = \int_{\Gamma} \psi(X, Y) \frac{\partial \phi(Y)}{\partial n_Y} d\Gamma_Y, \quad (7.29)$$

where  $\phi$  and  $\partial\phi/\partial n$  represent, respectively, the unknown velocity potential and its normal derivative with respect to the field point  $Y(\hat{\xi}, \hat{\eta})$  on the boundary  $\Gamma$ ;  $X(x, z)$  is the source point inside the domain  $\Omega$ ;  $\alpha = \tau/2\pi$ , where  $\tau$  is the angle in radians between points  $X$  and  $Y$  (Katsikadelis; 2002);  $\psi$  represents the fundamental solution of Laplace equation given by

$$\psi = \frac{1}{2\pi} \ln r. \quad (7.30)$$

where  $r = \sqrt{(x - \hat{\xi})^2 + (z - \hat{\eta})^2}$  is the distance between points  $X$  and  $Y$ ; and  $\partial\psi/\partial n$  is its normal derivative at point  $Y$  in  $\Gamma$ .

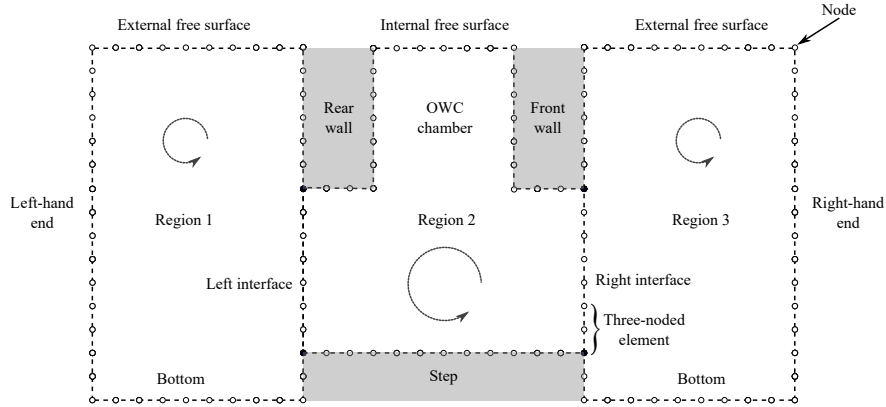


Figure 7.3: Meshing and matching of the regions with nodes arranged in an anti-clockwise direction.

The boundary integral equation (7.29) is then discretized by subdividing the boundary  $\Gamma$  into a number of boundary elements  $NE$  as follows

$$\alpha^i \phi^i + \sum_{j=1}^{NE} \int_{\Gamma} \phi \frac{\partial \psi}{\partial n} d\Gamma = \sum_{j=1}^{NE} \int_{\Gamma} \psi \frac{\partial \phi}{\partial n} d\Gamma. \quad (7.31)$$

with  $i$  indicating the boundary node and  $j$  the boundary element. The boundary is then divided into curved quadratic elements, where  $\phi$  and  $\partial\phi/\partial n$  are assumed to have three different values in each element, see Medina Rodríguez et al. (2020).

The fluxes will then have a single nodal value for each element, as explained by Dominguez (1993). Thus, the possibility of different values between neighbouring elements is considered, but in the connection between two adjacent elements, the velocity potentials only have a single value. Therefore, fluxes are organized in a  $3 \times NE$  array, whereas the velocity potentials are in an  $N_{bem}$  array, where  $N_{bem}$  is equivalent to the number of nodes equal to  $2NE$  for closed boundaries (Medina Rodríguez et al.; 2021).

### Matching of subdomains

The radiation and scattering BVPs are divided into three regions as shown in Figure 7.3, with common interfaces on both sides of Region 2. Since the far-field boundaries at  $\pm\infty$  must be placed far enough from the OWC chamber to avoid the effect of local disturbances, the domain as a whole becomes very long and numerical problems associated with the integration of the fundamental solution over long distances arise (Katsikadelis; 2002). The subdomain method is employed to overcome these numerical issues. This also helps to avoid numerical instabilities that appear when the wall thickness is very small (Rezanejad et al.; 2013).

The subdomain method is used to match the regions at the common interfaces. To obtain the final solution matrix, each subdomain is treated separately to form matrices that are coupled



together according to the relevant boundary conditions. The continuity of the velocity potential and the flux at the interfaces should therefore be defined, to match the regions (Katsikadelis; 2002; Becker; 1992). For this purpose, the nodes in the left and right interfaces are assumed to be in perfect contact, as shown in Figure 7.3. These velocity potential and flux continuity conditions at the interfaces are given by

$$\Phi_- = \Phi_+, \quad (7.32a)$$

$$\Phi_{n-} = -\Phi_{n+}, \quad (7.32b)$$

respectively.

The previously defined boundary conditions, Eqs. (7.2), (7.4), (7.6), (7.7) and (7.26), are then used, and the unknowns variables are shifted to the left-hand side, while the known variables to the right-hand side. Then, the matrix below is obtained

$$[A] \{X\} = \{B\}, \quad (7.33)$$

where the square matrix  $[A]$  has dimensions of  $N_{bem} \times N_{bem}$ ; the vector of unknown velocity potentials or fluxes  $\{X\}$ , with dimensions  $N_{bem} \times 1$ ; and the known vector  $\{B\}$  has dimensions of  $N_{bem} \times 1$  (Dominguez; 1993).

## 7.4 Efficiency relations

As proposed by Evans (1982), the radiation volume flux  $q^R$  is divided into real and imaginary parts as,

$$\frac{i\omega p}{\rho g} q^R = -(\hat{B} - i\hat{A}) p = -Zp, \quad (7.34)$$

where  $Z = \hat{B} - i\hat{A}$  is the complex admittance, while the real coefficients  $\hat{A}$  and  $\hat{B}$  are given by

$$\hat{A} = \frac{\omega}{\rho g} \text{Re}\{q^R\}, \quad (7.35a)$$

$$\hat{B} = \frac{\omega}{\rho g} \text{Im}\{q^R\}, \quad (7.35b)$$

which are related to the added mass and the radiation damping in a rigid body system, respectively (Evans and Porter; 1995).

Applying Green's theorem to the radiation potential and its conjugate yields

$$\int_U \left( \phi^R \frac{\partial \bar{\phi}^R}{\partial n} + \bar{\phi}^R \frac{\partial \phi^R}{\partial n} \right) dS = 0, \quad (7.36)$$

where  $U$  is the closed boundary composed of  $U = B_d + B_r + B_f + F_i + F_e + F_{+\infty} + F_{-\infty}$ , where  $F_{+\infty}$  and  $F_{-\infty}$  are the imposed far-field boundaries as  $x \rightarrow \infty$  and  $x \rightarrow -\infty$ , respectively, at

CHAPTER 7. THE INFLUENCE OF THE CHAMBER CONFIGURATION ON  
THE EFFICIENCY OF A FIXED-DETACHED OWC DEVICE

---

$-h < z < 0$ . By using the boundary conditions Eq. (7.2) and (7.3), the contributions from the boundaries  $B_d$ ,  $B_r$ ,  $B_f$  and  $F_e$  vanish. Then, with the aid of Eqs. (7.6), (7.16)a–b and (7.34), the contributions from  $F_i$ ,  $F_{+\infty}$  and  $F_{-\infty}$  are calculated and an expression for the radiation damping  $\hat{B}$  as a function of the complex amplitudes of the right and left radiated waves  $A^R$  and  $B^R$ , respectively, is obtained

$$\hat{B} = \frac{Kkh\omega}{\rho g} \left( |A^R|^2 + |B^R|^2 \right). \quad (7.37)$$

Now, applying the Green's theorem on the radiation and the scattered potentials as in Eq (7.36), and using the boundary conditions as in the previous case, a relation between the right radiated amplitude  $A^R$  and the induced volume flux in the scattering problem  $q^S$  is obtained as follows

$$q^S = -2iKkhA^R, \quad (7.38)$$

and is non-dimensionalised by the incident volume flux as in [Evans and Porter \(1995\)](#), giving rise to

$$\frac{|q^S|}{|q^I|} = \frac{|q^S|}{N_0^{-1/2} kb \sinh kb}. \quad (7.39)$$

Equations (7.37) and (7.38) can be computed by solving the radiation problem alone and are comparable to those derived by [Evans \(1982\)](#) and used by [Evans and Porter \(1995\)](#); [Rezanejad et al. \(2013\)](#). Equation (7.38) is linked to the volume flux across  $F_i$  due to the incident plus diffracted wave fields, and is proportional to the amplitude of the radiated waves in the direction from which the incident wave comes ([Evans; 1982](#)).

Now, by assuming that the pressure inside the chamber is uniform and the air exits to the atmosphere through the turbine without a phase lag, we have

$$q = \Lambda p \quad (7.40)$$

where the real control parameter  $\Lambda$  is related to the linear turbine damping induced by the airflow. This is a general characteristic of Wells turbines, which with constant rotational speed, show a linear relationship between pressure and volume flow rate ([Falcão et al.; 2012](#); [Gato and de O. Falcão; 1988](#)).

After combining Eqs. (7.9), (7.34) and (7.40), the imposed internal pressure gives

$$p = \frac{q^S}{\Lambda + Z}. \quad (7.41)$$

Now, the total rate of work performed by the pressure forces inside the OWC,  $Q(t) \times P(t)$ , is averaged over one wave period to obtain the total rate of power absorbed per unit width of pressure distribution as

$$W = \frac{1}{2} \text{Re}\{\bar{p}q\}, \quad (7.42)$$

CHAPTER 7. THE INFLUENCE OF THE CHAMBER CONFIGURATION ON  
THE EFFICIENCY OF A FIXED-DETACHED OWC DEVICE

---

where the horizontal bar ( $\bar{\phantom{x}}$ ) denotes the complex conjugate. Now, by inserting Eqs. (7.9) and (7.34) into Eq. (7.42) and simplifying, we have

$$W = \frac{1}{2} \text{Re}\{\bar{p}(q^S - Zp)\} = \frac{|q^S|^2}{8\hat{B}} - \frac{\hat{B}}{2} \left| p - \frac{q^S}{2\hat{B}} \right|^2, \quad (7.43)$$

where if  $\hat{B}^{-1}$  exists, the maximum work gives

$$W_{max} = \frac{|q^S|^2}{8\hat{B}}, \quad \text{for } p = \frac{q^S}{2\hat{B}}, \quad (7.44)$$

where  $\Lambda = \bar{Z}$  for maximum power. Thus, after combining Eqs. (7.41) and (7.43), we obtain

$$W = \frac{|q^S|^2}{8\hat{B}} \left[ 1 - \left( \frac{|\Lambda - Z|}{|\Lambda + Z|} \right)^2 \right]. \quad (7.45)$$

Now, the optimal power conversion efficiency must be obtained. This is performed by finding the optimum value of  $\Lambda$ , by applying zero value to the derivative with respect to  $\Lambda$  for the squared-right term inside the brackets of Eq. (7.45) (Şentürk and Özdamar; 2012), thus yielding

$$\Lambda_{opt} = |Z| = \left( \hat{B}^2 + \hat{A}^2 \right)^{1/2} \quad (7.46)$$

and after substituting the above expression into Eq. (7.45), we have

$$W_{opt} = \frac{|q^S|^2}{8\hat{B}} \left[ 1 - \frac{\Lambda_{opt} - \hat{B}}{\Lambda_{opt} + \hat{B}} \right], \quad (7.47)$$

where  $\hat{A}$ ,  $\hat{B}$  and  $\Lambda$  are a function of the angular frequency  $\omega$ .

Hence, an expression for the maximum hydrodynamic efficiency is given as

$$\eta_{max} = \frac{W_{opt}}{W_{max}} = \frac{2\hat{B}}{\Lambda_{opt} + \hat{B}}, \quad (7.48)$$

with  $\eta_{max}$  in the range 0 to 1.

As in Evans and Porter (1995), the following non-dimensionalised quantities are defined

$$\mu = \frac{\rho g}{\omega b} \hat{A}, \quad (7.49a)$$

$$\nu = \frac{\rho g}{\omega b} \hat{B}, \quad (7.49b)$$

which represent the coefficients of radiation susceptance and radiation conductance, respectively.

Finally, after inserting the above coefficients into Eq. (7.48), the hydrodynamic efficiency  $\eta_{max}$  gives

$$\eta_{max} = \frac{2}{\left[ 1 + \left( \frac{\mu}{\nu} \right)^2 \right]^{1/2} + 1}. \quad (7.50)$$

CHAPTER 7. THE INFLUENCE OF THE CHAMBER CONFIGURATION ON  
THE EFFICIENCY OF A FIXED-DETACHED OWC DEVICE

Table 7.1: Convergence of the maximum hydrodynamic efficiency  $\eta_{max}$  computed by using the EEM for different number of evanescent modes  $N$  with  $a_1/h = a_2/h = 0.5$ ,  $w_1/h = w_2/h = 0.125$   $b/h = 1.0$  and  $h_e/h = 1$  without the reflecting vertical wall.

$N$	$Kh = 0.5$	$Kh = 1.0$	$Kh = 1.5$	$Kh = 2.0$	$Kh = 2.5$	$Kh = 3.0$	$Kh = 3.5$
	$\eta_{max}$						
5	0.66955	0.98913	0.52865	0.24885	0.11934	0.05863	0.02973
10	0.67187	0.98611	0.52024	0.24406	0.11657	0.05699	0.02875
20	0.67273	0.98493	0.51725	0.24238	0.11562	0.05644	0.02842
30	0.67292	0.98465	0.51653	0.24198	0.11539	0.05630	0.02834
40	0.67303	0.98450	0.51620	0.24179	0.11529	0.05624	0.02831

Table 7.2: Calculation of the maximum hydrodynamic efficiency  $\eta_{max}$  by using the BEM for different distances at which the left and right radiation boundaries are truncated  $a_1/h = a_2/h = 0.5$ ,  $w_1/h = w_2/h = 0.125$   $b/h = 1.0$  and  $h_e/h = 1$  without the reflecting vertical wall.

Distance	$Kh = 0.5$	$Kh = 1.0$	$Kh = 1.5$	$Kh = 2.0$	$Kh = 2.5$	$Kh = 3.0$	$Kh = 3.5$
	$\eta_{max}$						
$2h$	0.67335	0.98449	0.51433	0.23774	0.11040	0.05176	0.02482
$3h$	0.67335	0.98449	0.51432	0.23768	0.11029	0.05158	0.02457
$4h$	0.67335	0.98449	0.51432	0.23768	0.11029	0.05158	0.02456
$5h$	0.67335	0.98449	0.51432	0.23768	0.11029	0.05158	0.02456

## 7.5 Convergence and truncation analyses

A convergence study for both EEM and BEM was done prior to performing the computations of the results. For the calculations, the water depth is assumed to be 7.90 m, and a wave period  $T$  bounded by  $2.50 \leq T \leq 30$  s, as in (Medina Rodríguez et al.; 2020). In the case of the EEM, see Table 7.1, a convergence analysis for the maximum hydrodynamic efficiency  $\eta_{max}$  is given for different values of the non-dimensional frequency  $Kh$  ( $= 0.5, 1.0, 1.5, 2.0, 2.5, 3.0$  and  $3.5$ ). From Table 7.1, it can be seen that roughly 30 evanescent modes are adequate to ensure that the analytical results converge to within three decimal places. However, it should be noted that the OWC geometry is relevant for the convergence, and the number of equations needed in the matched EEM, especially for the lower corners of the walls, since as “ $w_1$ ” and “ $w_2$ ” decrease, more terms are needed. For the case without the step, the results converge faster, to the desired accuracy even with 20 terms in the infinite series sums. However, on average 30 terms are sufficient for the desired accuracy and, therefore, in the present calculations,  $N = 30$  is used.

In Table 7.2, a truncation analysis was first carried out to avoid the effect of local disturbances at the far-field boundaries. From Table 7.2, it is seen that at a distance of 4

CHAPTER 7. THE INFLUENCE OF THE CHAMBER CONFIGURATION ON  
THE EFFICIENCY OF A FIXED-DETACHED OWC DEVICE

Table 7.3: Convergence of the maximum hydrodynamic efficiency  $\eta_{max}$  computed for different numbers of nodes  $N_{bem}$  with  $a_1/h = a_2/h = 0.5$ ,  $w_1/h = w_2/h = 0.125$   $b/h = 1.0$  and  $h_e/h = 1$  without the reflecting vertical wall.

$N$	$Kh = 0.5$	$Kh = 1.0$	$Kh = 1.5$	$Kh = 2.0$	$Kh = 2.5$	$Kh = 3.0$	$Kh = 3.5$
	$\eta_{max}$						
<b>648</b>	0.67318	0.98474	0.51493	0.23803	0.11048	0.05168	0.02462
<b>716</b>	0.67325	0.98464	0.51468	0.23789	0.11040	0.05164	0.02460
<b>784</b>	0.67331	0.98456	0.51448	0.23778	0.11034	0.05161	0.02458
<b>852</b>	0.67335	0.98449	0.51432	0.23768	0.11029	0.05158	0.02456
<b>920</b>	0.67338	0.98444	0.51418	0.23761	0.11024	0.05155	0.02455

times the water depth between the left and right faces of the OWC device and the left and right far-field boundaries, respectively, the results converge to five digits. In Table 7.3, using the BEM, the results of  $\eta_{max}$  for the same  $Kh$  values are given for different number of nodes ( $N$ ). In this case, around 800 nodes (400 quadratic elements) were determined to be sufficient to achieve numerical results convergence to three decimal places. As a result, the three-region BVP is discretized with around 800 nodes.

## 7.6 Comparison with experimental results

To validate the results obtained by the above-mentioned methods, the experimental results of He et al. (2016) and He and Huang (2016) were employed. In Figure 7.4a, comparisons are shown of the experimental data of He et al. (2016) and the present BEM results for the hydrodynamic efficiency versus  $b/\lambda$  with  $b/h = 1.0$  and  $w_1/h = w_2/h = 0.025$  for two different values of the walls draft to water depth ratio  $a_1/h = a_2/h$ . The damping coefficients for these results were  $\Lambda = 0.008$  and  $\Lambda = 0.00005$   $m^4 \cdot s/kg$  for  $a_1/h = a_2/h = 0.375$  and  $a_1/h = a_2/h = 0.50$ , respectively. To determine the damping coefficient  $\Lambda$ , the method described by Rezanejad et al. (2017) was employed. The ratio of slot opening to cross-sectional area of the OWC chamber considered by He et al. (2016) were 0.625% and 1.875% for  $a_1/h = a_2/h$  equal to 0.5 and 0.375, respectively. In Figure 7.4b, the hydrodynamic efficiency versus  $b/\lambda$  with  $b/h = 1.0$ ,  $a_1/h = a_2/h = 0.25$  and  $w_1/h = w_2/h = 0.025$  for two different values of the rear face to reflecting wall distance to chamber length ratio  $L/b$  is compared against the results obtained by He and Huang (2016). In this case, the damping coefficients were  $\Lambda = 0.0018$  and  $\Lambda = 0.0030$   $m^4 \cdot s/kg$  for  $L/b = 0.24$  and  $L/b = 0.97$ , respectively. Here, the opening ratio considered by He and Huang (2016) was 1.25% in both cases.

From these figures, it can be seen that the BEM results follow a similar trend to that observed in the experimental data. However, for the case of the highest draft  $a_1/h = a_2/h = 0.5$  with the smallest opening ratio, 0.625%, as is the case of the PTO mechanism in He et al. (2016), the difference is more significant. This discrepancy obtained with the present results arises from the assumption of an ideal fluid, where viscous effects and flow separation due to the OWC

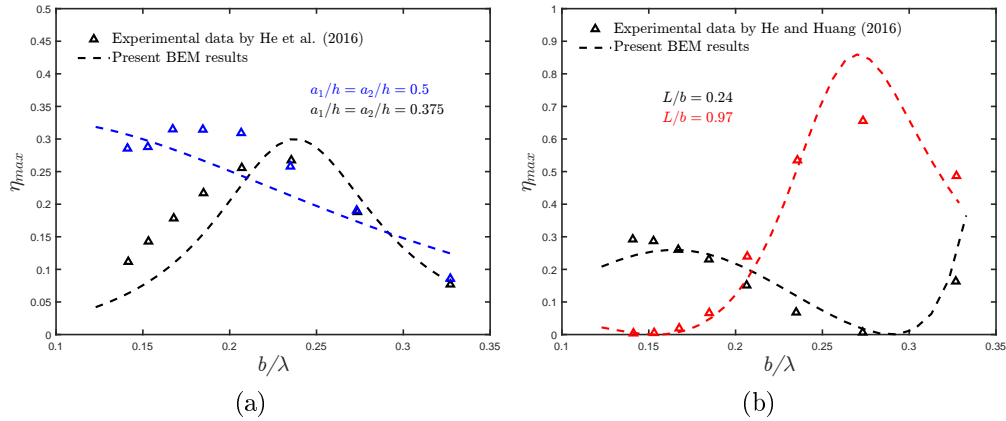


Figure 7.4: Comparison of the present results for the hydrodynamic efficiency  $\eta_{max}$  with the experimental results obtained by He et al. (2016) for a pile-supported OWC device and He and Huang (2016) for an OWC device near a reflecting vertical wall.

structure are ignored. This also leads to an overestimation of the hydrodynamic performance. Other factors that also contribute to the discrepancy are the modelled PTO system, as well as the energy loss through it by viscous dissipation during the tests.

## 7.7 Results and Discussion

Analytical and numerical results based on the previously described methodologies are provided in this section. The influence of the rear and front walls thickness to water depth ratio ( $w_1/h, w_2/h$ ), the chamber length to water depth ratio ( $b/h$ ), the rear and front walls draft to water depth ratio ( $a_1/h, a_2/h$ ), the step height to water depth ratio ( $h_e/h$ ) and the chamber to wall distance to water depth ratio ( $L/h$ ) on the hydrodynamic performance are analyzed.

### 7.7.1 Asymmetric fixed-detached OWC device over a flat bottom

The theoretical results of the hydrodynamic efficiency  $\eta_{max}$  versus  $Kh$  for different chamber lengths  $b/h (= 1/4, 1/2, 3/4, \text{ and } 1)$  are shown in Figure 7.5a. It can be seen in this figure that increasing the length of the chamber increases the bandwidth of the efficiency curves. In this regard, large motions occur in the internal water column when the fluid is excited into a resonant piston-like motion by the incident wave (Evans and Porter; 1995). The natural frequency of oscillation can be calculated for small values of the  $b/h$  ratio, allowing the water enclosed within the chamber to be treated as a solid body. By simple hydrostatic modelling, it results that the expected resonance occurs at  $Kh \approx h/a_1$ . For the cases shown in Figure 7.5a, this resonance would occur at  $Kh = 2$ , which appears to be approached for small  $b/h$ . Furthermore, it is observed that for large  $b/h$  ratios, the peak frequency value is shifted to lower frequencies. This is because increasing the chamber length increases the horizontal distance a fluid particle

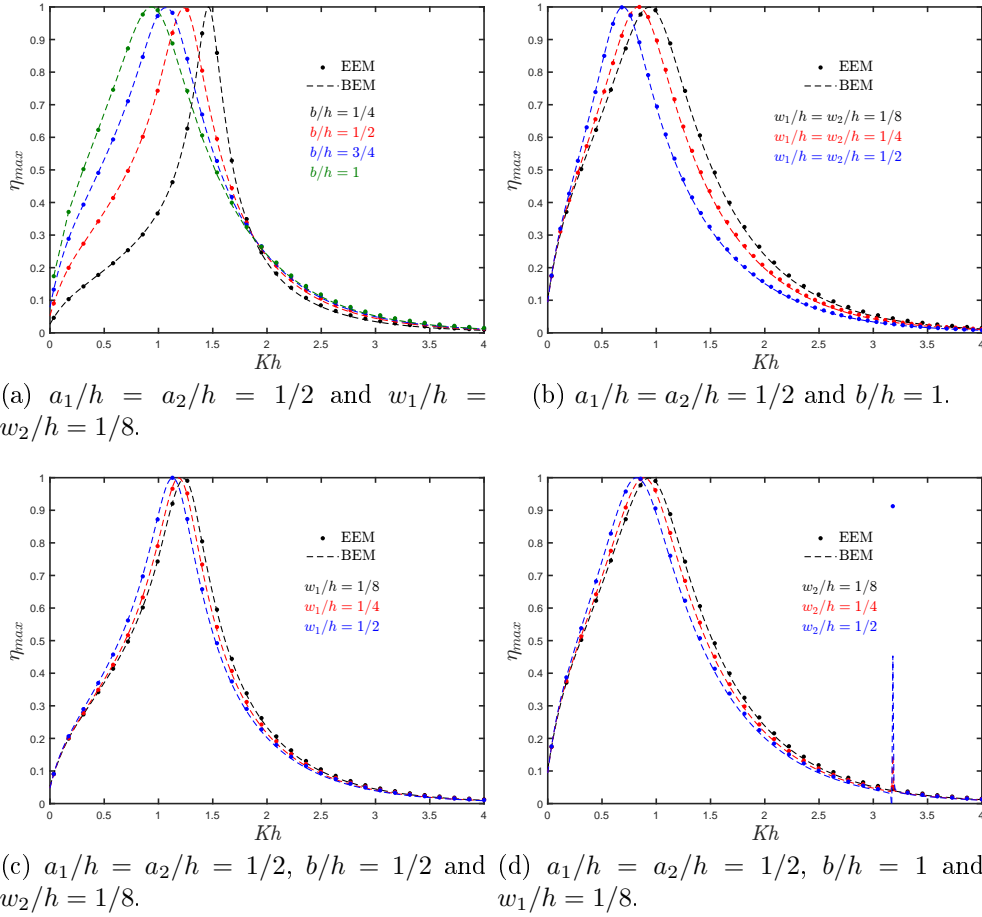


Figure 7.5: Maximum hydrodynamic efficiency  $\eta_{max}$  versus the non-dimensional frequency  $Kh$  for different (a) lengths of the OWC chamber  $b/h$ , (b) thickness of the rear and front walls,  $w_1/h$  and  $w_2/h$ , respectively. (c) thickness of the rear wall  $w_1/h$  and (d) thickness of the front wall  $w_2/h$ .

CHAPTER 7. THE INFLUENCE OF THE CHAMBER CONFIGURATION ON  
THE EFFICIENCY OF A FIXED-DETACHED OWC DEVICE

---

must travel during a period of motion, resulting in a reduction in the value at which resonance occurs. Furthermore, since a longer chamber allows for a greater local fluid motion, the solid-body concept of resonance breaks down, and the oscillation amplitude decreases (Evans and Porter; 1995).

The results of the hydrodynamic efficiency versus the non-dimensional frequency  $Kh$  for different thickness ratios of the front and rear walls  $w_1/h = w_2/h (= 1/8, 1/4, \text{ and } 1/2)$  are shown in Figure 7.5b. This figure shows that the bandwidth of the efficiency curves is reduced as the thickness of the walls is increased, and their peak frequency value is moved to lower values of the non-dimensional frequency  $Kh$ . This drop in efficiency at medium and high frequencies can be explained by the fact that the energy transfer due to wave motion for relatively small wavelengths decreases as wall thickness increases. On the other hand, Figures 7.5c and 7.5d show the variation of  $\eta_{max}$  versus  $Kh$  for different thicknesses of the rear and front walls, respectively. Similar to Figure 7.5b, in these figures is observed that the bandwidth of the efficiency and the peak frequency magnitude decrease when the thickness of the front or rear walls increases. Furthermore, a second resonance peak that occurs when conditions are similar to those in a closed tank with parallel walls is observed in Figure 7.5d. In such conditions, the incidence wave frequency is such that the fluid in the chamber is excited in an anti-symmetric sloshing mode (Evans and Porter; 1995). In this case, the sloshing frequencies are seen to occur at values of the dimensionless wavenumber  $kb = n\pi$ , with  $n$  being the sloshing mode. Thus, the second peaks in  $\eta_{max}$  caused by the first sloshing frequency occur at  $Kh \approx \pi$  for  $b/h = 1$ .

Figure 7.6a shows the effect on the efficiency of different submergence ratios  $a_1/h = a_2/h (= 1/8, 1/4, 1/2, \text{ and } 3/4)$  versus  $Kh$ . This figure shows that the effective area under the efficiency curve and the magnitude of the natural frequency both increase when the walls submergence ratio  $a_1/h$  and  $a_2/h$  decreases. However, while a small draft results in a better performance for a wider frequency range, in practice, tidal fluctuations and extreme waves may compromise its effectiveness since a small draft may mean that the trough of a wave propagates below the front wall. In this instance, the pressure inside the chamber would be equivalent to the ambient pressure, resulting in no power available within the OWC device. Furthermore, Figures 7.6b and 7.6c show the variation of  $\eta_{max}$  versus  $Kh$  for an asymmetric OWC device with different drafts of the front and rear walls, respectively. As in Figure 7.6a, these figures show that the bandwidth of the efficiency and the peak frequency magnitude decrease when the submergence of the front or rear walls increase. Additionally, in Figure 7.6b a second resonance mechanism due to the first sloshing frequency at  $Kh \approx \pi$  for  $b/h = 1$  is observed.

Figures 7.7a–c show the analytical results for the radiation susceptance and radiation conductance coefficients,  $\mu$  and  $\nu$ , respectively, and the non-dimensional induced volume flux due to the scattering potential  $|q^S|/|q^I|$  versus  $Kh$  for different values of  $b/h (= 1/4, 1/2, 3/4, \text{ and } 1)$ . Figure 7.7a shows that the peak and the range of positive values in the radiation susceptance coefficient increase when chamber length increases. From Figure 7.7b it is observed that the bandwidth in the radiation conductance curves decreases as  $b/h$  increases, similar to the trend observed in  $\eta_{max}$ , see Figure 7.5a. Moreover, the zero values in  $\mu$  are associated with the peak values in  $\nu$ ,  $|q^S|/|q^I|$ , Figure 7.7c, and  $\eta_{max}$ , due to the fundamental resonance inside the chamber.



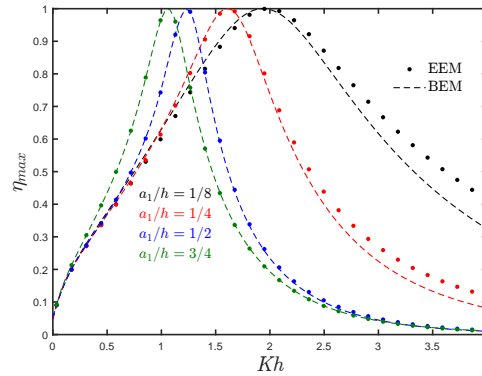
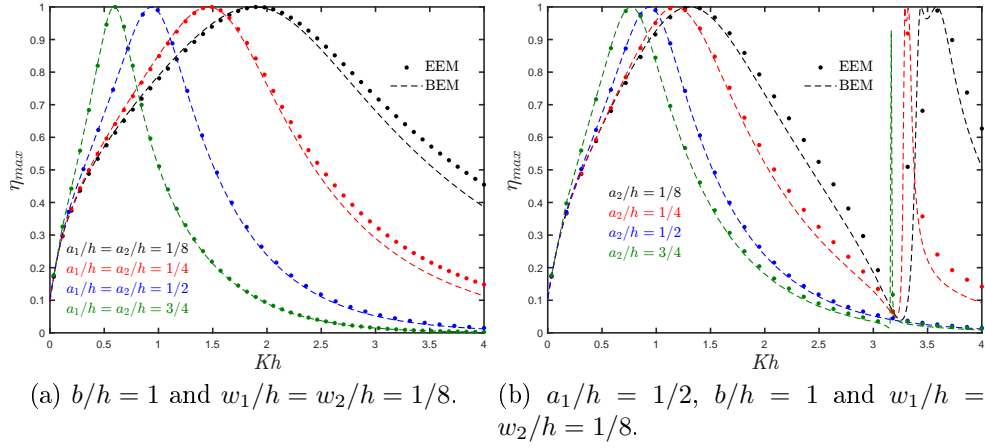


Figure 7.6: Maximum hydrodynamic efficiency  $\eta_{max}$  versus the non-dimensional frequency  $Kh$  for different (a) submergence depths of the rear and front walls,  $a_1/h$  and  $a_2/h$ , respectively. (b) submergence depths of the front wall  $a_2/h$  and (c) submergence depths of the rear wall  $a_1/h$ .

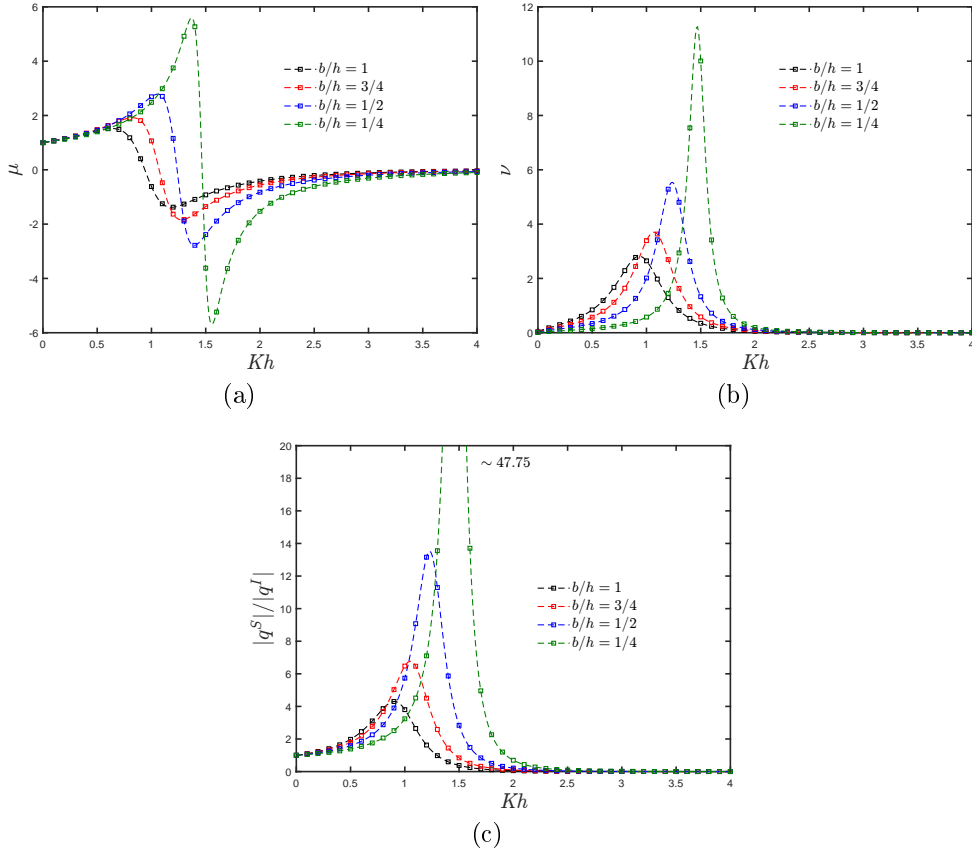
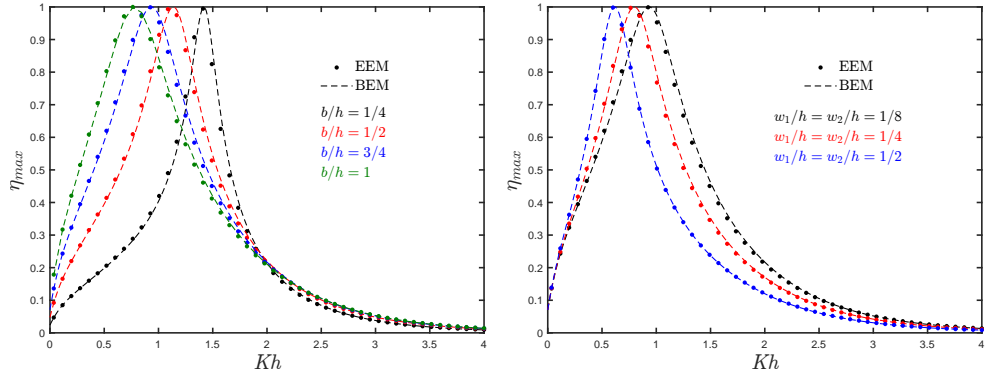
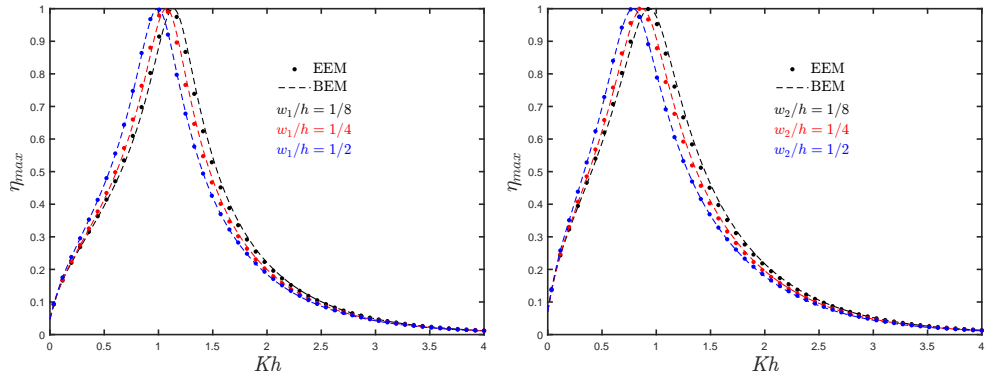


Figure 7.7: The influence of chamber length  $b/h$  on the (a) radiation susceptibility coefficient, (b) radiation conductance coefficient and (c) non-dimensional induced volume flux due to the scattering potential against  $Kh$  with  $a_1/h = a_2/h = 1/2$  and  $w_1/h = w_2/h = 1/8$ .



(a)  $a_1/h = a_2/h = 1/2$ ,  $h_e/h = 3/4$  and  $w_1/h = w_2/h = 1/8$ . (b)  $a_1/h = a_2/h = 1/2$ ,  $b/h = 3/4$  and  $h_e/h = 3/4$ .



(c)  $a_1/h = a_2/h = 1/2$ ,  $b/h = 1/2$ ,  $h_e/h = 3/4$  and  $w_2/h = 1/8$ . (d)  $a_1/h = a_2/h = 1/2$ ,  $b/h = 3/4$ ,  $h_e/h = 3/4$  and  $w_1/h = 1/8$ .

Figure 7.8: Maximum hydrodynamic efficiency  $\eta_{max}$  versus the non-dimensional frequency  $Kh$  for different (a) lengths of the OWC chamber  $b/h$ , (b) thickness of the rear and front walls,  $w_1/h$  and  $w_2/h$ , respectively. (c) thickness of the rear wall  $w_1/h$  and (d) thickness of the front wall  $w_2/h$ .

### 7.7.2 Asymmetric fixed-detached OWC device over a step

Figure 7.8a shows the analytical and numerical results of the hydrodynamic efficiency  $\eta_{max}$  versus  $Kh$  for different chamber lengths to water depth ratios  $b/h$  ( $= 1/4, 1/2, 3/4,$  and  $1$ ). This figure shows that the value of the resonance peak frequency decreases when the length of the chamber increases and, compared to the case when  $h_e/h = 1$  (Figure 7.5a), it is observed that the step contributes to a reduction in the value of  $Kh$  at which resonance occurs.

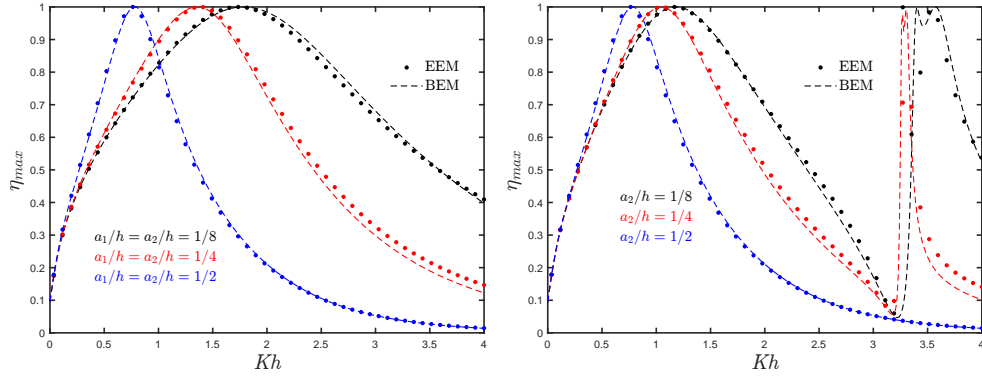
Figure 7.8b shows the theoretical results of the hydrodynamic efficiency versus the non-dimensional frequency  $Kh$  for different thickness ratios of the front and rear walls  $w_1/h = w_2/h$  ( $= 1/8, 1/4,$  and  $1/2$ ). In this case, it is seen that a reduction in the bandwidth of the efficiency curves is obtained when the thickness of the walls increases. Moreover, it is also observed that the magnitude of the resonance frequency  $Kh$  is reduced since, for a large thickness, longer waves are needed to excite the internal water column. On the other hand, the variation of  $\eta_{max}$  versus  $Kh$  for different thicknesses of the rear and front walls are shown in Figures 7.8c and 7.8d, respectively. Again, it is observed that whether the thickness of the rear or front wall increases, the resonance frequency  $Kh$  is reduced.

The effects of different submergence ratios  $a_1/h = a_2/h$  ( $= 1/8, 1/4,$  and  $1/2$ ) on the efficiency versus  $Kh$  are shown in Figure 7.9a. It is observed that performance for higher frequencies increases when the submergence ratio  $a_1/h$  and  $a_2/h$  decreases in the rear and front walls, respectively. Compared to Figure 7.6a where a flat bottom is considered, in this case, the value of the peak frequency is slightly decreased since the gap between the lip of the walls and the bottom is reduced. On the other hand, the variations of  $\eta_{max}$  versus  $Kh$  for different drafts of the front and rear walls are shown in Figures 7.9b and 7.9c, respectively. These figures show that the hydrodynamic performance is sensitive to variations in the draft of the walls, reducing its magnitude for high frequencies as the submergence increases. In Figure 7.9b it is also observed a second resonance mechanism at  $Kh \approx \pi$  as in Figure 7.6b, while in Figure 7.9c this will take place at  $Kh \approx 2\pi$  since  $b/h = 1/2$ .

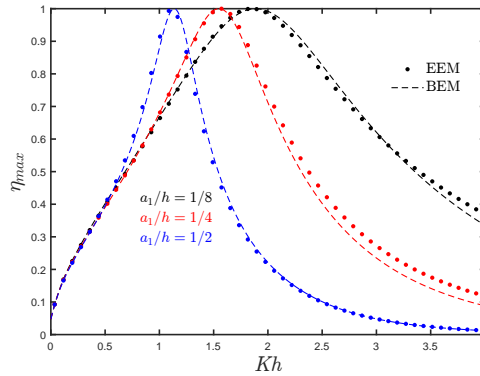
Figures 7.10a–c show the analytical results for the radiation susceptance and radiation conductance coefficients,  $\mu$  and  $\nu$ , respectively, and the non-dimensional induced volume flux due to the scattering potential  $|q^S|/|q^I|$  versus  $Kh$  for different values of  $w_1/h = w_2/h$  ( $= 1/8, 1/4,$  and  $1/2$ ). In Figure 7.10a it is observed the peak in  $\mu$  increases when the thickness in the walls also increases, while the peak shifts to the lower-frequency side. However, it is observed that the range of negative values increases as the thickness increases. Figure 7.10b shows that the curve in the radiation conductance coefficient becomes sharper as the thickness increases, which indicates a reduction in the frequency range for the energy transfer into the system. A decreasing trend in the peak of the non-dimensional induced volume flux due to the scattering potential when the thickness decreases is observed in Figure 7.10c.

### 7.7.3 Asymmetric fixed-detached OWC device near a reflecting wall

The analytical and numerical results of the hydrodynamic efficiency  $\eta_{max}$  versus  $Kh$  for an OWC device in the presence of a reflection wall with different chamber length to water depth



(a)  $b/h = 1$ ,  $h_e/h = 3/4$  and  $w_1/h = w_2/h = 1/8$ . (b)  $a_1/h = 1/2$ ,  $b/h = 1$ ,  $h_e/h = 3/4$  and  $w_1/h = w_2/h = 1/8$ .



(c)  $a_2/h = 1/2$ ,  $b/h = 1/2$ ,  $h_e/h = 3/4$  and  $w_1/h = w_2/h = 1/8$ .

Figure 7.9: Maximum hydrodynamic efficiency  $\eta_{max}$  versus the non-dimensional frequency  $Kh$  for different (a) submergence depths of the rear and front walls,  $a_1/h$  and  $a_2/h$ , respectively. (b) submergence depths of the front wall  $a_2/h$  and (c) submergence depths of the rear wall  $a_1/h$ .

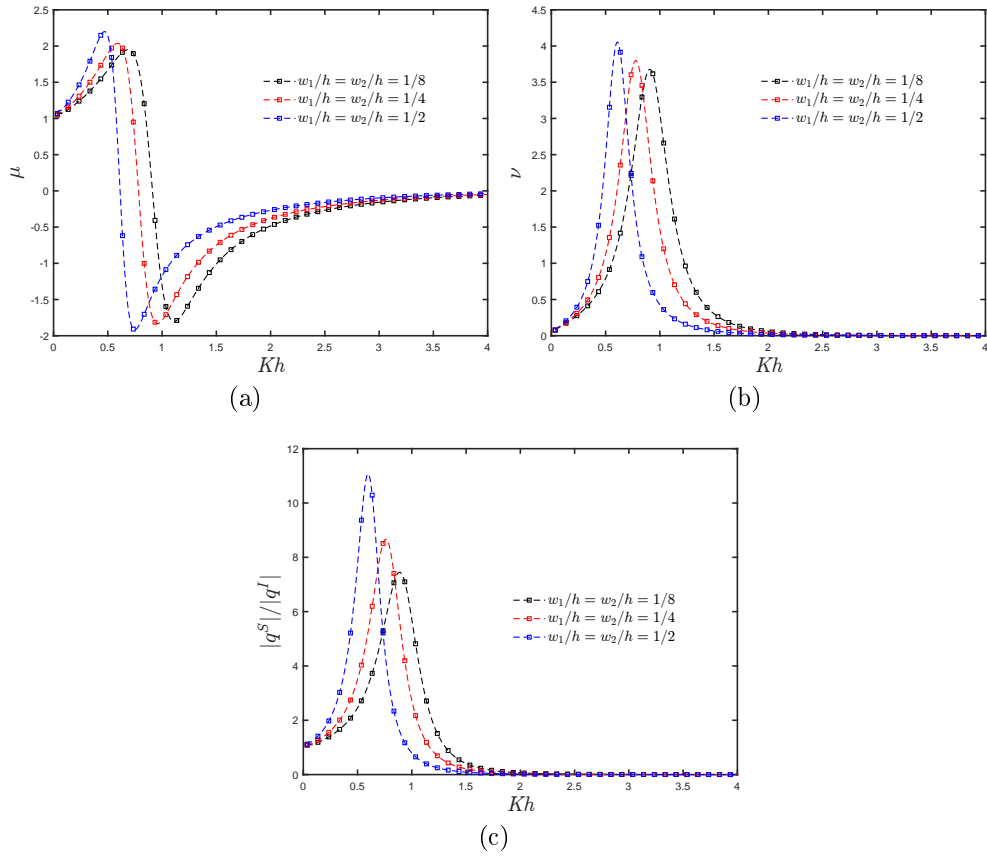


Figure 7.10: The influence of the thickness in the rear and front walls,  $w_1/h$  and  $w_2/h$ , respectively, on the (a) radiation susceptibility coefficient, (b) radiation conductance coefficient and (c) non-dimensional induced volume flux due to the scattering potential against  $Kh$  with  $a_1/h = a_2/h = 1/2$ ,  $b/h = 3/4$  and  $h_e/h = 3/4$ .

CHAPTER 7. THE INFLUENCE OF THE CHAMBER CONFIGURATION ON  
THE EFFICIENCY OF A FIXED-DETACHED OWC DEVICE

---

ratios  $b/h$  ( $= 1/4, 1/2, 3/4$ , and  $1$ ) are shown in Figure 7.11a. Compared to Figure 7.5a, it is observed that the efficiency bandwidth is reduced when a reflecting wall is considered. In this case, it is observed that due to the near trapped waves in the gap between the OWC chamber and the rigid vertical wall, a medium-height peak at low frequencies appears in the efficiency curves. This peak increases as the chamber length to water depth ratio increases. Furthermore, a zero efficiency value appears at  $0.45 < Kh < 0.61$  that reduces the possibility of wave energy extraction at large periods.

The results of the hydrodynamic efficiency versus  $Kh$  for various thickness ratios  $w_1/h = w_2/h$  ( $= 1/8, 1/4$ , and  $1/2$ ) are shown in Figure 7.11b. It is observed that an increase in the thickness of the walls, leads to both reduction of the bandwidth of the efficiency curves and the peak frequency value. Furthermore, it is seen that when  $w_1/h$  and  $w_2/h$  increase, the medium-height peak slightly increases, while the zero efficiency value is shifted to lower frequencies.

Figure 7.11c shows that with an increase in the rear wall thickness, the medium-height peak at low frequencies and the resonant frequency value of maximum efficiency both decrease. On the other hand, in Figure 7.11d for  $b/h = 1/2$ , it is observed that the bandwidth of the efficiency curves is highly reduced and the medium-height peak is increased when the front wall thickness increases. Furthermore, Figures 7.6a–d show a second resonance mechanism due to the first sloshing frequency at  $Kh \approx \pi$ .

The effect of different draft ratios  $a_1/h = a_2/h$  ( $= 1/8, 1/4$ , and  $1/2$ ) on the efficiency versus  $Kh$  for a symmetric OWC device is shown in Figure 7.12a. It is observed that the peak resonant frequency and the efficiency bandwidth are significantly reduced when the ratios  $a_1/h$  and  $a_2/h$  increase. Furthermore, the frequency value of zero efficiency increases and the peak at low frequencies decreases when the submergence in the front and rear walls decreases.

The variations of maximum efficiency  $\eta_{max}$  versus the non-dimensional frequency  $Kh$  for different drafts of the rear and front walls are shown in Figures 7.12b and 7.12c, respectively. In both of them, it is observed that by increasing the submergence of one of the walls, the values of the frequency at which resonance occurs are decreased. However, in Figure 7.12b, the efficiency bandwidth is increased when the submergence of the front wall decreases, while the peak at low frequencies decreases. On the other hand, in terms of the medium-height peak, Figure 7.12c shows an opposite trend to that observed in Figure 7.12b.

The results of the hydrodynamic efficiency versus the non-dimensional frequency  $Kh$  for different lengths of the gap between the rear and reflecting walls  $L/h$  ( $= 1, 2, 3$ , and  $4$ ) are shown in Figures 7.13a and 7.13b. In these two figures, it is observed that the bandwidth of the efficiency increases, while the medium-height peak at low frequencies reduces when the distance of separation between the fixed OWC and the reflecting wall increases. It is also observed that at  $L/h = 3$  and  $4$ , the shape of the curve tend to that observed in Figure 7.5a for  $b/h = 1$ , although a peaky trend is observed for  $L/h = 4$ . All these aspects should be considered at the design stage since the near trapped waves generated between the reflecting wall and the OWC device can reduce the efficiency bandwidth of a fixed-detached OWC device at high periods.

The analytical results for the radiation susceptance and radiation conductance coefficients,  $\mu$  and  $\nu$ , respectively, and the non-dimensional induced volume flux due to the scattering potential  $|q^S|/|q^I|$  versus the non-dimensional frequency  $Kh$  for different values of  $L/h$  ( $= 1, 2, 3$ , and  $4$ ) are shown in Figures 7.14a–d. Figure 7.14a shows a decrease in the negative values of  $\mu$  when the

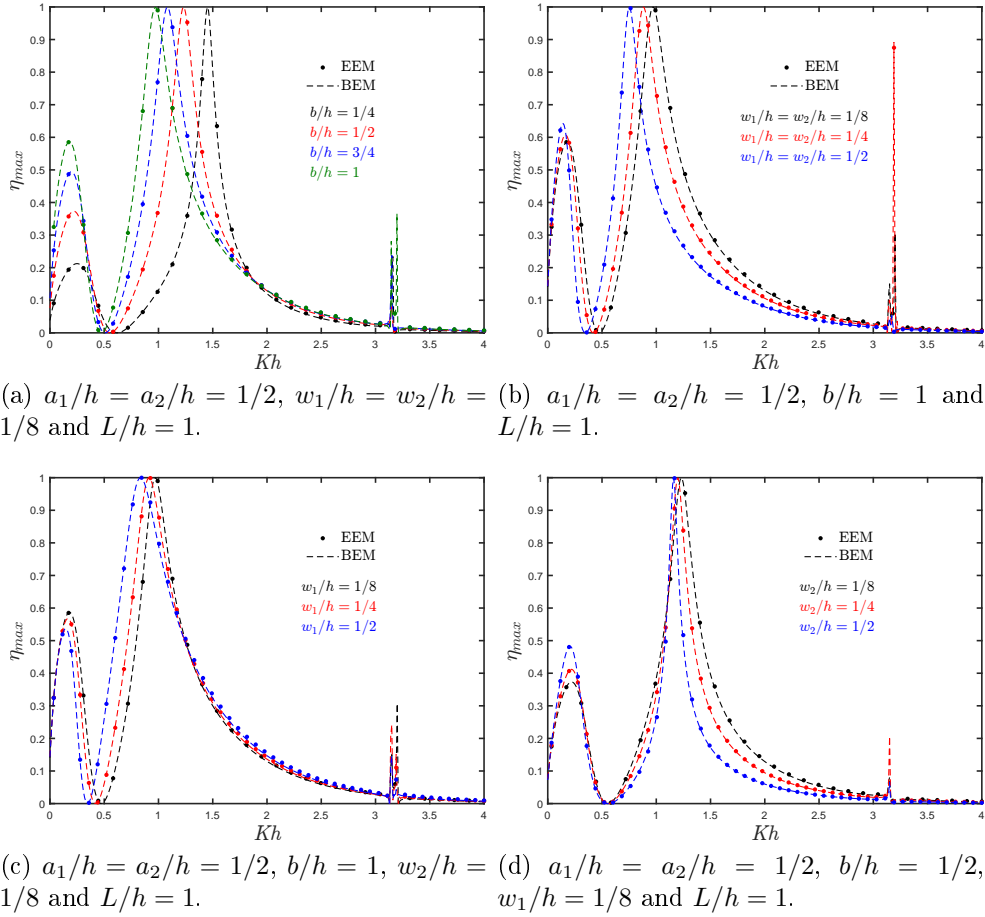
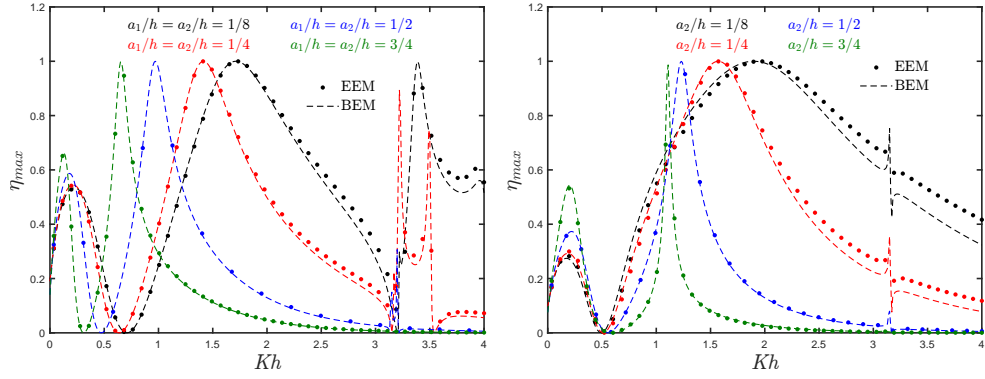
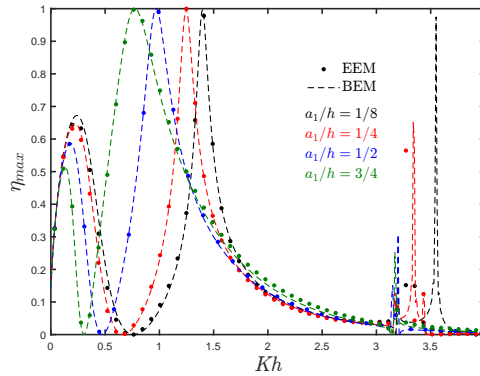


Figure 7.11: Maximum hydrodynamic efficiency  $\eta_{max}$  versus the non-dimensional frequency  $Kh$  for different (a) lengths of the OWC chamber  $b/h$ , (b) thickness of the rear and front walls,  $w_1/h$  and  $w_2/h$ , respectively. (c) thickness of the rear wall  $w_1/h$  and (d) thickness of the front wall  $w_2/h$ .





(a)  $b/h = 1$ ,  $w_1/h = w_2/h = 1/8$  and (b)  $a_1/h = 1/2$ ,  $b/h = 1/2$ ,  $w_1/h = w_2/h = 1/8$  and  $L/h = 1$ .



(c)  $a_2/h = 1/2$ ,  $b/h = 1$ ,  $w_1/h = w_2/h = 1/8$  and  $L/h = 1$ .

Figure 7.12: Maximum hydrodynamic efficiency  $\eta_{max}$  versus the non-dimensional frequency  $Kh$  for different (a) submergence depths of the rear and front walls,  $a_1/h$  and  $a_2/h$ , respectively. (b) submergence depths of the front wall  $a_1/h$  and (c) submergence depths of the rear wall  $a_2/h$ .

gap between the rear and reflecting walls also decreases. As in [Evans and Porter \(November 1997\)](#), in Figures 7.14a and 7.14b it is observed that at resonance, the total variation from positive to negative in the radiation susceptance coefficient is related to the peak values of the radiation conductance. Finally, from Figures 7.14b and 7.14c it is observed that the peak in  $\nu$  and  $|q^S|/|q^I|$ , respectively, at the fundamental resonance increase when  $L/h$  decrease.

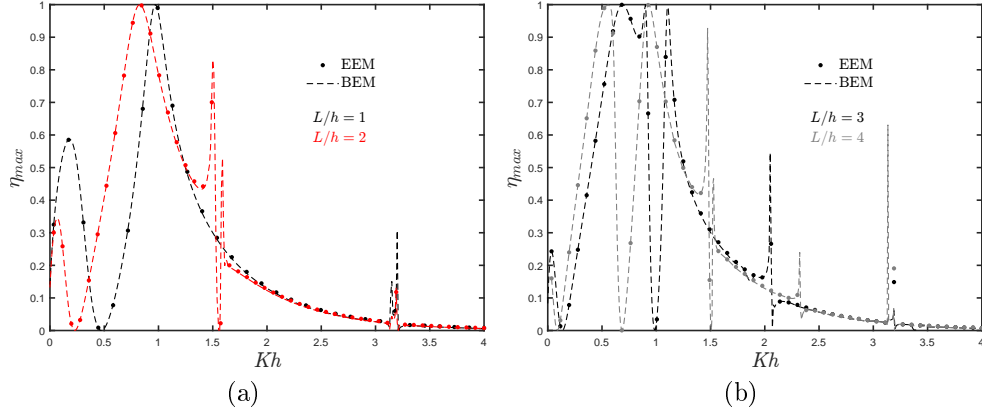


Figure 7.13: The influence of the length of the gap between the rear and reflecting walls  $L/h$  on the maximum hydrodynamic efficiency  $\eta_{max}$  versus the non-dimensional frequency  $Kh$  with  $a_1/h = a_2/h = 1/8$ ,  $b/h = 1$  and  $w_1/h = w_2/h = 1/8$ .

## 7.8 Conclusions

The influence of the geometric parameters of an asymmetric fixed-detached OWC device on the hydrodynamic efficiency was theoretically analyzed. The BEM with quadratic elements and the matched EEM were employed to solve the radiation and scattering problems. Comparisons were made between these two methods and a good agreement was obtained. A comparison was made between the experimental data of [He et al. \(2016\)](#); [He and Huang \(2016\)](#) giving a satisfactory agreement. Results for different hydrodynamic quantities of interest were then obtained for different physical configurations. The main conclusions of this study are:

- An increase in the chamber length leads to an increase in the bandwidth of the efficiency curves. This is similar to the findings for a land-fixed OWC device reported by [Evans and Porter \(1995\)](#).
- By increasing the thickness of the rear and front walls, the bandwidth of the efficiency curves and their peak frequency value are reduced. This reduction in efficiency, especially for short wavelengths, is due to the decrease in energy transfer owing to the wave motion when a large thickness is considered.

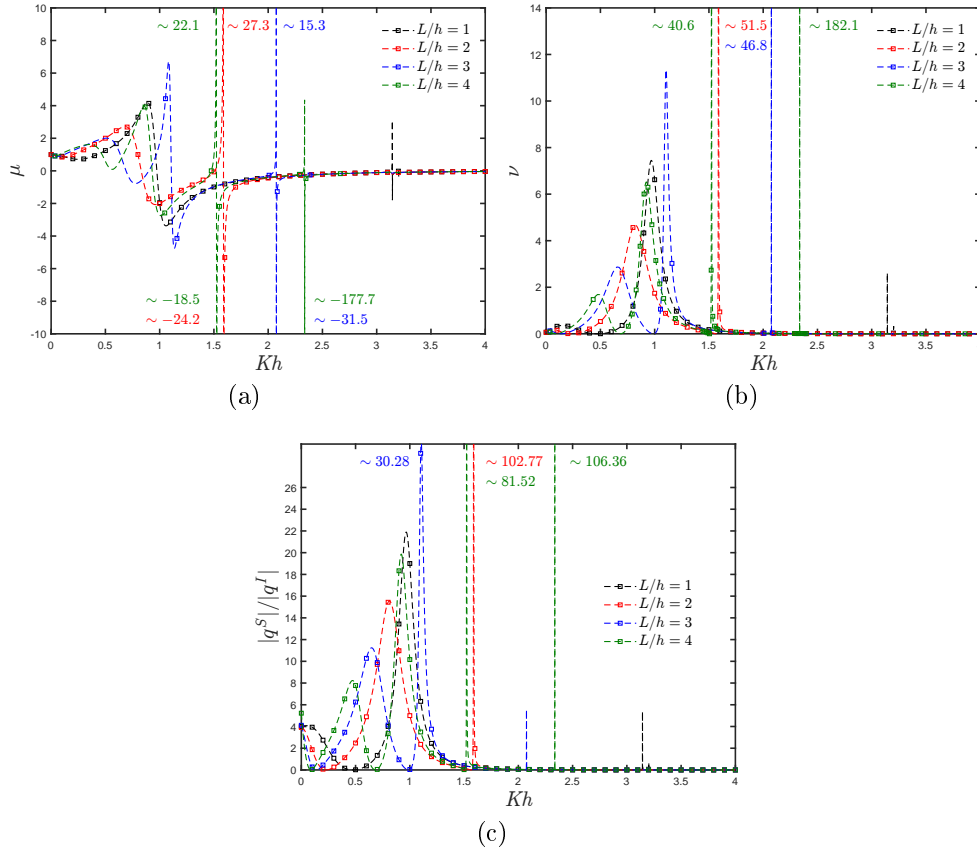


Figure 7.14: The influence of the length of the gap between the rear and reflecting walls  $L/h$  on the (a) radiation susceptance coefficient, (b) radiation conductance coefficient and (c) non-dimensional induced volume flux due to the scattering potential against  $Kh$  with  $a_1/h = a_2/h = 1/8$ ,  $b/h = 1$  and  $w_1/h = w_2/h = 1/8$ .

## CHAPTER 7. THE INFLUENCE OF THE CHAMBER CONFIGURATION ON THE EFFICIENCY OF A FIXED-DETACHED OWC DEVICE

---

- Both the effective area under the efficiency curves and the magnitude of the natural frequency increase when the submergence of the walls decreases. This is because a larger gap between the front wall lip and the bottom allows more energy to be transferred to the water column.
- Regarding the presence of a step, it was observed that this reduces the frequency at which resonance occurs since the effect is similar to reducing the gap between the lip of the walls and the bottom.
- When the separation distance is shorter, the near trapped and standing waves in the gap of the OWC chamber and the reflecting wall play a significant role in the hydrodynamic performance. It was observed that the efficiency bandwidth is reduced, and a medium-height peak appears at low frequencies.
- At low frequencies, the presence of constructive and destructive wave interference from the OWC device and the waves reflected by the wall results in zero efficiency. This phenomenon is extremely sensitive to changes in the OWC parameters and engineers should take it into account when constructing a fixed-detached OWC device near a vertical wall.

Finally, this work is only a theoretical investigation of the hydrodynamic performance of a fixed-detached OWC device. The construction of a fixed-detached OWC device near a rigid vertical wall may constitute an alternative for reducing the wave load on seawalls by absorbing the incident wave energy and can be extended to include an array of fixed-detached OWC devices. Numerical simulations and experimental tests of other geometrical conditions and non-linearities on the air compressibility and turbine damping due to viscous effects should be carried out in the future to improve the present results.

## Bibliography

- Becker, A. (1992). *The Boundary Element Method in Engineering: A Complete Course*, McGraw-Hill.  
**URL:** <https://books.google.com.mx/books?id=Co9YAAAAYAAJ>
- Calheiros-Cabral, T., Clemente, D., Rosa-Santos, P., Taveira-Pinto, F., Ramos, V., Morais, T. and Cestaro, H. (2020). Evaluation of the annual electricity production of a hybrid breakwater-integrated wave energy converter, *Energy* **213**: 118845.  
**URL:** <http://www.sciencedirect.com/science/article/pii/S0360544220319526>
- Deng, Z., Ou, Z., Ren, X., Zhang, D. and Si, Y. (2020). Theoretical analysis of an asymmetric offshore-stationary oscillating water column device with bottom plate, *Journal of Waterway, Port, Coastal, and Ocean Engineering* **146**(4): 04020013.
- Deng, Z., Wang, C., Wang, P., Higuera, P. and Wang, R. (2019). Hydrodynamic performance of an offshore-stationary owc device with a horizontal bottom plate: Experimental and

CHAPTER 7. THE INFLUENCE OF THE CHAMBER CONFIGURATION ON  
THE EFFICIENCY OF A FIXED-DETACHED OWC DEVICE

---

- numerical study, *Energy* **187**: 115941.  
**URL:** <https://www.sciencedirect.com/science/article/pii/S0360544219316251>
- Dominguez, J. (1993). *Boundary Elements in Dynamics*, Computational Engineering, Computational Mechanics Publications.  
**URL:** <https://books.google.com.mx/books?id=N4ghw092NIMC>
- Elhanafi, A., Fleming, A., Macfarlane, G. and Leong, Z. (2017a). Numerical hydrodynamic analysis of an offshore stationary–floating oscillating water column–wave energy converter using cfd, *International Journal of Naval Architecture and Ocean Engineering* **9**(1): 77–99.  
**URL:** <https://www.sciencedirect.com/science/article/pii/S2092678216304290>
- Elhanafi, A., Fleming, A., Macfarlane, G. and Leong, Z. (2017b). Underwater geometrical impact on the hydrodynamic performance of an offshore oscillating water column–wave energy converter, *Renewable Energy* **105**: 209–231.  
**URL:** <https://www.sciencedirect.com/science/article/pii/S0960148116310953>
- Elhanafi, A. and Kim, C. J. (2018). Experimental and numerical investigation on wave height and power take-off damping effects on the hydrodynamic performance of an offshore–stationary owc wave energy converter, *Renewable Energy* **125**: 518–528.  
**URL:** <https://www.sciencedirect.com/science/article/pii/S0960148118302830>
- Elhanafi, A., Macfarlane, G., Fleming, A. and Leong, Z. (2017). Investigations on 3d effects and correlation between wave height and lip submergence of an offshore stationary owc wave energy converter, *Applied Ocean Research* **64**: 203–216.  
**URL:** <https://www.sciencedirect.com/science/article/pii/S0141118716302917>
- Şentürk, U. and Özdamar, A. (2012). Wave energy extraction by an oscillating water column with a gap on the fully submerged front wall, *Applied Ocean Research* **37**: 174 – 182.  
**URL:** <http://www.sciencedirect.com/science/article/pii/S0141118712000405>
- Evans, D. and Porter, R. (1995). Hydrodynamic characteristics of an oscillating water column device, *Applied Ocean Research* **17**(3): 155 – 164.  
**URL:** <http://www.sciencedirect.com/science/article/pii/0141118795000089>
- Evans, D. and Porter, R. (November 1997). Efficient calculation of hydrodynamic properties of owc-type devices, *ASME Journal of Offshore Mechanics and Arctic Engineering* **119**(4): 210–218.
- Evans, D. V. (1976). A theory for wave-power absorption by oscillating bodies, *Journal of Fluid Mechanics* **77**(1): 1–25.
- Evans, D. V. (1981). Power from water waves, *Annual Review of Fluid Mechanics* **13**(1): 157–187.  
**URL:** <https://doi.org/10.1146/annurev.fl.13.010181.001105>

CHAPTER 7. THE INFLUENCE OF THE CHAMBER CONFIGURATION ON  
THE EFFICIENCY OF A FIXED-DETACHED OWC DEVICE

---

- Evans, D. V. (1982). Wave-power absorption by systems of oscillating surface pressure distributions, *Journal of Fluid Mechanics* **114**: 481–499.
- Falcão, A. F. and Henriques, J. C. (2016). Oscillating-water-column wave energy converters and air turbines: A review, *Renewable Energy* **85**: 1391 – 1424.  
**URL:** <http://www.sciencedirect.com/science/article/pii/S0960148115301828>
- Falcão, A. F., Henriques, J. C. and Cândido, J. J. (2012). Dynamics and optimization of the owc spar buoy wave energy converter, *Renewable Energy* **48**: 369–381.  
**URL:** <https://www.sciencedirect.com/science/article/pii/S0960148112003229>
- Falcão, A. F. O. (2010). Wave energy utilization: A review of the technologies, *Renewable Sustainable Energy Rev.* **14**(3): 899 – 918.  
**URL:** <http://www.sciencedirect.com/science/article/pii/S1364032109002652>
- Falnes, J. and McIver, P. (1985). Surface wave interactions with systems of oscillating bodies and pressure distributions, *Applied Ocean Research* **7**(4): 225–234.  
**URL:** <https://www.sciencedirect.com/science/article/pii/014111878590029X>
- Gato, L. and de O. Falcão, A. (1988). Aerodynamics of the wells turbine, *International Journal of Mechanical Sciences* **30**(6): 383–395.  
**URL:** <https://www.sciencedirect.com/science/article/pii/0020740388900124>
- Gunn, K. and Stock-Williams, C. (2012). Quantifying the global wave power resource, *Renewable Energy* **44**: 296 – 304.  
**URL:** <http://www.sciencedirect.com/science/article/pii/S0960148112001310>
- He, F. and Huang, Z. (2016). Using an oscillating water column structure to reduce wave reflection from a vertical wall, *Journal of Waterway, Port, Coastal, and Ocean Engineering* **142**(2): 04015021.
- He, F., Li, M. and Huang, Z. (2016). An experimental study of pile-supported owc-type breakwaters: Energy extraction and vortex-induced energy loss, *Energies* **9**(7).
- He, F., Zhang, H., Zhao, J., Zheng, S. and Iglesias, G. (2019). Hydrodynamic performance of a pile-supported owc breakwater: An analytical study, *Applied Ocean Research* **88**: 326–340.  
**URL:** <https://www.sciencedirect.com/science/article/pii/S0141118719300719>
- Iturrioz, A., Guanche, R., Armesto, J., Alves, M., Vidal, C. and Losada, I. (2014). Time-domain modeling of a fixed detached oscillating water column towards a floating multi-chamber device, *Ocean Engineering* **76**: 65–74.  
**URL:** <https://www.sciencedirect.com/science/article/pii/S0029801813004253>
- Iturrioz, A., Guanche, R., Lara, J., Vidal, C. and Losada, I. (2015). Validation of openfoam® for oscillating water column three-dimensional modeling, *Ocean Engineering* **107**: 222–236.  
**URL:** <https://www.sciencedirect.com/science/article/pii/S0029801815003649>

CHAPTER 7. THE INFLUENCE OF THE CHAMBER CONFIGURATION ON  
THE EFFICIENCY OF A FIXED-DETACHED OWC DEVICE

---

- Katsikadelis, J. (2002). *Boundary Elements. Theory and Applications*, Elsevier.
- Medina-Lopez, E., Allsop, W., Dimakopoulos, A. and Bruce, T. (2015). *Conjectures on the Failure of the OWC Breakwater at Mutriku*, pp. 592–603.  
**URL:** <https://ascelibrary.org/doi/abs/10.1061/9780784480304.063>
- Medina Rodríguez, A. A., Blanco Ilzarbe, J. M., Silva Casarín, R. and Izquierdo Ereño, U. (2020). The influence of the chamber configuration on the hydrodynamic efficiency of oscillating water column devices, *Journal of Marine Science and Engineering* **8(10)**: 751.
- Medina Rodríguez, A. A., Martínez Flores, A., Blanco Ilzarbe, J. M. and Silva Casarín, R. (2021). Interaction of oblique waves with an oscillating water column device, *Ocean Engineering* **228**: 108931.  
**URL:** <https://www.sciencedirect.com/science/article/pii/S0029801821003668>
- Mei, C. C. (1976). Power Extraction from Water Waves, *Journal of Ship Research* **20(02)**: 63–66.  
**URL:** <https://doi.org/10.5957/jsr.1976.20.2.63>
- Michele, S., Renzi, E., Perez-Collazo, C., Greaves, D. and Iglesias, G. (2019). Power extraction in regular and random waves from an owc in hybrid wind-wave energy systems, *Ocean Engineering* **191**: 106519.  
**URL:** <https://www.sciencedirect.com/science/article/pii/S0029801819306572>
- Morris-Thomas, M. T., Irvin, R. J. and Thiagarajan, K. P. (2006). An Investigation Into the Hydrodynamic Efficiency of an Oscillating Water Column, *Journal of Offshore Mechanics and Arctic Engineering* **129(4)**: 273–278.  
**URL:** <https://doi.org/10.1115/1.2426992>
- Qu, M., Yu, D., Dou, Z. and Wang, S. (2021). Design and experimental study of a pile-based breakwater integrated with owc chamber, *China Ocean Engineering* **35**: 443–453.
- Rezanejad, K., Bhattacharjee, J. and Guedes Soares, C. (2013). Stepped sea bottom effects on the efficiency of nearshore oscillating water column device, *Ocean Engineering* **70**: 25 – 38.  
**URL:** <http://www.sciencedirect.com/science/article/pii/S0029801813002229>
- Rezanejad, K., Guedes Soares, C., López, I. and Carballo, R. (2017). Experimental and numerical investigation of the hydrodynamic performance of an oscillating water column wave energy converter, *Renewable Energy* **106**: 1 – 16.  
**URL:** <http://www.sciencedirect.com/science/article/pii/S0960148117300034>
- Sarmiento, A. (1992). Wave flume experiments on two-dimensional oscillating water column wave energy devices, *Experiments in Fluids* (12): 286–292.
- Simonetti, I., Cappiotti, L., Elsafti, H. and Oumeraci, H. (2017). Optimization of the geometry and the turbine induced damping for fixed detached and asymmetric owc devices: A numerical

CHAPTER 7. THE INFLUENCE OF THE CHAMBER CONFIGURATION ON  
THE EFFICIENCY OF A FIXED-DETACHED OWC DEVICE

---

study, *Energy* **139**: 1197–1209.

**URL:** <https://www.sciencedirect.com/science/article/pii/S0360544217314111>

Sundar, S. K. V. and Sannasiraj, S. (2021). Hydrodynamic performance characteristics of an oscillating water column device integrated with a pile breakwater, *Journal of Ocean Engineering and Marine Energy* **7**: 229–241.

Wang, D., Katory, M. and Li, Y. (2002). Analytical and experimental investigation on the hydrodynamic performance of onshore wave-power devices, *Ocean Engineering* **29**(8): 871 – 885.

**URL:** <http://www.sciencedirect.com/science/article/pii/S0029801801000580>

Zabihi, M., Mazaheri, S. and Namin, M. M. (2019). Experimental hydrodynamic investigation of a fixed offshore oscillating water column device, *Applied Ocean Research* **85**: 20–33.

**URL:** <https://www.sciencedirect.com/science/article/pii/S0141118718304383>



## Chapter 8

# The Effects of Directional Waves and Chamber Configuration on the Efficiency of an OWC Device

So far, all calculations and analyses provided in this thesis for an OWC device have been conducted by separating the impacts of front wall thickness and water wave directionality. However, better performance of the OWC system will be assured by the right construction of the OWC chamber to ensure its survivability and a good tuning of the OWC natural frequency of oscillation with that of the oblique waves at the place where the OWC device will be deployed. As a result, the primary goal of this chapter is to investigate the combined impacts of oblique waves and chamber configuration by using both numerical and analytical approaches in order to answer the following research question: How much is the performance of a land-fixed OWC device affected by both oblique sea waves and the thickness of the front wall?

This chapter consists of the submitted journal article:

Medina Rodríguez A.A., Silva Casarín R., Blanco Ilzarbe J.M. (2021). “*The influence of oblique waves on the hydrodynamic efficiency of an onshore OWC wave energy converter*”. **Renewable Energy**. Under Review.

**The influence of oblique waves on the hydrodynamic efficiency of an onshore OWC wave energy converter**

Ayrton Alfonso Medina Rodríguez, Rodolfo Silva Casarín and Jesús María Blanco Ilzarbe

**Abstract**

In this work, the maximum theoretical hydrodynamic efficiency of an onshore Oscillating Water Column (OWC) device is investigated in relation to the incidence angle of the wave and the configuration of the chamber. Linearized water wave theory is used, and the full solution of the associated boundary value problem (BVP) is achieved by using the matched eigenfunction expansion method (EEM) and the boundary element method (BEM). This study is novel in addressing the influence of oblique water waves on the efficiency of an OWC with a thick front barrier. The hydrodynamic efficiency is analyzed for different directions of wave incidence and OWC chamber geometrical configurations. The semi-analytical and numerical approaches were found to be in good agreement with cases published in the specialized literature. The results show that both a thick front wall and a large incidence angle of the wave can significantly narrow the hydrodynamic efficiency band and modify the resonant frequency.

## 8.1 Introduction

Ocean wave energy has been suggested as a potential renewable source for attenuating the effect of global warming and supplying a significant portion of the electricity needs of the rapidly increasing world population (Pecher and Kofoed; 2017; Mishra et al.; 2020; Melikoglu; 2018). The estimated global energy resource for ocean waves is about 2.1 TW (Gunn and Stock-Williams; 2012), corresponding to approximately 18 400 TWh available annually, and equivalent to roughly 80% of the worldwide electricity demand in 2018 (Calheiros-Cabral et al.; 2020). However, although ocean waves have demonstrated to be one of the most abundant renewable energy resources, this clean resource remains virtually unharnessed (Howe and Nader; 2017). This is due to a wider tendency towards other clean resources (Melikoglu; 2018), insufficient funding for research (Mishra et al.; 2020), the unmaturing of current technologies and the lack of a reliable and cost-effective energy extraction technology from sea waves (Sheng; 2019; EC; 2016).

This clean resource energy has attracted numerous inventors who have proposed a wide variety of wave extraction technologies. The earliest of such technology was reported in France in 1799 by a father and a son named Girard, and to date, more than a thousand of wave energy technologies have been patented (Falcão; 2010; Ross; 2012). Particularly, the navigation buoys powered by wave energy, which were invented and developed in the 1940s by the former Japanese navy officer Yoshio Masuda, are regarded as the most successful systems for wave energy utilisation (Masuda; 1986; Sheng; 2019; Falcão; 2010). These navigation buoys are known, under the current terminology of wave energy technologies, as (floating) oscillating water columns devices, although they were first known as Masuda devices following the inventor's name (Sheng; 2019; Ross; 2012).

## CHAPTER 8. THE EFFECTS OF DIRECTIONAL WAVES AND CHAMBER CONFIGURATION ON THE EFFICIENCY OF AN OWC DEVICE

---

The technology currently available for wave energy is divided into four categories. These are attenuators, point absorbers, overtopping terminators, and oscillating wave column terminators (Mahnamfar and Altunkaynak; 2017). Among the proposed wave energy converters (WEC), the OWC stands out from the rest of technologies due to its practicability and inherent working principle. The main advantage of this device versus most other WECs is its simplicity, probably making it the most thoroughly studied system with the highest number of prototypes deployed into the sea so far (Falcão; 2010). Basically, OWC systems consist only of two main components: a partially submerged collecting chamber and a Power Take-Off (PTO) system, typically a turbine whose rotor is the only moving part of the mechanism for the extraction of energy and which is positioned above the water level to prevent direct exposure to seawater. It also possesses a basic working principle where the water column inside the collecting chamber is forced to vertically oscillate like a piston due to the incident waves, driving the confined airflow back and forth through a turbine in a duct coupled to a generator and connected to the atmosphere (Falcão; 2010; Service; 2007).

The OWC device is a worldwide well-established WEC system and it is expected to continue contributing to the progression of wave energy harnessing (Doyle and Aggidis; 2019). Due to its versatility, it possesses different design variations (shore-mounted, sea-bed and floating systems) which allowed it to be deployed onshore, nearshore and offshore. Particularly, the onshore OWC system is a fixed wave converter, which is generally designed to be mounted on the coast or integrated into already existing or in-development ocean structures such as breakwaters (Teixeira and Didier; 2021; Howe and Nader; 2017; Vicinanza et al.; 2019). Since one of the greatest issues of OWC systems is the economical aspect (Lin et al.; 2015), this integration offers some cost-reduction advantages as construction and maintenance costs are shared, the operation of the power plant becomes more accessible and it prevents the use of mooring systems and underwater electric cables. Additionally, the energy absorption into the OWC collecting chamber contributes to coastal protection, decreases the disruption of vessel traffic at port entrances and improves the hydraulic performance of the breakwater by reducing the wave reflection. Although less energetic waves are found compared to open and deep seas, these are less costly to exploit and wave energy can be more naturally concentrated towards the system due to shoaling, refraction and diffraction (Polinder and Scuotto; 2005).

The onshore OWC systems are basically designed to be a form of terminator device, where their principal axis is perpendicular to the predominant wave direction to gather most energy (Drew et al.; 2009). However, in real sea conditions, water waves direction is hardly perpendicular with respect to the OWC chamber transverse axis (Jin et al.; 2012). This can be in part due to the orientation of the OWC system and to the reflection and refraction of the waves generated by the shoreline and the surrounding bathymetry. The Mutriku Oscillating Water Column Energy Plant, located in Gipuzkoa (northern Spain), is an example of this, where the boomerang-shaped breakwater that houses the OWC power plant is north-northeast oriented and makes the sixteen chambers face the mostly north-western incoming sea waves at a different angle (Ibarra-Berastegi et al.; 2018). As a result, although the structural design of the chamber is the same, the pneumatic power produced on each of the 14 Wells turbines that operate varies.

In this sense, a critical condition in achieving maximum pneumatic power at the turbine is

## CHAPTER 8. THE EFFECTS OF DIRECTIONAL WAVES AND CHAMBER CONFIGURATION ON THE EFFICIENCY OF AN OWC DEVICE

---

by having the device operate as near to the resonance condition as possible. Resonance takes place when the incident wave frequency coincides with the natural frequency of the converter. For this purpose, the design of the OWC chamber plays an important role to operate optimally at resonance. Usually, the geometrical configuration of the chamber is chosen to generate a column whose natural oscillation frequency coincides with that of the most occurring wave at the position where the OWC will be installed (Delmonte et al.; 2016). In this sense, the variability of sea state conditions can affect the feasibility of the OWC, since the size and shape of the structure can hardly be modified once built.

The absorption of wave energy by OWC systems is a technically complicated hydrodynamic mechanism in which relatively complex diffraction and radiation wave processes take place (Falcão; 2010). A large part of the work on onshore OWC systems published in the last three decades was on theoretical hydrodynamics with a focus on the OWC-water wave interaction considering normal wave propagation towards the device (Evans and Porter; 1995; Morris-Thomas et al.; 2006; Şentürk and Özdamar; 2012; Rezanejad et al.; 2013; Koley and Trivedi; 2020). Wang et al. (2002) investigated the hydrodynamic performance of an OWC type shoreline-mounted wave energy device by using the BEM. The numerical model was validated through an experimental campaign and the authors reported that as the bottom slope increases, the peaks of the capture-width ratios will shift to lower values of frequency, while the effect on the OWC performance due to the change in water depth at the shoreline is significant. Morris-Thomas et al. (2006) experimentally studied the effect of front wall geometry on the OWC hydrodynamic efficiency. They found that the front wall geometry does not greatly influence the overall peak hydrodynamic efficiency but it does affect the overall shape and bandwidth of the efficiency curve. Martins-rivas and Mei (2009) theoretically studied the effects of coastline on wave power absorption of an OWC device installed on a straight coast. They reported that the shore reflection roughly doubles the energy absorption, while the considered PTO produces a higher efficiency over a broad frequency band. By carrying out experimental campaigns, Dizadji and Sajadian (2011) studied various geometrical designs of an OWC system to obtain the optimized configuration for the maximum energy harness. The authors reported that by decreasing the angle of the front wall, a considerable increment in the air outflow from the chamber is observed, while the parallel arrangement of the front and back walls resulted in a relative maximization of the air outflow. The theoretical analysis of an OWC with a gap on its fully submerged front wall was studied by Şentürk and Özdamar (2012) and found that by choosing the appropriate geometrical parameters, it is possible to improve the OWC efficiency with a surface piercing barrier type front wall.

Rezanejad et al. (2013) analyzed the impact of stepped bottom topography in the efficiency of a nearshore OWC. In their work, the authors reported that the inclusion of a properly tuning artificial step at the sea bottom could significantly increase the capacity of power absorption. The performance of a fixed OWC device based on a time-domain higher-order BEM in a 2D fully nonlinear numerical wave flume was investigated by Ning et al. (2015), and it was found that the geometric parameters of the air chamber play a significant role on the hydrodynamic efficiency. An experimental investigation of the influence of four different bottom profiles (flat, circular, curved and sloped) on the OWC hydrodynamic performance was carried out by John Ashlin et al. (2016). The authors concluded that the natural frequency of the system was unaltered by

## CHAPTER 8. THE EFFECTS OF DIRECTIONAL WAVES AND CHAMBER CONFIGURATION ON THE EFFICIENCY OF AN OWC DEVICE

---

these four profiles, while a better performance in terms of its effective wave energy conversion was obtained for a circular curve bottom profile. [Ning, Wang, Zou and Teng \(2016\)](#) experimentally studied the hydrodynamic performance of a fixed OWC device. The authors reported that the bottom slope has a little influence on the resonant frequency, while the optimal hydrodynamic efficiency increases with an increase of bottom slope. [Mahnamfar and Altunkaynak \(2017\)](#) performed both a numerical model and an experimental campaign to analyze the effect of the OWC geometrical configuration on its optimization. [Malara et al. \(2017\)](#) carried out a numerical analysis of the three-dimensional effects affecting the U-OWC performance and showed that 3D effects are significant when the device width is smaller than 20 m, which results in an improvement in power output per unit width.

[Zheng, Zhang and Iglesias \(2019\)](#) proposed a theoretical model to study the performance of a circular cylindrical OWC along a vertical coast/breakwater considering the thickness of the chamber wall. It was found that the incidence wave direction and the thickness of the chamber wall both influence the wave power captured by the OWC. A theoretical model to evaluate the hydrodynamic performance of multiple circular cylinder OWCs installed along a vertical straight coast was developed by [Zheng, Antonini, Zhang, Greaves, Miles and Iglesias \(2019\)](#). The authors found that the OWC hydrodynamic performance of the array was enhanced significantly for a certain range of wave conditions due to the constructive wave interference from the OWCs array and the coast. [Zheng et al. \(2020\)](#) developed an analytical model to study an OWC integrated into a tubular structure. They demonstrated that a small wall thickness of the chamber offers benefits for wave power extraction while increasing the height of the opening leads to a broader efficiency band. A coupled EEM-BEM analysis of the hydrodynamic performance of an OWC device placed on an undulated seabed was carried out by [Koley and Trivedi \(2020\)](#) and concluded that the OWC structural and bottom configuration can significantly enhance the hydrodynamic efficiency. [Belibassakis et al. \(2020\)](#) developed a 2D BEM model for analyzing the OWC response in general bathymetry regions and showed that the effects of the bottom slope and curvature on the performance can be relevant. [Medina Rodríguez et al. \(2020\)](#) numerically analyzed the effects of the front wall thickness and the bottom profile of an OWC device on its efficiency and found that an increment on the thickness can significantly reduce the efficiency bandwidth.

Recently, [Teixeira and Didier \(2021\)](#) developed a numerical analysis of an onshore OWC device to investigate differences of random incident waves from regular ones in the OWC performance. They reported that the OWC efficiency of regular and random waves reaches a difference of 28% around the resonance with small differences at high wave periods. A numerical analysis of the performance of two OWC devices at the different front and back wall slopes was carried out by [Gaspar et al. \(2020\)](#) and found that an OWC with inclined walls is more efficient than an OWC with vertical walls. The influence of the compressibility effect on the air inside the OWC chamber was investigated via a numerical model by [Gonçalves et al. \(2020\)](#) and the authors showed that air compressibility, which is generally ignored in small scale experiments and numerical simulations, has a significant influence on the OWC performance. [Zhu et al. \(2020\)](#) employed a 2D numerical wave tank based on the weakly compressible smoothed particle hydrodynamics (SPH) method to investigate the performance of an OWC. The authors found that an OWC with thinner walls has a better performance in terms of power absorption.

Although the above-listed works have the ability to quantify the hydrodynamic performance, both the water wave obliquity and the thickness of the front barrier are not accounted for by the formulations for onshore land-fixed OWC systems. A further theoretical study of the previously investigated onshore OWC studies is the model considered in this work and is restricted to neither normal wave propagation nor a thin front wall OWC device. This is in order to examine its effect on the OWC performance and thereby to provide additional possibilities for enhancing the efficiency of onshore OWC systems in different sea states. The basic hypothesis of the present research is that these two aspects play a significant role in hydrodynamic efficiency band and the peak resonant frequency.

The linear wave theory for a constant sea depth is used under the potential flow method and the viscous effects and nonlinear air compressibility are ignored. To solve the associated BVP, two different mathematical techniques are presented. The first is the well-known semi-analytic matched EEM, where, along with the orthogonal property of the eigenfunctions, the continuity of velocity potential and flux was used to reduce the BVP into a linear system of algebraic equations. The other one is the BEM, which is a numerical technique based on the application of an integral equation. Here, to account for the variation of the potential and flux on the boundaries, the BEM with three-noded elements will be used. Throughout this work, findings obtained by these approaches are compared and validation is accomplished by recovering prior reported cases of [Evans and Porter \(1995\)](#) and [Medina Rodríguez et al. \(2020\)](#). The aims of this analysis are to examine the modification in bandwidth on the efficiency curves and the shifting on the peak resonant frequency due to the obliquity of incident waves interacting with an OWC system with a thick front wall. Analytical and numerical calculations for the hydrodynamic efficiency are then presented and analyzed for a range of different non-dimensional parameters.

## 8.2 Boundary value problem

The fluid-OWC structure system and the Cartesian coordinate system with the  $z$ -axis pointing upwards and the  $x - y$  plane on the mean position of the free surface are shown in Fig. 8.1. The origin of the coordinate system is located on the undisturbed free surface in water of depth  $h$ . The waves approach the land-fixed-OWC device from  $x$  direction making an angle  $\theta$  with the  $x$ -axis. The OWC is modelled by a surface-piercing barrier at  $x = b$ , with draft  $h_a$  and thickness  $w$ , and a rigid wall located at  $x = 0$ . The trapped air inside the chamber with a height  $h_c$  is assumed to be connected to the atmosphere by a turbine. To only consider the 2-dimensional case, the OWC is assumed to be infinitely long and parallel to the incoming wave crest.

The domain is separated into three regions: Region 1 ( $0 \leq x \leq b, -h \leq z \leq 0$ ) defines the fluid inside the OWC chamber; Region 2 ( $b \leq x \leq f_w, -h \leq z \leq h_a$ ) delimits the fluid below the front barrier; and Region 3 ( $b \leq x < \infty, -h \leq z \leq 0$ ) the fluid out of the OWC structure. We denote the thick-front barrier by  $B_b = \{(x, z) : (x = b, -h_a \leq z \leq 0) \cup (b < x < f_w, z = -h_a) \cup (x = f_w, -h_a \leq z \leq 0)\}$ , the rigid vertical wall by  $B_w = \{(x, z) : x = 0, -h < z < 0\}$ , the internal free surface inside the chamber by  $F_i = \{(x, z) : 0 \leq x \leq b, z = 0\}$ , the external free surface by  $F_f = \{(x, z) : f_w \leq x \leq \infty, z = 0\}$ , the flat bottom by  $B_d =$

CHAPTER 8. THE EFFECTS OF DIRECTIONAL WAVES AND CHAMBER CONFIGURATION ON THE EFFICIENCY OF AN OWC DEVICE

$\{(x, z) : (0 < x < \infty, z = -h)\}$  and the vertical length of the gap below the barrier by  $B_g = \{(x, z) : x = b, -h \leq z \leq -h_a\}$ .

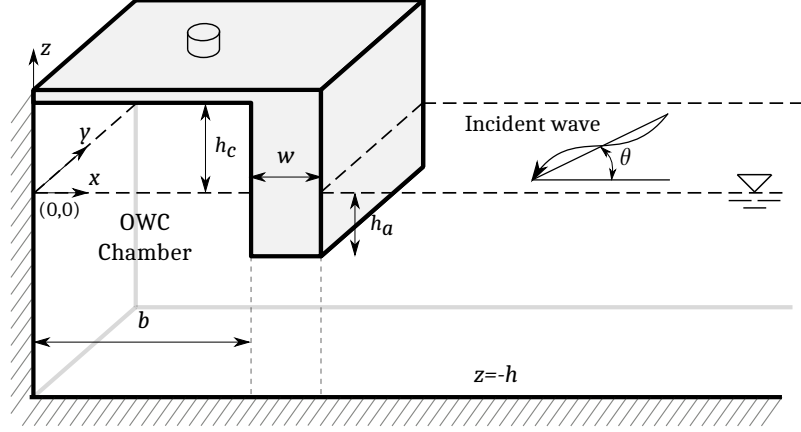


Figure 8.1: Definition sketch of the interaction of a thick front barrier OWC device with oblique waves.

The seawater is assumed inviscid and incompressible, and the flow is irrotational. The wave motion is considered to be represented adequately by the linearized wave theory, disregarding surface tension effects and hence potential theory is used. By assuming a simple harmonic flow with angular frequency  $\omega$ , we define a velocity potential  $\Phi(x, z, t)$  with  $\Phi(x, z, t) = \text{Re}\{\phi(x, z)e^{-i\omega t + i\kappa y}\}$ , where  $\text{Re}\{\}$  denotes the real part of a complex expression,  $\beta = k \sin \theta$ ,  $k$  is the wavenumber of the plane progressive wave and  $t$  is the time. Under the assumptions above, the spatial velocity potential  $\phi$  satisfies the Helmholtz equation

$$\left( \frac{\partial^2}{\partial x^2} + \frac{\partial^2}{\partial z^2} - \beta^2 \right) \phi = 0, \quad (8.1)$$

with the no-flow boundary conditions applied at the bottom, the thick-front barrier and the left-rigid vertical wall as

$$\frac{\partial \phi}{\partial n} = 0 \quad \text{for } (x, z) \in B_d, B_b \text{ and } B_w, \quad (8.2)$$

respectively. The continuity of pressure and horizontal velocity on both lateral sides of the gap are given by

$$\phi_- = \phi_+ \quad \text{and} \quad \frac{\partial \phi}{\partial x_-} = \frac{\partial \phi}{\partial x_+} \quad \text{on } x = b \text{ and } f_w \quad \text{with} \quad -h \leq z \leq -h_a, \quad (8.3)$$

where  $f_w = b + w$ .

The internal and external linearized free surface boundary conditions are

$$\frac{\partial \phi}{\partial z} - K\phi = \begin{cases} \frac{i\omega p}{\rho g} & \text{on } z = 0, \quad 0 < x < b, \\ 0 & \text{on } z = 0, \quad f_w < x < \infty, \end{cases} \quad (8.4)$$

CHAPTER 8. THE EFFECTS OF DIRECTIONAL WAVES AND CHAMBER  
CONFIGURATION ON THE EFFICIENCY OF AN OWC DEVICE

---

respectively, where  $p$  is the harmonic pressure distribution in the internal free surface,  $K = \omega^2/g$ , with  $g$  being the gravitational constant and  $\rho$  the seawater density.

Following the methodology proposed by Evans (1982), the velocity potential is separated into a scattered potential  $\phi^S$  and a radiated potential  $\phi^R$  as follows

$$\phi(x, z) = \phi^S + \frac{i\omega p}{\rho g} \phi^R, \quad (8.5)$$

where  $\phi^S$  satisfies Eqs. (8.1)–(8.4) with  $p = 0$  inside the chamber; while  $\phi^R$  satisfies Eqs. (8.1)–(8.4) with Eq. (8.4) replaced by

$$\frac{\partial \phi^R}{\partial z} - K \phi^R = 1 \quad \text{on} \quad z = 0, \quad 0 < x < b. \quad (8.6)$$

The Sommerfeld radiation condition is imposed at the right-hand end ( $x \rightarrow +\infty$ ) of the domain

$$\frac{\partial \phi^{D,R}}{\partial x} - ik \cos \theta \phi^{D,R} = 0 \quad \text{as} \quad x \rightarrow +\infty, \quad (8.7)$$

where  $\phi^D$  represents the diffracted potential that together with the incident potential  $\phi^I$  composed the scattered potential  $\phi^S$ , while the wavenumber  $k$  is the positive real root of the wave dispersion relation given by

$$\omega^2 = gk \tanh kh. \quad (8.8)$$

As previously done with the velocity potential, the time harmonic induced volume flux across  $S_i$  is also decomposed into scattering and radiation volume fluxes,  $q^S$  and  $q^R$ , respectively, as follows

$$q = \int_{F_i} \frac{\partial \phi}{\partial z} dx = q^S + \frac{i\omega p}{\rho g} q^R, \quad (8.9)$$

while the continuity of volume flux across the internal free surface and the gap bellow the barrier tip is ensured by

$$q^{S,R} = \int_{F_i} \frac{\partial \phi^{S,R}}{\partial z} dx = \int_{B_g} \frac{\partial \phi^{S,R}}{\partial x} dz. \quad (8.10)$$

In the next section, the solution procedures for the BVP are described.

## 8.3 Solution method

### 8.3.1 Matched Eigenfunction Expansion Method

#### Definition of velocity potentials

In this subsection, the solution procedure for the radiation and the scattering problems based on the matched EEM is described. In the case of the radiation problem, by employing the



CHAPTER 8. THE EFFECTS OF DIRECTIONAL WAVES AND CHAMBER  
CONFIGURATION ON THE EFFICIENCY OF AN OWC DEVICE

---

method of separation of variables, the velocity potentials in the three regions are represented by the eigenfunctions expansions as

$$\phi_1^R(x, z) = B_0^R \cos k_x x \Psi_0(z) + \sum_{n=1}^{\infty} B_n^R \cosh k_{nx} x \Psi_n(z) - \frac{1}{K}, \quad (8.11a)$$

$$\phi_2^R(x, z) = \sum_{n=0}^{\infty} \left[ C_n^R \frac{\cosh \gamma_{nx} (f_w - x)}{\cosh \gamma_{nx} w} + D_n^R \frac{\sinh \gamma_{nx} (f_w - x)}{\sinh \gamma_{nx} w} \right] \chi_n(z), \quad (8.11b)$$

$$\phi_3^R(x, z) = A^R e^{ik_x(x-f_w)} \Psi_0(z) + \sum_{n=1}^{\infty} A_n^R e^{-k_{nx}(x-f_w)} \Psi_n(z), \quad (8.11c)$$

for Regions 1, 2 and 3, respectively, and where  $k_x = \sqrt{k^2 - \beta^2}$ ,  $k_{nx} = \sqrt{k_n^2 + \beta^2}$  and  $\gamma_{nx} = \sqrt{(n\pi/(h-h_a))^2 + \beta^2}$  for  $n = 0, 1, \dots$ . Additionally, the term  $-1/K$  on  $\phi_1^R$  was introduced to satisfy Eq. (8.6) and the coefficients  $A^R$ ,  $A_n^R$  for  $n = 1, 2, \dots$  and  $B_n^R$ ,  $C_n^R$  and  $D_n^R$  for  $n = 0, 1, \dots$  are the unknown constants to be determined. The eigenfunctions  $\Psi$  and  $\chi$  are defined by

$$\Psi_n(z) = \frac{1}{\sqrt{N_n}} \cos k_n (z + h), \quad \text{for } n = 0, 1, 2, \dots, \quad (8.12a)$$

$$\chi_n(z) = \frac{1}{\sqrt{W_n}} \cos n\pi \frac{(z+h)}{h-h_a}, \quad \text{for } n = 0, 1, 2, \dots, \quad (8.12b)$$

where

$$N_n = \frac{1}{2} \left[ 1 + \frac{\sin 2k_n h}{2k_n h} \right], \quad \text{for } n = 0, 1, 2, \dots, \quad (8.13a)$$

$$W_0 = \left[ 1 - \frac{h_a}{h} \right], \quad (8.13b)$$

$$W_n = \frac{1}{2} \left[ 1 - \frac{h_a}{h} \right], \quad \text{for } n = 1, 2, \dots \quad (8.13c)$$

with  $k_0 = ik$  and  $ik_n$  for  $n \geq 1$  indicates the purely imaginary roots of the dispersion relation in  $k$  given by Eq. (8.8). The eigenfunctions  $\Psi_n$  and  $\chi_n$  are orthonormal with respect to the inner product

$$\langle \Psi_n, \Psi_m \rangle = \frac{1}{h} \int_{-h}^0 \Psi_n(z) \Psi_m(z) dz = \delta_{nm}, \quad (8.14a)$$

$$\langle \chi_n, \chi_m \rangle = \frac{1}{h} \int_{-h}^{-h_a} \chi_n(z) \chi_m(z) dz = \delta_{nm}, \quad (8.14b)$$

where  $\delta_{nm}$  is the Kronecker delta.

As described previously for the radiation problem, the velocity potentials for the scattering problem are also expanded in terms of appropriate eigenfunctions. The expansion of velocity

CHAPTER 8. THE EFFECTS OF DIRECTIONAL WAVES AND CHAMBER  
CONFIGURATION ON THE EFFICIENCY OF AN OWC DEVICE

---

potential  $\phi_2^R$  remains exactly the same as in the case of the radiation problem (Eq. 8.11b), while for velocity potentials in Regions 1 and 3, these are expressed as follows

$$\phi_1^S(x, z) = B_0^R \cos k_x x \Psi_0(z) + \sum_{n=1}^{\infty} B_n^R \cosh k_{nx} x \Psi_n(z), \quad (8.15a)$$

$$\phi_3^S(x, z) = \left( e^{-ik_x(x-f_w)} + R e^{ik_x(x-f_w)} \right) \Psi_0(z) + \sum_{n=1}^{\infty} A_n^R e^{-k_{nx}(x-f_w)} \Psi_n(z), \quad (8.15b)$$

where the associated eigenvalues and the eigenfunctions are the same as defined above.

In the special case of normal incidence ( $\theta = 0^\circ$ ), the expansion for the velocity potential  $\phi_2^{R,S}$  in region 2 will take the following form:

$$\phi_2^{R,S}(x, z) = \left( C_0^R + D_0^R \frac{(f_w - x)}{w} \right) \chi_0(z) + \sum_{n=1}^{\infty} \left[ C_n^R \frac{\cosh \gamma_{nx} (f_w - x)}{\cosh \gamma_{nx} w} + D_n^R \frac{\sinh \gamma_{nx} (f_w - x)}{\sinh \gamma_{nx} w} \right] \chi_n(z). \quad (8.16)$$

The far-field behaviour of the scattered and radiated potentials is given by

$$\phi^R \sim A^R e^{ik_x(x-f_w)} \Psi_0(z), \quad \text{as } x \rightarrow +\infty, \quad (8.17)$$

$$\phi^S \sim \left( e^{-ik_x(x-f_w)} + R e^{ik_x(x-f_w)} \right) \Psi_0(z), \quad \text{as } x \rightarrow +\infty \quad (8.18)$$

where  $A^R$  represents the amplitude of the radiated wave to  $+\infty$  while  $R$  the amplitude of the reflected wave in the scattering problem with  $|R| = 1$  since all the incident wave energy is reflected due to the OWC structure.

### Matching of the regions

Now, application of the second matching condition Eq. (8.3) at  $x = f_w$  on the velocity potentials described by Eqs. (8.11b) and (8.11c), together with the boundary condition Eq. (8.2) at  $x = f_w$  and  $0 \leq z \leq -h_a$  applied to the velocity potential Eq. (8.11c), adding their corresponding results, exploiting the orthonormality of the eigenfunctions as defined in Eq. (8.14a) and truncating the infinite series after  $N_{em}$  terms, we have

$$A^R = -\frac{1}{ik_x h} \sum_{n=0}^{N_{em}} \frac{D_n^R \gamma_{nx}}{\sinh \gamma_{nx} w} \int_{-h}^{-h_a} \chi_n(z) \Psi_0(z) dz, \quad \text{for } m = 0, \quad (8.19a)$$

$$A_m^R = \frac{1}{k_{mx} h} \sum_{n=0}^{N_{em}} \frac{D_n^R \gamma_{nx}}{\sinh \gamma_{nx} w} \int_{-h}^{-h_a} \chi_n(z) \Psi_m(z) dz, \quad \text{for } m \geq 1. \quad (8.19b)$$

Next, by using the first matching condition of Eq. (8.3) at  $x = f_w$  with the velocity potentials, Eqs. (8.11b) and (8.11c), exploiting the orthonormality of the eigenfunctions as defined in Eq. (8.14b) and truncating the infinite series, we obtain

$$A^R \int_{-h}^{-h_a} \Psi_0(z) \chi_m(z) dz + \sum_{n=1}^{N_{em}} A_n^R \int_{-h}^{-h_a} \Psi_n(z) \chi_m(z) dz - \frac{C_m^R h}{\cosh \gamma_{nx} w} = 0, \quad \text{for } m \geq 0. \quad (8.20)$$

CHAPTER 8. THE EFFECTS OF DIRECTIONAL WAVES AND CHAMBER  
CONFIGURATION ON THE EFFICIENCY OF AN OWC DEVICE

---

By applying the second matching condition of Eq. (8.3) at  $x = b$  on the velocity potentials of Regions 1 and 2, Eqs. (8.11a) and (8.11b), respectively, in conjunction with the application of boundary condition Eq. (8.2) at  $x = b$  and  $0 \leq z \leq -h_a$  on the velocity potential Eq. (8.11a), adding their results, making use of the orthonormality of the eigenfunctions as given by Eq. (8.14a) and truncating the infinite series after  $N_{em}$  terms, results

$$B_m^R = -\frac{1}{k_{mx}h \sinh k_{mx}b} \sum_{n=0}^{N_{em}} \gamma_{nx} \left[ C_n^R \tanh \gamma_{nx}w + D_n^R \coth \gamma_{nx}w \right] \int_{-h}^{-h_a} \chi_n(z) \Psi_m(z) dz = 0, \quad \text{for } m \geq 0, \quad (8.21)$$

with  $k_{0x} = ik_x$ .

Finally, applying the first matching condition of Eq. (8.3) at  $x = b$  on Eqs. (8.11a) and (8.11b), multiplying by  $\chi_m$ , integrating from  $-h$  to  $-h_a$  and using the orthonormal properties of the eigenfunction  $\chi_m$  (Eq. 8.14b), we obtain

$$-\sum_{n=0}^{N_{em}} B_n^R \frac{\cosh k_{nx}b}{h} \int_{-h}^{-h_a} \Psi_n(z) \chi_m(z) dz + C_m^R + D_m^R = -\frac{1}{Kh} \int_{-h}^{-h_a} \chi_m(z) dz, \quad \text{for } m \geq 0. \quad (8.22)$$

Then, by substituting Eqs. (8.19a) and (8.19b) into Eq. (8.20), yields

$$\begin{aligned} & \frac{C_m^R h}{\cosh \gamma_{mx}w} + \frac{1}{ik_x h} \sum_{n=0}^{N_{em}} \frac{D_n^R \gamma_{nx}}{\sinh \gamma_{nx}w} \int_{-h}^{-h_a} \chi_n(z) \Psi_0(z) dz \int_{-h}^{-h_a} \Psi_0(z) \chi_m(z) dz - \\ & \sum_{n=0}^{N_{em}} \frac{D_n^R \gamma_{nx}}{\sinh \gamma_{nx}w} \sum_{l=1}^{N_{em}} \frac{1}{k_{lx}h} \int_{-h}^{-h_a} \chi_n(z) \Psi_l(z) dz \int_{-h}^{-h_a} \Psi_l(z) \chi_m(z) dz = 0, \quad \text{for } m \geq 0. \end{aligned} \quad (8.23)$$

and substituting Eq. (8.21) into Eq. (8.22), results

$$\begin{aligned} & -\frac{\cot k_x b}{k_x h} \sum_{n=0}^{N_{em}} \left[ C_n^R \gamma_{nx} \tanh \gamma_{nx}w + D_n^R \gamma_{nx} \coth \gamma_{nx}w \right] \int_{-h}^{-h_a} \chi_n(z) \Psi_0(z) dz \int_{-h}^{-h_a} \Psi_0(z) \chi_m(z) dz + \\ & \sum_{l=0}^{N_{em}} \left[ C_l^R \gamma_{lx} \tanh \gamma_{lx}w + D_l^R \gamma_{lx} \coth \gamma_{lx}w \right] \sum_{n=1}^{N_{em}} \frac{\coth k_{nx}b}{k_{nx}h} \int_{-h}^{-h_a} \chi_l(z) \Psi_n(z) dz \int_{-h}^{-h_a} \Psi_n(z) \chi_m(z) dz + \\ & \left( C_m^R + D_m^R \right) h = -\frac{1}{K} \int_{-h}^{-h_a} \chi_m(z) dz, \quad \text{for } m \geq 0. \end{aligned} \quad (8.24)$$

Equations (8.23) and (8.24) provide a linear system of algebraic equations to solve for the unknowns  $C_n^R$  and  $D_n^R$ . The unknowns  $A^R$ ,  $A_n^R$  and  $B_n^R$  can be obtained from Eqs. (8.19a), (8.19b) and (8.21), respectively, once  $C_n^R$  and  $D_n^R$  are determined. In the case of normal incidence, the linear system of algebraic equations for the determination of the unknowns is given in Appendix 8.7. On the other hand, the solution procedure for the scattering problem is similar to the one described above for the radiation problem.

### 8.3.2 Boundary Element Method

#### Boundary integral equation

The boundary integral equation representation of Helmholtz expression (8.1) is of the form

$$\alpha(X)\phi(X) + \int_{\Gamma} \phi(Y) \frac{\partial \psi(X, Y)}{\partial n_Y} d\Gamma_Y = \int_{\Gamma} \psi(X, Y) \frac{\partial \phi(Y)}{\partial n_Y} d\Gamma_Y, \quad (8.25)$$

where  $\phi$  and  $\partial\phi/\partial n$  are, respectively, the unknown velocity potential and its normal derivative with respect to the field point  $Y$  ( $\hat{\xi}, \hat{\eta}$ ) on the boundary  $\Gamma$ ;  $X(x, z)$  is the source point inside the domain  $\Omega$ ;  $\psi$  and  $\partial\psi/\partial n$  represent, respectively, the fundamental solution of Helmholtz equation and its normal derivative at point  $Y$  in  $\Gamma$ ; and  $\alpha = \tau/2\pi$ , where  $\tau$  is the angle in radians between points  $X$  and  $Y$  (Katsikadelis; 2002).

It follows that the fundamental solution of Helmholtz equation is given by

$$\psi = \frac{K_0(kr \sin \theta)}{2\pi}, \quad (8.26)$$

where  $K_0$  is the modified Bessel function of the second kind and zeroth order which satisfies Eq. (8.1) and  $r = \sqrt{(x - \hat{\xi})^2 + (z - \hat{\eta})^2}$  is the distance between points  $X$  and  $Y$ .

For normal incidence ( $\theta = 0$ ), the velocity potential  $\phi$  is governed by the Laplace equation given by

$$\left( \frac{\partial^2}{\partial x^2} + \frac{\partial^2}{\partial z^2} \right) \phi = 0, \quad (8.27)$$

whose fundamental solution is

$$\psi = \frac{1}{2\pi} \ln r. \quad (8.28)$$

#### Discretization of the boundary integral equation

The boundary integral equation (8.25) is then discretized by subdividing the boundary  $\Gamma$  into  $N_{be}$  boundary elements as follows

$$\alpha^i \phi^i + \sum_{j=1}^{N_{be}} \int_{\Gamma} \phi \frac{\partial \psi}{\partial n} d\Gamma = \sum_{j=1}^{N_{be}} \int_{\Gamma} \psi \frac{\partial \phi}{\partial n} d\Gamma. \quad (8.29)$$

where the superscript  $i$  indicates the boundary node and  $j$  the boundary element. The boundary is then divided into curved quadratic elements, where  $\phi$  and  $\partial\phi/\partial n$  are assumed to have three different values on each element. To account for this variation,  $\phi$  and  $\partial\phi/\partial n$  must be defined in terms of interpolation functions,  $\hat{\varphi}_{1,2,3}$ , which are a function of a homogeneous coordinate  $\xi$ , thus

$$\phi(\xi) = \hat{\varphi}_1(\xi)\phi^1 + \hat{\varphi}_2(\xi)\phi^2 + \hat{\varphi}_3(\xi)\phi^3, \quad (8.30a)$$

$$\frac{\partial \phi(\xi)}{\partial n} = \hat{\varphi}_1(\xi) \frac{\partial \phi^1}{\partial n} + \hat{\varphi}_2(\xi) \frac{\partial \phi^2}{\partial n} + \hat{\varphi}_3(\xi) \frac{\partial \phi^3}{\partial n}, \quad (8.30b)$$

and the same definition must be performed on the  $x$  and  $z$  coordinates

$$x = \hat{\varphi}_1(\xi)x^1 + \hat{\varphi}_2(\xi)x^2 + \hat{\varphi}_3(\xi)x^3, \quad (8.31a)$$

$$z = \hat{\varphi}_1(\xi)z^1 + \hat{\varphi}_2(\xi)z^2 + \hat{\varphi}_3(\xi)z^3, \quad (8.31b)$$

with the interpolation functions defined by

$$\hat{\varphi}_1 = \frac{1}{2}\xi(\xi - 1), \quad \hat{\varphi}_2 = \frac{1}{2}(1 - \xi)(1 + \xi), \quad \text{and} \quad \hat{\varphi}_3 = \frac{1}{2}\xi(1 + \xi), \quad (8.32)$$

where  $\xi$  varies from -1 to 1 and the superscript indicates the number of the node on the corresponding element. After inserting Eqs. (8.30a) and (8.30b) into Eq. (8.29), the calculation of the Jacobian is required to compute the integrals. This is obtained by

$$d\Gamma = \left[ \sqrt{\left(\frac{dx}{d\xi}\right)^2 + \left(\frac{dz}{d\xi}\right)^2} \right] d\xi = |J|d\xi. \quad (8.33)$$

Thus, Eq. (8.29) can now be written as

$$\alpha^i \phi^i + \sum_{j=1}^{N_{be}} \left[ H_1^{ij}, H_2^{ij}, H_3^{ij} \right] \cdot \begin{Bmatrix} \phi^1 \\ \phi^2 \\ \phi^3 \end{Bmatrix}^j = \sum_{j=1}^{N_{be}} \left[ G_1^{ij}, G_2^{ij}, G_3^{ij} \right] \cdot \begin{Bmatrix} \phi_n^1 \\ \phi_n^2 \\ \phi_n^3 \end{Bmatrix}^j, \quad (8.34)$$

where

$$H_k^{ij} = \int_{-1}^1 \hat{\varphi}_k(\xi) \frac{\partial \psi}{\partial n} |J| d\xi, \quad (8.35a)$$

$$G_k^{ij} = \int_{-1}^1 \hat{\varphi}_k(\xi) \psi |J| d\xi, \quad (8.35b)$$

with  $k = 1, 2$  and  $3$ . The integrals  $H_k^{ij}$  and  $G_k^{ij}$  are computed by applying a 10-point Gaussian quadrature rule to account for the quadratic variation on each element (Dominguez; 1993).

As mentioned above, fluxes and potentials have a three noded variation. Following Dominguez (1993), fluxes will have a unique nodal value on each element so the possibility of having different values between adjacent elements is considered, whereas velocity potentials will always hold a unique value in the connection between two adjoining elements. Therefore, fluxes are arranged in a  $3 \times N_{be}$  array while velocity potentials in an  $N$  array, where  $N$  is the number of nodes equal to  $2N_{be}$  for closed boundaries. This leads to the following representation

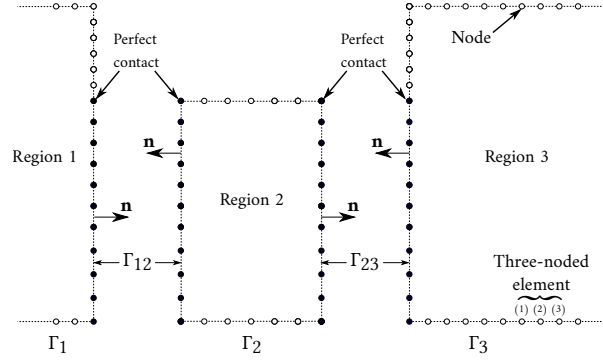


Figure 8.2: Discretization and matching of the regions.

of Eq. (8.34) as

$$\alpha^i \phi^i + [\hat{H}^{i1}, \dots, \hat{H}^{iN}] \cdot \begin{Bmatrix} \phi^1 \\ \vdots \\ \phi^N \end{Bmatrix}^j = [\hat{G}^{i1}, \dots, \hat{G}^{iN_{be}}] \cdot \begin{Bmatrix} \begin{Bmatrix} \phi_n^1 \\ \phi_n^2 \\ \phi_n^3 \end{Bmatrix}^1 \\ \vdots \\ \begin{Bmatrix} \phi_n^1 \\ \phi_n^2 \\ \phi_n^3 \end{Bmatrix}^{N_{be}} \end{Bmatrix}^j, \quad (8.36)$$

where the coefficients  $\hat{H}^{ij}$  are equal to the  $H_1$  term of a  $j$ -element plus the  $H_3$  term of the  $(j-1)$ -element for odd nodes, while for central nodes the coefficients  $\hat{H}^{ij}$  are equal to the  $h_2$  term of the corresponding  $j$  element. The coefficients  $\hat{G}^{ij}$  are  $1 \times 3$  matrices defined by  $[G_1^{ij}, G_2^{ij}, G_3^{ij}]$ . Then, Eq. (8.36) can be simplified as

$$\mathbf{H}\Phi = \mathbf{G}\Phi_{\mathbf{n}}, \quad (8.37)$$

with  $\mathbf{H}$  and  $\mathbf{G}$  being square ( $N \times N$ ) and rectangular ( $N \times 3N_{be}$ ) matrixes, respectively, while  $\Phi$  and  $\Phi_{\mathbf{n}}$  are vectors with dimensions  $N \times 1$  and  $3N_{be} \times 1$ , respectively.

### Matching of the subdomains

The three-region domain with the common interfaces on both lateral sides of Region 2 is shown in Fig. 8.2. Following Rezanejad et al. (2013), the method of subdomains is used to match the regions and to avoid numerical instabilities. The continuity of velocity potential and flux at the common interfaces should therefore be defined in order to match the regions. (Katsikadelis; 2002; Becker; 1992). For this purpose, the nodes in the common interfaces  $\Gamma_{12}$  and  $\Gamma_{23}$  of Regions 1–2 and Regions 2–3, respectively, are assumed to be in perfect contact, Fig. 8.2.

These velocity potential and flux continuity conditions are given by

$$\Phi_{12}^1 = \Phi_{12}^2, \quad \Phi_{23}^2 = \Phi_{23}^3, \quad (8.38a)$$

$$\Phi_{n12}^1 = -\Phi_{n12}^2, \quad \Phi_{n23}^2 = -\Phi_{n23}^3, \quad (8.38b)$$

respectively.

Boundary conditions previously defined in Eqs. (8.2), (8.4), (8.6) and (8.7), are then inserted into Eq. (8.34) and the known variables are moved to the right-hand side while the unknowns to the left-hand side. Then, the following matrix is obtained

$$[A] \{X\} = \{B\}, \quad (8.39)$$

where  $[A]$  is a square matrix of dimensions  $N \times N$ ; the vector  $\{X\}$  with dimensions  $N \times 1$  contains the unknown values of the velocity potential or fluxes on the boundaries and the common interfaces; and  $\{B\}$  is a known vector of dimension  $N \times 1$  (Dominguez; 1993).

## 8.4 Efficiency relations

Following the decomposition of the radiation volume flux  $q^R$  into real and imaginary parts as proposed by Evans (1982), we have

$$\frac{i\omega p}{\rho g} q^R = -(\hat{B} - i\hat{A})p = -Zp, \quad (8.40)$$

where  $Z = \hat{B} - i\hat{A}$  is the complex admittance, while the real coefficients  $\hat{A}$  and  $\hat{B}$  are given by

$$\hat{A} = \frac{\omega}{\rho g} \text{Re}\{q^R\}, \quad (8.41a)$$

$$\hat{B} = \frac{\omega}{\rho g} \text{Im}\{q^R\}, \quad (8.41b)$$

and are called the radiation susceptance and the radiation conductance parameters, respectively, and are related to the added mass and the radiation damping in a rigid body system (Evans and Porter; 1995).

By assuming that there exists a linear relationship between pressure drop and the volume flow rate without a phase lag in the turbine connected to the OWC chamber, we have

$$q = (\Lambda - i\epsilon)p, \quad (8.42)$$

where the real control parameter  $\Lambda$  is related to the linear turbine damping induced to the airflow. The term  $\epsilon = \omega\hat{V}/(\gamma p_a)$  has been introduced to account for the linear compressibility of the trapped air inside the OWC chamber with  $\hat{V}$  being the air volume,  $\gamma = 1.4$  is the specific

CHAPTER 8. THE EFFECTS OF DIRECTIONAL WAVES AND CHAMBER  
CONFIGURATION ON THE EFFICIENCY OF AN OWC DEVICE

---

heat ratio of air and  $p_a$  the atmospheric air pressure (Rezanejad et al.; 2017). After combining Eqs. (8.9), (8.40) and (8.42), the imposed internal pressure results

$$p = \frac{q^S}{\Lambda + Z - i\epsilon}. \quad (8.43)$$

Now, the total rate of work performed by the pressure forces inside the OWC,  $Q(t) \times P(t)$ , is averaged over one wave period to obtain the total rate of power absorbed per unit width of pressure distribution as

$$W = \frac{1}{2} \text{Re}\{\bar{p}q\}, \quad (8.44)$$

with the horizontal bar ( $\bar{\phantom{x}}$ ) denoting the complex conjugate. Now, by inserting Eqs. (8.9) and (8.40) into Eq. (8.44) and simplifying, results

$$W = \frac{1}{2} \text{Re}\{\bar{p}(q^S - Zp)\} = \frac{|q^S|^2}{8\hat{B}} - \frac{\hat{B}}{2} \left| p - \frac{q^S}{2\hat{B}} \right|^2, \quad (8.45)$$

where if  $\hat{B}^{-1}$  exists, the maximum work gives

$$W_{max} = \frac{|q^S|^2}{8\hat{B}}, \quad \text{for } p = \frac{q^S}{2\hat{B}}, \quad (8.46)$$

where  $\Lambda = \overline{(Z - i\epsilon)}$  for maximum power. Thus, after combining Eqs. (8.43) and (8.45), we obtain

$$W = \frac{|q^S|^2}{8\hat{B}} \left[ 1 - \left( \frac{|\Lambda - Z + i\epsilon|}{|\Lambda + Z - i\epsilon|} \right)^2 \right]. \quad (8.47)$$

Now, the optimal power conversion efficiency must be obtained. This is performed by finding the optimum value of  $\Lambda$ , which is obtained by applying zero value to the derivative with respect to  $\Lambda$  for the squared-right term inside the brackets of Eq. (8.47) (Şentürk and Özdamar; 2012), thus yielding

$$\Lambda_{opt} = |Z - i\epsilon| = \left( \hat{B}^2 + (\hat{A} + \epsilon)^2 \right)^{1/2} \quad (8.48)$$

and after substituting the above expression into Eq. (8.47), results

$$W_{opt} = \frac{|q^S|^2}{8\hat{B}} \left[ 1 - \frac{\Lambda_{opt} - \hat{B}}{\Lambda_{opt} + \hat{B}} \right], \quad (8.49)$$

where  $\hat{A}$ ,  $\hat{B}$  and  $\Lambda$  are a function of the angular frequency  $\omega$ .

Hence, an expression for the maximum hydrodynamic efficiency can now be obtained as

$$\eta_{max} = \frac{W_{opt}}{W_{max}} = \frac{2\hat{B}}{\Lambda_{opt} + \hat{B}}, \quad (8.50)$$

with  $\eta_{max}$  in the range 0 to 1.



CHAPTER 8. THE EFFECTS OF DIRECTIONAL WAVES AND CHAMBER CONFIGURATION ON THE EFFICIENCY OF AN OWC DEVICE

Table 8.1: Maximum hydrodynamic efficiency  $\eta_{max}$  computed for different number of evanescent modes  $N_{em}$  with  $h_a/h = 0.125$ ,  $b/h = 1.0$ ,  $w/b = 1.0$  and  $\theta = 60^\circ$ .

$N_{em}$	$Kh = 0.5$	$Kh = 1.0$	$Kh = 1.5$	$Kh = 2.0$	$Kh = 2.5$	$Kh = 3.0$	$Kh = 3.5$
	$\eta_{max}$						
<b>10</b>	0.32826	0.33171	0.49410	0.20517	0.03628	0.00954	0.00286
<b>20</b>	0.32832	0.33203	0.49639	0.20382	0.03613	0.00949	0.00284
<b>30</b>	0.32838	0.33227	0.49809	0.20308	0.03606	0.00948	0.00284
<b>40</b>	0.32838	0.33226	0.49803	0.20309	0.03606	0.00948	0.00284
<b>50</b>	0.32838	0.33226	0.49805	0.20307	0.03606	0.00948	0.00284

As in [Evans and Porter \(1995\)](#), the following non-dimensionalised quantities are defined

$$\mu = \frac{\rho g}{\omega b} \hat{A}, \quad (8.51a)$$

$$\nu = \frac{\rho g}{\omega b} \hat{B}, \quad (8.51b)$$

which represent the coefficients of radiation susceptance and radiation conductance, respectively. The radiation susceptance coefficient  $\mu$  represents the energy that remains un-captured while the radiation conductance coefficient  $\nu$  accounts for the energy transfer into the system ([Rezanejad et al.; 2013](#)).

Finally, after inserting the above coefficients into Eq. (8.50), the hydrodynamic efficiency  $\eta_{max}$  gives

$$\eta_{max} = \frac{2}{\left[1 + \left(\frac{\mu}{\nu} + \frac{\rho g \epsilon}{\omega b \nu}\right)^2\right]^{1/2} + 1}, \quad (8.52)$$

and by neglecting the effect of air compressibility, i.e.,  $\epsilon = 0$ , it results in the expression previously reported by [Evans and Porter \(1995\)](#).

## 8.5 Results and Discussion

### 8.5.1 Convergence analysis

In this section, analytical and numerical results based on the previously discussed methods are presented. The effects of the incidence wave angle ( $\theta$ ), the front wall thickness to chamber length ratio ( $w/b$ ), the chamber length to water depth ratio ( $b/h$ ), the front wall draft to water depth ratio ( $h_a/h$ ) and the trapped air column height to water depth ratio ( $h_c/h$ ) on the maximum hydrodynamic efficiency are analyzed. In all the calculations, the water depth is assumed to be 7.90 m as in ([Medina Rodríguez et al.; 2020](#)) with a wave period  $T$  in the range of  $2.50 \leq T \leq 30$  s.

Before performing the calculations, a convergence analysis for both EEM and BEM was carried out. In the case of the EEM, see Table 8.1, the results obtained for the maximum hydrodynamic efficiency  $\eta_{max}$  are given for different values of the non-dimensional frequency

CHAPTER 8. THE EFFECTS OF DIRECTIONAL WAVES AND CHAMBER CONFIGURATION ON THE EFFICIENCY OF AN OWC DEVICE

Table 8.2: Maximum hydrodynamic efficiency  $\eta_{max}$  computed for different number of nodes  $N$  with  $h_a/h = 0.125$ ,  $b/h = 1.0$ ,  $w/b = 1.0$  and  $\theta = 60^\circ$ .

$N$	$Kh = 0.5$	$Kh = 1.0$	$Kh = 1.5$	$Kh = 2.0$	$Kh = 2.5$	$Kh = 3.0$	$Kh = 3.5$
	$\eta_{max}$						
<b>316</b>	0.33586	0.33624	0.49359	0.20449	0.03540	0.00913	0.00269
<b>388</b>	0.33478	0.33572	0.49467	0.20400	0.03546	0.00917	0.00271
<b>460</b>	0.33402	0.33536	0.49546	0.20368	0.03551	0.00920	0.00272
<b>532</b>	0.33346	0.33509	0.49602	0.20347	0.03555	0.00923	0.00273
<b>604</b>	0.33302	0.33488	0.49643	0.20331	0.03559	0.00925	0.00274

$Kh(= 0.5, 1.0, 1.5, 2.0, 2.5, 3.0$  and  $3.5)$ . From Table 8.1 it is observed that around 30 evanescent modes are adequate to ensure convergence of the analytical results within four decimal places; therefore, in the present calculations,  $N_{em} = 30$  are employed. Then, in Table 8.2, by using the BEM, the results of  $\eta_{max}$  for the same  $Kh$  values are given for different number of nodes ( $N$ ). Here, to avoid the effect of local disturbances at the far-field boundary, a distance of 4 times the water depth  $h$  between the right face of the front wall and the far-field boundary was considered. In this case, around 532 nodes (256 quadratic elements) were found to be enough for ensuring the convergence of the numerical results within three decimal places. Therefore, the BVP is discretized through 532 nodes.

### 8.5.2 Validation

To validate the results obtained by the above-mentioned methods, the results for the limiting cases of Evans and Porter (1995) and Medina Rodríguez et al. (2020) were employed. First, in Fig. 8.3a, the hydrodynamic efficiency versus  $Kh$  with  $b/h = 1.0$ ,  $h_a/h = 0.125$  and  $\theta = 0^\circ$  for different values of front wall thickness to chamber length ratio  $w/b$  are shown. On one hand, for  $w/b = 0.01$ , the results obtained by the present formulations were compared with the corresponding results of Evans and Porter (1995) for an OWC device with a thin front wall and normal wave propagation. On the other hand, by using the EEM described above, calculations were compared with results obtained by Medina Rodríguez et al. (2020) in the case of normal incidence and different values of  $w/b$ . In both cases, it can be seen that the results agree very well.

Then, in Fig. 8.3a, the hydrodynamic efficiency versus  $Kh$  with  $h_a/h = 0.50$  and  $w/b = 0.01$  for different values of the chamber length to water depth ratio  $b/h$  are shown. In general, it is observed that results agree very well, except for small values of  $b/h$  and  $Kh > 1$ , where the semi-analytic results obtained by the EEM are not in a precise agreement with the results obtained by Evans and Porter (1995) and the present BEM for  $\theta = 1^\circ$ .

### 8.5.3 Effect of the chamber configuration

The numerical and analytical results of the maximum hydrodynamic efficiency  $\eta_{max}$  versus the non-dimensional frequency  $Kh$  with  $h_a/h = 0.125$  and  $b/h = 1.0$  for various angles of

CHAPTER 8. THE EFFECTS OF DIRECTIONAL WAVES AND CHAMBER CONFIGURATION ON THE EFFICIENCY OF AN OWC DEVICE

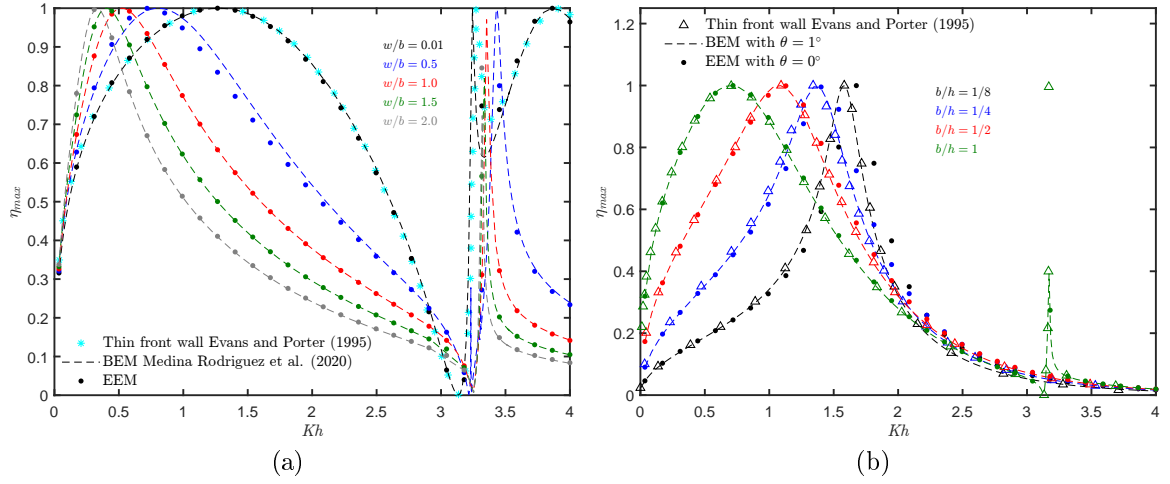


Figure 8.3: Maximum hydrodynamic efficiency versus non-dimensional frequencies  $Kh$  compared with previous results obtained by [Evans and Porter \(1995\)](#) and [Medina Rodríguez et al. \(2020\)](#). (a) For  $b/h = 1.0$ ,  $h_a/h = 0.125$ ,  $\theta = 0^\circ$  and different  $w/b$  ratios. (b) For  $h_a/h = 0.5$ ,  $w/b = 0.01$  and various  $b/h$  ratios.

incidence  $\theta(= 15^\circ, 30^\circ, 45^\circ, 60^\circ$  and  $75^\circ)$  and four different front barrier thickness to chamber length ratios  $w/b(= 0.5, 1.0, 1.5$  and  $2.0)$  are shown in Figs. 8.4a–d, respectively. It is observed that the semi-analytical and numerical results obtained by, respectively, the EEM and the BEM are in good agreement. Figures 8.4a-d show that the non-dimensional frequency  $Kh$  at which resonance occurs increases when the angle of incidence increases, while the hydrodynamic efficiency bandwidth is significantly reduced with an increase  $\theta$ . It is also found that the efficiency in the entire  $Kh$  spectrum is significantly diminished for large wave incidence angles due to the null excitation of the oblique waves on the oscillating water column. It can be shown that by comparing the Figs. 8.4a-d, an increase in the thickness of the front wall contributes to a decrease in both the efficiency bandwidth and the peak frequency value. For thick front barriers, this decrease in performance is attributed to the fact that the energy flow from the incoming wave to the internal free surface is limited. A reduction in energy transfer corresponds to a decrease in the internal free surface oscillation for driving the air column, which consequently diminishes the output power.

The results of the maximum hydrodynamic efficiency  $\eta_{max}$  versus  $Kh$  with  $h_a/h = 0.125$  and  $w/b = 1.0$  for various angles of incidence  $\theta(= 15^\circ, 30^\circ, 45^\circ, 60^\circ$  and  $75^\circ)$  and four different chamber length to water depth ratios  $b/h(= 3/4, 1/2, 1/4$  and  $1/8)$  are shown in Figs. 8.5a–d, respectively. By comparing these four figures it is observed that a shorter chamber length leads to an increment in the resonant peak frequency value. This is explained by the fact that a shorter chamber length allows less local fluid motion inside the OWC, thus decreasing the horizontal distance that a fluid particle must travel during a period of motion, which then leads to an increment in  $Kh$  value at which resonance takes place. In comparison, for a shorter chamber, a larger hydrodynamic efficiency band is obtained. This is an important design factor

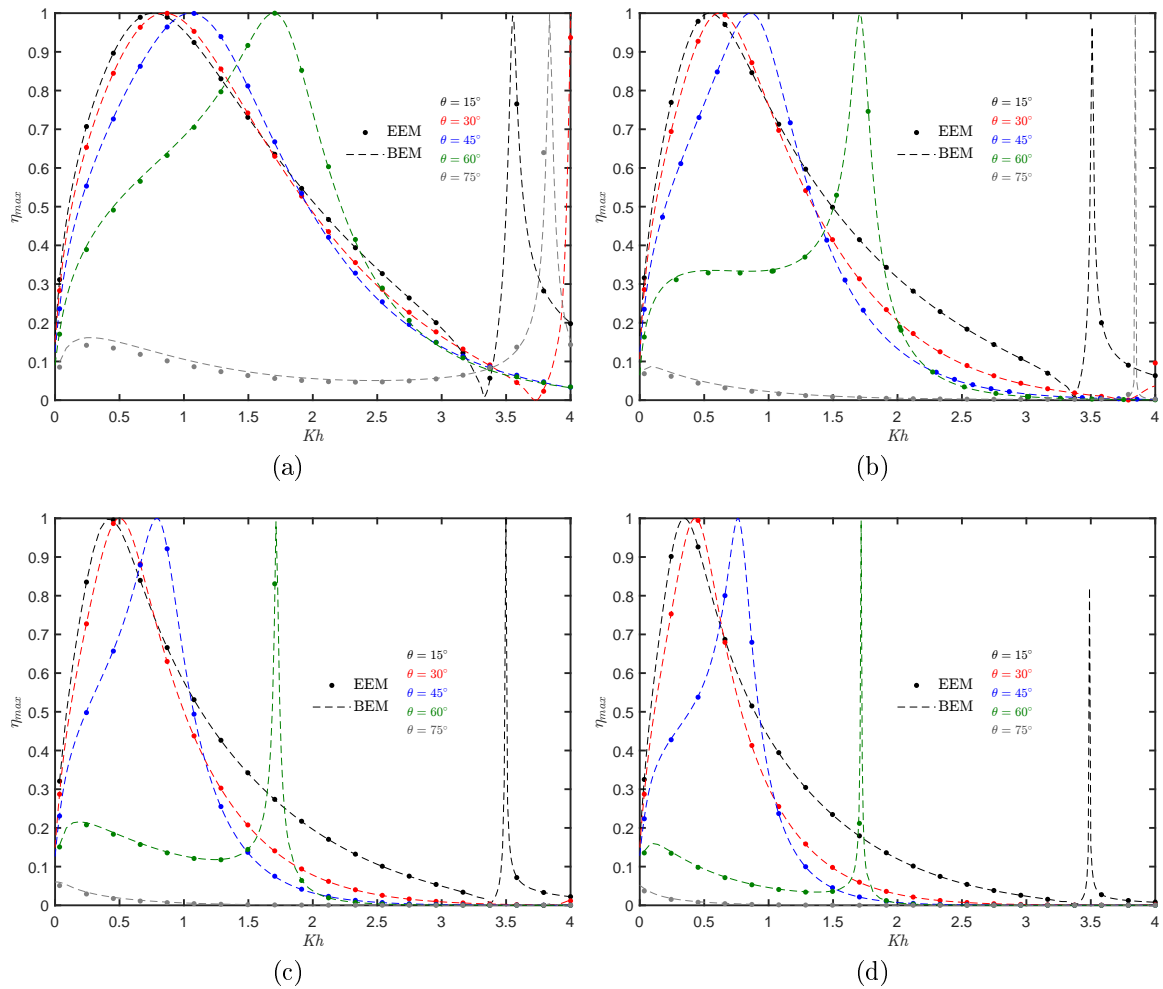


Figure 8.4: Maximum hydrodynamic efficiency versus  $Kh$  for different incidence wave angles  $\theta$  with  $h_a/h = 0.125$  and  $b/h = 1.0$ . (a) For  $w/b = 0.5$ . (b) For  $w/b = 1.0$ . (c) For  $w/b = 1.5$ . (d) For  $w/b = 2.0$ .

CHAPTER 8. THE EFFECTS OF DIRECTIONAL WAVES AND CHAMBER CONFIGURATION ON THE EFFICIENCY OF AN OWC DEVICE

for the optimization of an OWC system, as the available wave energy can be best used by an OWC chamber that is designed to fit the prevailing wave period. On the other hand, it is noted that the greater the angle of incidence, the greater the peak resonant frequency magnitude.

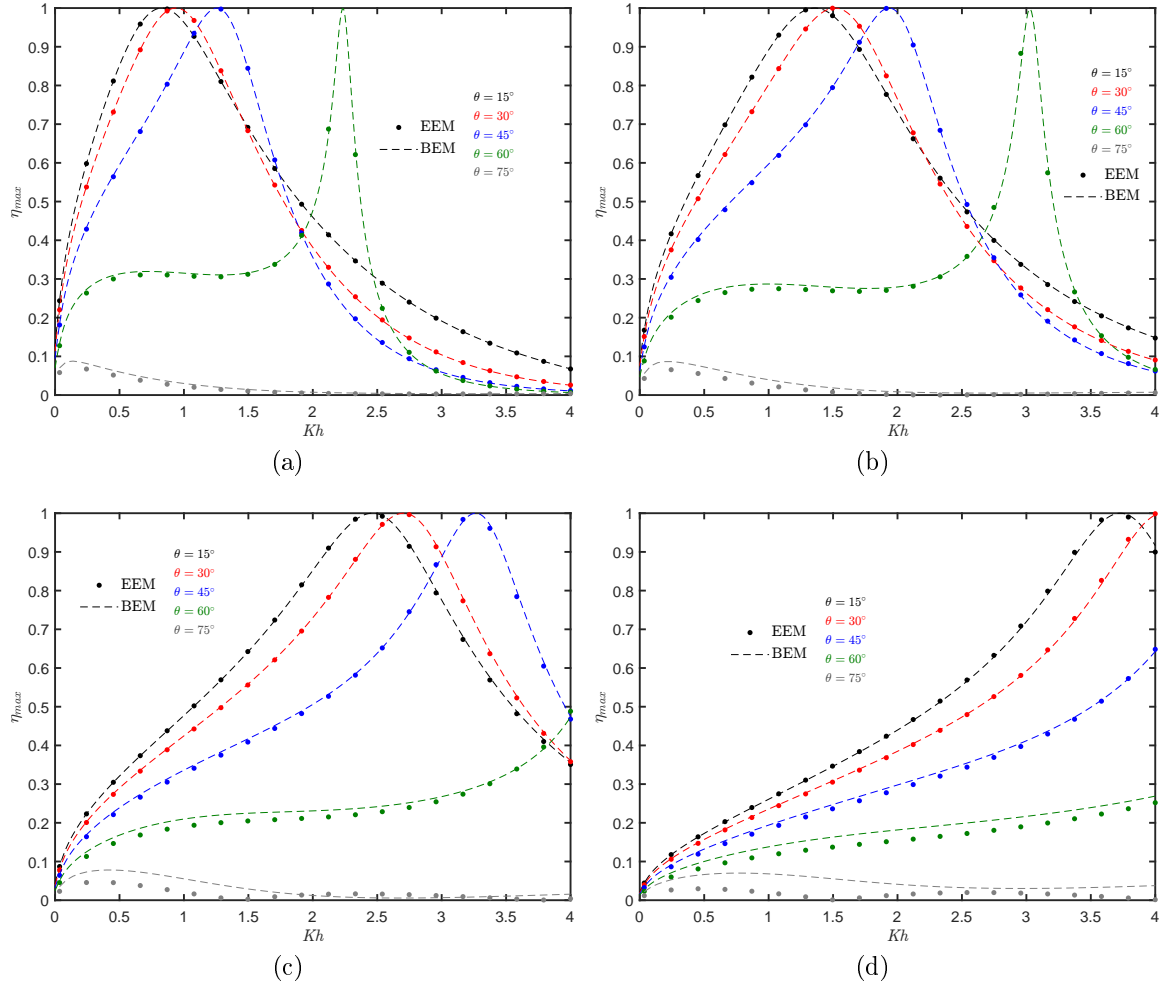


Figure 8.5: Maximum hydrodynamic efficiency versus  $Kh$  for different incidence wave angles  $\theta$  with  $h_a/h = 0.125$  and  $w/b = 1.0$ . (a) For  $b/h = 3/4$ . (b) For  $b/h = 1/2$ . (c) For  $b/h = 1/4$ . (d) For  $b/h = 1/8$ .

Figures 8.6a–c show the results of the maximum hydrodynamic efficiency  $\eta_{max}$  versus the non-dimensional frequency  $Kh$  with  $b/h = 1.0$  and  $w/b = 1.0$  for various wave incidence angles  $\theta (= 15^\circ, 30^\circ, 45^\circ, 60^\circ$  and  $75^\circ)$  and three different front wall draft to water depth ratios  $h_a/h (= 1/4, 1/2$  and  $3/4)$ , respectively. In these figures it can be seen that a wider performance bandwidth is obtained by decreasing the immersion of the front wall,  $h_a/h$ , whereas the value of the peak resonant frequency is increased. Similar to a modification in the chamber length, a shorter draft decreases the vertical distance a fluid particle travels in a period of motion, thus

leading to an increase of  $Kh$  at which resonance occurs. Regarding the influence of the angle of incidence, it is observed that by increasing  $\theta$ , the peak frequency values are shifted to the right.

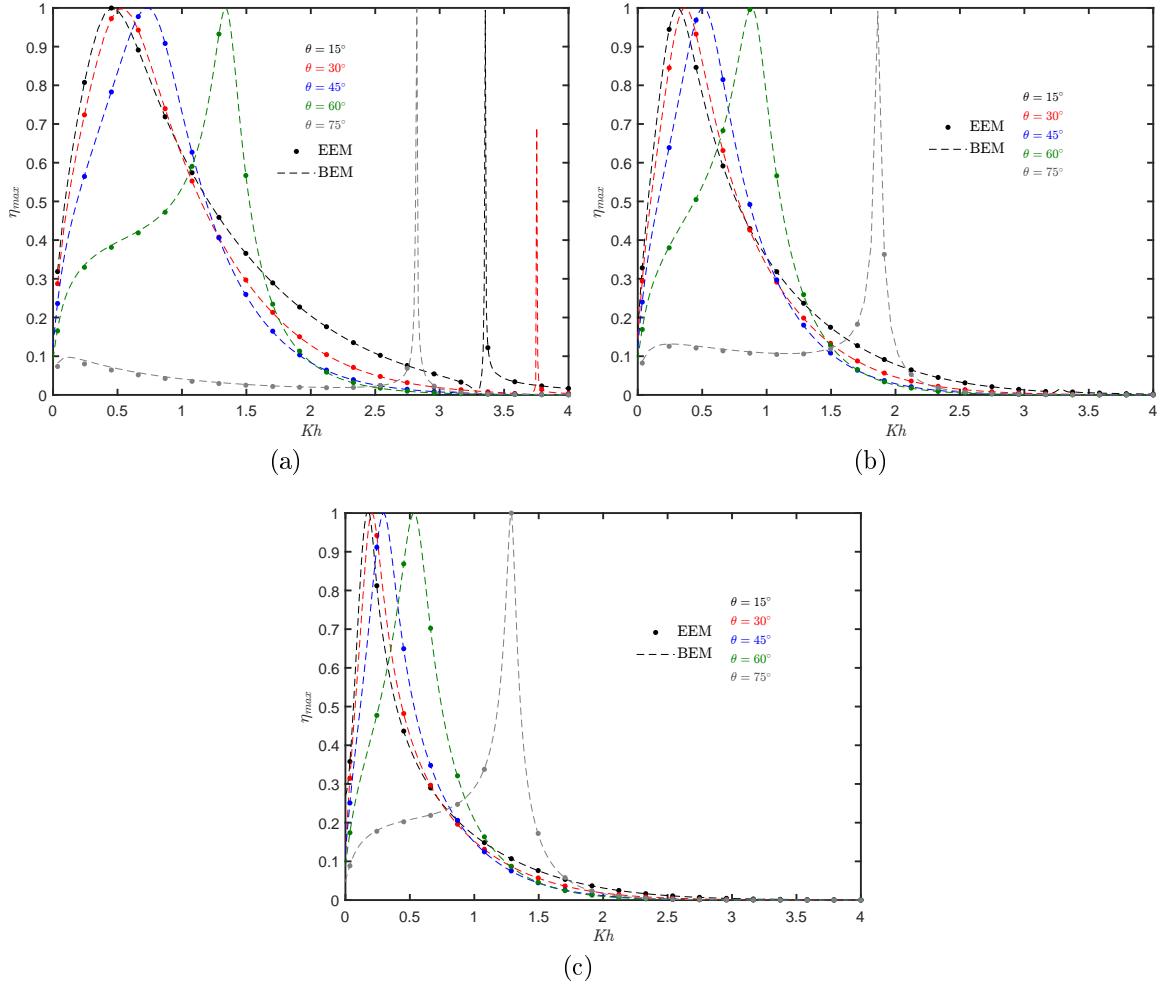


Figure 8.6: Maximum hydrodynamic efficiency versus  $Kh$  with  $b/h = 1.0$  and  $w/b = 1.0$ . (a) For  $h_a/h = 1/4$ . (b) For  $h_a/h = 1/2$ . (c) For  $h_a/h = 3/4$ .

### 8.5.4 Effect of the wave angle of incidence

The variation of the maximum hydrodynamic efficiency versus the angle of incidence  $\theta$  in the range of  $0^\circ \leq \theta \leq 90^\circ$  for different values of  $Kh$  ( $= 1.0, 2.0$  and  $3.0$ ) are shown in Figs. 8.7a–d. It can be seen that for  $Kh = 1$ , compared with the cases of large  $Kh$ ,  $\eta_{max}$  is higher in most of the range of  $\theta$ . It is also observed that for both large  $Kh$  and large thickness ratio,  $w/b$ , the hydrodynamic efficiency curves drop fastly as  $\theta$  increases. Additionally, the maximum

CHAPTER 8. THE EFFECTS OF DIRECTIONAL WAVES AND CHAMBER CONFIGURATION ON THE EFFICIENCY OF AN OWC DEVICE

hydrodynamic efficiency becomes zero when  $\theta$  tends to  $90^\circ$  since the inside water column is not significantly excited by the almost parallel incident waves.

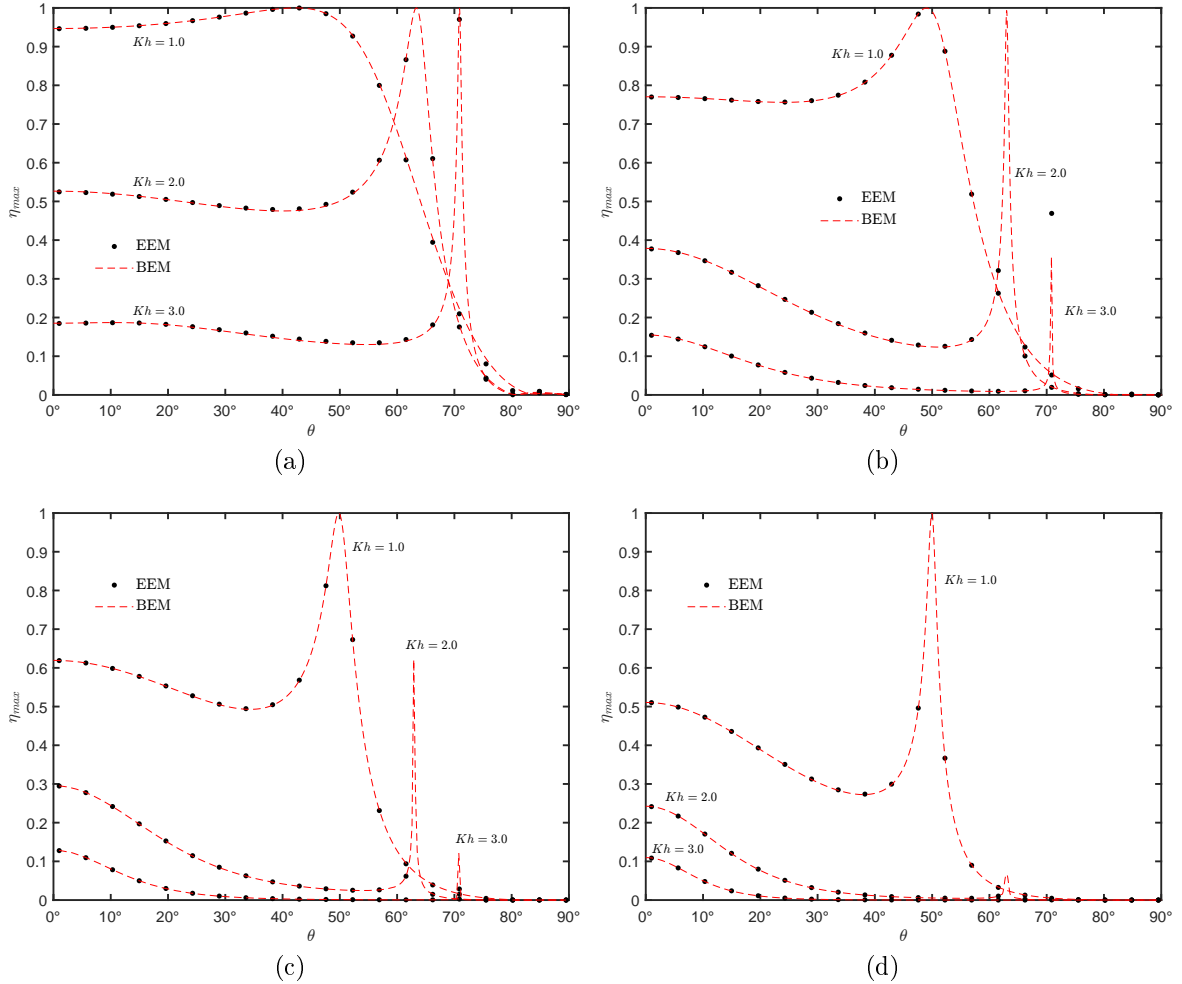


Figure 8.7: Maximum hydrodynamic efficiency versus  $\theta$  for different non-dimensional frequencies  $Kh$  with  $h_a/h = 0.125$  and  $b/h = 1.0$ . (a) For  $w/b = 0.5$ . (b) For  $w/b = 1.0$ . (c) For  $w/b = 1.5$ . (d) For  $w/b = 2.0$ .

The numerical results of  $\eta_{max}$  versus the non-dimensional frequency  $Kh$  and the angle of incidence  $\theta$  for  $w/b (= 0.5, 1.0, 1.5$  and  $2.0)$  are shown in Figs. 8.8a–j. From Figs. 8.9a–j it can be seen two areas of high values of the hydrodynamic efficiency. The biggest one is due to large motions inside the chamber that occurs when the fluid inside the chamber is excited by the incident wave into a resonant piston-type motion. This area of high hydrodynamic efficiency will provide the opportunity to harness wave energy effectively as it shows that for a wide variety of non-dimensional frequencies and incident wave directions, high values of  $\eta_{max}$  are available. On the other hand, the second red area, located on the left corner for relatively small angles of

incidence ( $0^\circ \leq \theta \leq 40^\circ$ ), is due to a resonance mechanism that occurs when the incident wave frequency is such that the fluid inside the chamber is excited into an antisymmetric sloshing mode. These sloshing frequencies occur at values of the dimensionless wavenumber  $kb = n\pi$ , with  $n$  being the sloshing mode. For this case, it can be seen that peak values in  $\eta_{max}$ , due to the first sloshing frequency, take place close to  $Kh \approx \pi$ . Then, it is observed that by increasing the front wall thickness,  $w/b$ , the above-mentioned areas of high hydrodynamic efficiency are significantly reduced, with the biggest area limited to low values of  $Kh$  and  $\theta < 60^\circ$ , while the smallest area almost disappearing. As mentioned above, this is explained by the fact that a thicker front wall reduces the energy transfer due to wave motion, leading to a reduction in the inside water column oscillations for driving the trapped air. However, to consider a very thin wall for obtaining a broader efficiency band, as in Fig. 8.8a, is not feasible because OWC systems will be exposed to heavy loads at periods of high water levels and extreme storm events due to direct wave action (Viviano et al.; 2016; Pawitan et al.; 2019; Viviano et al.; 2019; Pawitan et al.; 2020), which may lead to severe structural damage as occurred with the Mutriku Wave Energy Plant (MWEP) (Medina-Lopez et al.; 2015).

### 8.5.5 Influence of the trapped air inside the OWC chamber

The maximum hydrodynamic efficiency  $\eta_{max}$  versus  $Kh$  for different air column height to water depth ratios  $h_c/h$  ( $= 0.75, 1.0, 1.5$  and  $2.0$ ) and various incidence wave angles  $\theta$  ( $= 15^\circ, 30^\circ, 45^\circ, 60^\circ$  and  $75^\circ$ ) are shown in Figs. 8.9a–d. By comparing these figures, it is observed that as  $h_c/h$  increases, the peak values of maximal hydrodynamic efficiency are decreased for small wave angles. This is attributable to the fact that with a bigger trapped air volume within the chamber, the optimum damping induced to the airflow by the linear turbine increases and, as clearly observed from Eq. (8.52),  $\eta_{max}$  decreases. Furthermore, for large wave angles, the efficiency band is reduced and a spiky trend is observed. On the other hand, it can be seen that an increment in the air column height  $h_c/h$  does not seem to influence the magnitude of the frequency at which resonance occurs.

### 8.5.6 Case of study: the MWEP

Hydrodynamic efficiency is evaluated in this subsection based on the physical dimensions of a single MWEP chamber. Two cases were studied based on the highest and lowest equinoctial spring tides in the MWEP. The non-dimensional parameters  $h_a/h$ ,  $b/h$ ,  $w/h$  and  $h_c/h$  were considered in all the cases and comparisons were made between the past and present front barrier designs, Figs 8.10a and 8.10b, respectively. As reported by Medina-Lopez et al. (2015), severe storms regularly impact the Mutriku Port and during the construction of the power plant, three storms hit the MWEP producing severe structural damage to a number of the OWC chambers. As a consequence, to survive the wave loads, the front wall of the chambers was strengthened and now the thickness of the front wall has doubled the length of the chambers (see Fig. 8.10). The purpose of this subsection is to theoretically analyze the effect of this alteration of the structure on the device performance.



CHAPTER 8. THE EFFECTS OF DIRECTIONAL WAVES AND CHAMBER CONFIGURATION ON THE EFFICIENCY OF AN OWC DEVICE

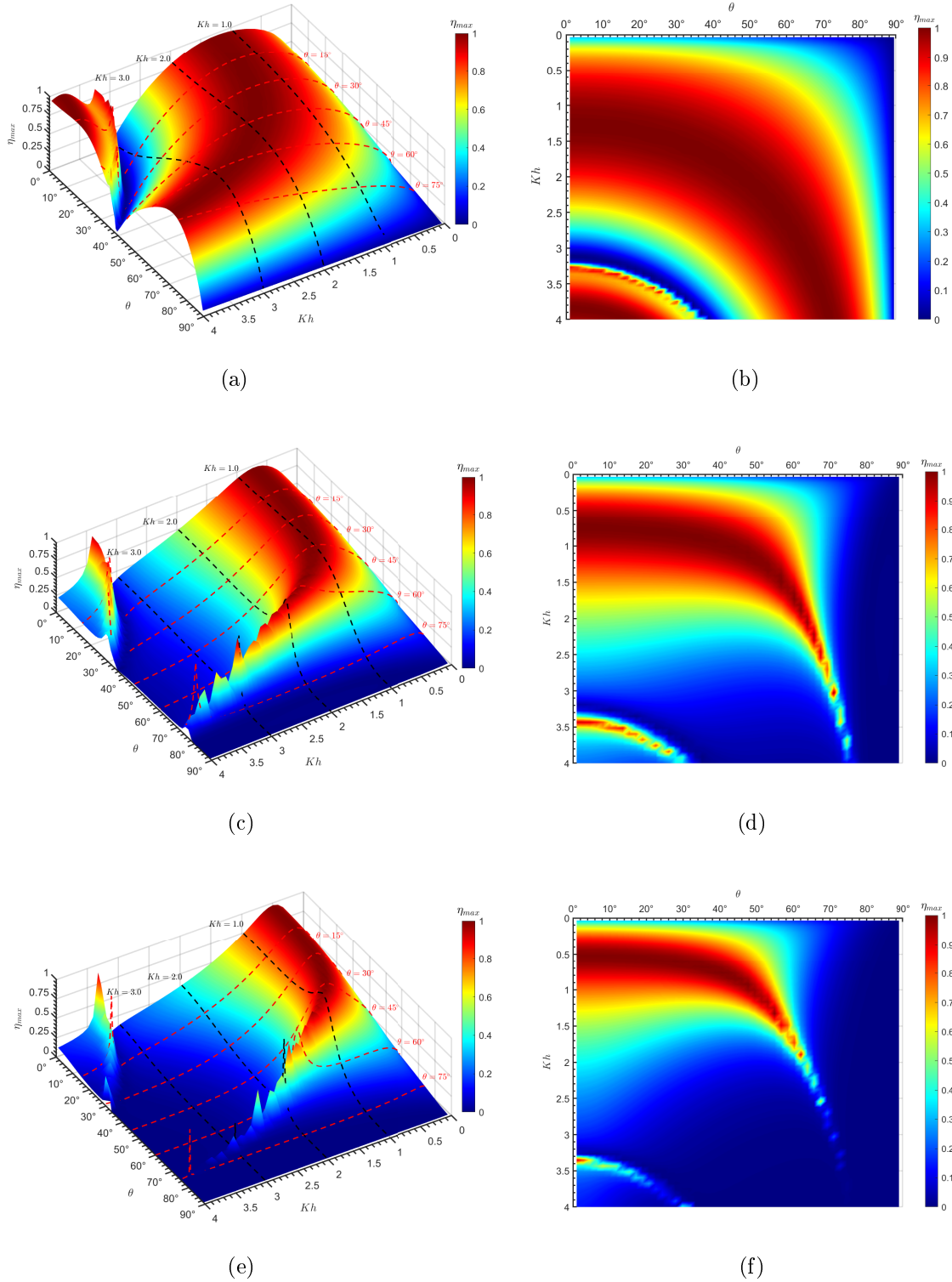
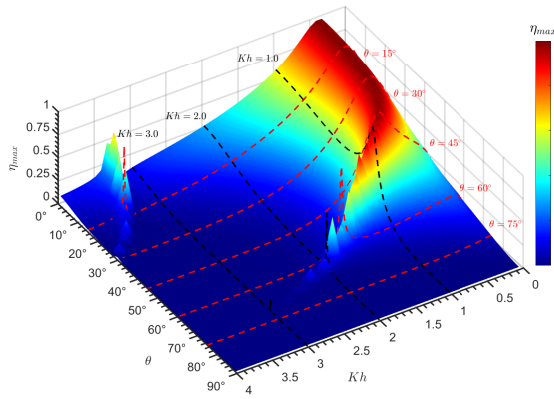
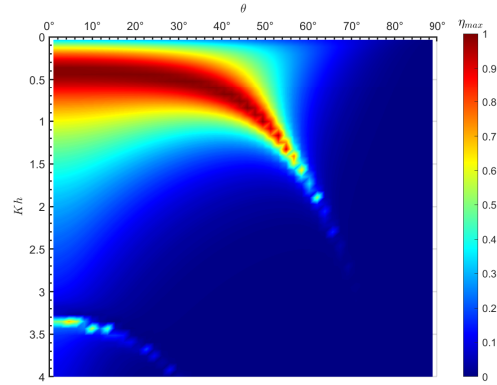


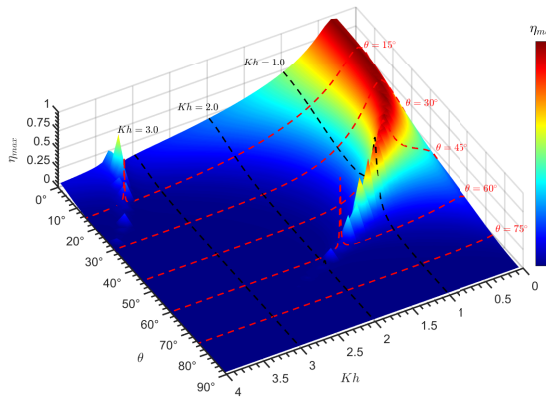
Figure 8.8: Numerical results for the maximum hydrodynamic efficiency as function of  $\theta$  and  $Kh$  with  $h_a/h = 0.125$  and  $b/h = \frac{1}{186}$ . (a)-(b) For  $w/b = 0.01$ . (c)-(d) For  $w/b = 0.5$ . (e)-(f) For  $w/b = 1.0$ .



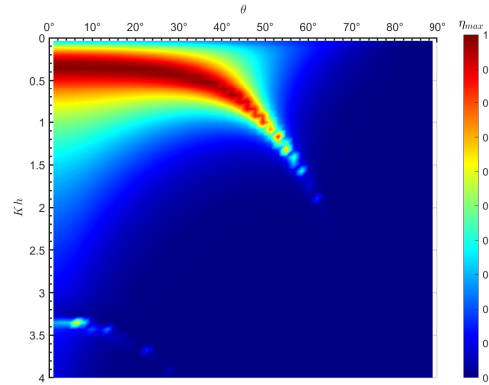
(g)



(h)



(i)



(j)

Figure 8.8: Numerical results for the maximum hydrodynamic efficiency as function of  $\theta$  and  $Kh$  with  $h_a/h = 0.125$  and  $b/h = 1.0$ . (g)-(h) For  $w/b = 1.5$ . (i)-(j) For  $w/b = 2.0$ .

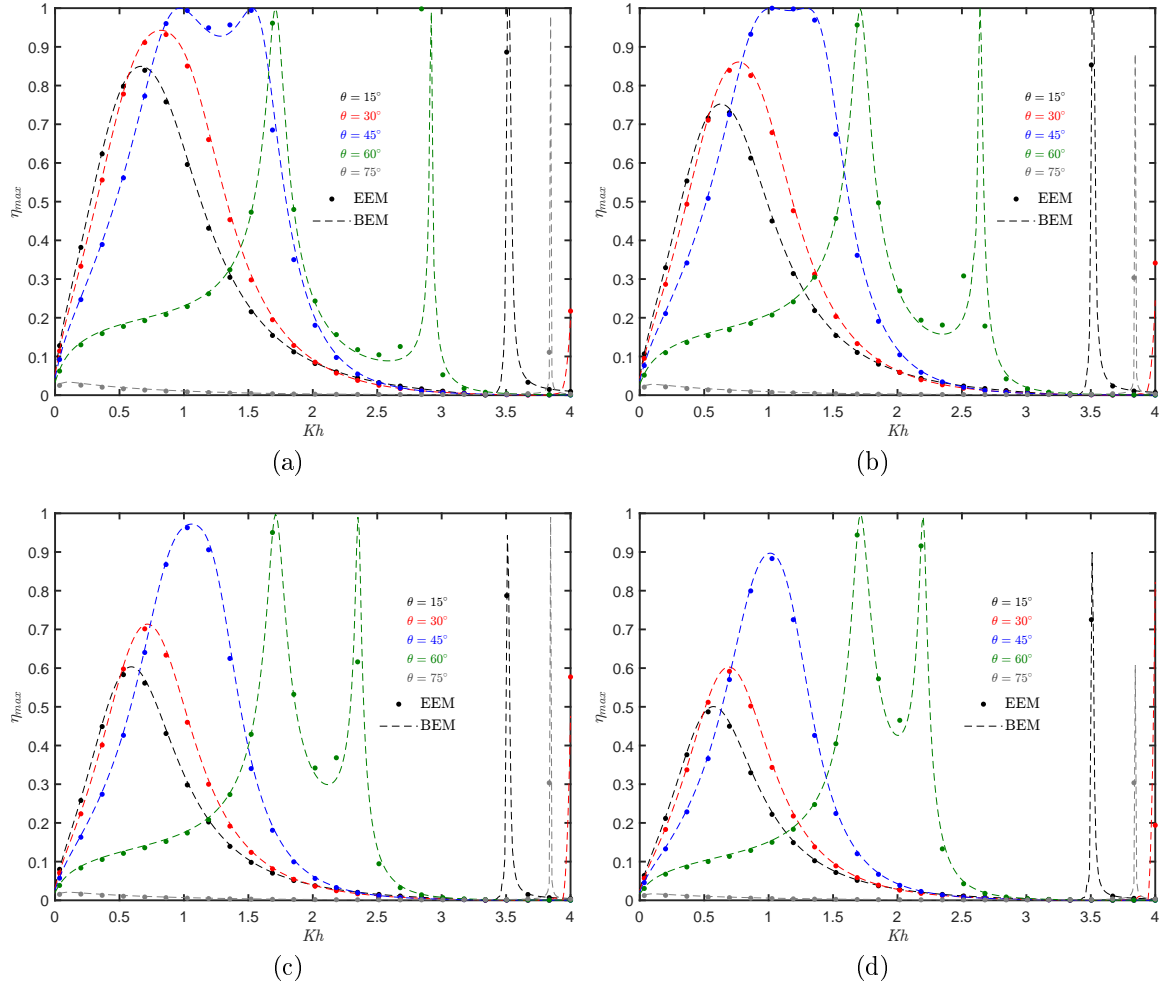


Figure 8.9: Maximum hydrodynamic efficiency versus  $Kh$  for different air column height to water depth ratios  $h_c/h$  with  $h_a/h = 0.125$ ,  $b/h = 1.0$  and  $w/b = 1.0$ . (a) For  $h_c/h = 0.75$ . (b) For  $h_c/h = 1.0$ . (c) For  $h_c/h = 1.5$ . (d) For  $h_c/h = 2.0$ .

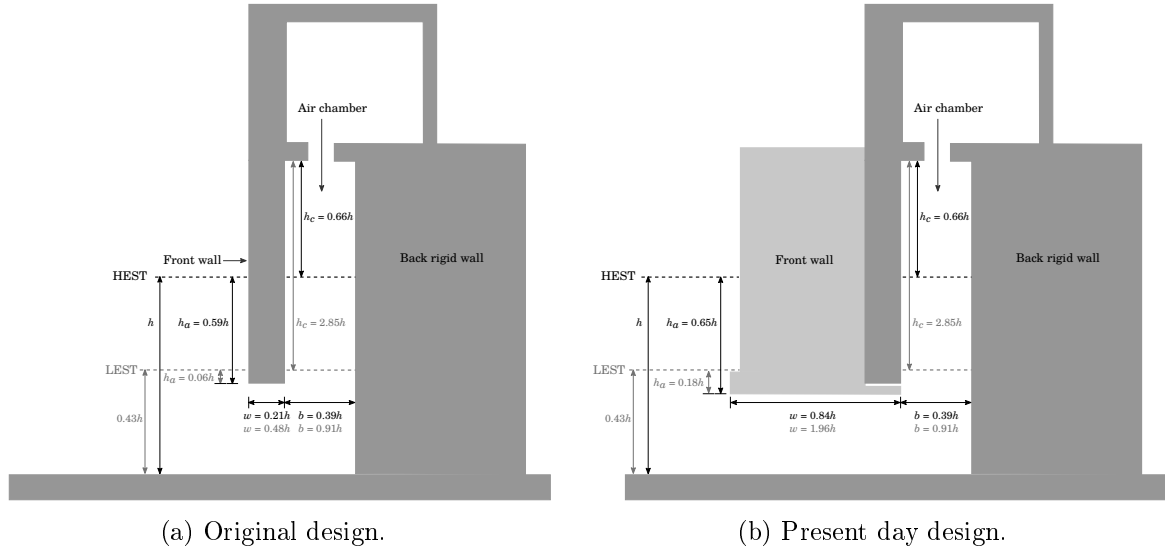


Figure 8.10: Sketch of a single chamber in the MWEF for the highest and lowest equinoctial spring tides, HEST (black dimensions) and LEST (gray dimensions), respectively.

First, Figs. 8.11a and 8.11b show the hydrodynamic efficiency versus  $Kh$  for different wave angle of incidence with  $h_a/h = 0.59$ ,  $b/h = 0.39$ ,  $w/h = 0.21$  and  $h_c/h = 0$  and  $h_c/h = 0.66$ , respectively, for the highest equinoctial spring tide and the past front barrier design. It can be seen that by considering the air column height  $h_c/h$ , a second peak in the efficiency curves appears, while the resonant frequency value of the first peak in the efficiency curves seems to be not affected by the air column height  $h_c/h$ . Then, in Figs 8.11c and 8.11d, the hydrodynamic efficiency versus  $Kh$  for various wave angles  $\theta$  with  $h_a/h = 0.65$ ,  $b/h = 0.39$ ,  $w/h = 0.84$  and  $h_c/h = 0$  and  $h_c/h = 0.66$ , respectively, are shown for the highest equinoctial spring tide and the present front barrier design. Compared with Figs. 8.11a and 8.11b, it is observed that due to the longer front wall draft ( $h_a/h$ ) and thickness ( $w/h$ ), the efficiency band is notably reduced and the values of the peak resonance frequencies are shifted to lower values. Again, the longer the angle  $\theta$ , the greater the magnitude of the peak resonance frequency.

Figures 8.12a and 8.12b show the hydrodynamic efficiency versus  $Kh$  for different incidence wave angles  $\theta$  with  $h_a/h = 0.06$ ,  $b/h = 0.91$ ,  $w/h = 0.48$  and  $h_c/h = 0$  and  $h_c/h = 2.85$ , respectively, for the lowest equinoctial spring tide and the past front barrier design. Now, compared with the previous case, it is observed that a broader efficiency band is obtained due to the lower front wall draft,  $h_a/h$ , that allows a higher wave energy transfer due to the orbital motion. However, in Fig. 8.12b, since a higher trapped air column is considered, the peak values and bandwidth of the hydrodynamic efficiency are highly reduced. Furthermore, for very large incidence wave angles, it can be seen that the efficiency is close to zero. On the other hand, the hydrodynamic efficiency versus  $Kh$  for the present chamber design and the lowest equinoctial

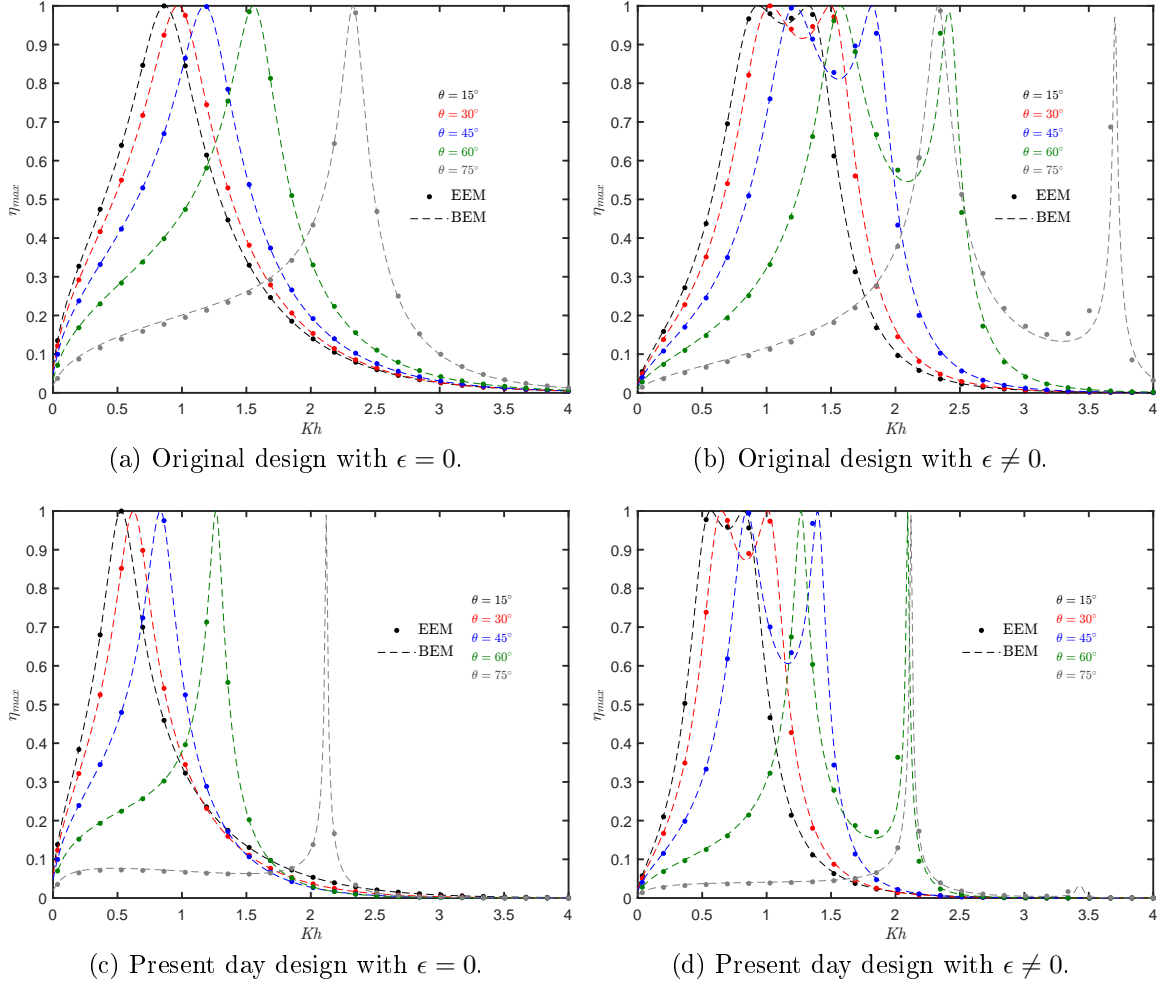


Figure 8.11: Maximum hydrodynamic efficiency versus  $Kh$  for different incidence wave angles  $\theta$  in the case of HEST. (a)-(b) For  $h_a/h = 0.59$ ,  $b/h = 0.39$ ,  $w/h = 0.21$  and  $h_c/h = 0$  and  $h_c/h = 0.66$ , respectively. (c)-(d) For  $h_a/h = 0.65$ ,  $b/h = 0.39$ ,  $w/h = 0.84$  and  $h_c/h = 0$  and  $h_c/h = 0.66$ , respectively.

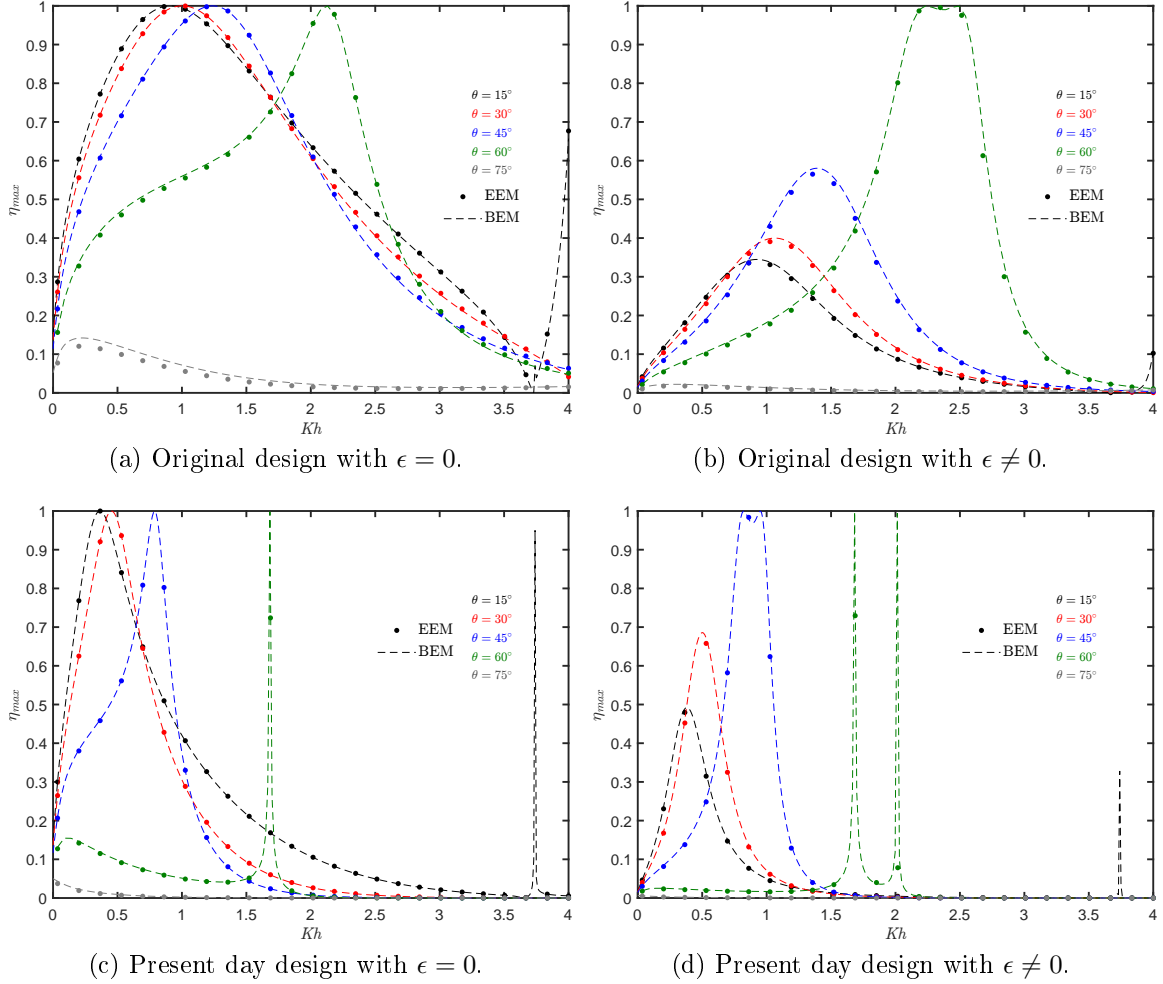


Figure 8.12: Maximum hydrodynamic efficiency versus  $Kh$  for different incidence wave angles  $\theta$  in the case of LEST. (a)-(b) For  $h_a/h = 0.06$ ,  $b/h = 0.91$ ,  $w/h = 0.48$  and  $h_c/h = 0$  and  $h_c/h = 2.85$ , respectively. (c)-(d) For  $h_a/h = 0.18$ ,  $b/h = 0.91$ ,  $w/h = 1.96$  and  $h_c/h = 0$  and  $h_c/h = 2.85$ , respectively.

spring tide with  $h_a/h = 0.18$ ,  $b/h = 0.91$ ,  $w/h = 1.96$  and  $h_c/h = 0$  and  $h_c/h = 2.85$  are shown in Figs. 8.12c and 8.12d, respectively. This time, for both figures, due to the larger front wall draft and thickness, the efficiency bands are narrower, while the values of the peak resonant frequencies are smaller and the efficiency curves appreciably decrease for large wave angles.

## 8.6 Conclusions

Under the hypotheses of linearized wave theory, the maximum theoretical hydrodynamic performance of an OWC wave energy converter is studied. The influence of the wave angle of incidence and the OWC chamber configuration on the hydrodynamic efficiency were analyzed. The solution to the problem was found by means of the matched EEM and the BEM using quadratic elements. In the EEM, continuity conditions across the interfaces are used along with the orthogonal property of the eigenfunctions to reduce the BVP into a linear system of algebraic equations. These continuity conditions are also utilized to match the regions in the BEM, where the BVP was discretized with three-noded elements. Convergence analyses were satisfactorily performed for both EEM and BEM. Validation was carried out by comparisons between these two methods and results published by [Evans and Porter \(1995\)](#); [Medina Rodríguez et al. \(2020\)](#) and an optimal agreement was achieved. Furthermore, results obtained by EEM and BEM demonstrated to agree very well. Several results of the OWC maximum hydrodynamic efficiency for various non-dimensional parameters were then obtained and discussed. The main conclusions drawn from this study are:

- An increase in the front wall thickness leads to a reduction in both the efficiency bandwidth and the value of the peak frequency. This reduction is explained by the fact that for thick front barriers, the energy transfer from the incoming wave to the internal free surface is decreased, resulting in a decrease in the internal free surface oscillation for the driving of the air column.
- For oblique waves, when the OWC chamber length to water depth ratio  $b/h$  is decreased, the efficiency bandwidth increases, while the wave period of maximum hydrodynamic efficiency is shorter. This is a similar trend to that reported by [Evans and Porter \(1995\)](#) for normal wave incidence.
- Regarding the front wall draft, the hydrodynamic efficiency bandwidth and the peak resonant frequency increase when the front wall draft to water depth ratio  $h_a/h$  decreases.
- By increasing the wave angle of incidence, the wave frequency at which resonance occurs also increases.
- For large incidence wave angles, where the wave crest is almost perpendicular to the OWC chamber, the maximum hydrodynamic efficiency notably decreases due to the null excitation of the internal water column by the parallel incident waves.
- It was found that for a wide range of frequencies and angles of incidence, high hydrodynamic efficiency values  $\eta_{max}$  are available, offering the ability for land-fixed

OWC systems to effectively harvest wave energy based on the prevailing wave period and direction of a particular location.

- By modifying the trapped air volume, it was found that for small angles of incidence, the maximum hydrodynamic efficiency is reduced when the air column height increases.

In general, the incidence wave angle and the front wall thickness of an OWC chamber demonstrated to be two important aspects to be taken into account when analyzing the OWC performance. More theoretical and experimental studies involving dissipative energy processes (due to viscous effects, friction, flow separation), thermodynamic process inside the chamber, as well as others non-linear effects, should be carried out in the future in order to provide more reliable estimates of the OWC performance under real conditions. In this sense, energy losses due to vortex shedding and flow separation that occur near the OWC front wall have been previously considered by [Ning et al. \(2015\)](#); [Ning, Wang, Zou and Teng \(2016\)](#); [Ning, Wang, Gou, Zhao and Teng \(2016\)](#); [Wang et al. \(2018\)](#); [Wang and Ning \(2020\)](#). Finally, the findings of this work are intended to promote further analysis of OWC onshore technologies and provide useful knowledge for the effective harnessing of wave energy.

## 8.7 Appendix

For normal incidence ( $\theta = 0^\circ$ ), the following expressions provide the linear system of algebraic equations for the determination of the unknowns  $A^R$ ,  $A_n^R$ ,  $B_n^R$ ,  $C_n^R$  and  $D_n^R$ :

$$A^R = -\frac{D_0^R}{ik_x h w} \int_{-h}^{-h_a} \chi_0(z) \Psi_0(z) dz - \frac{1}{ik_x h} \sum_{n=1}^{N_{em}} \frac{D_n^R \gamma_{nx}}{\sinh \gamma_{nx} w} \int_{-h}^{-h_a} \chi_n(z) \Psi_0(z) dz, \quad \text{for } m = 0, \quad (8.53a)$$

$$A_m^R = \frac{D_0^R}{k_{mx} h w} \int_{-h}^{-h_a} \chi_0(z) \Psi_m(z) dz + \frac{1}{k_{mx} h} \sum_{n=1}^{N_{em}} \frac{D_n^R \gamma_{nx}}{\sinh \gamma_{nx} w} \int_{-h}^{-h_a} \chi_n(z) \Psi_m(z) dz, \quad \text{for } m \geq 1, \quad (8.53b)$$

$$B_m^R = -\frac{D_0^R}{k_{mx} h w \sinh k_{mx} b} \int_{-h}^{-h_a} \chi_0(z) \Psi_m(z) dz - \frac{1}{k_{mx} h \sinh k_{mx} b} \sum_{n=1}^{N_{em}} \gamma_{nx} \left[ C_n^R \tanh \gamma_{nx} w + D_n^R \coth \gamma_{nx} w \right] \int_{-h}^{-h_a} \chi_n(z) \Psi_m(z) dz = 0, \quad \text{for } m \geq 0, \quad (8.54)$$



$$\begin{aligned}
 C_0^R h + D_0^R & \left[ \frac{1}{ik_x h w} \int_{-h}^{-h_a} \chi_0(z) \Psi_0(z) dz \int_{-h}^{-h_a} \Psi_0(z) \chi_0(z) dz + \right. \\
 & \left. \sum_{n=1}^{N_{em}} \frac{1}{k_{nx} h w} \int_{-h}^{-h_a} \chi_0(z) \Psi_n(z) dz \int_{-h}^{-h_a} \Psi_n(z) \chi_0(z) dz \right] + \\
 & \frac{1}{ik_x h} \sum_{n=1}^{N_{em}} \frac{D_n^R \gamma_{nx}}{\sinh \gamma_{nx} w} \int_{-h}^{-h_a} \chi_n(z) \Psi_0(z) dz \int_{-h}^{-h_a} \Psi_0(z) \chi_0(z) dz - \\
 & \sum_{n=1}^{N_{em}} \frac{D_n^R \gamma_{nx}}{\sinh \gamma_{nx} w} \sum_{l=1}^{N_{em}} \frac{1}{k_{lx} h} \int_{-h}^{-h_a} \chi_n(z) \Psi_l(z) dz \int_{-h}^{-h_a} \Psi_l(z) \chi_0(z) dz = 0, \quad \text{for } m = 0, \quad (8.55)
 \end{aligned}$$

$$\begin{aligned}
 \frac{C_m^R h}{\cosh \gamma_{mx} w} + D_0^R & \left[ \frac{1}{ik_x h w} \int_{-h}^{-h_a} \chi_0(z) \Psi_0(z) dz \int_{-h}^{-h_a} \Psi_0(z) \chi_m(z) dz + \right. \\
 & \left. \sum_{n=1}^{N_{em}} \frac{1}{k_{nx} h w} \int_{-h}^{-h_a} \chi_0(z) \Psi_n(z) dz \int_{-h}^{-h_a} \Psi_n(z) \chi_m(z) dz \right] + \\
 & \frac{1}{ik_x h} \sum_{n=1}^{N_{em}} \frac{D_n^R \gamma_{nx}}{\sinh \gamma_{nx} w} \int_{-h}^{-h_a} \chi_n(z) \Psi_0(z) dz \int_{-h}^{-h_a} \Psi_0(z) \chi_m(z) dz - \\
 & \sum_{n=1}^{N_{em}} \frac{D_n^R \gamma_{nx}}{\sinh \gamma_{nx} w} \sum_{l=1}^{N_{em}} \frac{1}{k_{lx} h} \int_{-h}^{-h_a} \chi_n(z) \Psi_l(z) dz \int_{-h}^{-h_a} \Psi_l(z) \chi_m(z) dz = 0, \quad \text{for } m \geq 1, \quad (8.56)
 \end{aligned}$$

$$\begin{aligned}
 D_0^R & \left[ -\frac{\cot k_x b}{k_x h w} \int_{-h}^{-h_a} \chi_0(z) \Psi_0(z) dz \int_{-h}^{-h_a} \Psi_0(z) \chi_m(z) dz + \right. \\
 & \left. \sum_{n=1}^{N_{em}} \frac{\coth k_{nx} b}{k_{nx} h w} \int_{-h}^{-h_a} \chi_0(z) \Psi_n(z) dz \int_{-h}^{-h_a} \Psi_n(z) \chi_m(z) dz \right] + \\
 & -\frac{\cot k_x b}{k_x h} \sum_{n=1}^{N_{em}} \left[ C_n^R \gamma_{nx} \tanh \gamma_{nx} w + D_n^R \gamma_{nx} \coth \gamma_{nx} w \right] \int_{-h}^{-h_a} \chi_n(z) \Psi_0(z) dz \int_{-h}^{-h_a} \Psi_0(z) \chi_m(z) dz + \\
 & \sum_{l=1}^{N_{em}} \left[ C_l^R \gamma_{lx} \tanh \gamma_{lx} w + D_l^R \gamma_{lx} \coth \gamma_{lx} w \right] \sum_{n=1}^{N_{em}} \frac{\coth k_{nx} b}{k_{nx} h} \int_{-h}^{-h_a} \chi_l(z) \Psi_n(z) dz \int_{-h}^{-h_a} \Psi_n(z) \chi_m(z) dz + \\
 & \left( C_m^R + D_m^R \right) h = -\frac{1}{K} \int_{-h}^{-h_a} \chi_m(z) dz, \quad \text{for } m \geq 0. \quad (8.57)
 \end{aligned}$$

## Bibliography

- Becker, A. (1992). *The Boundary Element Method in Engineering: A Complete Course*, McGraw-Hill.  
**URL:** <https://books.google.com.mx/books?id=Co9YAAAAYAAJ>
- Belibassakis, K., Magkouris, A. and Rusu, E. (2020). A BEM for the hydrodynamic analysis of oscillating water column systems in variable bathymetry, *Energies* **13**(13): 3403.
- Calheiros-Cabral, T., Clemente, D., Rosa-Santos, P., Taveira-Pinto, F., Ramos, V., Morais, T. and Cestaro, H. (2020). Evaluation of the annual electricity production of a hybrid breakwater-integrated wave energy converter, *Energy* **213**: 118845.  
**URL:** <http://www.sciencedirect.com/science/article/pii/S0360544220319526>
- Delmonte, N., Barater, D., Giuliani, F., Cova, P. and Buticchi, G. (2016). Review of oscillating water column converters, *IEEE Transactions on Industry Applications* **52**(2): 1698–1710.
- Dizadji, N. and Sajadian, S. E. (2011). Modeling and optimization of the chamber of owc system, *Energy* **36**(5): 2360 – 2366.  
**URL:** <http://www.sciencedirect.com/science/article/pii/S0360544211000119>
- Dominguez, J. (1993). *Boundary Elements in Dynamics*, Computational Engineering, Computational Mechanics Publications.  
**URL:** <https://books.google.com.mx/books?id=N4ghw092NIMC>
- Doyle, S. and Aggidis, G. A. (2019). Development of multi-oscillating water columns as wave energy converters, *Renewable & Sustainable Energy Reviews* **107**: 75 – 86.  
**URL:** <http://www.sciencedirect.com/science/article/pii/S1364032119301145>
- Drew, B., Plummer, A. and Sahinkaya, M. (2009). A review of wave energy converter technology, *Proceedings of The Institution of Mechanical Engineers Part A-journal of Power and Energy* **223**: 887–902.
- EC (2016). *Study on lessons for ocean energy development*.  
**URL:** [http://publications.europa.eu/resource/cellar/3a4f6411-6777-11e7-b2f2-01aa75ed71a1.0001.01/DOC\\_1](http://publications.europa.eu/resource/cellar/3a4f6411-6777-11e7-b2f2-01aa75ed71a1.0001.01/DOC_1)
- Şentürk, U. and Özdamar, A. (2012). Wave energy extraction by an oscillating water column with a gap on the fully submerged front wall, *Applied Ocean Research* **37**: 174 – 182.  
**URL:** <http://www.sciencedirect.com/science/article/pii/S0141118712000405>
- Evans, D. and Porter, R. (1995). Hydrodynamic characteristics of an oscillating water column device, *Applied Ocean Research* **17**(3): 155 – 164.  
**URL:** <http://www.sciencedirect.com/science/article/pii/0141118795000089>
- Evans, D. V. (1982). Wave-power absorption by systems of oscillating surface pressure distributions, *Journal of Fluid Mechanics* **114**: 481–499.

CHAPTER 8. THE EFFECTS OF DIRECTIONAL WAVES AND CHAMBER  
CONFIGURATION ON THE EFFICIENCY OF AN OWC DEVICE

---

- Falcão, A. F. O. (2010). Wave energy utilization: A review of the technologies, *Renewable Sustainable Energy Rev.* **14**(3): 899 – 918.  
**URL:** <http://www.sciencedirect.com/science/article/pii/S1364032109002652>
- Gaspar, L. A., Teixeira, P. R. and Didier, E. (2020). Numerical analysis of the performance of two onshore oscillating water column wave energy converters at different chamber wall slopes, *Ocean Engineering* **201**: 107119.  
**URL:** <http://www.sciencedirect.com/science/article/pii/S0029801820301840>
- Gonçalves, R. A., Teixeira, P. R., Didier, E. and Torres, F. R. (2020). Numerical analysis of the influence of air compressibility effects on an oscillating water column wave energy converter chamber, *Renewable Energy* **153**: 1183 – 1193.  
**URL:** <http://www.sciencedirect.com/science/article/pii/S0960148120302755>
- Gunn, K. and Stock-Williams, C. (2012). Quantifying the global wave power resource, *Renewable Energy* **44**: 296 – 304.  
**URL:** <http://www.sciencedirect.com/science/article/pii/S0960148112001310>
- Howe, D. and Nader, J.-R. (2017). Owc wec integrated within a breakwater versus isolated: Experimental and numerical theoretical study, *International Journal of Marine Energy* **20**: 165 – 182.  
**URL:** <http://www.sciencedirect.com/science/article/pii/S2214166917300632>
- Ibarra-Berastegi, G., Sáenz, J., Ulazia, A., Serras, P., Esnaola, G. and Garcia-Soto, C. (2018). Electricity production, capacity factor, and plant efficiency index at the mutriku wave farm (2014–2016), *Ocean Engineering* **147**: 20 – 29.  
**URL:** <http://www.sciencedirect.com/science/article/pii/S0029801817306157>
- Jin, J., Liu, Z., Hyun, B.-S. and Hong, K. (2012). Effects of wave direction on performance of oscillating water column type wave energy convertor, *Proceedings of the International Offshore and Polar Engineering Conference* pp. 582–587.
- John Ashlin, S., Sundar, V. and Sannasiraj, S. (2016). Effects of bottom profile of an oscillating water column device on its hydrodynamic characteristics, *Renewable Energy* **96**: 341 – 353.  
**URL:** <http://www.sciencedirect.com/science/article/pii/S0960148116303937>
- Katsikadelis, J. (2002). *Boundary Elements. Theory and Applications*, Elsevier.
- Koley, S. and Trivedi, K. (2020). Mathematical modeling of oscillating water column wave energy converter devices over the undulated sea bed, *Engineering Analysis with Boundary Elements* **117**: 26 – 40.  
**URL:** <http://www.sciencedirect.com/science/article/pii/S0955799720300801>
- Lin, Y., Bao, J., Liu, H., Li, W., Tu, L. and Zhang, D. (2015). Review of hydraulic transmission technologies for wave power generation, *Renewable & Sustainable Energy Reviews* **50**: 194 – 203.  
**URL:** <http://www.sciencedirect.com/science/article/pii/S1364032115004116>

CHAPTER 8. THE EFFECTS OF DIRECTIONAL WAVES AND CHAMBER  
CONFIGURATION ON THE EFFICIENCY OF AN OWC DEVICE

---

- Mahnamfar, F. and Altunkaynak, A. (2017). Comparison of numerical and experimental analyses for optimizing the geometry of owc systems, *Ocean Engineering* **130**: 10 – 24.  
**URL:** <http://www.sciencedirect.com/science/article/pii/S0029801816305583>
- Malara, G., Gomes, R., Arena, F., Henriques, J., Gato, L. and Falcão, A. (2017). The influence of three-dimensional effects on the performance of u-type oscillating water column wave energy harvesters, *Renewable Energy* **111**: 506 – 522.  
**URL:** <http://www.sciencedirect.com/science/article/pii/S0960148117303452>
- Martins-rivas, H. and Mei, C. C. (2009). Wave power extraction from an oscillating water column along a straight coast, *Ocean Engineering* **36**(6): 426 – 433.  
**URL:** <http://www.sciencedirect.com/science/article/pii/S002980180900002X>
- Masuda, Y. (1986). An experience of wave power generator through tests and improvement, in D. V. Evans and A. F. O. de Falcão (eds), *Hydrodynamics of Ocean Wave-Energy Utilization*, Springer Berlin Heidelberg, Berlin, Heidelberg, pp. 445–452.
- Medina-Lopez, E., Allsop, W., Dimakopoulos, A. and Bruce, T. (2015). *Conjectures on the Failure of the OWC Breakwater at Mutriku*, pp. 592–603.  
**URL:** <https://ascelibrary.org/doi/abs/10.1061/9780784480304.063>
- Medina Rodríguez, A. A., Blanco Ilzarbe, J. M., Silva Casarín, R. and Izquierdo Ereño, U. (2020). The influence of the chamber configuration on the hydrodynamic efficiency of oscillating water column devices, *Journal of Marine Science and Engineering* **8**(10): 751.
- Melikoglu, M. (2018). Current status and future of ocean energy sources: A global review, *Ocean Engineering* **148**: 563 – 573.  
**URL:** <http://www.sciencedirect.com/science/article/pii/S002980181730714X>
- Mishra, S., Mohanta, D., Appasani, B. and Kabalci, E. (2020). *OWC-Based Ocean Wave Energy Plants: Modeling and Control*, Energy Systems in Electrical Engineering Series, Springer Singapore Pte. Limited.  
**URL:** <https://books.google.com.mx/books?id=-TMLEAAQBAJ>
- Morris-Thomas, M. T., Irvin, R. J. and Thiagarajan, K. P. (2006). An Investigation Into the Hydrodynamic Efficiency of an Oscillating Water Column, *Journal of Offshore Mechanics and Arctic Engineering* **129**(4): 273–278.  
**URL:** <https://doi.org/10.1115/1.2426992>
- Ning, D.-Z., Shi, J., Zou, Q.-P. and Teng, B. (2015). Investigation of hydrodynamic performance of an owc (oscillating water column) wave energy device using a fully nonlinear hoberm (higher-order boundary element method), *Energy* **83**: 177 – 188.  
**URL:** <http://www.sciencedirect.com/science/article/pii/S0360544215001644>
- Ning, D.-Z., Wang, R.-Q., Gou, Y., Zhao, M. and Teng, B. (2016). Numerical and experimental investigation of wave dynamics on a land-fixed owc device, *Energy* **115**: 326 – 337.  
**URL:** <http://www.sciencedirect.com/science/article/pii/S0360544216312324>

CHAPTER 8. THE EFFECTS OF DIRECTIONAL WAVES AND CHAMBER  
CONFIGURATION ON THE EFFICIENCY OF AN OWC DEVICE

---

- Ning, D.-Z., Wang, R.-Q., Zou, Q.-P. and Teng, B. (2016). An experimental investigation of hydrodynamics of a fixed owc wave energy converter, *Applied Energy* **168**: 636 – 648.  
**URL:** <http://www.sciencedirect.com/science/article/pii/S0306261916300952>
- Pawitan, K. A., Dimakopoulos, A. S., Vicinanza, D., Allsop, W. and Bruce, T. (2019). A loading model for an owc caisson based upon large-scale measurements, *Coastal Engineering* **145**: 1 – 20.  
**URL:** <http://www.sciencedirect.com/science/article/pii/S0378383918302114>
- Pawitan, K. A., Vicinanza, D., Allsop, W. and Bruce, T. (2020). Front wall and in-chamber impact loads on a breakwater-integrated oscillating water column, *Journal of Waterway, Port, Coastal, and Ocean Engineering* **146**(5): 04020037.  
**URL:** <https://ascelibrary.org/doi/abs/10.1061/%28ASCE%29WW.1943-5460.0000595>
- Pecher, A. and Kofoed, J. (2017). *Handbook of Ocean Wave Energy*.
- Polinder, H. and Scuotto, M. (2005). Wave energy converters and their impact on power systems, *2005 International Conference on Future Power Systems*, pp. 9 pp.–9.
- Rezanejad, K., Bhattacharjee, J. and Guedes Soares, C. (2013). Stepped sea bottom effects on the efficiency of nearshore oscillating water column device, *Ocean Engineering* **70**: 25 – 38.  
**URL:** <http://www.sciencedirect.com/science/article/pii/S0029801813002229>
- Rezanejad, K., Guedes Soares, C., López, I. and Carballo, R. (2017). Experimental and numerical investigation of the hydrodynamic performance of an oscillating water column wave energy converter, *Renewable Energy* **106**: 1 – 16.  
**URL:** <http://www.sciencedirect.com/science/article/pii/S0960148117300034>
- Ross, D. (2012). *Energy from the Waves*, Elsevier Science.  
**URL:** <https://books.google.com.mx/books?id=gZ47AAAAQBAJ>
- Service, U. S. M. M. (2007). *Alternative Energy Development and Production and Alternate Use of Facilities on the Outer Continental Shelf: Environmental Impact Statement*, Alternative Energy Development and Production and Alternate Use of Facilities on the Outer Continental Shelf: Environmental Impact Statement.  
**URL:** <https://books.google.com.mx/books?id=oUI3AQAAMAAJ>
- Sheng, W. (2019). Motion and performance of bdbb owc wave energy converters: I, hydrodynamics, *Renewable Energy* **138**: 106 – 120.  
**URL:** <http://www.sciencedirect.com/science/article/pii/S0960148119300163>
- Teixeira, P. R. and Didier, E. (2021). Numerical analysis of the response of an onshore oscillating water column wave energy converter to random waves, *Energy* **220**: 119719.  
**URL:** <http://www.sciencedirect.com/science/article/pii/S0360544220328267>

CHAPTER 8. THE EFFECTS OF DIRECTIONAL WAVES AND CHAMBER CONFIGURATION ON THE EFFICIENCY OF AN OWC DEVICE

---

- Vicinanza, D., Lauro, E. D., Contestabile, P., Gisonni, C., Lara, J. L. and Losada, I. J. (2019). Review of innovative harbor breakwaters for wave-energy conversion, *Journal of Waterway, Port, Coastal, and Ocean Engineering* **145**(4): 03119001.  
**URL:** <https://ascelibrary.org/doi/abs/10.1061/%28ASCE%29WW.1943-5460.0000519>
- Viviano, A., Musumeci, R. E., Vicinanza, D. and Foti, E. (2019). Pressures induced by regular waves on a large scale owc, *Coastal Engineering* **152**: 103528.  
**URL:** <http://www.sciencedirect.com/science/article/pii/S0378383919301589>
- Viviano, A., Naty, S., Foti, E., Bruce, T., Allsop, W. and Vicinanza, D. (2016). Large-scale experiments on the behaviour of a generalised oscillating water column under random waves, *Renewable Energy* **99**: 875 – 887.  
**URL:** <http://www.sciencedirect.com/science/article/pii/S0960148116306826>
- Wang, D., Katory, M. and Li, Y. (2002). Analytical and experimental investigation on the hydrodynamic performance of onshore wave-power devices, *Ocean Engineering* **29**(8): 871 – 885.  
**URL:** <http://www.sciencedirect.com/science/article/pii/S0029801801000580>
- Wang, R.-Q. and Ning, D.-Z. (2020). Dynamic analysis of wave action on an owc wave energy converter under the influence of viscosity, *Renewable Energy* **150**: 578 – 588.  
**URL:** <http://www.sciencedirect.com/science/article/pii/S0960148120300082>
- Wang, R.-Q., Ning, D.-Z., Zhang, C.-W., Zou, Q.-P. and Liu, Z. (2018). Nonlinear and viscous effects on the hydrodynamic performance of a fixed owc wave energy converter, *Coastal Engineering* **131**: 42 – 50.  
**URL:** <http://www.sciencedirect.com/science/article/pii/S0378383917300637>
- Zheng, S., Antonini, A., Zhang, Y., Greaves, D., Miles, J. and Iglesias, G. (2019). Wave power extraction from multiple oscillating water columns along a straight coast, *Journal of Fluid Mechanics* **878**: 445–480.
- Zheng, S., Zhang, Y. and Iglesias, G. (2019). Coast/breakwater-integrated owc: A theoretical model, *Marine Structures* **66**: 121 – 135.  
**URL:** <http://www.sciencedirect.com/science/article/pii/S0951833918304180>
- Zheng, S., Zhu, G., Simmonds, D., Greaves, D. and Iglesias, G. (2020). Wave power extraction from a tubular structure integrated oscillating water column, *Renewable Energy* **150**: 342 – 355.  
**URL:** <http://www.sciencedirect.com/science/article/pii/S0960148120300094>
- Zhu, G., Graham, D., Zheng, S., Hughes, J. and Greaves, D. (2020). Hydrodynamics of onshore oscillating water column devices: A numerical study using smoothed particle hydrodynamics, *Ocean Engineering* **218**: 108226.  
**URL:** <http://www.sciencedirect.com/science/article/pii/S0029801820311495>

## Chapter 9

# A Three-Dimensional Analysis of the Hydrodynamic Performance of a Land-Fixed OWC Device

In the previous chapters, two-dimensional studies were conducted to evaluate the performance of OWC devices with various chamber configurations and wave directionality. However, the essential quantity utilized to assess the performance of OWC systems in three-dimensional (3D) model studies is the capture width ( $CW$ ), whose maximization leads to optimal wave energy harvesting.

In 3D theoretical and experimental works, apart from the consideration that the front wall in the OWC chamber is very narrow, air compressibility is often neglected due to practical difficulties, even though it is known that these two aspects affect the performance of OWC systems. Thus, the major goal of this chapter is to determine how the inclusion of linear air compressibility affects the capture width and the hydrodynamic parameters of the OWC device when a thick front wall is considered. As a result, this chapter is intended to offer a solution to the following research question using a 3D numerical approach: What is the influence of chamber design and air compressibility on the hydrodynamic performance of a land-fixed OWC device?

This chapter consists of the submitted journal article:

Medina Rodríguez A.A., Silva Casarín R., Blanco Ilzarbe J.M. (2021). “*A 3D boundary element method for analysing the hydrodynamic performance of a land-fixed oscillating water column device*”. **Engineering Analysis with Boundary Elements**. Under Review.

**A 3D boundary element method for analysing the hydrodynamic performance of a land-fixed oscillating water column device**

Ayrton Alfonso Medina Rodríguez, Rodolfo Silva Casarín and Jesús María Blanco Ilzarbe

**Abstract**

In this work, the theoretical hydrodynamic performance of an onshore Oscillating Water Column (OWC) device, subjected to normal wave incidence, is investigated. Based on linear surface-wave theory, the full solution of the boundary value problem (BVP) is obtained by using a three-dimensional (3D) boundary element method (BEM) with nine-noded quadrilateral elements. The method of subdomains is used to solve the BVP by applying the BEM separately to each of its regions, and the continuity of velocity potential and flux are used to match the problem. The capture width, hydrodynamical coefficients and free surface elevations are analysed for different OWC geometric parameters of the chamber. Numerical results for the hydrodynamic performance were found to be in good agreement with cases reported elsewhere. The findings show that the chamber configuration and the linearized air compressibility have a significant impact on the capture width bandwidth, the resonant frequency and the free surface elevation within the chamber.

## 9.1 Introduction

Of all the wave energy converters (WECs), the OWC is probably the most extensively investigated device, and has the largest number of prototypes deployed in the sea to date (Falcão; 2010). It is the only technology in which a central component of the device mimics a naturally occurring structure; the blow holes found in limestone cliffs on the coast (Heath; 2012). Compared to most other WECs, the OWC system stands out because of its simplicity. Basically, it consists of two main components: a partially submerged collecting chamber, made of concrete or steel, which is open to the sea at the bottom, and a Power Take-Off (PTO) system, which converts wave energy to mechanical or electrical energy. The PTO system is typically a turbine, run by a rotor, which is the only moving part of the mechanism and which is located above the water level to prevent direct exposure to seawater. The working principle is similar to a moving piston; a water column is captured inside the chamber and is forced to oscillate up and down by the wave action. This alternately compresses and rarifies the trapped air, driving the airflow back and forth through the turbine in a duct, which is coupled to a generator and connected to the atmosphere (Falcão; 2010; Service; 2007).

The first OWCs were deployed in the sea in the 1960s and 1970s. These navigation buoys and the Kaimei, a floating testing platform that housed several OWCs, were developed in Japan under the coordination of Yoshio Masuda (Falcão; 2010). The navigation buoys are regarded as the most successful wave energy harvesting systems (Masuda; 1986; Sheng; 2019; Falcão; 2010). Using modern wave energy system terminology, these buoys are classified as (floating) OWC devices, but they were first known as Masuda devices after the inventor (Sheng; 2019; Ross; 2012).



## CHAPTER 9. A THREE-DIMENSIONAL ANALYSIS OF THE HYDRODYNAMIC PERFORMANCE OF A LAND-FIXED OWC DEVICE

---

Other ocean wave power stations were later built in Norway, Japan, the UK, China and elsewhere, most of which were OWC stations. In Europe, research and development of wave energy increased after the decision taken by the European Commission, in 1991, to include it in their R&D program on renewable energies (Falcão and Henriques; 2016). This led to the design and development of the first two full-scale OWC fixed-structure plants, one on the island of Pico, in the Azores, Portugal (Falcao; 2000; Falcão et al.; 2020), and the other on the island of Islay, Scotland, UK (Heath et al.; 2001).

Due to its few moving components and simple working principle, the OWC system can be adapted and used in a range of locations: on the coastline, in the nearshore region or floating offshore. Onshore OWCs are fixed and deployed close to the coastline or can be built into coastal structures, such as breakwaters (Teixeira and Didier; 2021; Howe and Nader; 2017; Vicinanza et al.; 2019). While the costs involved in OWC systems are generally a disadvantage (Lin et al.; 2015), onshore OWC devices offer some cost-reductions, as the installation and maintenance are relatively cheap if the structure is easily accessible. Additionally, in near-shore areas and coastal cliffs, due to the refraction, shoaling and diffraction processes, wave energy can be more naturally concentrated towards some coastal sections (Polinder and Scuotto; 2005). The absorption of energy into the OWC collecting chamber contributes to coastal protection, does not interfere with vessel traffic at port entrances and if integrated into a breakwater (Torre-Enciso et al.; 2009; Cabral et al.; 2020; Rosa-Santos et al.; 2019), increases its hydraulic efficiency by minimizing wave reflection. Thus, wave energy extraction using OWC systems can achieve competitive costs and high reliability, to become trusted wave-energy technology.

Several theoretical and experimental studies have been conducted to analyse the hydrodynamic aspects of OWC devices. Pioneering studies of wave energy absorbers based on rigid body models were performed by Evans (1976, 1981); Mei (1976); Evans (1982); Falnes and McIver (1985). Count and Evans Count and Evans (1984) developed a theoretical model for studying the hydrodynamic performance of an OWC device equipped with projecting sidewalls. The results demonstrated that the addition of a harbour can increase the performance of the device. Evans and Porter analysed the performance of an OWC device consisting of a thin rigid surface piercing barrier near a vertical wall Evans and Porter (1995) and a vertical, partially immersed circular cylinder, open at either end Evans and Porter (November 1997), by using the matched eigenfunction expansion and the Galerkin method in constant water depth.

The BEM has been employed in two and three dimensions to find a solution for the interaction of incident waves with an OWC device (Brito-Melo et al.; 1999; Wang et al.; 2002; Delauré and Lewis; 2003; Hong et al.; 2004; Josset and Clément; 2007; Hasanabad; 2015; Medina Rodríguez et al.; 2020). Wang et al. Wang et al. (2002) carried out a numerical study on the hydrodynamic performance of a shoreline-mounted OWC device using the BEM. The results were verified by testing a physical model in a wave basin under regular wave conditions. Using the potential flow approach, Delauré and Lewis (2003) used a 3D BEM to analyse the hydrodynamic properties of a bottom-mounted OWC power plant. Josset and Clément (2007) used the 3D BEM to analyse the OWC hydrodynamic performance in time-domain. The numerical method was applied to the wave energy power plant located on Pico Island, Azores, to estimate the annual performance of the plant and find ways to improve its productivity.

Improving the efficiency of the OWC devices is important for the commercialization of

this technology, and therefore this has been the focus of intense study for many researchers. Some of the investigations have concentrated on analysing the effect of the geometry of the OWC chamber and the bottom configuration on the performance of the device (Morris-Thomas et al.; 2006; Dizadji and Sajadian; 2011; Şentürk and Özdamar; 2012; Rezanejad et al.; 2013; Ning et al.; 2015; John Ashlin et al.; 2016; Ning et al.; 2016; Mahnamfar and Altunkaynak; 2017). Dizadji and Sajadian Dizadji and Sajadian (2011) carried out experiments with different geometrical OWC designs, to obtain the optimum setup for harnessing ocean energy. The authors reported that a substantial increase in air outflow from the chamber was found by decreasing the angle of the front wall. The configuration of parallel front and back walls resulted in a relative maximization of air outflow. Rezanejad et al. (2013) analysed the impact of a step-type bottom topography on the efficiency of a nearshore OWC, concluding that the inclusion of an artificial step in the sea bottom may lead to a significant increase in the absorption of power.

Ning et al. (2015) analysed the performance of a fixed OWC device, using a time-domain higher-order BEM, in a two-dimensional (2D), fully nonlinear, numerical wave flume. It was found that the geometric parameters of the chamber play an important role in its hydrodynamic performance. John Ashlin et al. (2016) focused on the effects of the bottom profile configuration on the hydrodynamic performance of the OWC. Flat, circular, curved and sloped bottoms were tested, and the authors concluded that the natural frequency of the system was not changed by these four profiles, while the circular curved bottom profile provides better performance in terms of its effective wave energy conversion. An experimental study of the hydrodynamic performance of a fixed OWC device was performed by Ning et al. (2016). They found that the bottom slope has a small effect on the resonant frequency, while increased steepness in the slope of the bottom improves the hydrodynamic performance. To analyse the effect of the OWC geometry on its optimization, Mahnamfar and Altunkaynak (2017) applied a numerical model and experiments. Gaspar et al. (2020) conducted a numerical analysis of the performance of two OWC devices with different front and back wall slopes. They found that an OWC with an inclined wall is more effective than a vertical-walled OWC system. To investigate the efficiency of an OWC, Zhu et al. (2020) employed a 2D numerical wave tank, using the weakly compressible, smoothed particle hydrodynamics (SPH) method. They found that, in terms of power absorption, an OWC with thinner walls is more efficient.

In order to examine the variations in random waves from regular waves in the OWC performance, Teixeira and Didier (2021) recently developed a numerical analysis of an onshore OWC system. They reported that at high wave periods, the OWC efficiency for regular and random waves approaches a 28% difference around the resonance with slight variations. The impact of the compressibility effect on the air within the OWC chamber was investigated by Gonçalves et al. (2020) through a numerical model. The authors showed that air compressibility has a major impact on the efficiency of the OWC, something which is usually ignored in small-scale experiments and numerical simulations.

In this work, the 3D interaction of normal incident waves with a thick-front wall OWC device is investigated. Using the potential flow method, the linear wave theory for a constant sea depth is applied and the viscous effects and nonlinear air compressibility are disregarded. A 3D BEM with nine-noded quadrilateral panels is used to solve the corresponding BVP. These

panels are discretised by nine nodes, with eight nodes placed on the edges, and one in the centre. By applying the BEM separately to each of its regions, the subdomains approach is used to solve the BVP and the continuity conditions of velocity potential and flux are used to match the subregions. This work also compares the present 3D results with the experimental data obtained by [Morris-Thomas et al. \(2006\)](#) and [Rezanejad et al. \(2017\)](#) and the 2D analytical results of [Evans and Porter \(1995\)](#). The study aims to analyse the bandwidth change on the capture width curves, and the modification of the peak resonant frequency and free surface elevation due to the geometrical configuration of the OWC chamber and the linear compressibility of the trapped air. For a range of various non-dimensional parameters, numerical estimates for the capture width, hydrodynamical coefficients and free surface elevation are then provided and analysed.

## 9.2 Boundary value problem

The OWC device-fluid system and the Cartesian coordinate system are shown in Fig. 9.1. The origin of the coordinate system,  $O$ , is located at the intersection of the undisturbed free surface water level, the back wall and the middle of the OWC chamber. This chamber is modelled by a partially immersed front wall at  $x = b$ , with draft  $a$  and thickness  $w$ , and the back rigid wall, located at  $x = 0$ , both of width  $d$ . Waves approach the device from the  $x$  direction in water of depth  $h$ . Both the fluid and the OWC system are confined between two parallel walls, of separation  $d$  (not shown in the figure). The air within the OWC chamber is assumed to be linked to the atmosphere by a turbine. The height of the chamber is denoted by  $c$ .

The front wall is denoted as  $B_b = \{(x, y, z) : (x = b, |y| \leq d/2, -a \leq z \leq 0) \cup (b < x < L, |y| \leq d/2, z = -a) \cup (x = L, |y| \leq d/2, -a \leq z \leq 0)\}$ , the back rigid wall by  $B_w = \{(x, y, z) : x = 0, |y| \leq d/2, -h < z < 0\}$ , the internal free surface inside the chamber by  $F_i = \{(x, y, z) : 0 \leq x \leq b, |y| \leq d/2, z = 0\}$ , the external free surface by  $F_f = \{(x, y, z) : L \leq x \leq \infty, |y| \leq d/2, z = 0\}$ , the flat bottom by  $B_d = \{(x, y, z) : (0 < x < \infty, |y| \leq d/2, z = -h)\}$  and the vertical plane area of the gap below the front barrier by  $B_g = \{(x, y, z) : x = L, |y| \leq d/2, -h \leq z \leq -a\}$ . The BVP is separated into two regions, with Region 1 conformed by the OWC chamber and the gap below the front barrier, while Region 2 consists of the propagation zone of the external free surface.

The seawater is assumed to be inviscid and incompressible and the wave motion is considered to be adequately represented by the linearized water wave theory, omitting the effect of surface tension. By assuming a simple harmonic flow with angular frequency  $\omega$ , we define a velocity potential  $\Phi(x, y, z, t)$  with  $\Phi(x, y, z, t) = \text{Re}\{\phi(x, y, z)e^{-i\omega t}\}$ , where  $\text{Re}\{\}$  denotes the real part of a complex expression, and  $t$  is the time. Thus, the spatial velocity potential  $\phi$  satisfies the Laplace equation

$$\left( \frac{\partial^2}{\partial x^2} + \frac{\partial^2}{\partial y^2} + \frac{\partial^2}{\partial z^2} \right) \phi = 0, \quad (9.1)$$

with the no-flow boundary conditions applied at the bottom, the front barrier, the back and

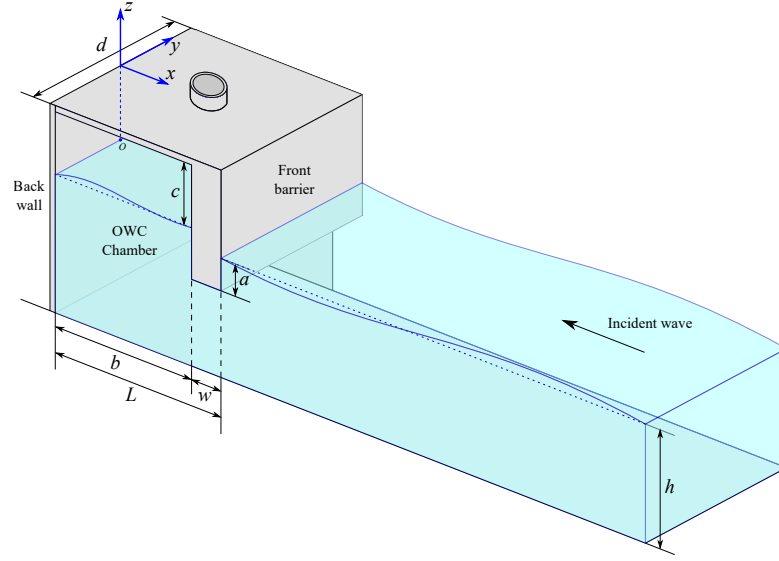


Figure 9.1: Definition sketch of the 3D interaction of a land-fixed OWC device with perpendicular incident waves.

lateral walls as

$$\frac{\partial \phi}{\partial n} = 0. \quad (9.2)$$

By imposing a pressure distribution  $P(t)$  over the internal free surface, and after considering simple harmonic motions for the free surface  $\bar{\eta} = \text{Re}\{\zeta(x, y, z)e^{-i\omega t}\}$  and  $P(t) = \text{Re}\{p(x, y, z)e^{-i\omega t}\}$ , the dynamic free surface boundary conditions are as follows

$$\phi + \frac{ig}{\omega}\zeta = -\frac{i}{\rho\omega}p \quad \text{on } z = 0, \quad 0 < x < b, \quad |y| \leq \frac{d}{2}, \quad (9.3a)$$

$$\phi + \frac{ig}{\omega}\zeta = 0 \quad \text{on } z = 0, \quad L < x < \infty, \quad |y| \leq \frac{d}{2}, \quad (9.3b)$$

in the internal and external free surface (with  $p = 0$ ), respectively. In the case of the kinematic free surface boundary condition, this is of the form

$$\frac{\partial \phi}{\partial z} + i\omega\zeta = 0 \quad \text{on } z = 0, \quad |y| \leq \frac{d}{2}, \quad 0 < x < b, \quad \text{and } L < x < \infty. \quad (9.4)$$

Therefor, by combining Eqs. (9.3) and (9.4), the internal and external linearized free surface boundary conditions are

$$\frac{\partial \phi}{\partial z} - K\phi = \begin{cases} \frac{i\omega p}{\rho g} & \text{on } z = 0, \quad 0 < x < b, \quad |y| \leq \frac{d}{2}, \\ 0 & \text{on } z = 0, \quad L < x < \infty, \quad |y| \leq \frac{d}{2}, \end{cases} \quad (9.5)$$

CHAPTER 9. A THREE-DIMENSIONAL ANALYSIS OF THE HYDRODYNAMIC  
PERFORMANCE OF A LAND-FIXED OWC DEVICE

---

respectively, where  $K = \omega^2/g$ , with  $g$  being the gravitational constant and  $\rho$  the seawater density.

As proposed by Evans (1982), the velocity potential is decomposed as

$$\phi(x, y, z) = \phi^S + \frac{i\omega p}{\rho g} \phi^R, \quad (9.6)$$

where  $\phi^S$  and  $\phi^R$  represent, respectively, the scattered and radiated velocity potentials. The scattered potential  $\phi^S$  satisfies Eqs. (9.1)–(9.5) with  $p = 0$  inside the chamber; while the radiated potential  $\phi^R$  satisfies Eqs. (9.1)–(9.5) with Eq. (9.5) replaced by

$$\frac{\partial \phi^R}{\partial z} - K \phi^R = 1 \quad \text{on} \quad z = 0, \quad 0 < x < b. \quad (9.7)$$

Similarly, the scattered potential is separated into an incident part ( $\phi^I$ ) and a diffracted ( $\phi^D$ ) part as

$$\phi^S = \phi^I + \phi^D. \quad (9.8)$$

where the incident potential  $\phi^I$  is defined by

$$\phi^I = -\frac{igA \cosh k(z+h)}{\omega \cosh kh} e^{-ikx}, \quad (9.9)$$

where  $A$  is the incident wave amplitude and the wavenumber  $k$  is the positive real root of the wave dispersion relation, given by

$$\omega^2 = gk \tanh kh. \quad (9.10)$$

The diffracted and radiated potentials satisfy the Sommerfeld radiation condition at the far field, given by

$$\frac{\partial \phi^{D,R}}{\partial x} - ik \phi^{D,R} = 0 \quad \text{as} \quad x \rightarrow +\infty. \quad (9.11)$$

Furthermore, the time harmonic induced volume flux across the internal free surface ( $F_i$ ) is also separated into scattering and radiation volume fluxes,  $q^S$  and  $q^R$ , respectively, as follows

$$q = \int_{F_i} \frac{\partial \phi}{\partial z} dS = q^S + \frac{i\omega p}{\rho g} q^R, \quad (9.12)$$

and the continuity of volume flux across  $F_i$  is ensured by

$$q^{S,R} = \int_{F_i} \frac{\partial \phi}{\partial z} dS^{S,R}. \quad (9.13)$$

### 9.3 Efficiency relations

Following the decomposition proposed by Evans (1982), the radiation volume flux  $q^R$  is separated into real and imaginary parts as follows

$$\frac{i\omega p}{\rho g} q^R = -(\hat{\mathcal{B}} - i\hat{\mathcal{A}}) p = -Zp, \quad (9.14)$$

where  $Z = \hat{\mathcal{B}} - i\hat{\mathcal{A}}$  represents the complex admittance, while  $\hat{\mathcal{A}}$  and  $\hat{\mathcal{B}}$  are related to the added mass and the radiation damping in a rigid body system, respectively. These are defined by

$$\hat{\mathcal{A}} = \frac{\omega}{\rho g} \text{Re}\{q^R\}, \quad (9.15a)$$

$$\hat{\mathcal{B}} = \frac{\omega}{\rho g} \text{Im}\{q^R\} \quad (9.15b)$$

and are called the radiation susceptance and radiation conductance parameters, respectively (Evans and Porter; 1995).

By assuming that the volume flux through the turbine is linearly proportional to the pressure drop across the internal free surface, we have

$$q = (\Lambda - i\Theta) p, \quad (9.16)$$

where  $\Lambda$  is a real control parameter related to the damping induced by the linear turbine to the air flow. The term  $\Theta = \omega V_0 / (\gamma p_a)$  represents the linear compressibility of the trapped air inside the chamber with volume  $V_0$ ,  $\gamma = 1.4$  is the specific heat ratio of air and  $p_a$  the atmospheric air pressure (Rezanejad et al.; 2017). An expression for the imposed internal pressure is obtained after combining Eqs. (9.12), (9.14) and (9.16), thus resulting in

$$p = \frac{q^S}{\Lambda + Z - i\Theta}. \quad (9.17)$$

The total rate of work done by the pressure forces inside the OWC is now averaged over one wave period, to obtain the total rate of power absorbed per unit width of pressure distribution as follows:

$$W = \frac{1}{2} \text{Re}\{\bar{p}q\}, \quad (9.18)$$

with  $\bar{p}$  denoting the complex conjugate of  $p$ . Using Eqs. (9.12) and (9.14) into Eq. (9.18), the following equation is obtained

$$W = \frac{1}{2} \text{Re}\{\bar{p}(q^S - Zp)\} = \frac{|q^S|^2}{8\hat{\mathcal{B}}} - \frac{\hat{\mathcal{B}}}{2} \left| p - \frac{q^S}{2\hat{\mathcal{B}}} \right|^2, \quad (9.19)$$

Thus, if  $\hat{\mathcal{B}}^{-1}$  exists, the maximum work is

$$W_{max} = \frac{|q^S|^2}{8\hat{\mathcal{B}}}, \quad \text{for } p = \frac{q^S}{2\hat{\mathcal{B}}}, \quad (9.20)$$

and  $\Lambda = \overline{(Z - i\Theta)}$  for maximum power. Now, after combining Eqs. (9.17) and (9.19),  $W$  can be written as

$$W = \frac{|q^S|^2}{8\hat{\mathcal{B}}} \left[ 1 - \left( \frac{|\Lambda - Z + i\Theta|}{|\Lambda + Z - i\Theta|} \right)^2 \right]. \quad (9.21)$$

Then, to obtain the optimal power conversion efficiency, the optimum value of  $\Lambda$  must be calculated. As explained by Şentürk and Özdamar (2012), this is obtained by applying zero value to the derivative with respect to  $\Lambda$  for the squared-right term inside the brackets of Eq. (9.21), thus giving

$$\Lambda_{opt} = |Z - i\Theta| = \sqrt{\hat{\mathcal{B}}^2 + (\hat{\mathcal{A}} + \Theta)^2} \quad (9.22)$$

and after the substitution of Eq. (9.22) into Eq. (9.21),

$$W_{opt} = \frac{|q^S|^2}{8\hat{\mathcal{B}}} \left[ 1 - \frac{\Lambda_{opt} - \hat{\mathcal{B}}}{\Lambda_{opt} + \hat{\mathcal{B}}} \right] \quad (9.23)$$

is given.

Similar to the work of Evans and Porter (November 1997) for a vertical cylindrical OWC device, the following non-dimensionalised quantities are defined

$$\mu = \frac{\rho g}{\omega b d} \hat{\mathcal{A}}, \quad (9.24a)$$

$$\nu = \frac{\rho g}{\omega b d} \hat{\mathcal{B}}, \quad (9.24b)$$

which are, respectively, the radiation susceptance and radiation conductance coefficients.

The capture width ( $CW$ ), which considers the total power absorbed by a WEC, is the fundamental quantity used to evaluate the performance of OWC systems in 3D model analyses. The  $CW$  is defined as the ratio of the mean wave power absorbed by the device to the mean wave power per unit crest length of the incident wave ( $P_w$ ) (Evans and Porter; November 1997). The maximum  $CW$  is then given by

$$CW_{max} = \frac{W_{opt}}{P_w}, \quad (9.25)$$

where  $P_w$  is given by

$$P_w = \frac{\omega \rho g A^2}{4k} \left[ 1 + \frac{2kh}{\sinh 2kh} \right]. \quad (9.26)$$

By substituting Eq. (9.23) into Eq. (9.25), the resulting maximum  $CW$  is then expressed by

$$CW_{max} = \frac{|q^S|^2}{4P_w} \cdot \frac{1}{\Lambda_{opt} + \hat{\mathcal{B}}}. \quad (9.27)$$

Since Eq. (9.23) is in units of  $\text{Js}^{-1}$ , while the energy flux of the incident waves  $P_w$  is in units of  $\text{Js}^{-1}\text{m}^{-1}$ , hence, the  $CW_{max}$ , Eq. (9.27), has the dimensions of length (m).

The hydrodynamic efficiency, sometimes referred to as the relative capture width, is the normalised  $CW$  with the representative dimension of the device. For a land-fixed OWC system that is used as a terminator type WEC, this representative dimension is the width of the chamber ( $d$ ). An expression for the maximum hydrodynamic efficiency can now be obtained as

$$\eta_{max} = \frac{W_{opt}}{W_{max}} = \frac{2\hat{\mathcal{B}}}{\Lambda_{opt} + \hat{\mathcal{B}}}, \quad (9.28)$$

with  $\eta_{max}$  in the range 0 to 1. Then, after inserting the coefficients (9.24) into Eq. (9.28), the hydrodynamic efficiency  $\eta_{max}$  is

$$\eta_{max} = \frac{2}{\left[1 + \left(\frac{\mu}{\nu} + \frac{\rho g}{\omega b d} \frac{\Theta}{\nu}\right)^2\right]^{1/2} + 1}, \quad (9.29)$$

and when the effect of air compressibility is omitted, i.e.,  $\Theta = 0$ , the expression reported by [Evans and Porter \(1995\)](#) is recovered. In the following section, the solution procedure for the radiation and scattering problem are described.

## 9.4 Method of solution

### 9.4.1 Boundary Element Method

#### Boundary integral equation

The boundary integral representation of the Laplace equation (9.1) for a boundary point  $i$  is defined by

$$\alpha^i \phi^i + \int_{\Gamma} \phi \frac{\partial \psi}{\partial n} d\Gamma = \int_{\Gamma} \psi \frac{\partial \phi}{\partial n} d\Gamma, \quad (9.30)$$

where  $\phi$  and  $\partial\phi/\partial n$  are the unknown velocity potential and its normal derivative, respectively, on the boundary  $\Gamma$  of the domain  $\Omega$ , while  $\psi$  and  $\partial\psi/\partial n$  represent the fundamental solution of the Laplace equation and its normal derivative, respectively; and  $c$ , which is a free term, is a parameter that depends on the shape of the boundary ([Dominguez; 1993](#)).

The fundamental solution of the Laplace equation in 3D (9.1) is of the form

$$\psi = \frac{1}{4\pi r}, \quad (9.31)$$

and its normal derivative

$$\frac{\partial \psi}{\partial n} = -\frac{1}{4\pi r^2} \frac{\partial r}{\partial n}, \quad (9.32)$$

where  $r$  is the distance between the source and field points inside the domain. Equation (9.30) is the boundary integral equation to be solved numerically.



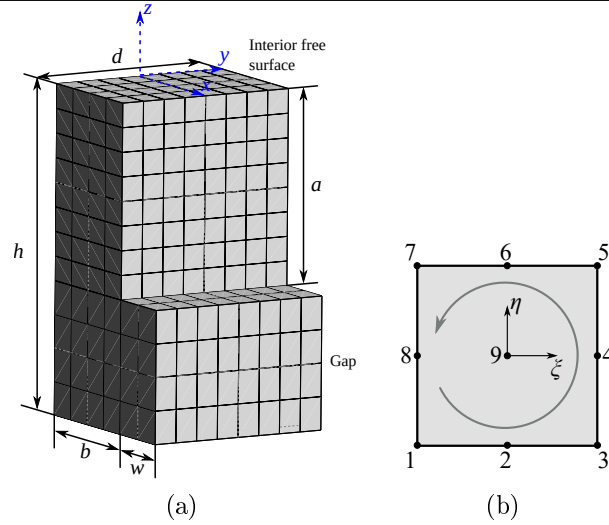


Figure 9.2: BVP discretization. (a) Discretization of Region 1 which is conformed by the OWC chamber and the gap below the front barrier. (b) Nine-noded quadrilateral element (nodes are ordered in the anticlockwise direction).

### Discretization

The boundary surfaces of the two regions are discretized into a series of elements over which the potential  $\phi$  and the flux  $\phi_n$  are written in terms of their values at a series of nodal points. In this work, quadrilateral type elements are chosen to discretize the domain, Fig. 9.2a. A second order discretization is employed with a nine-noded quadratic variation on each element, Fig. 9.2b. The variables  $\phi$  and  $\phi_n$  over each element  $j$  are defined in terms of their nine nodal values as

$$\phi(\xi, \eta) = [v_1(\xi, \eta), v_2(\xi, \eta) \dots v_9(\xi, \eta)] \cdot \begin{Bmatrix} \phi^1 \\ \phi^2 \\ \vdots \\ \phi^9 \end{Bmatrix}^j = \Upsilon \phi^j, \quad (9.33a)$$

$$\frac{\partial \phi(\xi, \eta)}{\partial n} = \Upsilon \frac{\partial \phi^j}{\partial n}, \quad (9.33b)$$

where  $\phi^j$  and  $\phi_n^j$  are vectors containing the nodal potentials and fluxes of the elements, and  $v_1, v_2, \dots, v_9$  are two dimensional polynomial interpolation functions (also called shape functions) such that  $v_k$ , for  $k = 1, 2, \dots, 9$ , has a unit value at node  $k$  and zero at all other nodes of the element. The element geometry can be defined from the position of the nodes, using the same type of interpolation function. Thus,  $x$ ,  $y$  and  $z$  coordinates can be expressed as

$$x(\xi, \eta) = \Upsilon x^j, \quad y(\xi, \eta) = \Upsilon y^j \quad \text{and} \quad z(\xi, \eta) = \Upsilon z^j, \quad (9.34)$$

with the interpolation functions given in terms of homogeneous coordinates  $\xi$  and  $\eta$  defined by

$$\begin{aligned} v_1 &= \frac{1}{4}\xi(\xi-1)\eta(\eta-1), & v_2 &= \frac{1}{2}(1-\xi^2)\eta(\eta-1), & v_3 &= \frac{1}{4}\xi(1+\xi)\eta(\eta-1), \\ v_4 &= \frac{1}{2}\xi(1+\xi)(1-\eta^2), & v_5 &= \frac{1}{4}\xi(1+\xi)\eta(1+\eta), & v_6 &= \frac{1}{2}(1-\xi^2)\eta(1+\eta), \\ v_7 &= \frac{1}{4}\xi(\xi-1)\eta(1+\eta), & v_8 &= \frac{1}{2}\xi(\xi-1)(1-\eta^2) & \text{and } v_9 &= (1-\xi^2)(1-\eta^2), \end{aligned} \quad (9.35)$$

where  $\xi$  and  $\eta$  vary from -1 to 1, and the superscript in Eqs. (9.33) and 9.34 indicates the number of the node on the corresponding element.

After discretizing the boundary  $\Gamma$  of the body  $\Omega$  into  $NE$  elements and on each element the boundary values are represented by Eq. (9.33), Eq. (9.30) can now be written for any nodal point  $i$  as

$$\alpha^i \phi^i + \sum_{j=1}^{NE} \left[ \int_{\Gamma_j} \frac{\partial \psi}{\partial n} \Upsilon d\Gamma \right] \phi^j = \sum_{j=1}^{NE} \left[ \int_{\Gamma_j} \psi \Upsilon d\Gamma \right] \frac{\partial \phi^j}{\partial n}. \quad (9.36)$$

The summation for  $j = 1$  to  $NE$  indicates summation in all  $NE$  elements on the surface and  $\Gamma_j$  is the surface of a  $j$  element. The variables  $\phi^j$  and  $\phi_n^j$  stand for the nodal potentials and fluxes on the element  $j$ . Equation (9.36) can then be written as

$$\alpha^i \phi^i + \sum_{m=1}^N H^{im} \phi^m = \sum_{j=1}^{NE} G^{ij} \frac{\partial \phi^j}{\partial n}, \quad (9.37)$$

where  $N$  is the total number of nodes and  $\phi^m$  is the potential at node  $m$ . In Eq. (9.37), the summation on the left-hand side extends over the nodes, since there is only one possible value of the velocity potential per node, while on the right-hand side the summation extends over the elements because when a node belongs to more than one element, it may have different values for the flux of the different elements. The influence coefficients  $H^{im}$  and  $G^{ij}$  are

$$H^{im} = \sum_l \int_{\Gamma_l} \frac{\partial \psi}{\partial n} v_k d\Gamma, \quad (9.38a)$$

$$G^{ij} = \int_{\Gamma_j} \psi v_k d\Gamma, \quad (9.38b)$$

where the summation over  $l$  extends to all the elements to which the node  $m$  belongs and  $k$  is the number of the node  $m$  within the element  $l$ .

For the evaluation of the integrals  $H^{im}$  and  $G^{ij}$ , when the collocation point  $i$  is not on the integration element  $j$ , these integrals are calculated using a standard Gaussian quadrature, where the numerical integration formulae are given in terms of the homogeneous coordinates  $\xi$  and  $\eta$ . Therefore, to transform the differential of surface in the cartesian system  $d\Gamma$  to the homogeneous coordinate system, a change of coordinates is required.

A differential of area is given by

$$d\Gamma = \left| \frac{\partial r}{\partial \xi} \times \frac{\partial r}{\partial \eta} \right| d\xi d\eta = |J| d\xi d\eta \quad (9.39)$$

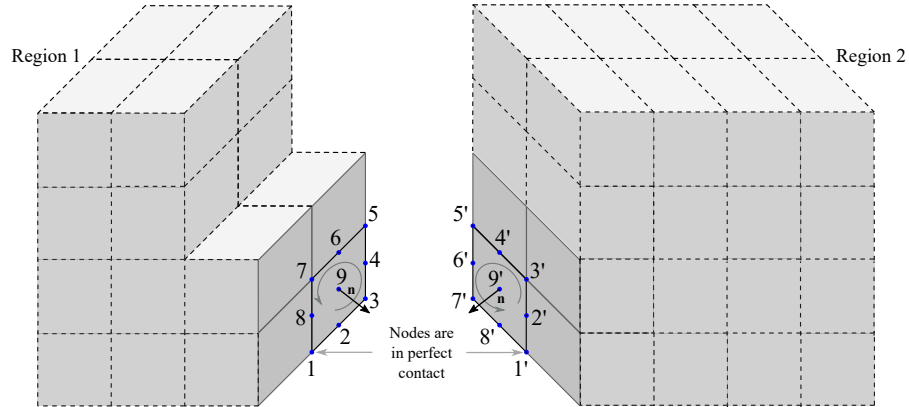


Figure 9.3: Matching of the regions on the gap at  $x = L$ .

with

$$\frac{\partial r}{\partial \xi} = \begin{Bmatrix} \frac{\partial x}{\partial \xi} \\ \frac{\partial y}{\partial \xi} \\ \frac{\partial z}{\partial \xi} \end{Bmatrix} \quad \text{and} \quad \frac{\partial r}{\partial \eta} = \begin{Bmatrix} \frac{\partial x}{\partial \eta} \\ \frac{\partial y}{\partial \eta} \\ \frac{\partial z}{\partial \eta} \end{Bmatrix} \quad (9.40)$$

where  $J$  is a reduced Jacobian, and its magnitude  $|J|$  is simply that of the normal vector at the point. Thus, the integrals over the boundary elements can be written as

$$G^{ij} = \int_{\xi} \int_{\eta} \psi v_k |J| d\xi d\eta, \quad (9.41a)$$

$$H^{im} = \int_{\xi} \int_{\eta} \frac{\partial \psi}{\partial n} v_k |J| d\xi d\eta, d\Gamma, \quad (9.41b)$$

which can be computed using the numerical integration formula. The lower and upper limits of these integrals are, respectively, -1 and 1.

On the other hand, when the collocation point belongs to the integration element, the required integrals over the boundary elements need some transformation before a numerical formula is applied. In order to solve the integrals, the boundary elements are subdivided into triangular regions with a corner point at the collocation node. For instance, in the case of a rectangular element with a collocation point at a mid-size node, the element is subdivided and a new system of coordinates is defined in such a way that the Jacobian becomes zero at the collocation point. Thus, the transformed domain in the new system of coordinates is a square. Then, in order to compute the integrals by using a standard Gaussian quadrature, the square domain in the new system is transformed into a square with a length of the sides equal to 2 by changing again the coordinates. More details regarding the above procedure can be found in [Dominguez \(1993\)](#).

### Matching of subdomains

Figure 9.3 shows the two-region, 3D domain with a common interface on the gap  $B_g$ , below the front barrier at  $x = L$ . Numerical instabilities may occur when a thin front wall OWC system is considered, and can be avoided by using the method of subdomains. For the matching of the regions, the continuity conditions of velocity potential and flux at the common interface are employed, and the nodes at this interface are assumed to be in perfect contact, Fig. 9.3 (Katsikadelis; 2002; Becker; 1992). These velocity potential and flux continuity conditions are of the form

$$\Phi_{B_g}^1 = \Phi_{B_g}^2, \quad (9.42a)$$

$$\frac{\partial \Phi_{\mathbf{n}}^1}{\partial x_{B_g}} = -\frac{\partial \Phi_{\mathbf{n}}^2}{\partial x_{B_g}}, \quad (9.42b)$$

respectively, where  $\Phi$  and  $\Phi_{\mathbf{n}}$  indicate the vectors containing the velocity potential and flux values, respectively.

As mentioned earlier, the fluxes and potentials have a nine-noded variation, where fluxes will have a unique nodal value on each element so the possibility of having different values between adjacent elements is considered. Meanwhile, velocity potentials will always hold a unique value in the connection between adjoining elements (Dominguez; 1993). Thus, fluxes are arranged in a  $9 \times NE$  array, and velocity potentials in an  $N$  array. Once the boundary conditions for the radiation and scattering problems are applied and inserted into Eq. (9.37), the known variables are moved to the right-hand side, and the unknowns to the left-hand side. Then, the following matrix is obtained

$$[A] \{X\} = \{B\}, \quad (9.43)$$

and the system can be solved to obtain the unknown boundary values. In Eq. (9.43),  $[A]$  is a square matrix of dimensions  $N \times N$ ; the vector  $\{X\}$  with dimensions  $N \times 1$  contains the unknown values of the velocity potential or fluxes on the boundaries and the common interface; and  $\{B\}$  is a known vector of dimension  $N \times 1$ .

## 9.5 Truncation and convergence analyses

Truncation and convergence analyses were performed before carrying out the numerical calculations. A water depth of 7.90 m and a wave period  $T$ , bounded by  $2.50 \leq T \leq 30$  s, were considered in all the calculations. It is worth noting that the calculated performance is not dependent on the wave amplitude in the numerical approach, as the linear wave theory was implemented in formulating the problem. To generate the mesh, the 3D finite element mesh generator GMSH (Geuzaine and Remacle.; 2009) was employed.

Figures 9.4a–d show the variation of the hydrodynamic efficiency with respect to the distance at which the radiation boundary is truncated for four different non-dimensional frequencies  $Kh (= 0.5, 1.5, 2.5$  and  $3.5)$ . For these cases, it can be seen that the results converge at a distance of 3 to 5 times the water depth between the right face of the front wall and the far-field

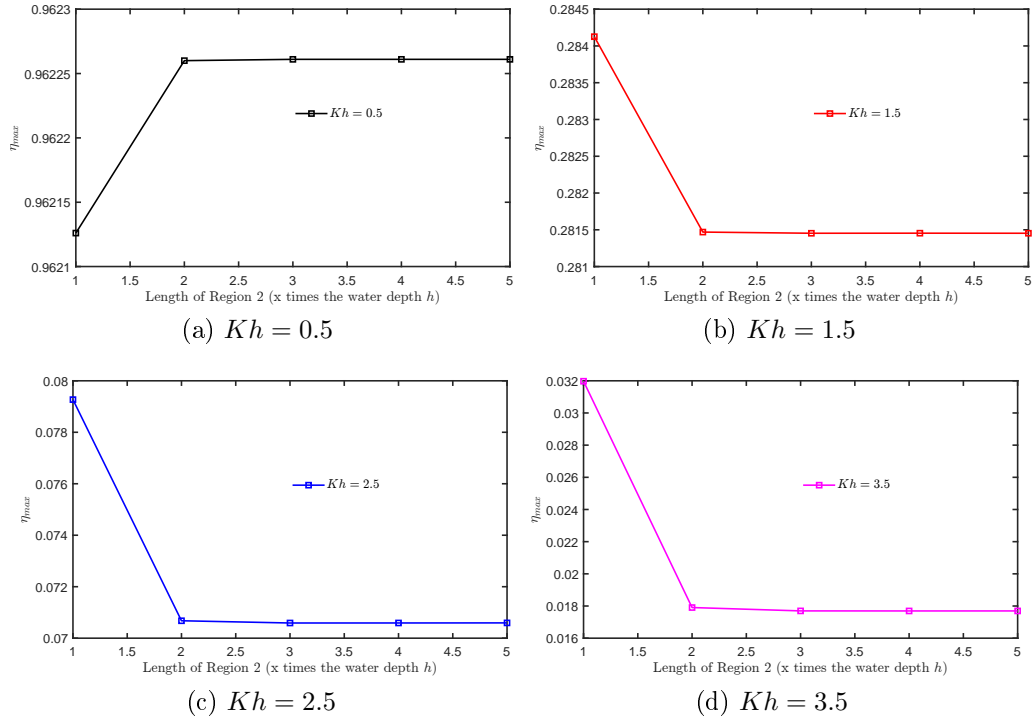


Figure 9.4: Hydrodynamic efficiency against the length of Region 2 with  $a/h = 1/2$ ,  $b/h = 1$ ,  $w/h = 1/2$  and  $d/h = 1/2$ .

boundary. Therefore, a distance of 4 times the water depth  $h$  is considered in the calculations, to minimize the effect of local disturbances.

Then, Tables 9.1 and 9.2 show the results obtained for the maximum hydrodynamic efficiency  $\eta_{max}$ , the radiation susceptance  $\mu$  and radiation conductance  $\nu$  with  $\Theta = 0$  for different values of the non-dimensional frequency  $Kh (= 0.5, 1.5$  and  $2.5)$ . The meshes for the convergence analysis were carefully selected to have similar spacing ( $ds$ ) between neighbouring nodes in the  $x$ ,  $y$  and  $z$  directions. The number of nodes  $N$  must be chosen carefully, as small values for  $N$  lead to truncation errors, especially when a low number of elements are modelled in the OWC chamber and the gap below the front wall. In Table 9.1 it is observed that around 10000 nodes, with an average spacing  $\overline{ds} \approx 0.31$  m, are enough to ensure convergence of the numerical results to an accuracy of three decimal places, when the chamber width to water depth ratio  $d/h$  is equal to  $1/2$ . On the other hand, in Table 9.2, for  $d/h = 2$ , it can be seen that approximately 14500 nodes,  $\overline{ds} \approx 0.40$  m, are needed to ensure convergence for the same number of decimal places. Thus, in the present calculations, depending on the structural configuration

CHAPTER 9. A THREE-DIMENSIONAL ANALYSIS OF THE HYDRODYNAMIC PERFORMANCE OF A LAND-FIXED OWC DEVICE

Table 9.1: Maximum hydrodynamic efficiency  $\eta_{max}$ , radiation susceptance  $\mu$  and radiation conductance  $\nu$  computed for different number of nodes  $N$  and average distance between two neighbouring nodes  $\overline{ds}$  with  $a/h = 1/2$ ,  $b/h = 1$ ,  $w/h = 1/2$  and  $d/h = 1/2$ .

$N$	$\overline{ds}$ (m)	$Kh=0.5$			$Kh=1.5$			$Kh=2.5$		
		$\eta_{max}$	$\mu$	$\nu$	$\eta_{max}$	$\mu$	$\nu$	$\eta_{max}$	$\mu$	$\nu$
<b>8836</b>	0.34053	0.96244	-0.61633	1.53027	0.28159	-0.33080	0.05495	0.07062	-0.16313	0.00598
<b>9124</b>	0.32831	0.96235	-0.61690	1.52972	0.28152	-0.33071	0.05492	0.07061	-0.16309	0.00597
<b>9412</b>	0.31891	0.96226	-0.61745	1.52921	0.28145	-0.33062	0.05489	0.07059	-0.16306	0.00597
<b>9916</b>	0.31036	0.96226	-0.61744	1.52920	0.28146	-0.33062	0.05489	0.07059	-0.16305	0.00597
<b>10676</b>	0.30722	0.96226	-0.61743	1.52921	0.28146	-0.33062	0.05489	0.07059	-0.16306	0.00597
<b>11052</b>	0.29860	0.96226	-0.61750	1.52931	0.28144	-0.33062	0.05489	0.07059	-0.16306	0.00597

Table 9.2: Maximum hydrodynamic efficiency  $\eta_{max}$ , radiation susceptance  $\mu$  and radiation conductance  $\nu$  computed for different number of nodes  $N$  and average distance between two neighbouring nodes  $\overline{ds}$  with  $a/h = 1/2$ ,  $b/h = 1$ ,  $w/h = 1/2$  and  $d/h = 2$ .

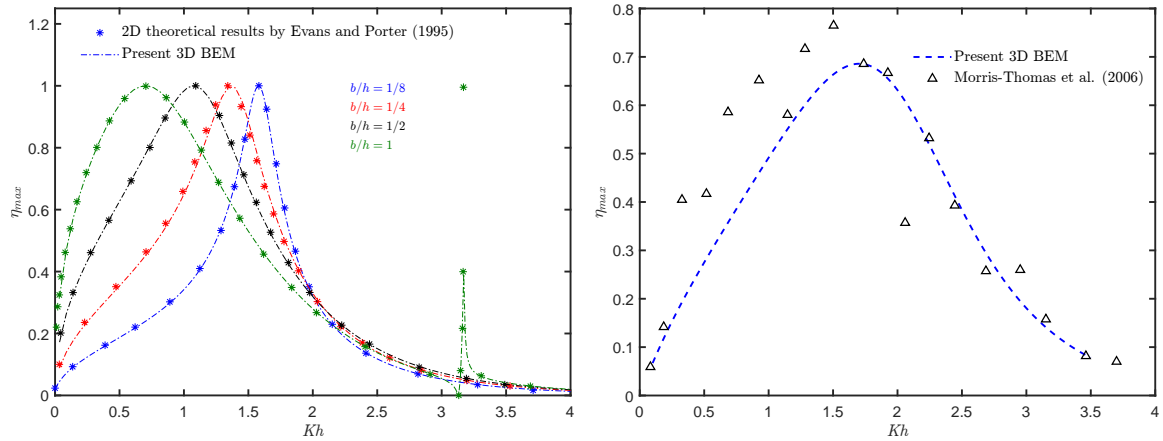
$N$	$\overline{ds}$ (m)	$Kh=0.5$			$Kh=1.5$			$Kh=2.5$		
		$\eta_{max}$	$\mu$	$\nu$	$\eta_{max}$	$\mu$	$\nu$	$\eta_{max}$	$\mu$	$\nu$
<b>12844</b>	0.43419	0.96178	-0.62127	1.52825	0.28023	-0.33027	0.05455	0.07001	-0.16285	0.00591
<b>13492</b>	0.43020	0.96178	-0.62126	1.52826	0.28023	-0.33027	0.05455	0.07001	-0.16285	0.00591
<b>13924</b>	0.41956	0.96178	-0.62127	1.52830	0.28023	-0.33028	0.05455	0.07001	-0.16285	0.00591
<b>14508</b>	0.40440	0.96228	-0.61754	1.52985	0.28131	-0.33066	0.05486	0.07052	-0.16307	0.00596
<b>14932</b>	0.39328	0.96226	-0.61771	1.52987	0.28126	-0.33065	0.05485	0.07049	-0.16306	0.00596
<b>15164</b>	0.39187	0.96226	-0.61769	1.52985	0.28126	-0.33064	0.05485	0.07049	-0.16306	0.00596

of the OWC device, different numbers of nodes are selected to discretize the corresponding BVP.

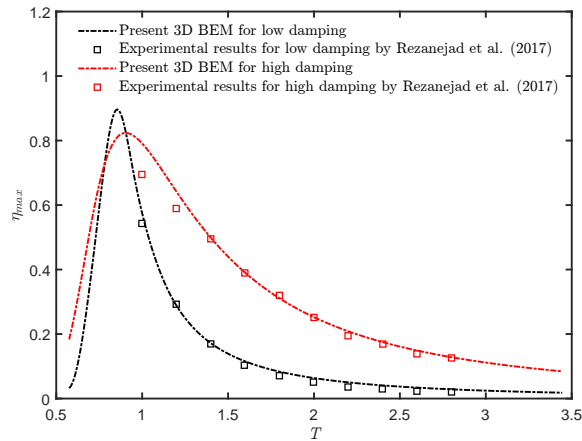
## 9.6 Comparison with previous results

Figures 9.5a–c show a comparison of the present methodology with the 2D analytical results of [Evans and Porter \(1995\)](#), and experimental data from [Morris-Thomas et al. \(2006\)](#) and [Rezanejad et al. \(2017\)](#). From these figures, it can be seen that the present results agree very well with the 2D analytical results, while the agreement with the experimental results is satisfactory.

It should be noted that the present numerical results are based on the assumption of an ideal fluid, so viscous effects and flow separation due to the front wall may contribute to the discrepancy between the results and lead to an overestimation on the hydrodynamic performance. Furthermore, the rate of energy extraction modelled by the PTO system, as well as the energy loss through it by viscous dissipation during the tests, might also influence the results.



(a) For  $a/h = 1/2$ ,  $d/h = 1/4$ ,  $w/h = 0.105$  and (b) For  $a/h = 0.16$ ,  $b/h = 0.7$ ,  $c/h = 0.48$ ,  $d/h = 1.49$  and  $w/h = 0.09$ ,  $\Theta = 0$ .



(c) For  $a/h = 0.19$ ,  $b/h = 0.30$ ,  $c/h = 0.70$ ,  $d/h = 1.54$  and  $w/h = 0.05$ .

Figure 9.5: Hydrodynamic efficiency against the non-dimensional frequency  $Kh$  and wave period  $T$ .

## 9.7 Results and Discussion

In this section, the influence of the chamber configuration and the linearized air compressibility on the  $CW_{max}$ , hydrodynamical coefficients and free surface elevation is analysed.

Figures 9.6a and 9.6b show the numerical results for the  $CW_{max}$  against the non-dimensional frequency  $Kh$  for various ratios of chamber width to water depth  $d/h$  ( $= 1/4, 1/2, 1$  and  $2$ ). It can be seen that the effective area of the  $CW_{max}$  under the curves increases when the chamber width ratio  $d/h$  increases. This is because the capture width indicates that the device is expected to extract the power from a width of incident wave equal to the representative dimension of the OWC device ( $d = 1.975, 3.95, 7.90$  and  $15.8$  m). Furthermore, it is shown that the curves of the maximum capture width increase to a maximum and then decrease. This peak is due to large water motions inside the chamber that occur when the internal water column is excited by the incident wave into a resonant piston-type motion. The OWC device is highly dependent on wave frequency and performs well when interacting with waves that are closer to the natural resonance frequency of the structure. Therefore, a clear understanding is required of the wave frequency band available at a given potential site for an OWC plant. If the OWC performance bandwidth is broad it implies the device will be efficient over a wider range of frequencies.

Fig. 9.6b shows the effect of the air compressibility when the height of the trapped air column is equal to the water depth. Comparing Figs. 9.6a and b it is seen that the capture width bandwidth is broadened, while the value of the resonant peak frequency is slightly increased. Thus, for the air chamber volume taken into account in this case, more energy from the waves is absorbed for  $Kh$  values greater than the resonance frequency. In Fig 9.6a, this resonance occurs at  $Kh = 0.4396$ , while in Fig 9.6b it occurs at  $Kh = 0.5205$ .

The three dimensional surface plots of the free surface elevation for  $a/h = 1/2, b/h = 1, w/h = 1/2$  and  $d/h = 1/2$  are shown in Figs. 9.7a and 9.7b. It can be seen that at the resonance peak frequency, the free surface elevations inside the chamber are similar, while at  $\Theta \neq 0$ , resonance takes place when shorter wavelengths interact with the OWC structure.

Figures 9.8a and b show the numerical results of the capture width  $CW_{max}$  against the non-dimensional frequency  $Kh$  for various ratios of chamber length to water depth  $b/h$  ( $= 1/4, 1/2, 3/4$  and  $1$ ). It can be seen that the frequency at which resonance occurs decreases as chamber length increases compared to water depth. Physically, this is due to the fact that by increasing the length of the device, the horizontal distance that a typical fluid particle must travel during a period of motion increases. As a consequence, the value of  $Kh$  at which resonance occurs is reduced, and since an increase in  $b/h$  allows more local fluid motion within the chamber, this leads to a breakdown in the solid-body model of resonance, and the amplitude of oscillation decreases. On the other hand, Fig. 9.8b shows that when the linearized air compressibility is considered, the  $CW_{max}$  is increased for medium frequency values and a trough in the  $CW_{max}$  curves appears, which becomes more pronounced as the ratio  $b/h$  decreases.

The numerical results for the coefficients of radiation conductance and radiation susceptance against  $Kh$  for  $a/h = 1/2$  and  $w/h = 1/2$  for different values of  $b/h$  ( $= 1/4, 1/2, 3/4$  and  $1$ ) are shown in Figures 9.8c and 9.8d, respectively. Figure 9.8c shows that when the length of the chamber,  $b$ , increases with respect to the depth,  $h$ , the maximum radiation conductance coefficients last for longer. As a result, since  $\nu$  is a measure of the transfer of energy into the



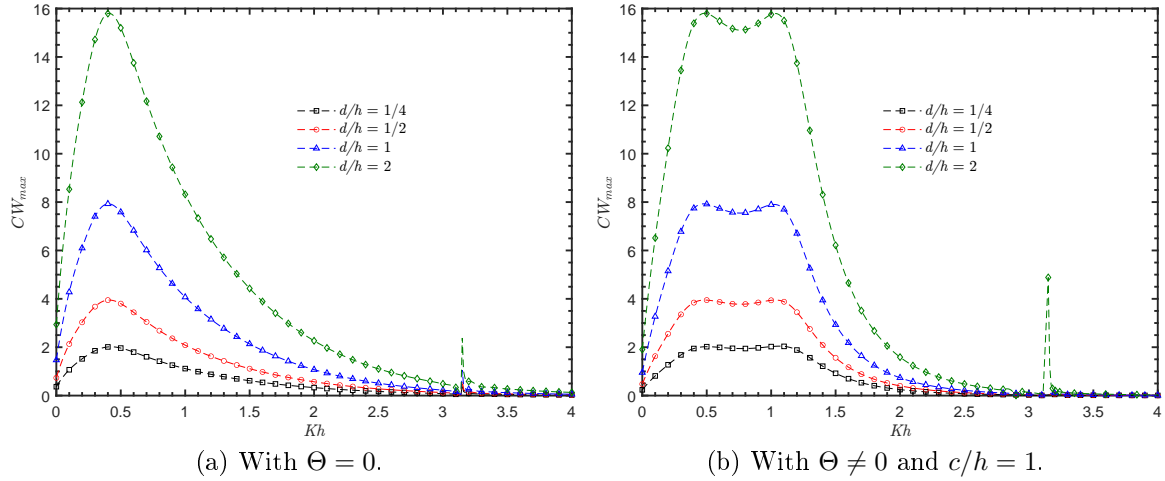


Figure 9.6: Capture width with  $a/h = 1/2$ ,  $b/h = 1$  and  $w/h = 1/2$  versus  $Kh$  for different chamber width to water depth ratios  $d/h (= 1/4, 1/2, 1$  and  $2)$ .

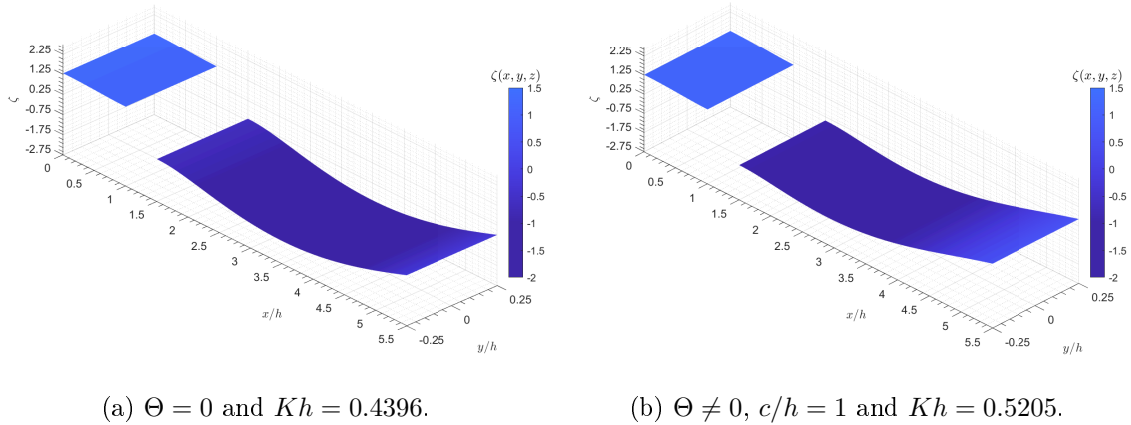


Figure 9.7: Free surface elevation with  $a/h = 1/2$ ,  $b/h = 1$ ,  $w/h = 1/2$  and  $d/h = 1/2$  at the resonant peak frequency.

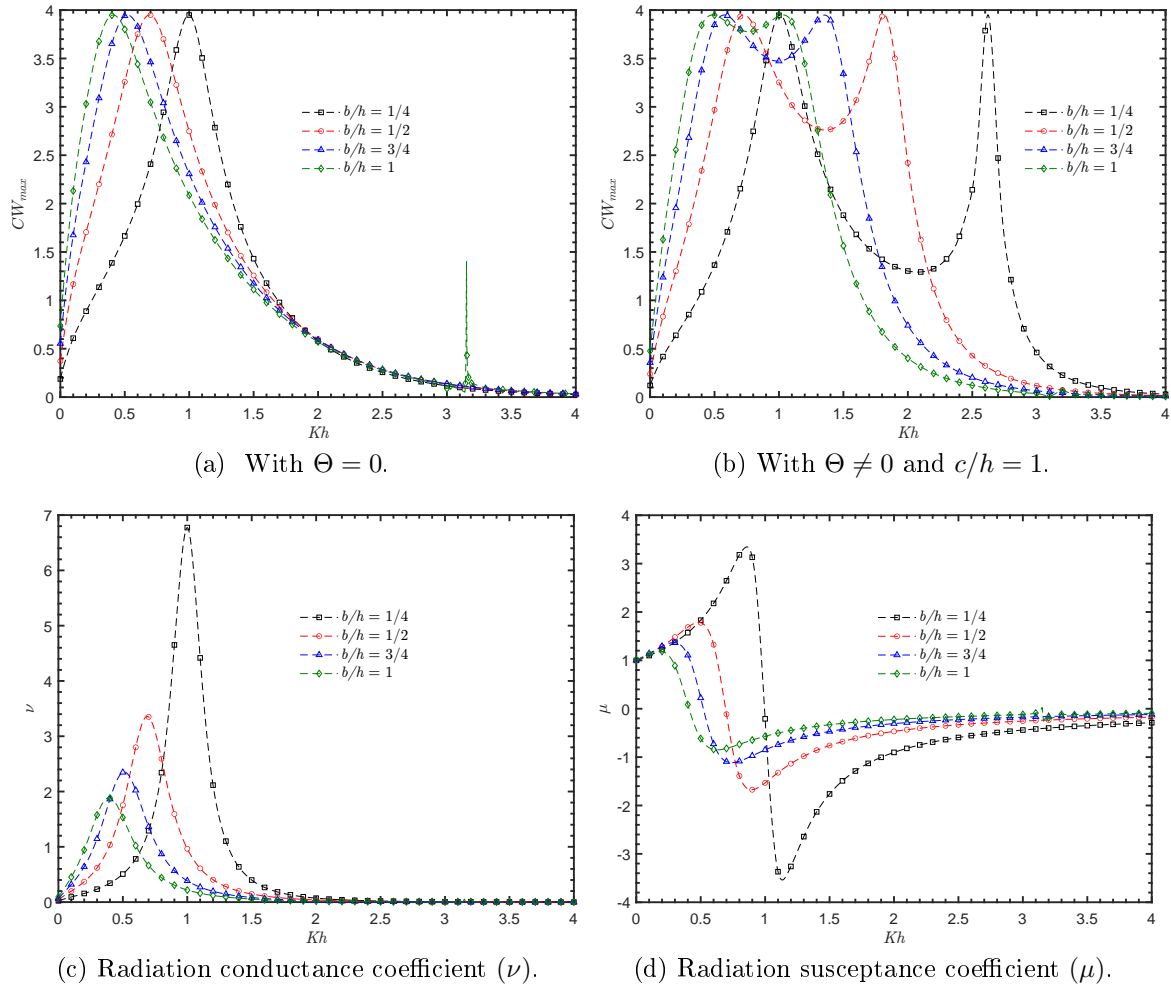


Figure 9.8: Capture width and radiation conductance and susceptance coefficients with  $a/h = 1/2$ ,  $w/h = 1/2$  and  $d/h = 1/2$  versus  $Kh$  for different chamber length to water depth ratios  $b/h$  ( $= 1/4, 1/2, 3/4$  and  $1$ ).

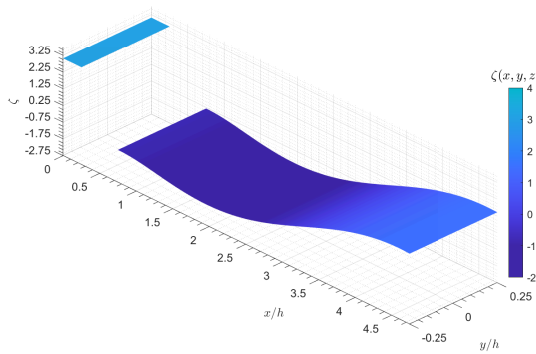
system, it may be advantageous to design the chamber length of the OWC device so that the range of frequency bandwidth in the radiation conductance corresponds with the most common wave frequency of a given site, thereby maximizing the exploitation of the available wave energy. On the other hand, Fig. 9.8d shows that when the chamber length is small, compared to the water depth, the range of the non-dimensional frequency  $Kh$  for which the radiation susceptance is negative decreases. In this sense, negative values in  $\mu$ , which is related to the added mass, are may be due to the effects of the internal free surface which is enclosed by the back and the thick front walls. Negative added mass values are a common phenomena in the theory of floating and submerged moving bodies, as when one or more components of a structure enclose a portion of the free surface or 2D cylinders are close to the free surface (McIver and Evans; 1984; McIver and McIver; 2016).

Figures 9.9a–f show the three dimensional surface plots of the free surface elevation for  $a/h = 1/2$ ,  $w/h = 1/2$  and  $d/h = 1/2$  for different values of  $b/h (= 1/4, 1/2$  and  $3/4)$ . First, it can be observed that the free surface elevations inside the chamber are higher when the chamber length to water depth ratios  $b/h$  are small. As mentioned earlier, by increasing the ratio  $b/h$ , a larger local fluid motion inside the chamber is allowed, thus leading to a breakdown in the solid-body model of resonance, and decreasing oscillation amplitude. Second, these figures show that the longer the OWC chamber, the longer the wavelength must be for the OWC device to achieve resonance.

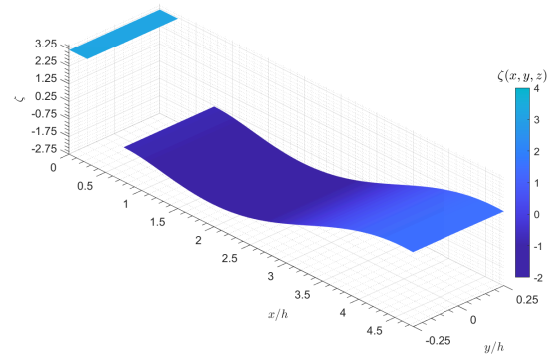
Figs. 9.10a and 9.10b show the effect on the  $CW_{max}$  due to different ratios of front wall submergence to water depth  $a/h = (1/8, 1/4, 1/2$  and  $3/4)$ . In these figures, it can be seen that the effective area of  $CW_{max}$ , under the curve, and the magnitude of the first natural frequency, both increase when the front wall submergence ratio  $a/h$  decreases. However, for a relatively small  $a/h$ , and taking into account that changes in water level due to tidal fluctuations and extreme waves can occur, a small draft can suggest that the trough of a wave propagates below the front wall. This should be considered during the design process since, in this case, the pressure inside the chamber would be equal to ambient pressure, implying that the power available within the OWC system would be zero, resulting in decreased efficiency. Regarding the effect of the air compressibility, by comparing these figures it is observed that the  $CW_{max}$  bandwidth is increased when  $\Theta$  is considered.

The numerical results for the radiation conductance and radiation susceptance coefficients against  $Kh$  for  $b/h = 1$  and  $w/h = 1/2$  for different submergence ratios  $a/h = (1/8, 1/4, 1/2$  and  $3/4)$  are shown in Figures 9.10c and 9.10d, respectively. Fig. 9.10c shows that a larger draft decreases the frequency at which resonance occurs while the band is reduced. It can also be observed that the peak resonance is more prominent as the barrier is more submerged. With large submergence of the front wall, conditions are similar to those in a closed tank of parallel sides, where a second resonance mechanism occurs when the incident wave frequency is such that the fluid inside the chamber is excited into an antisymmetric sloshing mode (Evans and Porter; 1995). The sloshing frequencies, in this case, occur at values of the dimensionless wavenumber  $kb = n\pi$ , with  $n$  being the sloshing mode. In Fig. 9.10c, it can be seen that the second peaks in  $\nu$  due to the first sloshing frequency take place close to  $Kh = \pi$ . On the other hand, in Fig. 9.10d it can be seen that by increasing the front wall draft  $a$  with respect to  $h$ , the value of  $Kh$  for which  $\mu$  first becomes zero decreases, while the range

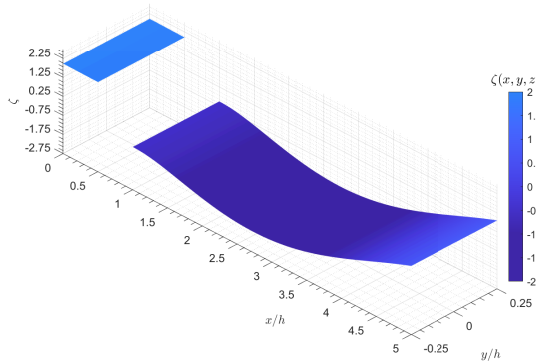
CHAPTER 9. A THREE-DIMENSIONAL ANALYSIS OF THE HYDRODYNAMIC PERFORMANCE OF A LAND-FIXED OWC DEVICE



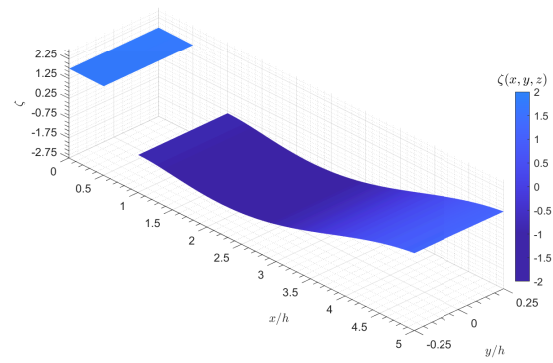
(a)  $b/h = 1/4$ ,  $Kh = 1.0060$  and  $\Theta = 0$ .



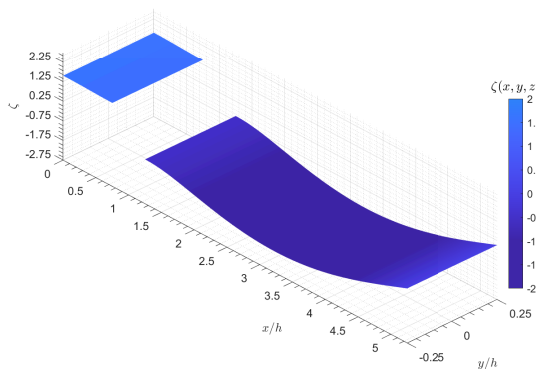
(b)  $b/h = 1/4$ ,  $Kh = 1.0060$  and  $c/h = 1$ .



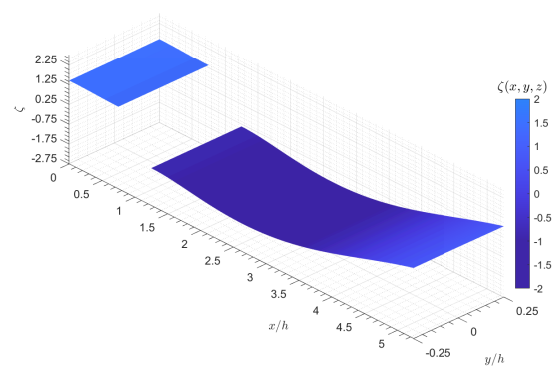
(c)  $b/h = 1/2$ ,  $Kh = 0.6823$  and  $\Theta = 0$ .



(d)  $b/h = 1/2$ ,  $Kh = 0.7633$  and  $c/h = 1$ .



(e)  $b/h = 3/4$ ,  $Kh = 0.5205$  and  $\Theta = 0$ .



(f)  $b/h = 3/4$ ,  $Kh = 0.6014$  and  $c/h = 1$ .

Figure 9.9: Free surface elevation with  $a/h = 1/2$ ,  $w/h = 1/2$  and  $d/h = 1/2$ .

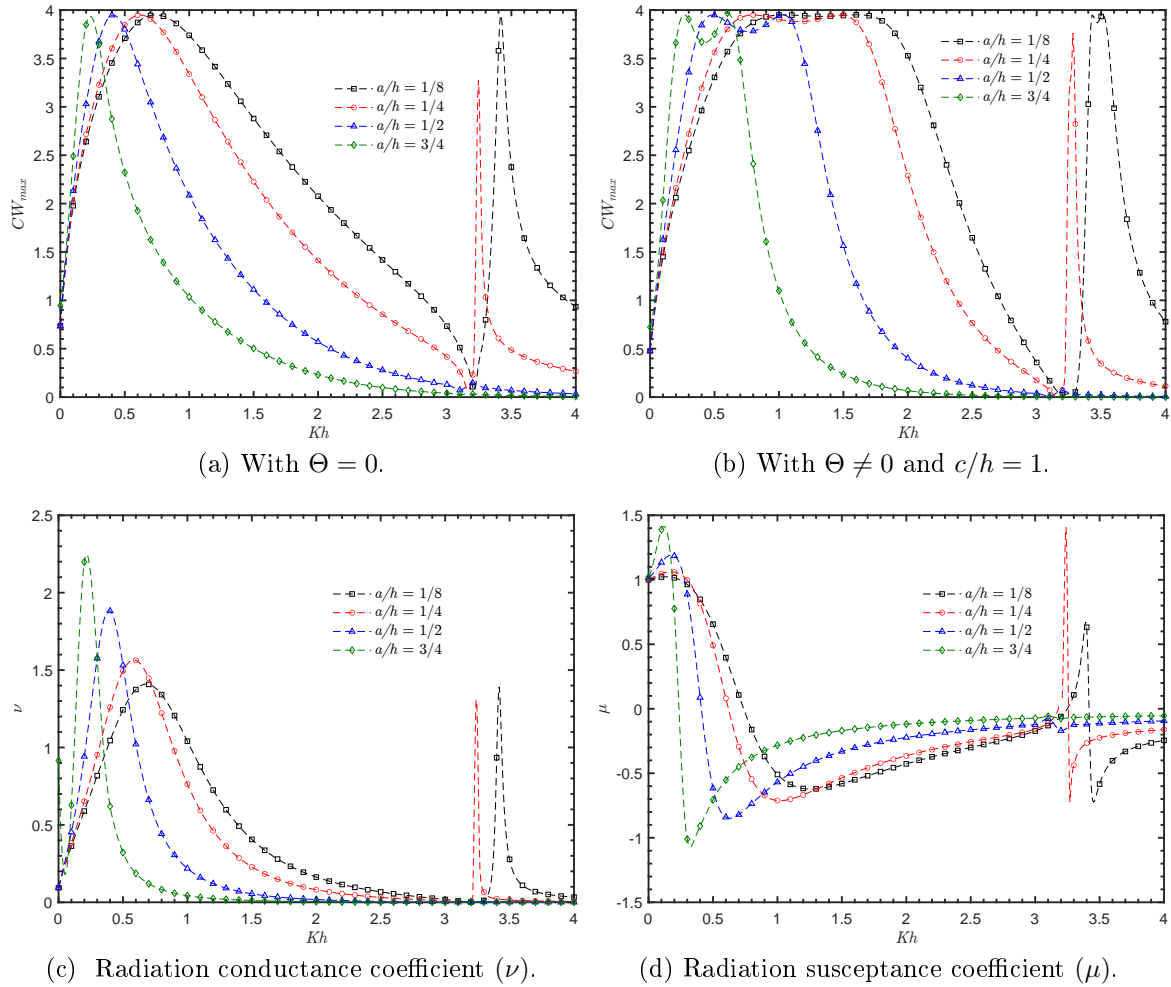


Figure 9.10: Capture width and radiation conductance and susceptance coefficients with  $b/h = 1$ ,  $w/h = 1/2$  and  $d/h = 1/2$  versus  $Kh$  for different front barrier draft to water depth ratios  $a/h (= 1/8, 1/4, 1/2$  and  $3/4)$ .

of  $Kh$  for negative values of  $\mu$  increases. These zero values in the radiation susceptance  $\mu$  are associated with the peak values in the maximum capture width, Fig. 9.10a.

The three dimensional plots of the free surface elevation  $\zeta$  with  $b/h = 1$ ,  $w/h = 1/2$  and  $d/h = 1/2$  for different values of front wall submergence ratio  $a/h (= 1/8, 1/4 \text{ and } 3/4)$  are shown in Figs. 9.11a–f. First, it can be seen that the free surface elevations inside the OWC chamber are small when the front wall submergence to water depth ratios  $a/h$  are also small. Then, the smaller the front wall submergence is, with respect to the water depth, the shorter must be the wavelength for resonance to occur in the OWC chamber. It is shown that, in each case, when the air compressibility is taken into account, the resonance frequency is higher compared to the case when  $\Theta = 0$ .

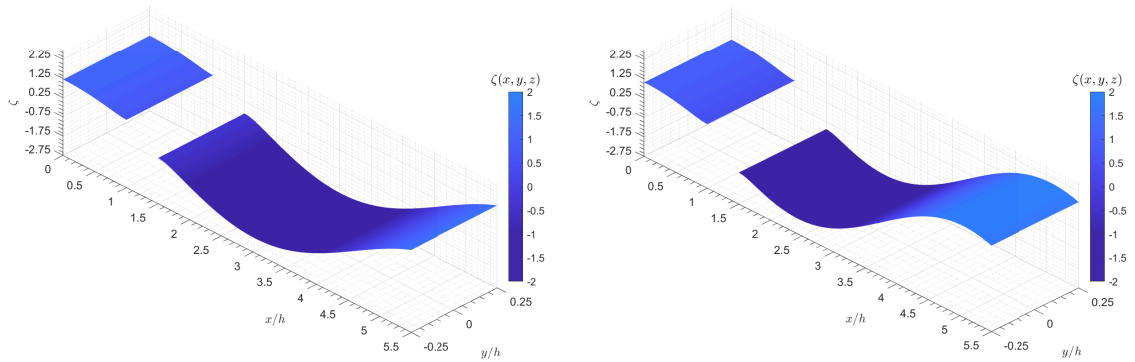
The numerical results of the maximum capture width  $CW_{max}$  against  $Kh$  for different front wall thickness to water depth ratios  $w/h (= 1/8, 1/4, 1/2 \text{ and } 1)$  are shown in Figs. 9.12a and 9.12b. In these figures, it can be seen that by increasing the thickness of the front wall, the bandwidth of the capture width curves is reduced, while the peak frequency value is shifted to lower values of the non-dimensional frequency  $Kh$ . This reduction in the maximum capture width is explained by the fact that the energy transfer due to the wave motion for shorter wavelengths is reduced when the front wall is thicker. On the other hand, comparing both figures, it is seen that the volume of the air chamber considered broadens the capture width bandwidth and slightly increases the magnitude of the peak frequency value.

Figures 9.12c and 9.12d show the radiation conductance and radiation susceptance coefficients, respectively, against  $Kh$  for  $b/h = 1$  and  $a/h = 1/2$  for various ratios of front wall thickness to water depth  $w/h (= 1/8, 1/4, 1/2 \text{ and } 1)$ . Figure 9.12c shows that the peaks in radiation conductance are associated with those observed in Fig. 9.12a. In this sense, the radiation conductance coefficient represents the extent to which the device absorbs energy at various frequencies. Together with Fig. 9.12d, this shows that by increasing the radiation conductance coefficient  $\nu$ , with respect to the radiation susceptance coefficient  $\mu$ , the power extraction capacity can be increased. Furthermore, Figs. 9.12c and 9.12d show that when the ratio  $w/h$  increases, the peak values in  $\nu$  also increase; however, the range of the non-dimensional frequency  $Kh$  for which  $\mu$  is negative also increases.

Figures 9.13a–f show the three dimensional plots of the free surface elevation for  $b/h = 1$ ,  $a/h = 1/2$  and  $d/h = 1/2$  for different values of  $w/h (= 1/8, 1/4 \text{ and } 1)$ . It can be seen that the thicker the front wall, the longer the wavelength must be, for the OWC device to reach resonance. In addition, the greater the  $w/h$  ratio, the higher the free surface elevation at the resonance frequency. Similar to the previous free water surface plots, it is observed that a shorter wavelength is needed for the OWC device to reach the state of resonance when the air compressibility is considered.

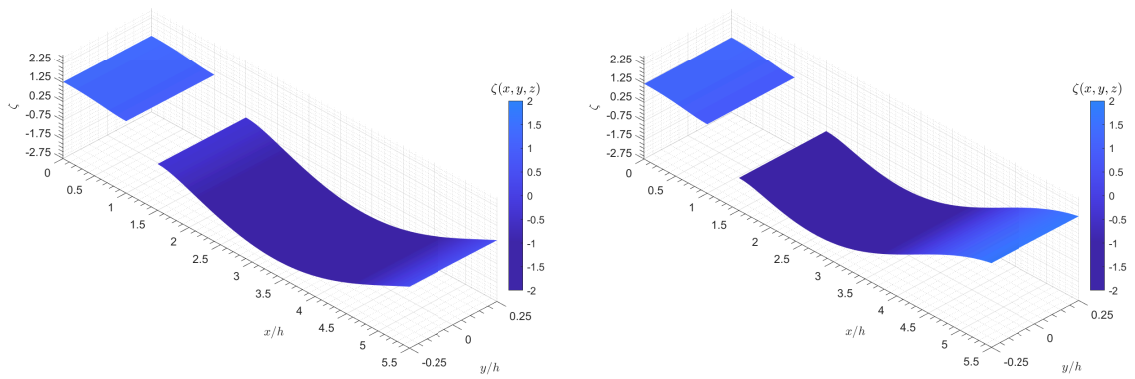
Figure 9.14 illustrates the effect of air compressibility on the OWC performance for different ratios of air column height to water depth  $c/h (= 1/2, 3/4, 1 \text{ and } 3/2)$ . Compared to the case when the air compressibility is neglected, i. e.,  $\Theta = 0$ , it is found that air compressibility helps optimize the power absorption and significantly influences the capture width bandwidth. This is a significant aspect since it might be possible to increase the OWC performance for a wider range of wave frequencies by designing the pneumatic chamber appropriately. When the height trapped air is greater than the water depth, it is seen that the effective area under the capture

CHAPTER 9. A THREE-DIMENSIONAL ANALYSIS OF THE HYDRODYNAMIC PERFORMANCE OF A LAND-FIXED OWC DEVICE



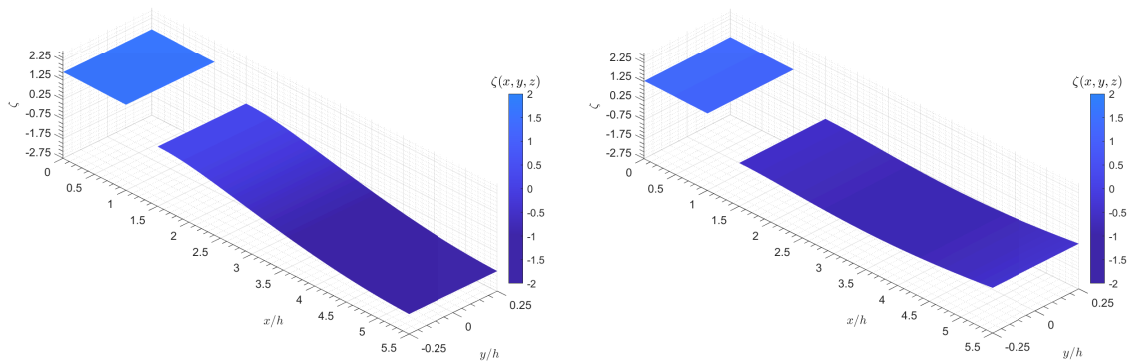
(a)  $a/h = 1/8$ ,  $Kh = 0.7632$  and  $\Theta = 0$ .

(b)  $a/h = 1/8$ ,  $Kh = 1.0060$  and  $c/h = 1$ .



(c)  $a/h = 1/4$ ,  $Kh = 0.6014$  and  $\Theta = 0$ .

(d)  $a/h = 1/4$ ,  $Kh = 0.7633$  and  $c/h = 1$ .



(e)  $a/h = 3/4$ ,  $Kh = 0.1968$  and  $\Theta = 0$ .

(f)  $a/h = 3/4$ ,  $Kh = 0.2778$  and  $c/h = 1$ .

Figure 9.11: Free surface elevation with  $b/h = 1$ ,  $w/h = 1/2$  and  $d/h = 1/2$ .

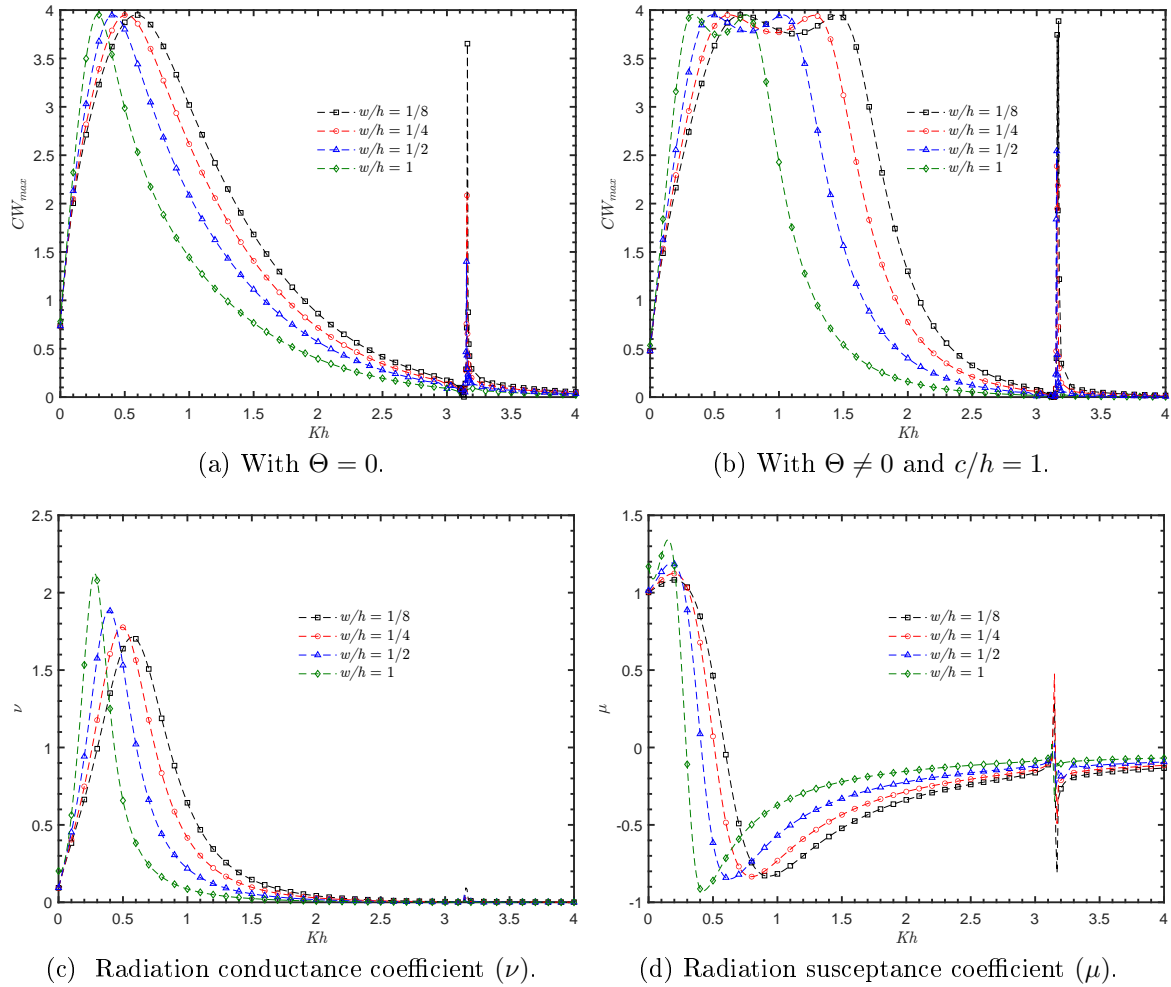
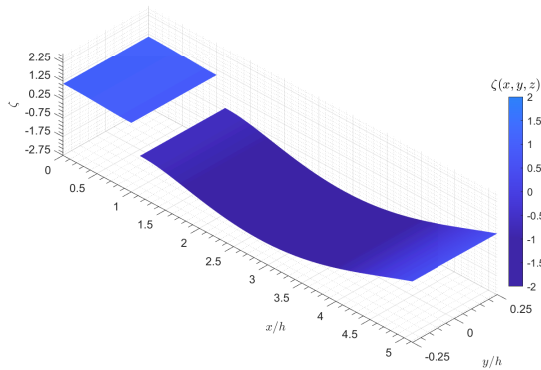


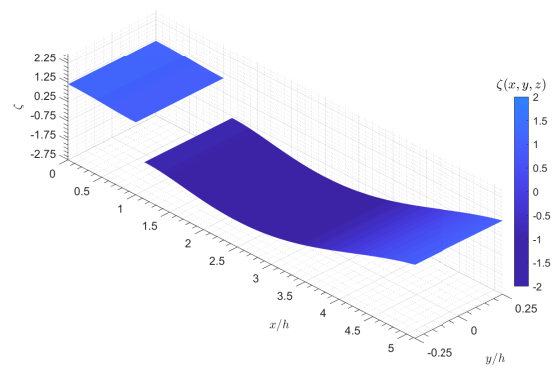
Figure 9.12: Capture width and radiation conductance and susceptance coefficients with  $b/h = 1$ ,  $a/h = 1/2$  and  $d/h = 1/2$  versus  $Kh$  for different front wall thickness to water depth ratios  $w/h (= 1/8, 1/4, 1/2$  and  $1)$ .



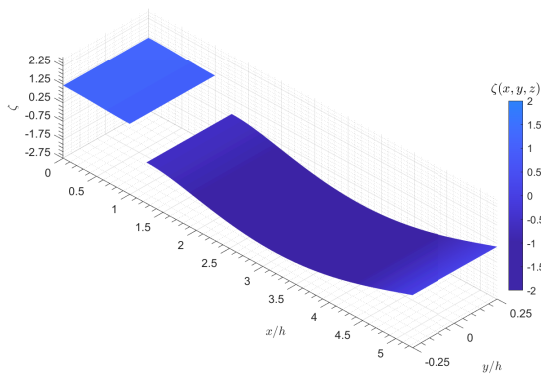
CHAPTER 9. A THREE-DIMENSIONAL ANALYSIS OF THE HYDRODYNAMIC PERFORMANCE OF A LAND-FIXED OWC DEVICE



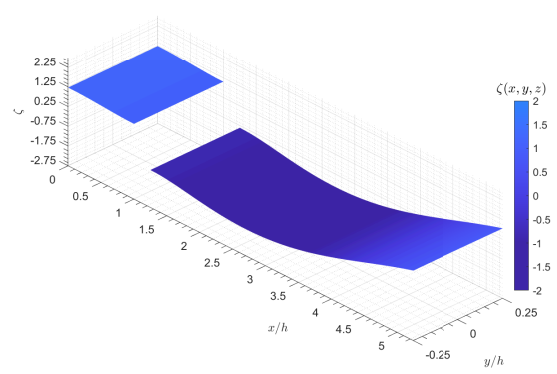
(a)  $w/h = 1/8$ ,  $Kh = 0.6014$  and  $\Theta = 0$ .



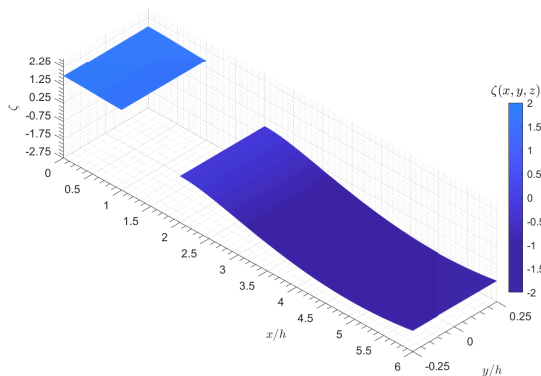
(b)  $w/h = 1/8$ ,  $Kh = 0.6823$  and  $c/h = 1$ .



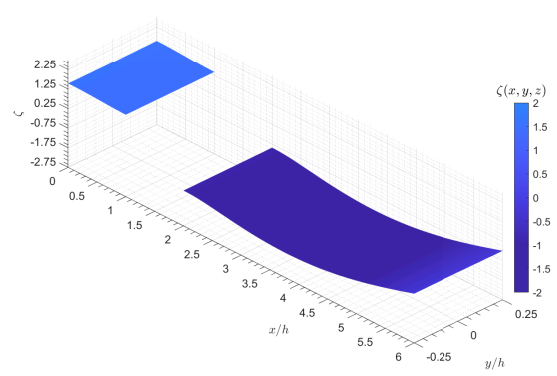
(c)  $w/h = 1/4$ ,  $Kh = 0.5205$  and  $\Theta = 0$ .



(d)  $w/h = 1/4$ ,  $Kh = 0.6014$  and  $c/h = 1$ .



(e)  $w/h = 1$ ,  $Kh = 0.2778$  and  $\Theta = 0$ .



(f)  $w/h = 1$ ,  $Kh = 0.3587$  and  $c/h = 1$ .

Figure 9.13: Free surface elevation with  $b/h = 1$ ,  $a/h = 1/2$  and  $d/h = 1/2$ .

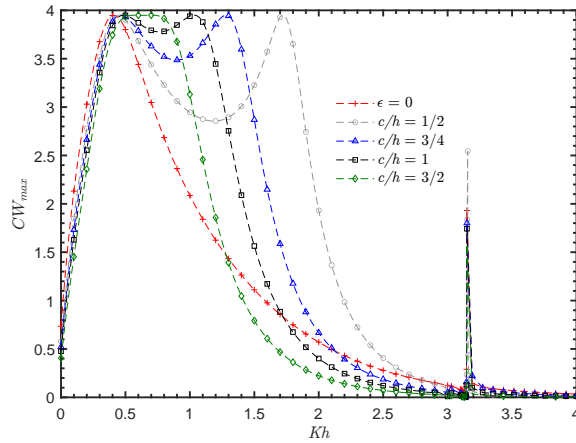


Figure 9.14: Capture width with  $b/h = 1$ ,  $w/h = 1/2$  and  $d/h = 1/2$  against  $Kh$  for different air column height to water depth ratios  $c/h = (1/2, 3/4, 1 \text{ and } 3/2)$ .

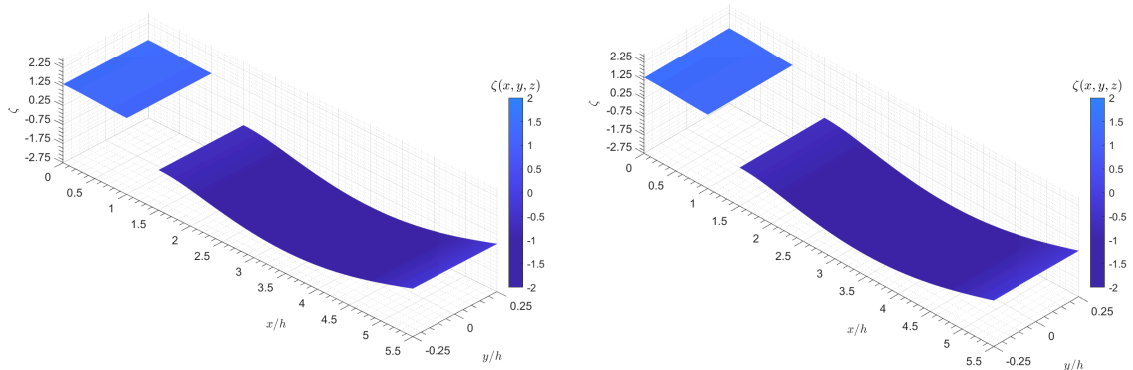
width curve is reduced, and a less hydrodynamic performance is achieved. On the other hand, when the ratio of the height of the air column to the water depth is small, a trough in the curve between the maximum values of  $CW_{max}$  appears and it becomes more prominent as  $c/h$  decreases.

The three dimensional surface plots of the free surface elevation  $\zeta$  with  $b/h = 1$ ,  $w/h = 1/2$  and  $d/h = 1/2$  for different ratios of air column height to water depth  $c/h (= 1/2, 3/4 \text{ and } 3/2)$  are shown in Figs. 9.15a–c. It can be seen that the magnitude of the free surface elevations inside the OWC chamber are not significantly affected by the variation in the height of the trapped air. In addition, with the support of Fig. 9.7b, these figures show that larger wavelengths are needed for the OWC device to reach the resonance condition as  $c/h$  decreases.

## 9.8 Conclusions

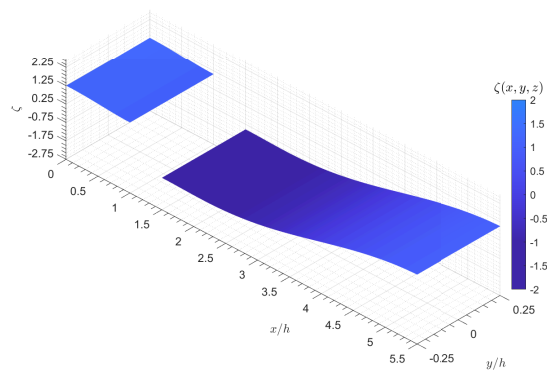
The effects of the OWC chamber design and the linearized air compressibility on the OWC performance were investigated in this work. The three dimensional BEM with nine-noded quadrilateral panels were used to solve the associated BVP. The domain was separated into two regions and the BEM was applied separately. Then, the subdomains were matched by the application of the continuity conditions of velocity potential and flux at the common interface. Comparisons were performed with cases addressed by [Evans and Porter \(1995\)](#), [Morris-Thomas et al. \(2006\)](#) and [Rezanejad et al. \(2017\)](#). Numerical calculations for the maximum capture width, hydrodynamical coefficients and free surface elevation were then obtained and analysed for different physical configurations.

Regarding the effect of the OWC chamber structural configuration, the results showed that by increasing the width of the OWC chamber, the wave frequency at which resonance occurs is not modified while the effective area of the capture width under the curve increases. It was found that by increasing the chamber length compared to water depth, the frequency at which



(a)  $c/h = 1/2$  and  $Kh = 0.4396$ .

(b)  $c/h = 3/4$  and  $Kh = 0.4396$ .



(c)  $c/h = 3/2$  and  $Kh = 0.6823$ .

Figure 9.15: Free surface elevation with  $b/h = 1$ ,  $a/h = 1/2$ ,  $w/h = 1/2$  and  $d/h = 1/2$ .

resonance occurs decreases while the capture width bandwidth is not significantly modified.

Furthermore, for a small  $b/h$  ratios, the peaks of radiation conductance coefficient are maximum for longer frequencies, while the range of negative values in the radiation susceptance coefficient is shortened. In the case of the front wall draft, it was found that the effective area of capture width and the magnitude of the first natural frequency, both increase when the front draft decreases. A larger draft also reduces the band in the radiation conductance coefficient, while increasing the range of negative values in the radiation susceptance coefficient. By increasing the thickness of the front wall, it was found that the bandwidth of the capture width curves and the peak frequency value are reduced. An increase in the ratio  $w/h$  leads to a decrease in the radiation conductance bandwidth, while an increase in the range of negative values in the radiation susceptance is obtained. When the height of the trapped air column was analyzed, it was seen that air compressibility increases the capture width bandwidth and the magnitude of the peak resonant frequency.

On the other hand, in the case of the free surface elevation, for small  $b/h$  ratios, it was observed that the amplitude of oscillation was higher, whereas for small  $a/h$  ratios the trend was the opposite. Furthermore, for front wall thickness, it was observed that an increase in the  $w/h$  ratio, increases the free surface elevation at the resonance frequency, while the wavelength must be longer for the OWC device to achieve the state of resonance. Regarding the variation of the air volume within the chamber, it was found that shorter wavelengths are needed for the OWC device to reach the resonance condition when the air column height to the water depth ratio increases. In general, when the air compressibility is taken into account, it was found that to reach resonance, higher wave frequencies are needed.

In conclusion, the OWC chamber design and the air compressibility are two important aspects to be taken into account when analysing the OWC capture width. Under the proposed assumptions, the present 3D BEM model was seen to be a useful technique for obtaining a solution to the BVP; however, more studies should be carried out in the future in order to provide more reliable estimates of the OWC capture width, under real conditions. It is hoped that the findings of this work will promote further 3D analysis of OWC onshore technologies, and provide useful knowledge for the effective harnessing of wave energy.

## Bibliography

- Becker, A. (1992). *The Boundary Element Method in Engineering: A Complete Course*, McGraw-Hill.  
URL: <https://books.google.com.mx/books?id=Co9YAAAAYAAJ>
- Brito-Melo, A., Sarmiento, A., Clement, A. and Delhommeau, G. (1999). A 3d boundary element code for the analysis of owc wave-power plants, *Proceedings of the 9th International Offshore and Polar Engineering Conference (Volume 1)*, I pp. 188–195.
- Cabral, T., Clemente, D., Rosa-Santos, P., Taveira-Pinto, F., Morais, T., Belga, F. and Cestaro, H. (2020). Performance assessment of a hybrid wave energy converter integrated into a harbor

CHAPTER 9. A THREE-DIMENSIONAL ANALYSIS OF THE HYDRODYNAMIC PERFORMANCE OF A LAND-FIXED OWC DEVICE

---

- breakwater, *Energies* **13**(1).  
**URL:** <https://www.mdpi.com/1996-1073/13/1/236>
- Count, B. M. and Evans, D. V. (1984). The influence of projecting sidewalls on the hydrodynamic performance of wave-energy devices, *Journal of Fluid Mechanics* **145**: 361–376.
- Delauré, Y. and Lewis, A. (2003). 3d hydrodynamic modelling of fixed oscillating water column wave power plant by a boundary element methods, *Ocean Engineering* **30**(3): 309–330.  
**URL:** <https://www.sciencedirect.com/science/article/pii/S002980180200032X>
- Dizadji, N. and Sajadian, S. E. (2011). Modeling and optimization of the chamber of owc system, *Energy* **36**(5): 2360 – 2366.  
**URL:** <http://www.sciencedirect.com/science/article/pii/S0360544211000119>
- Dominguez, J. (1993). *Boundary Elements in Dynamics*, Computational Engineering, Computational Mechanics Publications.  
**URL:** <https://books.google.com.mx/books?id=N4ghw092NIMC>
- Şentürk, U. and Özdamar, A. (2012). Wave energy extraction by an oscillating water column with a gap on the fully submerged front wall, *Applied Ocean Research* **37**: 174 – 182.  
**URL:** <http://www.sciencedirect.com/science/article/pii/S0141118712000405>
- Evans, D. and Porter, R. (1995). Hydrodynamic characteristics of an oscillating water column device, *Applied Ocean Research* **17**(3): 155 – 164.  
**URL:** <http://www.sciencedirect.com/science/article/pii/0141118795000089>
- Evans, D. and Porter, R. (November 1997). Efficient calculation of hydrodynamic properties of owc-type devices, *ASME Journal of Offshore Mechanics and Arctic Engineering* **119**(4): 210–218.
- Evans, D. V. (1976). A theory for wave-power absorption by oscillating bodies, *Journal of Fluid Mechanics* **77**(1): 1–25.
- Evans, D. V. (1981). Power from water waves, *Annual Review of Fluid Mechanics* **13**(1): 157–187.  
**URL:** <https://doi.org/10.1146/annurev.fl.13.010181.001105>
- Evans, D. V. (1982). Wave-power absorption by systems of oscillating surface pressure distributions, *Journal of Fluid Mechanics* **114**: 481–499.
- Falcao, A. (2000). The shoreline owc wave power plant at the azores, *Proceedings of the 4th European Wave Energy Conference, Aalborg, Denmark* pp. 42–47.
- Falcão, A. F. and Henriques, J. C. (2016). Oscillating-water-column wave energy converters and air turbines: A review, *Renewable Energy* **85**: 1391 – 1424.  
**URL:** <http://www.sciencedirect.com/science/article/pii/S0960148115301828>

CHAPTER 9. A THREE-DIMENSIONAL ANALYSIS OF THE HYDRODYNAMIC PERFORMANCE OF A LAND-FIXED OWC DEVICE

---

- Falcão, A. F. O. (2010). Wave energy utilization: A review of the technologies, *Renewable Sustainable Energy Rev.* **14**(3): 899 – 918.  
**URL:** <http://www.sciencedirect.com/science/article/pii/S1364032109002652>
- Falcão, A. F., Sarmiento, A. J., Gato, L. M. and Brito-Melo, A. (2020). The pico owc wave power plant: Its lifetime from conception to closure 1986–2018, *Applied Ocean Research* **98**: 102104.  
**URL:** <https://www.sciencedirect.com/science/article/pii/S0141118719305875>
- Falnes, J. and McIver, P. (1985). Surface wave interactions with systems of oscillating bodies and pressure distributions, *Applied Ocean Research* **7**(4): 225–234.  
**URL:** <https://www.sciencedirect.com/science/article/pii/014111878590029X>
- Gaspar, L. A., Teixeira, P. R. and Didier, E. (2020). Numerical analysis of the performance of two onshore oscillating water column wave energy converters at different chamber wall slopes, *Ocean Engineering* **201**: 107119.  
**URL:** <http://www.sciencedirect.com/science/article/pii/S0029801820301840>
- Geuzaine, C. and Remacle., J. (2009). Gmsh: a three-dimensional finite element mesh generator with built-in pre- and post-processing facilities, *International Journal for Numerical Methods in Engineering* **79**(11): 1309–1331.
- Gonçalves, R. A., Teixeira, P. R., Didier, E. and Torres, F. R. (2020). Numerical analysis of the influence of air compressibility effects on an oscillating water column wave energy converter chamber, *Renewable Energy* **153**: 1183 – 1193.  
**URL:** <http://www.sciencedirect.com/science/article/pii/S0960148120302755>
- Hasanabad, M. G. (2015). Free surface modeling in owc chamber with parabolic side walls using 3d bem, *AIP Conference Proceedings* **1648**(1): 770005.  
**URL:** <https://aip.scitation.org/doi/abs/10.1063/1.4912975>
- Heath, T. (2012). A review of oscillating water columns, *Philosophical Transactions of the Royal Society A* **370**: 235–45.
- Heath, T., Whittaker, T. and Boake, C. (2001). The design, construction and operation of the limpet wave energy converter (islay, scotland)[land installed marine powered energy transformer].
- Hong, D., Hong, S. and Hong, S. (2004). Numerical study of the motions and drift force of a floating owc device, *Ocean Engineering* **31**(2): 139–164.  
**URL:** <https://www.sciencedirect.com/science/article/pii/S0029801803001185>
- Howe, D. and Nader, J.-R. (2017). Owc wec integrated within a breakwater versus isolated: Experimental and numerical theoretical study, *International Journal of Marine Energy* **20**: 165 – 182.  
**URL:** <http://www.sciencedirect.com/science/article/pii/S2214166917300632>

CHAPTER 9. A THREE-DIMENSIONAL ANALYSIS OF THE HYDRODYNAMIC PERFORMANCE OF A LAND-FIXED OWC DEVICE

---

- John Ashlin, S., Sundar, V. and Sannasiraj, S. (2016). Effects of bottom profile of an oscillating water column device on its hydrodynamic characteristics, *Renewable Energy* **96**: 341 – 353.  
**URL:** <http://www.sciencedirect.com/science/article/pii/S0960148116303937>
- Josset, C. and Clément, A. (2007). A time-domain numerical simulator for oscillating water column wave power plants, *Renewable Energy* **32**(8): 1379–1402.  
**URL:** <https://www.sciencedirect.com/science/article/pii/S0960148106001108>
- Katsikadelis, J. (2002). *Boundary Elements. Theory and Applications*, Elsevier.
- Lin, Y., Bao, J., Liu, H., Li, W., Tu, L. and Zhang, D. (2015). Review of hydraulic transmission technologies for wave power generation, *Renewable & Sustainable Energy Reviews* **50**: 194 – 203.  
**URL:** <http://www.sciencedirect.com/science/article/pii/S1364032115004116>
- Mahnamfar, F. and Altunkaynak, A. (2017). Comparison of numerical and experimental analyses for optimizing the geometry of owc systems, *Ocean Engineering* **130**: 10 – 24.  
**URL:** <http://www.sciencedirect.com/science/article/pii/S0029801816305583>
- Masuda, Y. (1986). An experience of wave power generator through tests and improvement, in D. V. Evans and A. F. O. de Falcão (eds), *Hydrodynamics of Ocean Wave-Energy Utilization*, Springer Berlin Heidelberg, Berlin, Heidelberg, pp. 445–452.
- McIver, M. and McIver, P. (2016). The added mass for two-dimensional floating structures, *Wave Motion* **64**: 1–12.  
**URL:** <https://www.sciencedirect.com/science/article/pii/S016521251600024X>
- McIver, P. and Evans, D. (1984). The occurrence of negative added mass in free-surface problems involving submerged oscillating bodies, *Journal of Engineering Mathematics* **18**: 7–22.
- Medina Rodríguez, A. A., Blanco Ilzarbe, J. M., Silva Casarín, R. and Izquierdo Ereño, U. (2020). The influence of the chamber configuration on the hydrodynamic efficiency of oscillating water column devices, *Journal of Marine Science and Engineering* **8**(10): 751.
- Mei, C. C. (1976). Power Extraction from Water Waves, *Journal of Ship Research* **20**(02): 63–66.  
**URL:** <https://doi.org/10.5957/jsr.1976.20.2.63>
- Morris-Thomas, M. T., Irvin, R. J. and Thiagarajan, K. P. (2006). An Investigation Into the Hydrodynamic Efficiency of an Oscillating Water Column, *Journal of Offshore Mechanics and Arctic Engineering* **129**(4): 273–278.  
**URL:** <https://doi.org/10.1115/1.2426992>
- Ning, D.-Z., Shi, J., Zou, Q.-P. and Teng, B. (2015). Investigation of hydrodynamic performance of an owc (oscillating water column) wave energy device using a fully nonlinear hoberm (higher-order boundary element method), *Energy* **83**: 177 – 188.  
**URL:** <http://www.sciencedirect.com/science/article/pii/S0360544215001644>

CHAPTER 9. A THREE-DIMENSIONAL ANALYSIS OF THE HYDRODYNAMIC PERFORMANCE OF A LAND-FIXED OWC DEVICE

---

- Ning, D.-Z., Wang, R.-Q., Zou, Q.-P. and Teng, B. (2016). An experimental investigation of hydrodynamics of a fixed owc wave energy converter, *Applied Energy* **168**: 636 – 648.  
**URL:** <http://www.sciencedirect.com/science/article/pii/S0306261916300952>
- Polinder, H. and Scuotto, M. (2005). Wave energy converters and their impact on power systems, *2005 International Conference on Future Power Systems*, pp. 9 pp.–9.
- Rezanejad, K., Bhattacharjee, J. and Guedes Soares, C. (2013). Stepped sea bottom effects on the efficiency of nearshore oscillating water column device, *Ocean Engineering* **70**: 25 – 38.  
**URL:** <http://www.sciencedirect.com/science/article/pii/S0029801813002229>
- Rezanejad, K., Guedes Soares, C., López, I. and Carballo, R. (2017). Experimental and numerical investigation of the hydrodynamic performance of an oscillating water column wave energy converter, *Renewable Energy* **106**: 1 – 16.  
**URL:** <http://www.sciencedirect.com/science/article/pii/S0960148117300034>
- Rosa-Santos, P., Taveira-Pinto, F., Clemente, D., Cabral, T., Fiorentin, F., Belga, F. and Morais, T. (2019). Experimental study of a hybrid wave energy converter integrated in a harbor breakwater, *Journal of Marine Science and Engineering* **7**(2).  
**URL:** <https://www.mdpi.com/2077-1312/7/2/33>
- Ross, D. (2012). *Energy from the Waves*, Elsevier Science.  
**URL:** <https://books.google.com.mx/books?id=gZ47AAAAQBAJ>
- Service, U. S. M. M. (2007). *Alternative Energy Development and Production and Alternate Use of Facilities on the Outer Continental Shelf: Environmental Impact Statement*, Alternative Energy Development and Production and Alternate Use of Facilities on the Outer Continental Shelf: Environmental Impact Statement.  
**URL:** <https://books.google.com.mx/books?id=oUI3AQAAMAAJ>
- Sheng, W. (2019). Motion and performance of bdbb owc wave energy converters: I, hydrodynamics, *Renewable Energy* **138**: 106 – 120.  
**URL:** <http://www.sciencedirect.com/science/article/pii/S0960148119300163>
- Teixeira, P. R. and Didier, E. (2021). Numerical analysis of the response of an onshore oscillating water column wave energy converter to random waves, *Energy* **220**: 119719.  
**URL:** <http://www.sciencedirect.com/science/article/pii/S0360544220328267>
- Torre-Enciso, Y., Ortubia, I., Aguilera, L. and Marqués, J. (2009). Mutriku wave power plant: From the thinking out to the reality, *Proceedings of the 8th European Wave and Tidal Energy Conference* pp. 319–329.
- Vicinanza, D., Lauro, E. D., Contestabile, P., Gissoni, C., Lara, J. L. and Losada, I. J. (2019). Review of innovative harbor breakwaters for wave-energy conversion, *Journal of Waterway, Port, Coastal, and Ocean Engineering* **145**(4): 03119001.  
**URL:** <https://ascelibrary.org/doi/abs/10.1061/%28ASCE%29WW.1943-5460.0000519>



CHAPTER 9. A THREE-DIMENSIONAL ANALYSIS OF THE HYDRODYNAMIC  
PERFORMANCE OF A LAND-FIXED OWC DEVICE

---

Wang, D., Katory, M. and Li, Y. (2002). Analytical and experimental investigation on the hydrodynamic performance of onshore wave-power devices, *Ocean Engineering* **29**(8): 871 – 885.

**URL:** <http://www.sciencedirect.com/science/article/pii/S0029801801000580>

Zhu, G., Graham, D., Zheng, S., Hughes, J. and Greaves, D. (2020). Hydrodynamics of onshore oscillating water column devices: A numerical study using smoothed particle hydrodynamics, *Ocean Engineering* **218**: 108226.

**URL:** <http://www.sciencedirect.com/science/article/pii/S0029801820311495>

# Chapter 10

## Conclusion

### 10.1 Overall conclusions

The research work presented in this thesis is devoted to the theoretical study of the OWC wave energy converter for different configurations. The performance of land-fixed and fixed-detached OWC devices were analysed using frequency-domain models within the framework of linear wave theory. To obtain a solution, the matched EEM and the BEM were employed. The main attention of this study was given to the effect of the chamber configuration and wave direction on the hydrodynamic performance.

First, by means of the BEM, the effects of the front wall thickness on the performance of a land-fixed OWC device were analyzed. It turned out that a wider efficiency band was obtained with a thinner front wall. However, in practice, this geometrical aspect plays an important role since a thinner front wall will be less capable to resist the impact of extreme waves. The model was then applied to a single chamber of the Mutriku Wave Energy Plant, and it was found that the proposed bottom profiles modify the efficiency curve slightly, giving the possibility of improving the efficiency of the device in the long-wave regime.

Then, the influence of wave direction on the hydrodynamic efficiency of a land-fixed OWC with a thin front barrier was investigated. The matched EEM using dual series relations and the BEM were used, and an optimal agreement between these two techniques was achieved. The findings revealed that by increasing the wave angle of incidence, the bandwidth of the efficiency curves and the resonance frequency both increase. This has advantages for wave power extraction in real sea conditions where OWC devices receive incoming waves at different angles.

The impacts of front wall thickness on the performance of an asymmetric fixed-detached OWC device were then investigated using the matched EEM and BEM. The effects of adding a step under the OWC chamber and a reflecting wall in the downstream region were also studied. The results demonstrated that the presence of a reflecting wall is important because, at low frequencies, the presence of constructive and destructive wave interference from the OWC device and the waves reflected by the wall results in zero efficiency. This phenomenon is very sensitive to changes in the OWC parameters and can lead to restrictions in wave energy harvesting at

long incident wavelengths.

By using the matched EEM and BEM, the combined effects of the front wall thickness and wave direction on the performance of a land-fixed OWC device were analyzed. These semi-analytical and numerical approaches were found to be in good agreement. The results showed that both a thick front wall and a large incidence angle of the wave can significantly narrow the hydrodynamic efficiency band and modify the resonant frequency.

Finally, a 3D BEM with nine-noded quadrilateral elements was employed to analyze the influence of different OWC geometric parameters on the capture width, hydrodynamical coefficients and free surface amplitude. It was found that the chamber configuration and the linearized air compressibility have a significant impact on the capture width bandwidth, the resonant frequency and the free surface amplitude within the chamber.

More detailed conclusions are provided in each article included in this thesis.

## 10.2 Original contributions

The main contributions of this thesis are as follows:

1. The development of a 2D multi-region BEM code with quadratic elements for analyzing the influence on the performance of land-fixed and fixed-detached OWC devices when interacting with perpendicular and oblique incident waves.
2. The development of a 3D multi-region BEM code with higher-order elements for analyzing the capture width of a land-fixed OWC device.
3. The implementation of dual series relations in matched EEM to investigate the effect of oblique waves in the performance of a land-fixed OWC device.
4. The use of the matched EEM to study the influence of thick front barriers and oblique waves in the efficiency of land-fixed and fixed-detached OWC devices.
5. Showing the significance of waves direction in the OWC device efficiency.
6. Demonstrating the effect of the thickness of the chamber barriers on the OWC device efficiency.
7. Investigating the variations on the device performance when a linear air compressibility model is considered.
8. Identifying the variations on the device performance caused by an asymmetrical configuration of the rear and front walls of a fixed-detached OWC device.
9. Analyzing the influence of a reflecting wall in the efficiency of a fixed-detached OWC device.
10. Highlighting the importance of chamber parameters and air compressibility in the free surface elevation.

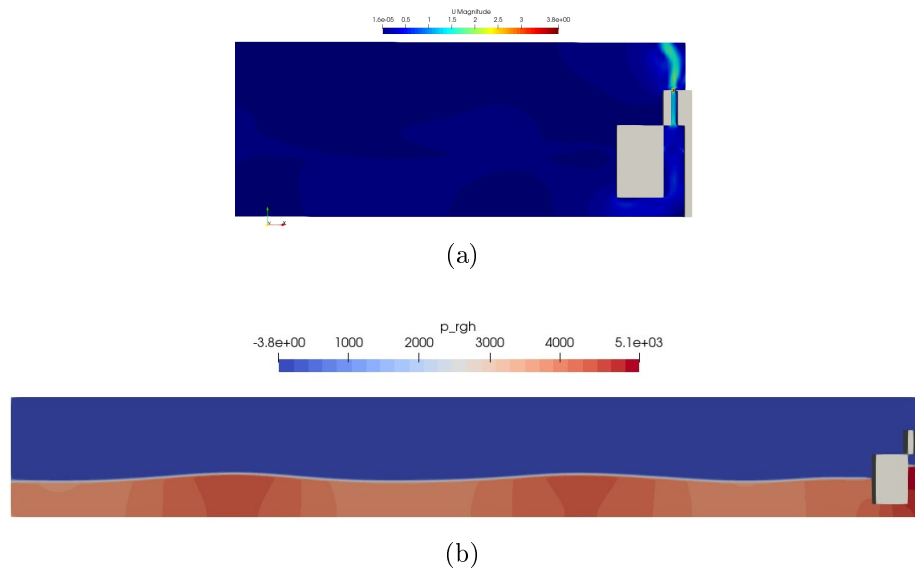


Figure 10.1: Numerical wave generation in OpenFOAM (a) Velocity magnitude and (b) Hydrostatic pressure of the interaction of water waves with a thick front barrier OWC device.

### 10.3 Recommendations for future work

In order to validate the theoretical results, several areas for further research were identified throughout this thesis.

#### High-performance numerical models

The main assumption in this thesis is related to the small motion amplitude and the use of the linear wave theory. However, dissipative energy processes (due to viscous effects, friction, flow separation), thermodynamic processes inside the chamber, as well as other non-linear effects, should be considered to provide more reliable estimates of the OWC performance under real conditions. Therefore, high-performance numerical models are required in order to identify the limits of linear wave theory and increase the knowledge about OWC devices, Fig. 10.1.

#### Model-scale experiments

The laboratory testing of different scale prototypes (1:25–1:20) should be conducted to validate: (i) the hydrodynamic models of the OWC devices used in this thesis (land-fixed and fixed-detached); (ii) the effect of the thickness of the front barrier on the resonant frequency; and (iii) the influence of wave direction on the OWC performance, Fig. 10.2. In addition, there is a need for experimental studies to model the PTO mechanism and the effect of air compressibility.

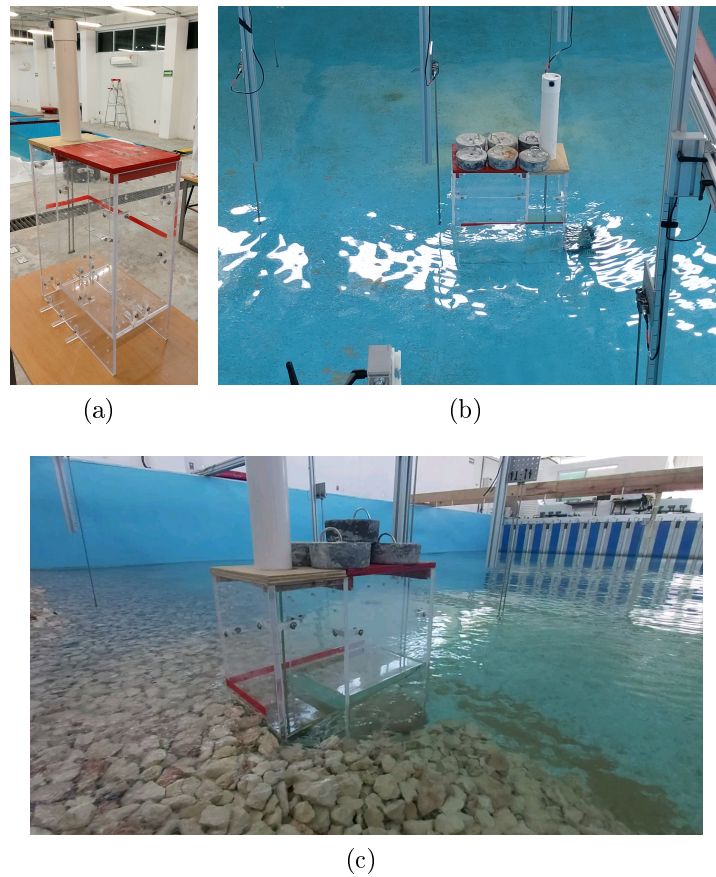


Figure 10.2: **(a)** Model scale of a thick front barrier OWC device and **(b)-(c)** testing in the multidirectional wave tank of the Autonomous University of Campeche.

## Array performance

The final development stage of any wave energy converter is related to the performance of a wave farm. The development of the array of OWC devices raises a number of research questions including: how the arrangement and distance between OWCs that operate affect the performance of the array? how the incoming waves at varying angles affect an integrated OWC-breakwater system such as the Mutriku Wave Energy Plant? how an array of fixed-detached OWCs can serve as a coastal protection measure while harnessing the energy from waves?